UNIVERSITY OF OKLAHOMA

GRADUATE COLLEGE

RATIONAL DESIGN, SYNTHESIS, CHARACTERIZATION AND OPTIMIZATION OF FACILITATED TRANSPORT MATERIALS IN NATURAL GAS AND PARAFFIN/OLEFIN SEPARATIONS

A DISSERTATION

SUBMTTED TO THE GRADUATE FACULTY

In partial fulfillment of the requirements for the

Degree of

DOCTOR OF PHILOSOPHY

By

MATTHEW THOMAS WEBB
Norman, Oklahoma
2024

RATIONAL DESIGN, SYNTHESIS, CHARACTERIZATION AND OPTIMIZATION OF FACILITATED TRANSPORT MATERIALS IN NATURAL GAS AND PARAFFIN/OLEFIN SEPARATIONS

A DISSERTATION APPROVED FOR THE

SCHOOL OF SUSTAINABLE, CHEMICAL, BIOLOGICAL, AND MATERIALS ENGINEERING

BY THE COMMITTEE CONSISTING OF

Dr. Michele Galizia, Chair

Dr. Sepideh Razavi, Co-Chair

Dr. Dimitrios V. Papavassiliou

Dr. Ngoc T. Bui

Dr. Mrinal C. Saha

I dedicate this work to my parents, Randy and Pamela Webb, who instilled in me the values of hard work and perseverance, making this achievement possible.

ACKNOWLEGDEMENTS

There are several people that I would like to acknowledge and thank, both for their support and friendship throughout my time at the University of Oklahoma. First and foremost, I would like to thank both my advisors, Dr. Michele Galizia and Dr. Sepideh Razavi. Their wisdom and guidance throughout my Ph.D has been instrumental in shaping both this work and my future endeavors. I would also like to thank the members of my committee, Dr. Dimitrios Papavassiliou, Dr. Ngoc Bui, and Dr. Mrinal Saha for their service and advise.

I am also grateful for meaningful collaborations that have pushed my bounds in terms of research and knowledge, for those at: the University of Valladolid Spain and/or the National Institute of Carbon, Angel Lozano, Cristina Álvarez, and Laura Matesanz-Niño; CSIRO, Anita Hill; the University of Oklahoma, Alberto Striolo, and Tran Le; the University of North Texas, Marco Buongiorno Nardelli; and Maxwell Robotics, Kristofer Gleason.

I also wish to extend my thanks to the Zach Smith Lab, and Pablo Dean, at MIT, for graciously allowing me to visit and work in their lab, expanding my knowledge on the design, construction, and operation of advanced gas transport techniques. Also, I would like to thank Preston Larson, Julian Sabisch, Tingting Gu, and Andy Madden at the Samuel Roberts Noble Microscopy Laboratory, whose integral knowledge and teachings assisted in numerous experiments, as well as my attainment of the OU Microscopic Imaging and Technology certificate.

I would like to acknowledge each and every individual that I was fortunate to work with and alongside on a daily basis in both the Colloid and Interfacial Science Lab, and the Membrane Lab at OU: Lucas Condes, Will Box, Harold Ly, Aditi Gali, Jacob Castaneda, Matt Casey,

Shivam Patel, Luke Wilson, Eduarda Barros de Oliveira, Blake Bartlett, Ashley Copelin, Addie Landry, Bryce Goodin, Grant Smith, Jing Deng, Elton Lima Correia, Siddharth Thakur, Nick Brown, Aanahita Ervin, and Salome Tavera. Additionally, I would like to thank Andrew D'Amico and Buck Sullivan for his advice and suggestions, as well as teaching me the design and machining aspects required for the construction of many of our experimental apparatuses.

I would like to thank my parents, Randy and Pamela Webb, who with their continuous support and providence, enabled me to pursue my path. Their installment of self-determination and persistence have helped me overcome many obstacles in my life.

Finally, and most importantly, I would like to thank my wife, Emily Webb, whose love and understanding have been the most potent force behind my endeavors. Emily, you've been my confidant, my rock, and my inspiration. Your wisdom and encouragement have often been the catalyst that kept me moving forward, especially during moments of doubt and exhaustion. Our wonderful dogs Penelope and Aurora, and Beans, our mischievous cat, who have been more than just companions. They've been the soul of our home, bringing laughter, comfort, and a much-needed respite from work.

I'd like to acknowledge the support of the National Science Foundation (NSF) through the award CBET-2005282. As well as the School of Sustainable Chemical, Biological and Materials Engineering (SCBME), and the University of Oklahoma for the resources and faculty that have guided and helped shape my path.

TABLE OF CONTENTS

LIST OF TABLES

LIST OF FIGURES

RATIONAL DESIGN, SYNTHESIS, AND CHARACTERIZATION OF FACILITATED TRANSPORT MATERIALS IN NATURAL GAS AND PARAFFIN/OLEFIN SEPARATIONS

ABSTRACT

Facilitated transport membranes (FTMs) have demonstrated the ability to simultaneously enhance permeability and selectivity, overcoming the traditional perm-selectivity trade-off observed in conventional polymer membranes. Despite showing high performance, metal ion carriers experience photo/chemical aging, which in turn, leads to a rapid decay in performance. Additionally, when embedded into polymer materials, structural defects may form at the metal-polymer interface that, despite accelerating small molecule transport, cause a parallel loss in selectivity. To address the issues mentioned above, we fabricated silver nanoparticles (NPs) stabilized using a series of poly(amic-acid)s (PAAs) derived from 4,4-oxydiphthalic anhydride and a polyetheramine, Jeffamine. Overall, this approach attempts to simultaneously *i)* achieve defect-free mixed matrix membranes (MMMs), *ii)* target CO_2 and ethylene (C_2H_4) selective transport, and *iii)* reduce photo/chemical-induced degradation.

As part of the particle design procedure, dynamic light scattering (DLS) is proposed as a more efficient alternative to traditional methods, such as viscometry measurements, to estimate the polymer solubility parameter (δ). In determining these values for the series of PAAs used throughout this work, justification and development of a liquid-liquid extraction process for producing silver NPs was established. The results show that DLS achieved similar δ values for an array of polymers, within 8%, to those found using viscometry measurements. The DLS method was further established by making a comparison to the group contribution method, for which we provide updated group contribution parameters, along with their uncertainty, according to the technique recently reported by Smith et al. These updated group contribution parameters

result in a mean absolute relative error of 9.0% in predicting the solubility parameter on a test set of 40 polymers, which is on par with the average 10% error reported previously.

The synthesized silver-PAA NPs, which were thoroughly characterized via TEM/EDS analysis, showed near spherical morphology (~5 nm) and lack of aggregation. The occurrence of the chelating reaction between silver and the PAA showed that favorable carbonyl-silver coordination interactions were achieved. The effect of the PAA length and ether functional group concentration on the structure and transport properties of the NPs were systematically investigated.

The silver-PAA NPs were added into a commercial polymer, Pebax 1657, to fabricate defect-free MMMs for CO_2/CH_4 and C_2H_4/C_2H_6 separations, whose structure and transport properties were examined at various NP loadings (0-4 wt%). Remarkably, the inclusion of only 2.5 wt% NPs in Pebax enhanced CO_2 and C_2H_4 permeability by 50% and 100%, respectively, while increasing both CO_2/CH_4 and C_2H_4/C_2H_6 selectivity between 80-100% relative to the neat polymer. A detailed analysis of the transport mechanism and underlying energetics, as well as changes in thermo-mechanical properties, was performed to elucidate the molecular origin of the observed membrane performance. This information was subsequently used to shorten the length of the PAA, in effort to minimize suppression of the glass transition temperature, i.e., increases in polymer chain mobility, as well as to prevent decreases of crystallinity at higher loadings of NPs, both of which negatively impact overall gas selectivity. Finally, the synthesized materials were exposed to hydrogen over 1 week to assess the long-term chemical stability. Each material exhibited drops between 10-30% in both CO_2 and C_2H_4 permeability, as well as CO_2/CH_4 and C_2H_4/C_2H_6 selectivity. However, despite the observed decline in performance, each MMM retains properties superior to that of neat Pebax.

In summary, this dissertation explores the design, synthesis, characterization, and optimization of novel facilitated transport membranes (FTMs) specifically tailored for natural gas and paraffin/olefin separations. The overarching goal of this work is to elucidate the fundamental mechanisms governing gas diffusivity, sorption, selectivity, and stability in these materials, providing insight into their potential use in advanced gas separation technologies.

Chapter 1. Motivation Introduction, and Theory

1.1. Motivation

The survival of humanity depends on having a sustainable supply of energy and chemicals. One such example is methane, a major component found in natural gas, which serves as a vital energy source for both industrial and domestic applications. However, before being put into practical use, excess carbon dioxide must be reduced to less than 2%, adding a significant cost to natural gas processing.[1,2] Amine absorption is commonly used to remove CO_2 from process streams. Despite being a well-established method, with CO_2 recovery rates up to 98%, liquid amines are both toxic to nature and corrosive to process equipment.[3] Additionally, periodic regeneration of the absorbents through pressure or thermal swings creates concern over operational expenditures.[4] In addition to being a contaminate within natural gas, CO_2 is also produced through various petrochemical processes. Globally, existing power plants emit billions of tons of CO_2 per year, accounting for nearly 65% of greenhouse gas emissions, creating implications that may affect the rate of global warming.[5] This effect also plays a role in the acidification of oceans, generation of lung afflicting smog, and more. If the amine absorption approach is adapted into every power station in the U.S., in order to limit these emissions, it is estimated that full implementation will cost as much as 30% of the total U.S. annual GDP growth.[6]

Not only relevant to natural gas processing, gas separations are a critical process in numerous industrial applications, including hydrogen production from methane steam reforming and olefin/paraffin separations.[7,8] For example, ethylene, is needed in high purity to produce polyethylene. Polyethylene represents nearly 35% of the world's plastic demand, with a global market volume of nearly 110 million metric tons.[9] To put this in perspective, ethylene production

is ranked as the second largest contributor of global energy consumption, nearly 2 EJ/year.[10] Yet, the separation of ethane from ethylene is complex and costly process, due to their nearly identical condensability and molecular sizes.[11,12]

The insurance of a more sustainable future requires a capture process that not only fits a targeted separation performance, but accomplishes it with minimal energy and economic input. It has been estimated that thermal driven separation processes (i.e., distillation, drying, evaporation, etc.) account for 80% of the energy consumed in U.S. separations.[6] Alternatives, such as membrane technologies, provides both energetic and economic advantages over competing technologies. Compared to other purification processes, membranes separation is known for its system compactness, energy efficiency, operational simplicity, and an ability to overcome thermodynamic limitations. Although membrane-based technologies can mitigate issues expedited by amine absorption, large-scale separations are still limited by an intrinsic trade-off between permeability and selectivity.[6,13]

Facilitated transport membranes (FTMs) have been demonstrated to be effective in simultaneously increasing permeability and selectivity, making them an alternative approach to overcome the perm-selectivity trade-off experienced by conventional polymer membrane.[14–16] Despite high performance, metal ion carriers experience photo/chemical aging, which, in turn, cause a rapid decay of their performance.[14,15] Moreover, when embedded in polymer materials to form mixed matrix membranes (MMMs), structural defects may form at the metal-polymer interface that, despite accelerating small molecule transport, cause a parallel selectivity loss. [17]

To address the issues mentioned above, in this work, we fabricated silver nanoparticles (NPs) stabilized using a polymer derived from 4,4-oxydiphthalic anhydride (ODPA) and a polyetheramine, Jeffamine. In conjunction with the metal core, polymer agents may be used to not

only provide stability against aggregation to the NP, but also evoke separate effects on gas transport properties through the simultaneous targeting of the diffusivity and solubility selectivity of dense polymer films. This is accomplished by means of the actions of the silver ions, which promotes CO_2 facilitated transport, and, in the case of CO_2, that of the Jeffamine ether groups, which promotes CO_2 solubility. Additionally, polymer agents can mediate an interphase between silver and the bulk polymer, while offering carrier sites protection from photo/chemical degradation.[18,19] It is within the goal of this study to elucidate the molecular mechanisms by which both silver and the Jeffamine ether groups contribute, both individually and synergistically, to the membrane transport properties by developing the corresponding structure-property correlations.

1.2. The Solution-Diffusion Model

1.2.1. Permeability

Beginning in the 1940s, the solution-diffusion model has been used to describe small molecule (e.g., gases) transport in dense, non-porous, polymeric membranes (cf. Eq. 1).[20] The solution-diffusion model assumes a constant, and uniform, pressure within the membrane, expressing the mass flux as being only concentration driven, i.e., following Fick's first law[20,21]:

$$J_i = \overline{D}_i \frac{dC_i}{dx} \qquad \text{(Eq. 1)}$$

Where J is the mass flux of gas species i, $\overline{D}_i$ is the concentration-averaged diffusivity of gas species i, and $\frac{dC_i}{dx}$ is the concentration gradient of gas species i across the membrane. In this model, the concentration-averaged diffusivity represents the average diffusivity that is observed, as the gas transitions from one concentration to another across the membrane material (cf. Eq. 2)[21].

$$\overline{D}_i = \frac{1}{C_{i,L} - C_{i,0}} \int_{C_{i,0}}^{C_{i,L}} D\left(C_{j,x}\right) dC \qquad \text{(Eq. 2)}$$

Where $D\left(C_{j,x}\right)$ is the effective local diffusivity, and $C_{i,0}$ and $C_{i,L}$ are the gas concentrations found at position $x = 0$ (i.e., the upstream interface) and $x = L$ (i.e., the downstream interface),

respectively. If we integrate these equations over the membrane thickness, L, and relate gas concentration to the external pressure (p) using a sorption coefficient (S), i.e., $C_i = p * S_i$, then Eq. 1 can be rewritten as follows (given the downstream concentration is negligible):

$$J = \frac{\bar{D}_i S_i \Delta p}{L} \equiv \frac{P_i \Delta p}{L} \quad \text{(Eq. 3)}$$

Where $\bar{D}_i$ is the concentration average diffusivity coefficient, S_i is the gas sorption coefficient, Δp is the transmembrane pressure, and P_i is the gas permeability coefficient. It becomes clearer that the separation process is defined to occur via two mechanisms, 1) condensation of an external fluidic phase into the polymer matrix, and 2) diffusion of these condensed species across the thickness of the film, driven by a concentration gradient, before being desorbed on the low-pressure face of the membrane. The solution-diffusion model therein presents the productivity of a material, the permeability (P_i), as the product of the penetrant mobility within the polymer (i.e., concentration averaged diffusivity $(\bar{D}_i)$), and its affinity towards the polymer phase (sorption (S_i)):

$$P_i = \bar{D}_\iota S_i \quad \text{(Eq. 4)}$$

Permeability therein, is the pressure and thickness normalized flux, and is therefore an intrinsic property of the material. This allows for direct comparisons in performance between different membrane materials.

1.2.2. Selectivity

An additional specification, made to quantify the separation ability between two penetrants, species i and j, is the selectivity (α_{ij}), defined as the ratio of permeability between both components (cf. Eq. 5)

$$\alpha_{ij} = \frac{P_i}{P_j} \quad \text{(Eq. 5)}$$

If we apply (Eq. 4) to (Eq. 5), the overall selectivity is broken into two separate parts, 1) the sorption-selectivity (α_{ij}^{S}), and 2) the diffusivity-selectivity $\left(\alpha_{ij}^{D}\right)$. Sorption-selectivity is typically driven through enthalpic factors, a thermodynamic measure of the difference in affinity for each gas to condense into the polymer materials. Diffusivity-selectivity is instead related to entropic factors, or how well the materials can discriminate differences between different gas sizes.[22]

$$\alpha_{ij} = \left(\frac{\bar{D}_i}{\bar{D}_j}\right)\left(\frac{S_i}{S_j}\right) = \alpha_{ij}^{D}\alpha_{ij}^{S} \qquad \text{(Eq. 6)}$$

Selectivity can also be defined as both the ideal selectivity, i.e., the ratio of permeabilities measured in single-component experiments, at a given pressure and temperature, or the real selectivity, i.e., the ratio of permeabilities measured in multi-component experiments, at a given pressure and temperature. In mixtures, gases can compete and interact with one another, which may affect both the sorption, and diffusivity of each component in the mixture.[23] Therefore, to design competitive materials capable of exceeding and/or replacing current separation processes, solubility and diffusivity must be engineered to enhance permeability and selectivity to an acceptable threshold value dependent on the application.

1.3. Facilitated Transport Mechanisms

Structure-property relations are developed by breaking permeability coefficients into their base contributions, $\bar{D}$ and S, as they relate to membrane structure and morphology. For example, penetrant solubility increases with an increased affinity to the polymer backbone.[24,25] Alternatively, diffusivity might be tuned by embedding inorganic particles in polymer matrices to fabricate MMMs.[17,26] In the past, size-selective fillers, such as zeolites or metal organic frameworks have been used. Because of high costs or dramatic losses in selectivity, due to the

formation of non-selective interfacial defects, they have had little large-scale appeal.[15,27] Alternatively, facilitated transport can be used to tune the permeability and selectivity through a reversible reaction between transport carriers (i.e., transition metals) and specific, targeted penetrant species (e.g., CO_2 and C_2H_4) (cf. Eq. 7 and Eq. 8).[28,29]

$$M^+ + CO_2 \leftrightarrow \mathrm{M}^+(CO_2) \quad \text{(Eq. 7)}$$

$$M^+ + C_2H_4 \leftrightarrow \mathrm{M}^+(C_2H_4) \quad \text{(Eq. 8)}$$

The formation of this metal-organic complex can be described by the Dewar-Chatt-Duncanson model. C_2H_4 and CO_2 donates electron density into the metal s-orbital from a π-symmetry bonding orbital, forming a σ bond. The metal then back-donates electrons from a filled d-orbital into the empty π^* orbital of C_2H_4 and CO_2, forming a π-complexation (cf. Figure 1).[30] Therefore, in the case of facilitated transport membranes (FTMs), the materials not only operate on solute partitioning and diffusion, but also on a reversible complexation reaction within the membrane. This then becomes analogous to chemical absorption and stripping on either side of the membrane material.

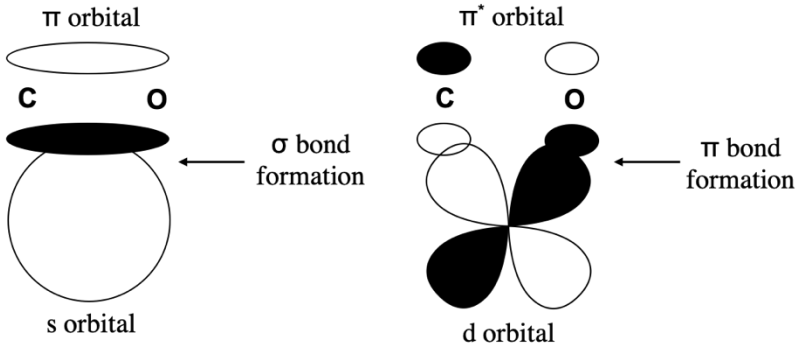

Figure 1: *Pi-complexation between CO_2 and a transition metal ion. 1) A sigma bond is formed from the donation of CO_2 pi electrons to an empty metal s orbital (left) and 2) A pi bond is formed from the back donation of electrons from a metal d orbital to the anti-pi orbital of CO_2 (right).*

After the solute dissolves into the membrane, it can readily diffuse from site to site across the FTM in the case of fixed carriers, e.g., silver nanoparticles. The total flux (J_T) can then be written as the flux due to normal solution-diffusion (J_{SD}) and the flux due to the facilitated mechanism (J_F) (cf. Eq. 9).

$$J_T = J_{SD} + J_F \quad \text{(Eq. 9)}$$

Thus, this process requires the carriers to have the ability to react quickly with C_2H_4 or CO_2, to form a complex that can easily be decomposed. Therefore, it is essential to use metals that form appropriate interactions with C_2H_4 and CO_2. Among those found, metal ions including Cu^+, Co^{2+}, Fe^{2+}, Au^+, Zn^{2+}, K^+, Cd^{2+}, and Ag^+ are capable of facilitated gas transport. In general, the electronegativity of these metal ions can be used to demonstrate the intensity between the metal and CO_2 during π-complexation. As a rule of thumb, an electronegativity between 1.6-2.3 is considered to form reversible π-complexations.[15,30] Additionally, it is important that the chemical hardness (resistance towards electron cloud polarization or deformation) remain as low as possible, with the idea of using metals more prone to react with C_2H_4 or CO_2. Thus, out of the candidates, Ag^+ and Cu^+ stick out, with an electronegativity/chemical hardness of 1.93/6.9 and 1.9/6.3 respectively.[30] The use of silver as a facilitator in this process, despite an economic disadvantage (Ag - \$0.73/g, Cu - \$0.009/g), becomes preferred due to Cu^+'s strong tendency to oxidize into Cu^{2+}, losing its facilitation ability.[15,31,32] However, silver ions are still readily attacked by UV radiation or through chemical species such as C_2H_2, H_2, or H_2S, which serves to shift silver ions into a new oxidation state, Ag^0. This also results in complete loss of the facilitated effect. Though, as we transition to the use of Ag NPs, where surface ions may not always be present, the use of an electron acceptor is typically used to activate the particle. This activation is the result of the surface

being positively polarized, thus strengthening silver's ability to undergo π-complexation.[33] Coincidentally, this polarization process also enhances the stability of the material, thus making this technique more favorable for long term applications.

1.4. Glassy vs Rubbery Polymers

Distinguishing the difference between rubbery and glassy polymers becomes important in understanding the various behaviors in thermal, mechanical, and transport properties that we observe in the work. Glassy polymers, which exist below the glass transition temperature (T_g), exhibit non-equilibrium free volume that is due to frustrated local polymer chain packing, ultimately exhibiting lower densities than their theoretical maximum (cf. Figure 2). Due to this excess free volume, glassy polymers contain small, unconnected voids called Langmuir sites that boost overall sorption.[34] Consequently, because this volume exists beyond its equilibrium phase, it tends to relax over time and densify the material. As a consequence, resistance to transport through the material will increase, a phenomenon known as physical ageing.[34]

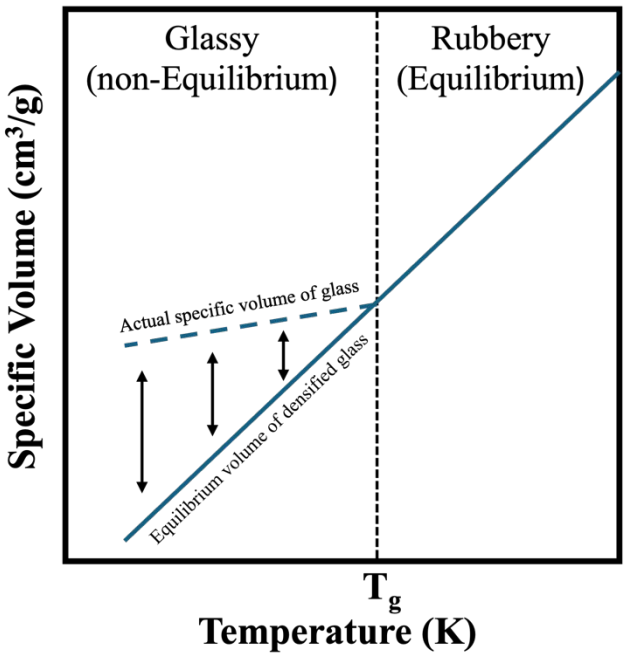

Figure 2: *Demonstration of polymer rubbery and glassy states using the specific volume as a function of temperature. Below the glass transition temperature (T_g), polymer chains lose the ability to pack efficiently quickly enough, freezing chains in place and exhibiting non-equilibrium excess free volume.*

Opposingly, because rubbery polymers are above their T_g and do not contain any excess non-equilibrium free volume, they do not physically age. This is an important concept to note as Pebax 1657, the polymer of interest in this work, is a co-block polymer containing both a rubbery poly(ethylene oxide) (PEO, ~60%, $T_g \approx -50°C$) and glassy poly(amide 6) (PA6, ~40%, $T_g \approx 60°C$) regions.[35,36] However, it has been extensively shown that the majority of transport occurs through the PEO segments, whilst PA6 serves as adding structural support (cf. Figure 3).[35,36]

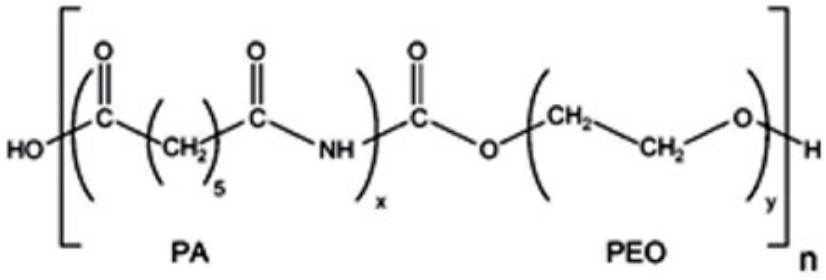

Figure 3: *Chemical structure of Pebax 1657, PA6 stands for polyamide 6 and PEO stands for poly(ethylene oxide). x=0.4 and y= 0.6)*

Thus, given this fact, Pebax 1657 is not considered susceptible to the phenomena of physical ageing. As it will be shown in Section 1.5.4, silver nanoparticles are susceptible to photo/chemical attack, hence, we might expect a slight decline in gas permeability over time. Therefore, it is advantageous to utilize a rubbery-type polymer, which allows us to easily distinguish changes in permeation that are specifically due to the ageing of the silver material, and not of the surrounding polymer matrix.

1.5. Membrane performance limitations

1.5.1. The Robeson upper bound

To design competitive materials capable of exceeding and/or replacing current separation processes, solubility and diffusivity must be engineered to enhance permeability and selectivity to an acceptable threshold value dependent on the application. However, as illustrated by Robeson in 1991, there exists an intrinsic trade-off between permeability and selectivity (perm-selectivity tradeoff), i.e., any attempt to enhance selectivity causes a decrease in selectivity and vice-versa.[16] Creating a log-log plot of these two parameters for specific penetrant pairs, and populating the figure with values reported for different polymer membranes, it is clear that an upper bound restricts the performance needed to meet industrial scales (cf. Figure 14, Figure 16 and Figure 23). The upper bound can be expressed through following equation, where k and n are constants that relate to the gas pairs being analyzed.

$$\alpha_{ij} = kP_{ij}^{n} \quad \text{(Eq. 10)}$$

Thus, it is an ongoing effort to discover materials that can transcend and move the upper bound.[34,37,38] For example, the 2008 upper bound for CO_2/CH_4 surpassed the prior 1991 upper bound with the addition of thermally rearranged polymers and polymers of intrinsic microporosity (PIMs).[39]

However, it should also be noted that the upper bound is not always indicative of membranes performance under real conditions, i.e., mixed-gas, high pressure/temperatures. These conditions can affect transport properties through phenomena such as plasticization or mixing effects.[23,40] Additionally, high pressure/temperatures can affect the structural/mechanical properties to become difficult to manage or break.[41,42] To try and account for some of these variables in this work, mixed-gas transport testing will be considered in Section 3.4.5.

1.5.2. Plasticization

In both rubbery and glassy polymers, highly condensable species (e.g., CO_2, vapor, hydrocarbons) can increase the mobility of polymer chains, thus causing the polymer matrix to plasticize. This change in chain mobility is accompanied by parallel losses in diffusivity selectivity (size-sieving ability), and more importantly, overall selectivity.[43,44] There are several techniques that have been used to encourage resistance to plasticization. For example, crosslinking, hydrogen-bonding, or the use of filler agents.[44–46] Thus, one important aspect and question that stems from this work is the impact of the embedded nanoparticles on plasticization resistance. The answer to this question will become more clear under mixed gas conditions, as shown in Section 3.4.5.

1.5.3. Interfacial compatibility

One key requirement that is necessary for industrial gas separations is material processability. The addition of inorganic filler molecules is a commonly used technique to tune gas transport properties, e.g., the use of zeolites to enhance diffusivity selectivity.[34,47] However, these types of composite materials commonly suffer from non-selective defects created from poor interfacial compatibility between the polymer and inorganic filler phase.[48] On top of this, this poor quality mixing can lead to poor mechanical properties, causing difficulty in processing the materials. Several techniques, both physical and chemical, have been attempted to mitigate the interface between inorganic filler and organic polymers.[34] For example, chemical cross-linking of metal-organic frameworks aid in the elimination of interfacial defects.[49] Thus, as an attempt to improve compatibility between silver nanoparticles in this work, and the bulk polymer being used, Pebax 1657, a polymer ligand is used to stabilize the silver nanoparticles. This ligand not only serves as a capping agent to stabilize the silver nanoparticles from agglomerating, but as a bridge between the silver and adjacent Pebax matrix. The specific capping agent used in this work is a polyether

based poly(amic-acid), with the hypothesis that polyether components will favorably interact with the polyether segments of Pebax.

1.5.4. Photo/chemical stability

Although FTMs tend to exhibit very high performance, this technology has struggled to be executed for commercial use.[50] A large issue with all silver-based facilitated transport processes is the strong reactivity of silver with trace impurities in the feed gas. For example, silver cations can be poisoned via hydrogen reduction, transforming Ag^+ to Ag^0. Likewise, hydrogen sulfide and acetylene (C_2H_2) can react with silver to create silver sulfide (Ag_2S) and silver carbide (Ag_2C_2), respectively.[15,51] It is worth mentioning that Ag_2C_2 is highly explosive, which can make the entire separation process extremely dangerous. Finally, Ag^+ is photosensitive, being reduced to Ag^0 upon prolonged exposure to light.[15,51,52]

A variety of strategies have been employed to mitigate the stability of FTMs, including, the introduction of surfactants,[53] the use of ionic liquids,[52] using inert polymers,[15] and the use of nanoparticles.[54] Due to the lower binding energies of the outer d-orbitals associated with silver nanoparticles, wherein surface electrons are delocalized, nanoparticles typically exhibited higher stability compared to their mobile carrier counterpart.[15] Thus, for the interest of this study, silver nanoparticles were chosen as the facilitating carrier.

1.6. Energetics of gas sorption, diffusion, and permeation

For Solution-Diffusion to occur, a change in energetic state must also occur, to allow for a gas, or other penetrating component to partition into the polymer phase and diffuse.[22] This associated energy is needed to open a site for the penetrating species to occupy in the interspatial space between adjacent polymer chains. Subsequently, diffusion through the material is an activated

process which provides a means for transient gaps in the polymer chains to become available for diffusion. The overall activation energy of permeation (E_p, cf. Eq. 11) is composed of both the energy associated with penetrant condensation and mixing with the polymer (ΔH_s, enthalpy of sorption), as well as the energy associated with diffusion (E_d, activation energy of diffusion).

$$P = P_0 \exp\left(-\frac{E_p}{RT}\right) = D_0 \exp\left(-\frac{E_d}{RT}\right) S_0 \exp\left(-\frac{\Delta H_s}{RT}\right) \quad \text{(Eq. 11)}$$

P_0, D_0, and S_0 are pre-exponential constants that relate to entropic contributions to the transport process, as will be discussed further in Section 3.4.3. E_p, E_d, and ΔH_s are the activation energy of permeation, activation energy of diffusion, and enthalpy of sorption, respectively. In rubbery polymers, where the mobility of the polymer is high, diffusion is assisted through polymer segmental motion. Alternatively, in glassy polymers, when polymer motion becomes more rigid and unoccupied volume becomes fixed, diffusion can be thought to occur in between these voids. To describe the transition through the activated process (e.g., the movement of a penetrant once polymer chains open), we can apply transition state theory.

$$D = \frac{1}{6}\lambda^2 \frac{k_B T}{h} \exp\left(\frac{S^+}{R}\right) \exp\left(-\frac{E_D}{RT}\right) \quad \text{(Eq. 12)}$$

Where k_b is the Boltzmann constant, h is the Plank constant, T is the absolute temperature, R is the universal gas constant, ΔS^+ is the entropy of diffusion at the transition state. The process of diffusion is not only defined by the energetics that go into providing this transition state, as well as the associated changes in energy reflected by the penetrant, but also by the total amount of length available for diffusion. Thus, λ represents the average jump length of a penetrant molecule in one diffusive jump. One of the first molecular models of diffusion in polymers was proposed by Meares (cf. Eq. 13).[14,55]

$$E_d = \frac{\pi}{4} d^2 N_A \lambda \delta^2 \quad \text{(Eq. 13)}$$

Where d describes the size of the penetrant molecule, N_A represents Avogadro's number, and δ^2 is the cohesive energy density (CED). The cohesive energy density represents the amount of energy needed to separate polymer chains to a distance infinitely far away, thus, it acts as a good proxy to the intermolecular strength of adjacent polymer chains.[56–58] To understand this model more fully, a graphical representation is provided in Figure 4.

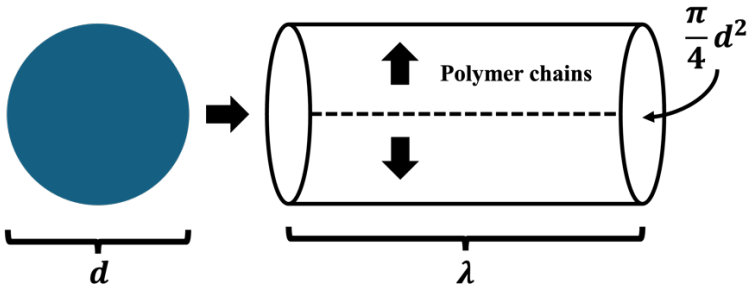

Figure 4: *Graphical representation of the Meares Model, wherein, the activation energy of diffusion is defined as the product of the average void volume* $\left(\frac{\pi}{4}d^2\lambda\right)$ *created during a diffusional jump, with the energy needed to be supplied per unit volume* (δ^2).

Since the average jump length is both dependent on the material and penetrant type, the values obtained in this work were obtained and discussed in further detail in Section 3.4.3 to elucidate the proper diffusion dependency on temperature. This becomes important when investigating the entropic and energetic differences of two penetrant species in the context of diffusion.

1.7. Summary of Dissertation Chapters

This dissertation explores the design, synthesis, characterization, and optimization of novel facilitated transport materials specifically tailored for natural gas and paraffin/olefin separations. The overarching goal of this work is to elucidate the fundamental mechanisms governing gas diffusivity, sorption, and selectivity in these materials, providing insight into their potential use in advanced gas separation technologies.

Chapter 2 introduces the central hypothesis-driven design of silver nanoparticles stabilized through poly(amic-acid) (PAA) capping agents. The capping agents are synthesized from 4,4'-oxydiphthalic anhydride and Jeffamine monomers by systematically varying its molecular weight, to exquisitely control the effect of the particle on overall gas transport. The PAA plays a crucial role in not only stabilizing each silver nanoparticle, but also fine-tuning several key parameters, such as the particle-polymer compatibility, and silver nanoparticle reactivity and stability. These factors influence, individually and synergistically, overall gas selectivity, and this Chapter outlines the rationale behind these design choices. Through base-material characterization, including the chelation mechanism, PAA grafting density, particle size, and preliminary gas transport testing, Chapter 2 lays the foundation for understanding how these nanoparticles interact with the polymer matrix and facilitate gas transport.

Chapter 3 extends this investigation to more challenging separations, such as paraffin/olefin mixtures, while also exploring the performance of the developed materials under a range of operating conditions, including various temperatures, pressures, and gas compositions as a means of gaining deeper understanding into the transport/structural behavior and effects of each particle-polymer system. A key focus in this Chapter is placed on how changes in nanoparticle loading and polymer matrix structures impact both permeability and selectivity. By investigating these parameters systematically, structure-property relationships are developed, linking transport properties such as gas diffusivity and diffusivity-selectivity to polymer characterizations, such as the glass transition temperature and crystallinity. The culmination of this Chapter leads to the optimization of the PAA-stabilized silver nanoparticles by identifying that shorter-chain PAAs result in better particle dispersion at higher loadings. As a result, a second-generation nanoparticle system exhibiting improved performance at elevated particle weight loadings was designed and

synthesized. Subsequently, to gauge the effectiveness of each material in more realistic scenarios, mixed gas permeability experiments were run. Finally, this Chapter reveals the resistance of each nanoparticle to chemical attack through hydrogen gas exposure, thus demonstrating the long-term stability of each system.

Chapter 4 is used to help justify experimental procedures executed in both Chapter 2 and Chapter 3, while also outlining novel techniques for the estimation of a polymer's solubility parameter. Dynamic light scattering is proposed as a more efficient alternative to traditional methods, such as viscometry measurements, to estimate the polymer solubility parameter. In determining these values for the series of poly(amid-acid)s used throughout this dissertation, justification and development of a liquid-liquid extraction process for producing silver nanoparticles was established. This Chapter also highlights computational methods used to estimate the solubility parameter, both by updating prior group contribution methods with updated molar volume estimations and by comparing this to modern machine learning methods. In conclusion, this Chapter highlights the need to obtain experimental values of the solubility parameter for various polymers to enhance our current understanding, which in turn will allow us to make better material property predictions. For example, the solubility parameter can be used to predict the solubility-selectivity of two liquid components within a membrane. Consequently, this Chapter provides a new tool, through dynamic light scattering, to accurately and efficiently reach this goal.

Chapter 2. Rational design, Synthesis, and Characterization of Facilitated Transport Membranes Exhibiting Enhanced Permeability, Selectivity, and Stability*

2.1. Abstract

This chapter begins to outlay the rational design, as well as the characterization, of new types of facilitated transport membranes (FTMs) materials for highly selective separations. Despite outperforming conventional polymer membranes in the short time frame, FTMs are prone to photo/chemical aging, which causes a rapid decay of their performance. Moreover, when embedded in polymer materials to fabricate mixed matrix membranes (MMMs), structural defects may form at the metal-polymer interface, causing a selectivity loss. This chapter works to address these issues through a series of poly(amic acid)s (PAAs), have been synthesized using 4,4'-oxydiphathalic anhydride (ODPA) and Jeffamine monomers of varying molecular weight, which are used to fabricate silver nanoparticles via the chelating reaction with silver ions. Overall, this approach attempts to simultaneously *i)* achieve defect-free mixed matrix membranes (MMMs), *ii)* target CO_2 selective transport, and *iii)* reduce photochemical induced degradation. The occurrence of the chelating reaction between silver and the PAA was confirmed, and as a result, individual and un-aggregated PAA-coated silver nanoparticles were obtained and incorporated into a commercial polymer, Pebax 1657, to fabricate defect-free mixed matrix membranes. The effect of the PAA length and ether functional group concentration on the structure and performance of the resulting mixed matrix membranes was systematically investigated. Remarkably, inclusion of only

---

*Reproduced, with permission from Webb, et al.[59]

2 wt% nanoparticles in Pebax enhances the CO_2 permeability by about 50% and CO_2 selectivity by about 100% relative to neat polymer. A detailed analysis of the sorption and diffusion coefficients was performed to elucidate the molecular origin of the observed membrane performance. Finally, preliminary data confirm that the newly synthesized materials exhibit high chemical stability upon exposure to pure H_2.

2.2. Introduction and Motivation

Nanoparticles (NPs) are of utmost interest due to their unique chemical-physical properties, which substantially differ from those of bulk materials. The tunable nature of NP properties enables their use in a variety of applications such as optics,[60–62] electronics,[63–65] nanomedicine,[66–68] drug delivery,[69] and molecular separations.[70,71] In this last regard, nanoparticles can be embedded in polymer materials to tune their transport properties and achieve superior selectivity/permeability performance in a variety of industrially relevant separations.[14,17,72–75] Specifically, silver ions/NPs have traditionally been used as facilitated transport carriers for specific gasses, such as carbon dioxide and ethylene.[15,76,77] As recommended by the 2019 NAS report "*A Research Agenda for Transforming Separation Sciences*", achieving high selectivity is the crucial factor to debottleneck membrane-based separations and make them competitive with conventional processes.[78] More in general, current research efforts in the membrane field are oriented towards enhancing selectivity and long-term durability.[13,34,37,38,79–82] This paper aims at proposing a novel strategy to enhance selectivity and stability in CO_2 separation systems.

Facilitated transport membranes (FTM) have been an active area of research in membrane science, providing materials that far exceed the separation performance of conventional polymer materials and position in the upper-right side of the Robeson upper bound.[14–16,83] As shown by Eriksen et al., an ethylene permeability of 26,800 Barrer and a corresponding ethylene/ethane (C_2H_4/C_2H_6)

selectivity of 1930 (i.e., > 99.9 wt% ethane purity) was achieved by soaking glycerin-swollen Nafion membranes into an aqueous solution of silver tetrafluororborate ($AgBF_4$).[84] By comparison, most membranes have an ethylene permeability between 1 to 1000 Barrer, with a C_2H_4/C_2H_6 selectivity less than 10.[85] However, due to the instability of the facilitated transport carrier (e.g., reduction of ions), as well as non-selective interfacial polymer-filler defects, these films fall short of commercial viability.[14] As an example, $AgBF_4$ incorporated into poly(2-oxazoline) suffered a 100% decrease in the C_2H_4/C_2H_6 selectivity in as little as 4 hours.[86]

Solid-state configurations with fixed carrier sites, which function based on a chained-carrier mechanism, are one avenue towards improving FTMs.[33,87–89] In 2015, Zhou et. al. doped Pebax polymer membranes with nanospheres formed by silver NPs chelated with polydopamine, observing a simultaneous increase in CO_2 permeability and CO_2/CH_4 selectivity relative to neat Pebax. Using a 15 wt% loading, the enhanced selectivity experienced an 8% decrease over the span of 7 days.[90] Although these pioneering results look promising, the individual and synergistic contributions from the silver and polymer ligand remain largely unknown. Furthermore, the exploration of different ligands and their effects on the long-term stability and performance of FTMs are crucially important in attempts to further enhance the performance and long-term stability of these systems.

To address the downsides associated with FTMs by use of NPs, it is necessary to carefully consider the design of the particle and its capping agents. Poly(amic-acid)s (PAAs) show favorable carbonyl-silver coordination interactions that ultimately are responsible for the formation of stable silver NPs via the chelating mechanism.[91] Secondly, electron acceptors within PAAs (e.g., carboxylic acids) polarize the particle surface, which helps tune selectivity and offers particle protection from photo/chemical degradation.[33] Additionally, by applying the solution-diffusion

separation principles,[20] incorporation of functional groups (i.e., ethers) that interact with target solutes (e.g., CO_2) can further benefit the separation performance of existing membrane systems.[24,25,92–94] Finally, improving the NPs compatibility with polymer matrices is expected to inhibit the formation of non-selective defects, thus providing an additional opportunity to enhance selectivity in membrane applications.[95,96]

In this chapter, rationally designed nanoparticles targeting CO_2 separation were synthesized by chelating silver NPs with PAAs. Each PAA was molecularly designed to include polyether segments to target CO_2 transport and achieve particle compatibility in polyether-based membranes. Using a variety of physical, chemical, and structural characterizations, the effect of the PAA on the structure and properties of NPs was systematically investigated. NPs were then incorporated, in the amount of 2 wt%, in Pebax 1657, a commercial polymer of practical interest for CO_2 separation, showing that CO_2 permeability can be enhanced by 50% and CO_2/CH_4 selectivity by 100%. The molecular origin of this behavior was elucidated by breaking permeability into its sorption and diffusion contributions. Finally, the stability of the newly synthesized materials was tested by exposing them to pure H_2 for 24h, after which CO_2 and CH_4 permeability and CO_2/CH_4 selectivity were rechecked. Therefore, the approach proposed in this study provides a unique avenue to achieve high CO_2 selectivity and permeability, while simultaneously prolonging the long-term durability of the ensuing systems.

2.3. Experimental Methods

2.3.1. Materials.

4,4'-Oxydiphathalic anhydride (ODPA) was purchased from Sigma-Aldrich (97 wt % purity), and two Jeffamine D-series grades, exhibiting molecular weight of 2000 (D2K) and 4000 g/mol (D4K),

were generously donated by Huntsman corporation (cf. Table 1). Prior to use, all monomers (i.e., Jeffamine and ODPA) were dried under vacuum for 24 hours at room temperature and stored in a desiccator. The PAA reaction medium, tetrahydrofuran (THF), was purchased from Fisher chemical with a water content of 0.02 %. The water content was further reduced using 3Å molecular sieves purchased from Sigma-Aldrich, for at least 24 hours. Methanol (>99 %), which was used to remove monomer/oligomers from the synthesized polymers, was purchased from Acros Organics. Deuterated chloroform, $CDCl_3$, to be used for nuclear magnetic resonance (NMR) characterization, was purchased from Cambridge Isotope Laboratories, Inc. (99.8%). Ethylene glycol (EG), to be used as the reducing agent in the NP synthesis, was purchased from Fisher chemical. The NP precursor, silver nitrate ($AgNO_3$), was purchased from Acros Organics with a purity >99 %. Chloroform ($CHCl_3$) was purchased from Sigma-Aldrich to extract the NPs from EG and to dissolve Pebax 1657 for membrane fabrication. Ultrapure water with an in-line resistivity of 18.2 MΩ-cm, used throughout the study, was produced via a MilliQ7000 purification system. White mineral oil with a flash point of 360-400 °F, to be used to control the reaction temperature, was obtained from Fischer Scientific. Pebax 1657 (Pebax) was purchased from Arkema to serve as the membrane bulk material. 200 proof ethanol (ETOH) was purchased from Fisher Chemical to dissolve Pebax for membrane fabrication via solution casting.

2.3.2. Synthesis of Poly(amic-acid).

The PAAs were synthesized through a nucleophilic substitution reaction by Jeffamine's amine group at one of ODPA's anhydride carbonyl carbons (cf. Figure 5). This reaction was performed in a 100 ml three-neck flask, manufactured by Chemglass, equipped with a Lab Fish mechanical stirrer and a water jacketed reflux column. A nitrogen blanket was first provided to the flask to

remove any traces of humidity. The flask was then charged with 30 ml of THF and 15 mmol of Jeffamine.[97] The same procedure was used for both Jeffamines, D2K or D4K.

Table 1: *Summary of Diamines Used in This Study.*

Name	Abbreviation	Molecular Weight (g/mol)	Chemical Structure	X	Resultant Polymer Abbreviation
Jeffamine D2000	D2K	2000	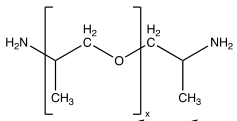	33	OD2K
Jeffamine D4000	D4K	4000		68	OD4K

Listed is the diamine commercial name, its abbreviation, molecular weight, structure, the number of internal repeated units (X), and the abbreviations used for the PAA resulting from the reaction between ODPA and each diamine.

The mixture was stirred at room temperature until homogeneous. Then, the solution was cooled to 0 ºC using an ice bath before adding 15 mmol of ODPA. The purpose of the ice bath during the initial monomer consumption was to improve the molecular weight of the resulting PAA, given the exothermic nature of the reaction.[98] The initial attack of the amine on the anhydride carbonyl occurs rapidly, within the first few minutes of the reaction. After 10 minutes, the flask was heated on a hot plate to 30 ºC using a bath of white mineral oil. The mixture was allowed to react for three hours to ensure a high molecular weight polymer was formed, capable of passivating the silver surface quickly in the NP synthesis. Following this step, the PAA was precipitated using a methanol/water (10/90 vol%) mixture and subsequently rinsed using this mixture over a vacuum filtration device. This step was done to remove any unreacted monomers and oligomers. The resulting PAAs (OD2K/OD4K) (cf. Figure 5 and Figure A1) were dried under vacuum for 24 hours at room temperature and stored in a chemical refrigerator at 4 ºC. The PAA derived from ODPA and D2K will be abbreviated by OD2K, while the PAA derived from ODPA and D4K will be abbreviated by OD4K.

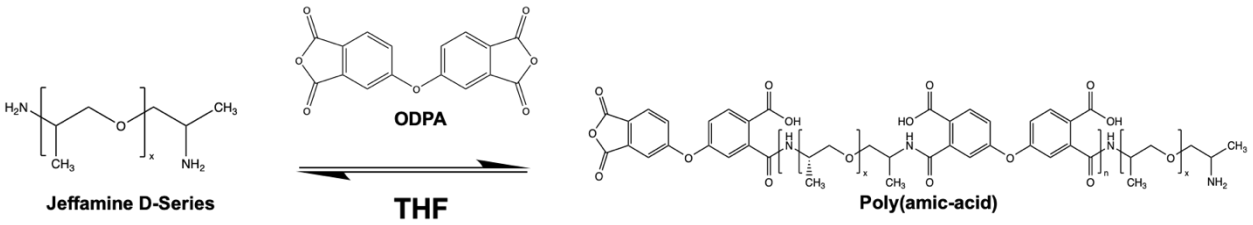

Figure 5: *Reaction between Jeffamine and ODPA for the synthesis of Poly(amic-acid) (PAA) in THF. The resulting PAA structure is shown. X denotes the number of repeating segments within each Jeffamine molecule (cf. Table 1). N denotes the number of repeating segments within the overall PAA.*

2.3.3. Synthesis of Silver Nanoparticles.

The NP synthesis was performed in a 100 ml three-neck flask from Chemglass equipped with a magnetic stirrer, water jacketed reflux column, and a nitrogen blanketed atmosphere. First, 200 mg of either OD2K or OD4K was added to the flask and completely dissolved in 40 ml of EG (cf. Figure 6, Step 1) This mixture was heated to 100 ºC on a hot plate using a mineral oil bath. $AgNO_3$ was dissolved in a separate beaker using ultrapure water at a concentration of 40 wt%, following the procedure by Kim *et al*.[99] 2 ml of this aqueous solution was rapidly injected into the flask using a syringe to induce particle nucleation (cf. Figure 6, Step 2). The resulting concentration of $AgNO_3$ after addition to the reaction volume was 0.5 M. The reaction was maintained at 100 ºC for 30 minutes, allowing time for particle growth. At this time, the solution was quickly cooled down to room temperature using a water bath at 20 ºC (cf. Figure 6, Step 3). To denote the particle type in an abbreviated manner, Ag is added to the end of the PAA that was used in the synthesis (e.g., OD2K-Ag are silver NPs synthesized using OD2K).

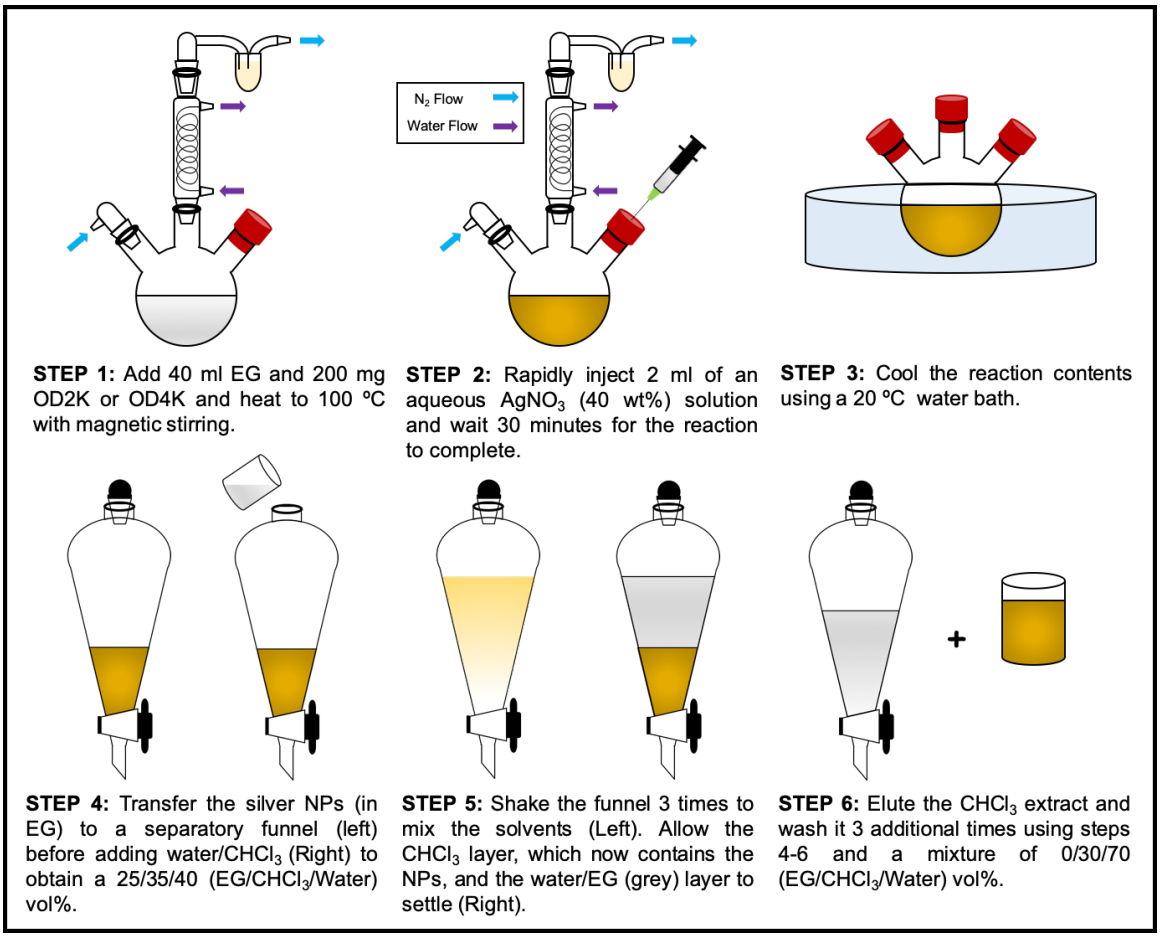

Figure 6: *Schematic of the silver nanoparticle synthesis.*

The nascent particles, still in EG, were then transferred to a 500 ml separatory funnel and mixed with $CHCl_3$ at a 40/60 ($EG/CHCl_3$) vol% ratio (cf. Figure 6, Step 4). The particles were pushed from EG into the $CHCl_3$ layer upon adding ultrapure water, at a vol% ratio of ~25/35/40 for $EG/CHCl_3/H_2O$, respectively. Likewise, EG was selectively removed by the aqueous layer. NPs were placed in chloroform, rather than remaining in EG, to facilitate their subsequent dispersion in polymers to fabricate the mixed matrix membranes. Such choice is based on: 1) chloroform's immiscibility with the aqueous phase to facilitate the extraction process, 2) chloroform's similarity of solubility parameter to the silver NP's steric polymer layer ($CHCl_3$ – 19 $MPa^{0.5}$, EG – 32.9 $MPa^{0.5}$, and OD2K/OD4K ~ 20.2/19.7 $MPa^{0.5}$) (cf. Sections A1 and A6) and 3) a low boiling point

(61 ºC) for $CHCl_3$ relative to EG (197 ºC). The funnel was shaken several times before allowing the solvent layers to settle (cf. Figure 6, Step 5). The $CHCl_3$ phase was removed, and the funnel was cleaned before adding the $CHCl_3$ extract back into the funnel (cf. Figure 6, Step 6). The $CHCl_3$ phase was then rinsed 3 additional times in the separatory funnel using ultrapure water at a 30/70 ($CHCl_3/H_2O$) vol % ratio. Between each wash, the $CHCl_3$ extract was removed, and the funnel was cleaned. The final particle suspension in $CHCl_3$ was placed in PTFE lined amber vials and stored in a refrigerator at 4 ºC.

2.3.4. Mixed Matrix Membranes Fabrication

Neat Pebax membranes were fabricated via the solution-casting procedure from a 2.5 wt% solution in ETOH/$CHCl_3$ (50/50 vol%), which was dissolved at 50 ºC. Both OD2K-Ag and OD4K-Ag were used to fabricate composite materials with Pebax by adding either of the respective particles to the described polymer solution. The final silver concentration in these materials was targeted around 2 wt%. Since the particles are also suspended in chloroform, the solvent composition used to dissolve Pebax was slightly altered, so as to obtain a final mixture of Pebax and particles that was 50/50 vol% (ETOH/$CHCl_3$). This was done to ensure that the total volume and composition of the mixture remained constant. Each mixture was sonicated for 5 minutes before being poured onto a leveled glass dish at room temperature and inside a nitrogen filled glove bag, so as to avoid oxidizing the sample. The samples were allowed to dry for 3 days prior to use. The membrane thickness was measured using a Mitutoyo micrometer ten times, with values ranging between 80-100 μm. Membranes containing 2 wt% OD2K-Ag and OD4K-Ag are referred to as Pebax+2OD2K-Ag and Pebax+2OD4K-Ag respectively.

2.4. Characterization Methods

2.4.1. Nuclear Magnetic Resonance (NMR).

OD2K and OD4K were characterized by ^{1}H NMR analysis using a VNMRS 500MHz-NMR spectrometer. Prior to the synthesis of OD2K and OD4K, D2K, D4K, and ODPA were examined using NMR to ensure that no impurities were present. Deuterated chloroform ($CDCl_3$) (99.8%, Cambridge Isotope Laboratories) was used as the solvent with a polymer concentration of 2 wt%. ^{1}H NMR spectra were referenced internally to $CDCl_3$ (δ = 7.26 ppm).

2.4.2. Fourier Transform Infrared Spectroscopy (FTIR).

OD2K, OD4K, OD2K-Ag, and OD4K-Ag were analyzed using a Nicolet iS50R Fourier Transform Infrared Spectroscope (FT-IR) in the iS50 attenuated total reflectance (ATR) mode using 64 scans with a resolution of 0.4821 cm^{-1} (cf. Section A2)).

2.4.3. Dynamic light scattering (DLS).

DLS was used to measure the effective hydrodynamic diameter of OD2K and OD4K in various solvents, in attempt to corroborate the solubility parameter calculated using the group contribution method (cf. Section A1). These measurements were performed on a NanoBrook Series Particle Analyzer using backscattered detection. For more information, cf. Section A6.

2.4.4. Transmission Electron Microscopy (TEM).

Micrographs of the OD2K-Ag and OD4K-Ag were obtained using a JEOL 2000FX transmission electron microscope (TEM) at 200kV with LaB_6 electron source. 20 μL of a silver NP suspension in $CHCl_3$ (~500 PPM) was dropped onto a 3mm copper grid with a carbon support film. The particle size distribution and morphology were determined based on 160 NPs, using Fiji image analysis.[100]

2.4.5. Ubbelohde Viscometer.

The intrinsic viscosity of OD2K and OD4K was found using a size 0C Ubbelohde viscometer purchased from Cannon Instruments, calibrated with a viscometer constant of 0.003309 cSt/s^2. The intrinsic viscosity was used to compare relative molecular sizes. OD2K and OD4K were prepared at concentrations ranging from 0.3 to 1 g dL^{-1} in $CHCl_3$ and tested at 35 ºC. The reduced viscosity (η_{red}) and inherent viscosity (η_{inh}) were measured at each concentration five times (cf. Figure A4). The intrinsic viscosity for OD2K and OD4K were determined by averaging the extrapolated value for the η_{red} and η_{inh} at a concentration of 0 g dL^{-1} (cf. Section A3). This relative trend was then compared to molecular weight estimates obtained from gel permeation chromatography measurements.

2.4.6. Gel Permeation Chromatography (GPC).

Using a Waters 717 plus auto sampler, 30 µL of a 0.1 w/w% polymer solution in $CHCl_3$ was injected into a 7.5 x 250 mm Agilent polypore column at a flowrate of 1 ml/min and at 40 ºC. The eluent was detected using a Waters 490E programmable multi-wavelength detector, set to 260 nm. Details surrounding the weight calculations, as well as the overall molecular weight distribution of OD2K and OD4K is available in Section A4.

2.4.7. Thermogravimetric Analysis (TGA).

TGA was used to individuate mass losses for OD2K, OD4K, OD2K-Ag, OD4K-Ag, Pebax, Pebax+2OD2KAg, and Pebax+2OD4K-Ag. About 10-20 mg (dry mass) of each sample was placed into a TA Instruments TGA Q500 under nitrogen gas, flowing at 10 ml/min. In the case of the silver NPs (OD2K-Ag and OD4K-Ag), which are suspended in $CHCl_3$, the TGA pan was first filled dropwise with the liquid. The $CHCl_3$ was allowed to evaporate, and the addition was repeated until sufficient particle dry mass was obtained. The samples were heated at a rate of 10 ºC /min

from 28 to 800 ºC, and any mass losses were recorded. First and second derivative analysis was used to determine temperature ranges of individual mass loss events (cf. Figure A6 - Figure A8). TGA was coupled with GPC and TEM information to calculate the polymer surface grafting density (σ) as follows[101]:

$$\sigma = \frac{N_A\left(\frac{g_{pol}}{g_{Ag}}\right)\rho_{Ag}r}{3M_n} \quad \text{(Eq. 14)}$$

where N_A is Avogadro's number (6.022E23 chains mol^{-1}), g_{pol} is the polymer mass, g_{Ag} is the silver mass, r is the equivalent radius of the nanoparticle (based on TEM measurements, cf. Figure 6 and Table 3), and ρ_{Ag} is the density of the silver nanoparticles, which was assumed to be nearly identical to that of bulk silver (i.e., 10.5 g cm^{-3}). Each TGA measurement exhibited an uncertainty of 5 %.

2.4.8. Scanning Electron Microscopy (SEM).

Scanning electron micrographs of Pebax, Pebax+2OD2K-Ag, and Pebax+2OD4K-Ag's cross-section were used to characterize structure morphology. Cross-sections were prepared via fracturing each membrane while immersing the sample in liquid nitrogen. Prior to imaging, each sample was sputter coated with iridium. Images were taken using a ThermoFisher Quattro device at 10 kx, with an accelerating voltage of 10 KeV.

2.4.9. Pure gas sorption and permeation measurements.

Pure gas (CH_4 and CO_2) permeability was measured at 1 bar and 35 ºC and pure gas solubility (CH_4 and CO_2) was measured from 5 to 20 bar at 35 ºC. Details about these measurements are provided in Section A7. Gas diffusivities were estimated using the solution diffusion model:

$$\overline{D} = \frac{P}{S} \quad \text{(Eq. 15)}$$

where P is the permeability, S is the solubility coefficient, and $\overline{D}$ is the concentration averaged diffusion coefficient. The ideal (i.e., pure-gas) CO_2/CH_4 selectivity (α^P) was estimated as shown in Eq. 16 and broken into its sorption (α^S) and diffusion (α^D) contributions:

$$\alpha^P = \frac{P_{CO_2}}{P_{CH_4}} = \frac{S_{CO_2}}{S_{CH_4}} \times \frac{D_{CO_2}}{D_{CH_4}} = \alpha^S \times \alpha^D \quad \text{(Eq. 16)}$$

2.4.10. Stability Testing.

Both Pebax+2OD2K-Ag and Pebax+2OD4K-Ag, were subjected to 1 atm H_2 at 35 °C for 24 hours. Prior to, and after the materials were treated with H_2, pure gas CH_4 and CO_2 permeability at 1 atm and 35 °C were measured. Changes in overall CO_2 permeability and CO_2/CH_4 selectivity as a result of H_2 exposure are tabulated and compared (cf. Table 4).

2.5. Results and Discussion

2.5.1. Poly(amic-acid) Characterizations

FTIR was used to provide evidence that the PAA was formed. Figure 7A shows the FTIR spectra of the synthesized OD2K compared to ODPA and D2K, while Figure 7B shows the FTIR spectra of the synthesized OD4K compared to ODPA and D4K in the wavelength range 1500 and 1900 cm^{-1}. The spectral features in this region show key changes in the carbonyl groups during the reaction, providing insight to the polymerization.

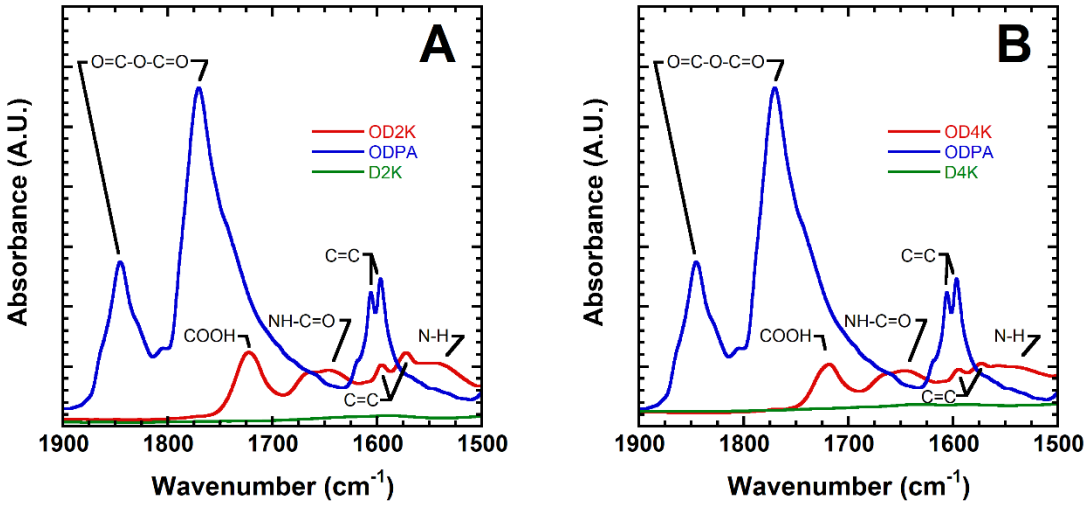

Figure 7: *A) ATR-FTIR spectra of the synthesized OD2K sample compared with the ODPA and D2K reactants, between 1500 and 1900 cm^{-1} wavenumbers. B) ATR-FTIR spectra of the synthesized OD4K sample compared with the ODPA and D4K reactants, between 1500 and 1900 cm^{-1} wavenumbers.*

The D2K and D4K samples exhibited low absorption in this region in contrast to the spectrum obtained for ODPA. ODPA has characteristic peaks at 1770 and 1846 cm^{-1} for the symmetric and asymmetric stretching of the anhydride carbonyl, respectively.[102] The loss of these peaks in both OD2K and OD4K's spectra indicates that the reactants are being mostly consumed by the reaction and removed by subsequent washings. The formation of the amic-acid group is supported by the appearance of peaks at 1655 and 1545 cm^{-1} that correspond to the Amide I (C=O stretching) and II (N-H bending) bands for a secondary amide.[103] Additionally, a peak at 1723 cm^{-1} shows the simultaneous appearance of the carboxylic acid carbonyl.[102] Finally, there is a clear red shift (i.e., a shift of around 10 cm^{-1} towards lower wavenumbers) in the aromatic alkene bonds from ODPA to its incorporation into the polymer due to the mesomeric effect.[103]

^{1}H NMR can further describe the results of the reaction by confirming the retention of basic reactant structures. In the ^{1}H NMR spectra of both OD2K (cf. Figure 8A) and OD4K (cf. Figure

8B), the main chain proton signals for aromatic protons of the dianhydride, aliphatic protons of the diamine, and terminating/side chain methyl groups appeared around 7-8, 3-4.5, and 1-1.5 ppm, respectively.[104] This is an indication that each of the three groups are retained from the reactants after the synthesis.

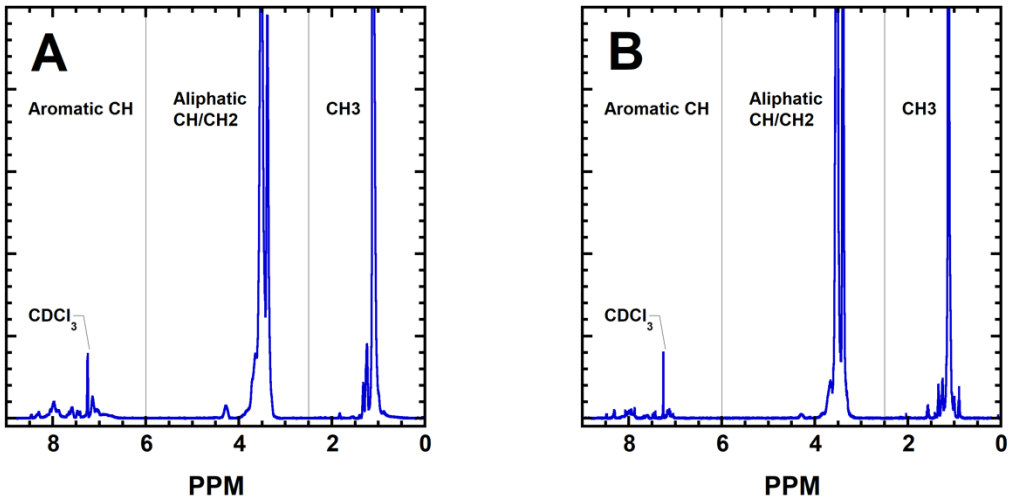

Figure 8: *A) ^{1}H NMR Spectra of OD2K at 2 wt% in $CDCl_3$. B) ^{1}H NMR Spectra of OD4K at 2 wt% in $CDCl_3$.*

The intrinsic viscosities of OD2K and OD4K in $CHCl_3$ at 35 ºC were 0.232 ± 0.001 and 0.255 ± 0.001 dL g^{-1}, respectively (cf. Table 2). The higher value of intrinsic viscosity exhibited by OD4K highlights its larger molecular weight relative to OD2K.[105] These results were corroborated with GPC data, which provided number average molecular weights of 20800 ± 4310 and 42800 ± 8890 g/mol for OD2K and OD4K, respectively (cf. Table 2). Although it appears that, on average, OD4K is nearly twice the projected (i.e., linear) length of OD2K, the two polymers are chemically similar. This is also shown via their solubility parameter, which was calculated using group contribution methods (cf. Section A1).[106] Based on this method, the solubility parameter of OD2K is 20.2 ± 0.3 MPa$^{0.5}$ and of OD4K is 19.7 ± 0.3 MPa$^{0.5}$. This similarity was also observed by DLS measurements

of OD2K and OD4K in a variety of organic solvents, which suggested that both OD2K and OD4K has a solubility parameter around 20 $MPa^{0.5}$, as shown in Figure A9. Therefore, the two independent measurements provide, within the experimental uncertainty, consistent results. Polymers should experience the greatest swelling in a solvent they are most similar to, and both polymers' hydrodynamic radii experienced a maximum in acetone, whilst OD4K was larger (2.5 nm) compared to OD2K (1.7 nm) (cf. Figure A9).[105]

Table 2: *Summary of OD2K/OD4K Intrinsic Viscosity, Molecular Weight, and Solubility Parameter.*

Name	Intrinsic Viscosity (dL/g)	Number Average Molecular Weight (g/mol)	Solubility Parameter ($MPa^{0.5}$)
OD2K	0.232 ± 0.001	20800 ± 4310	20.2 ± 0.3
OD4K	0.255 ± 0.001	42800 ± 8890	19.7 ± 0.3

Listed for OD2K and OD4K is the Intrinsic Viscosity (dL g^{-1}), measured in $CHCl_3$ at 35°C, the number average molecular weight (g mol^{-1}) obtained from GPC experiments, and the solubility parameter based on the group contribution method.[107]

2.5.2. Silver Nanoparticles Characterizations.

The formation of PAA-stabilized silver NPs was first verified by examining the FTIR absorption spectra of the NPs. To investigate the interaction that leads to stabilized silver NPs, FTIR was compared between the neat OD2K and the silver nanoparticles modified using OD2K (i.e., OD2K-Ag). As shown in Figure 9A, there is a clear red shift for the carboxylic acid carbonyl stretch from 1722 to 1715 cm^{-1} and for the amide carbonyl peak from 1645 to 1630 cm^{-1}. The red shifting of both carbonyls suggests that the carbonyl moieties are interacting with the silver surface.

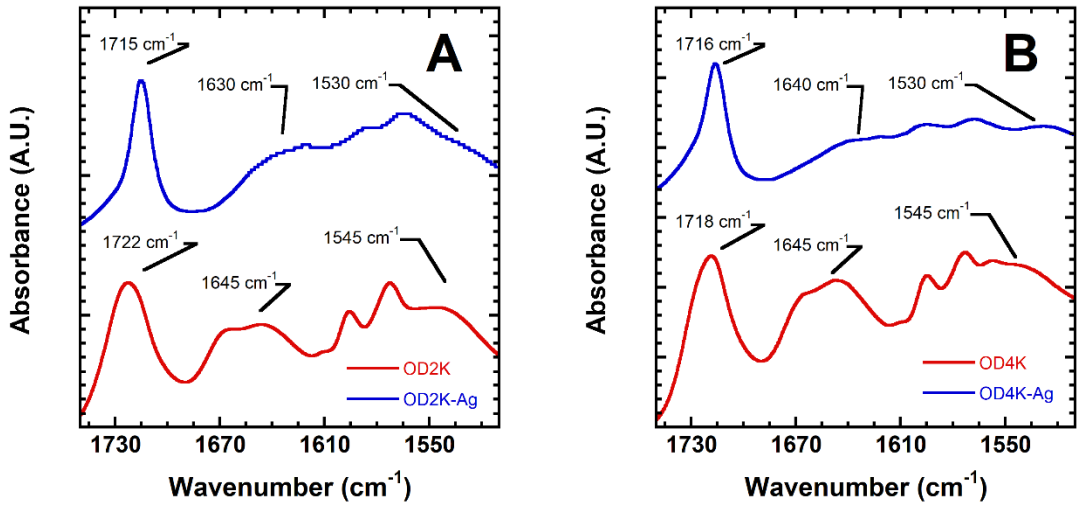

Figure 9: *A) ATR-FTIR spectra of OD2K and the silver nanoparticles stabilized by OD2K (OD2K-Ag) between 1510 and 1750 cm^{-1} wavenumbers. B) ATR-FTIR spectra of OD4K and the silver nanoparticles stabilized by OD4K (OD4K-Ag) between 1510 and 1750 cm^{-1} wavenumbers.*

This is likely due to the ability of the carbonyl lone electron pairs to complex with cationic silver ions located on the NP surface.[108] The amide, in its neutral state, is capable of forming adducts with metal ions at the carbonyl oxygen, but the amide nitrogen is incapable of coordinating with the NP surface without first substituting its hydrogen by deprotonating.[109] Given the poor acidity of secondary amides, this seems unlikely. Instead, shifting in the amide N-H bending from 1545 to 1530 cm^{-1} is more likely due to the positive charge placed on the nitrogen atom as a result of the chelation occurring at the amide carbonyl.[109] Thus, the shifting would be due to the strengthening of mesomeric effects. All other peaks do not experience shifts upon stabilization of silver NPs. A similar comparison was done for OD4K and OD4K-Ag with analogous results (cf. Figure 9B). Through this mechanism, OD2K and OD4K coordinate with the silver NPs to form a protective layer that sterically hinders the NP aggregation. This was confirmed by the TEM analysis, which is shown in the micrographs of Figure 10.

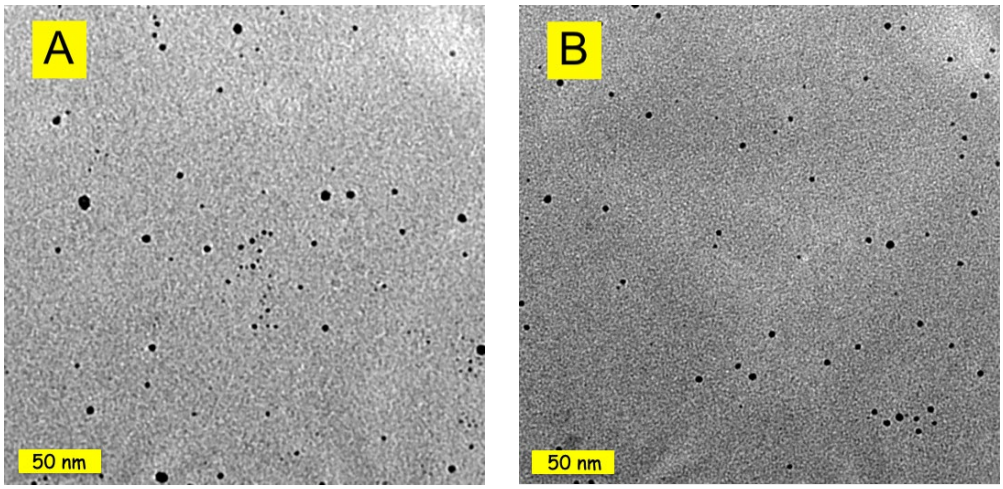

Figure 10: *TEM micrographs (A) OD2K-Ag and (B) OD4K-Ag, imaged at 250kX magnification.*

The OD2K-Ag and OD4K-Ag particles are well dispersed and mainly spherical in shape, with equivalent diameters of 6.2 ± 2.9 nm and 4.5 ± 2.5 nm, respectively (cf. Figure 10 and Table 3). Previous studies featuring facilitated transport of olefins, used NPs with diameters less than 30 nm.[110] The much lower NPs size obtained in this study, which leads to an increased particle surface-to-volume ratio, is expected to benefit the transport/separation properties, as shown later in this paper. Even though the molecular weight of OD2K and OD4K were different, stable nanoparticles exhibiting similar size and morphology were achieved. To further investigate any potential differences between the surface properties of the resulting nanoparticles, thermogravimetric analysis (TGA) was used (cf. Figure 11A/B).

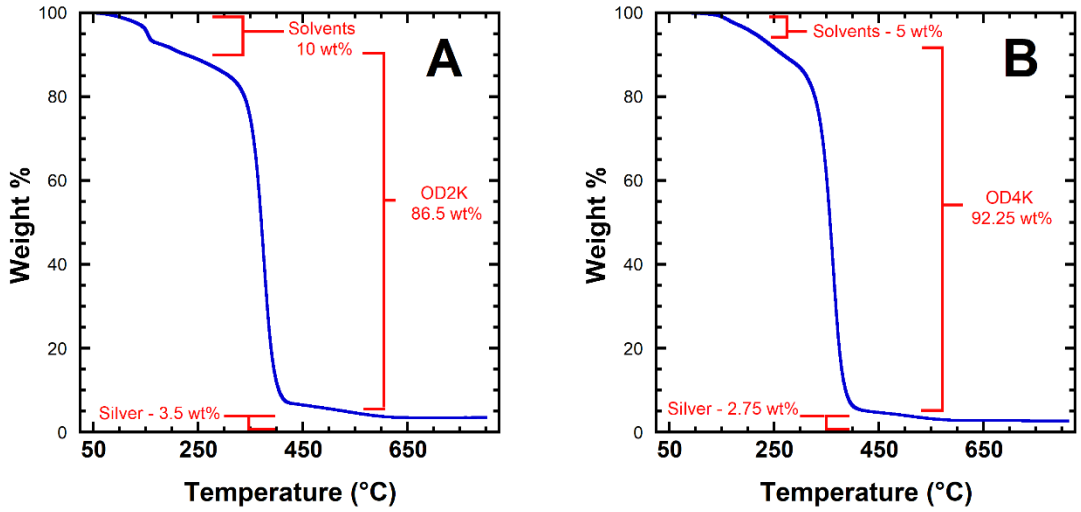

Figure 11: *TGA analysis illustrating the mass loss of A) OD2K-Ag and B) OD4K-Ag, between 28 and 800 ºC.*

Two main mass loss events occur for both particle types. Using first and second derivative analysis (cf. Figure A6), the first mass loss on both curves occurs between 100 and 200 ºC. This is most likely from residual solvents, such as ethylene glycol. The second mass loss occurs between 300 and 450 ºC, which corresponds to the main chain degradation in OD2K and OD4K (cf. Figure A7). The residual mass at 800 ºC is attributed to silver. The overall silver to polymer mass ratio was 4 and 2.9% for OD2K-Ag and OD4K-Ag, respectively (cf. Table 3). The similar mass ratios are consistent within the limit of increasingly smaller particles, whereas the amount of polymer mass needed to surround each particle becomes near constant.[111] Using these values and (Eq. 14), the surface grafting density of OD2K-Ag particles is calculated to be 7.6 chains/nm^2, which is approximately twice the estimated value of 4.2 chains/nm^2 for OD4K-Ag particles. Using the surface grafting density and polymer molecular weights, OD4K-Ag nanoparticles contain ~10% more ether groups relative to OD2K-Ag nanoparticles.

Despite the similarity in the particle silver/PAA mass ratio (4 for OD2K-Ag and 2.9 for OD4K-Ag), the grafting density of OD2K-Ag (7.6 chains/nm^2) is almost twice that of OD4K-Ag (4.2 chains/nm^2). Mathematically, the shift from a similar mass ratio to different grafting density is based on the molecular weights, which also differ by a factor of ~2 (OD4K – Mw = 42800 g/mol; OD2K – Mw = 20200 g/mol). However, a more detailed explanation can be found from Benoit et al.[101] In this paper, the surface grafting of thiolated polyethylene glycol (PEG) on the surface of gold nanoparticles was analyzed as a function of the PEG molecular weight. When polymer molecular weight increases, the probability of entanglement and chain overlap increases. As a result, when attempting to graft longer chains onto a particle surface, entanglements and added steric hindrance may hamper the efficient packing of polymer chains to the nanoparticle, thus lowering the effective surface grafting density.[101] It should also be noted that particle surface curvature plays a role. On highly curved surfaces (i.e., smaller particles), confinement impacts surface grafting by limiting attachment sites, while also influencing polymer chain conformation and orientation on the particle surface. For both these reasons, it is reasonable to expect a lower grafting density for OD4K-Ag, relative to OD2K-Ag.

Table 3: *Summary of Silver Nanoparticle Size, Composition, and Surface Grafting Density*

Name	Equivalent Diameter (nm)	Ag/Polymer Mass Ratio (%)	Grafting Density (Chains nm^{-2})
OD2K-Ag	6.2 ± 2.9	4.0 ± 0.2	7.6 ± 2.0
OD4K-Ag	4.5 ± 2.5	2.9 ± 0.2	4.2 ± 0.9

Listed for each NP is the equivalent diameter (nm), silver (Ag) to polymer mass ratio (%), and PAA polymer surface grafting density (chains/nm^2)

2.5.3. Mixed Matrix Membrane Structural Characterization.

Both OD2K-Ag and OD4K-Ag were incorporated in Pebax at a loading of 1.73 ± 0.09 and 2.06 ± 0.10 wt% silver, respectively, as calculated via TGA measurements (cf. Figure A11 and Figure

A12). Neat Pebax 1657 and its mixed matrix membranes (i.e., Pebax+2OD2K-Ag and Pebax+2OD4K-Ag) exhibit similar thermal stability, with a degradation onset starting at about 300 ºC (cf. Figure A11 and Figure A12). This finding is consistent with the very low NPs loading. Scanning electron micrographs showed no signs of structural defects in the Pebax-NPs mixed matrix membranes, thus demonstrating excellent Pebax-NPs compatibility at this loading (cf. Figure 12A-C).

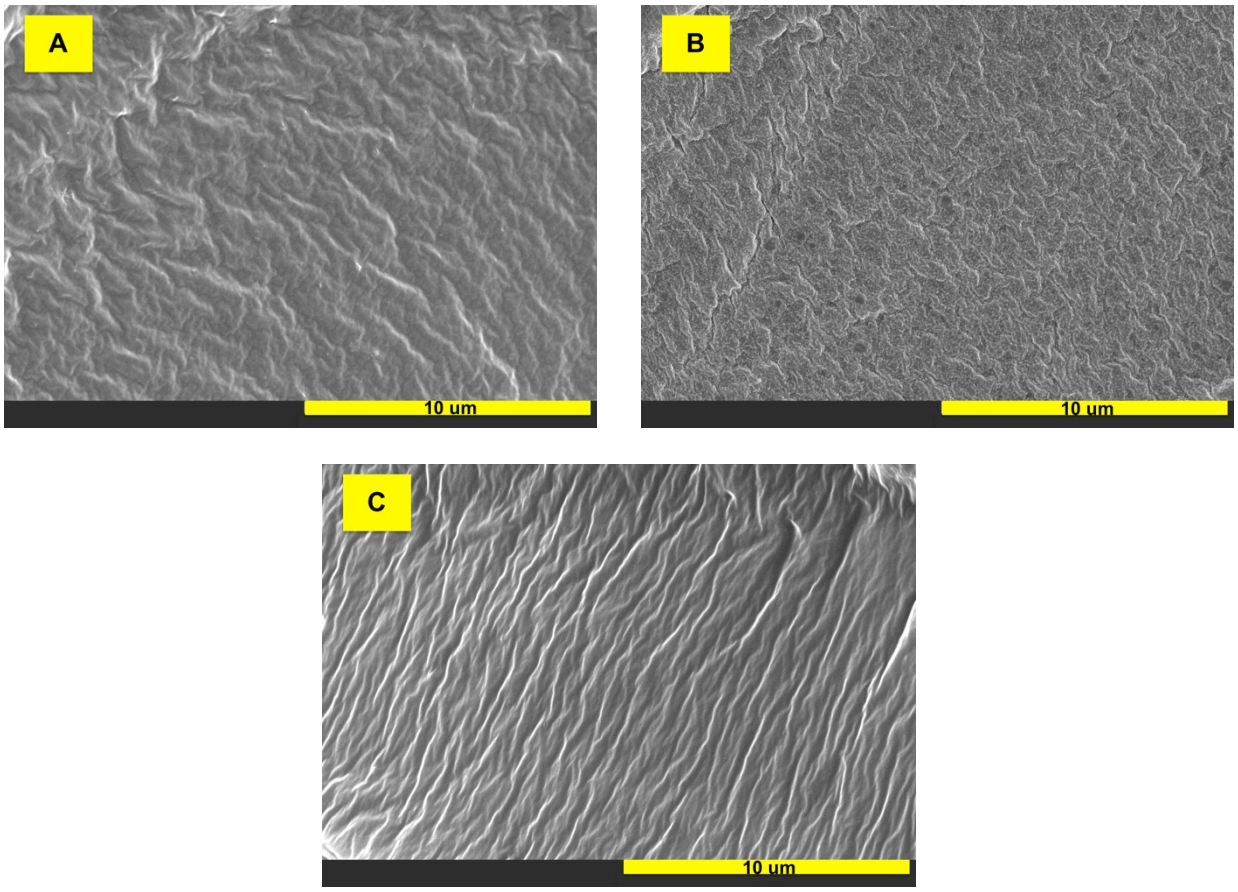

Figure 12: *SEM micrographs for the cross-section of a) Pebax, b) Pebax+2OD2K-Ag, c) Pebax+2OD4K-Ag at 10 kx and 10KeV.*

2.5.4. Membrane Transport Properties.

CO_2 and CH_4 sorption and permeability data in neat Pebax, which were collected to serve as a baseline in this study, exhibit good agreement with literature data.[112,113] Pure gas sorption

isotherms, as well as diffusion and permeability coefficients, are shown in Section A7. Experimental uncertainties were estimated via the error propagation method.[114] Upon incorporating OD2K-Ag in Pebax 1657, CO_2 permeability at 35°C and 1 atm increased by 46.8% while CO_2/CH_4 ideal selectivity increased by 84.8% relative to the neat Pebax (cf. Figure 13A). Similarly, incorporation of OD4K-Ag in Pebax 1657 increased CO_2 permeability by 51.1% and CO_2/CH_4 ideal selectivity by 109.6% relative to neat Pebax (cf. Figure 13A).

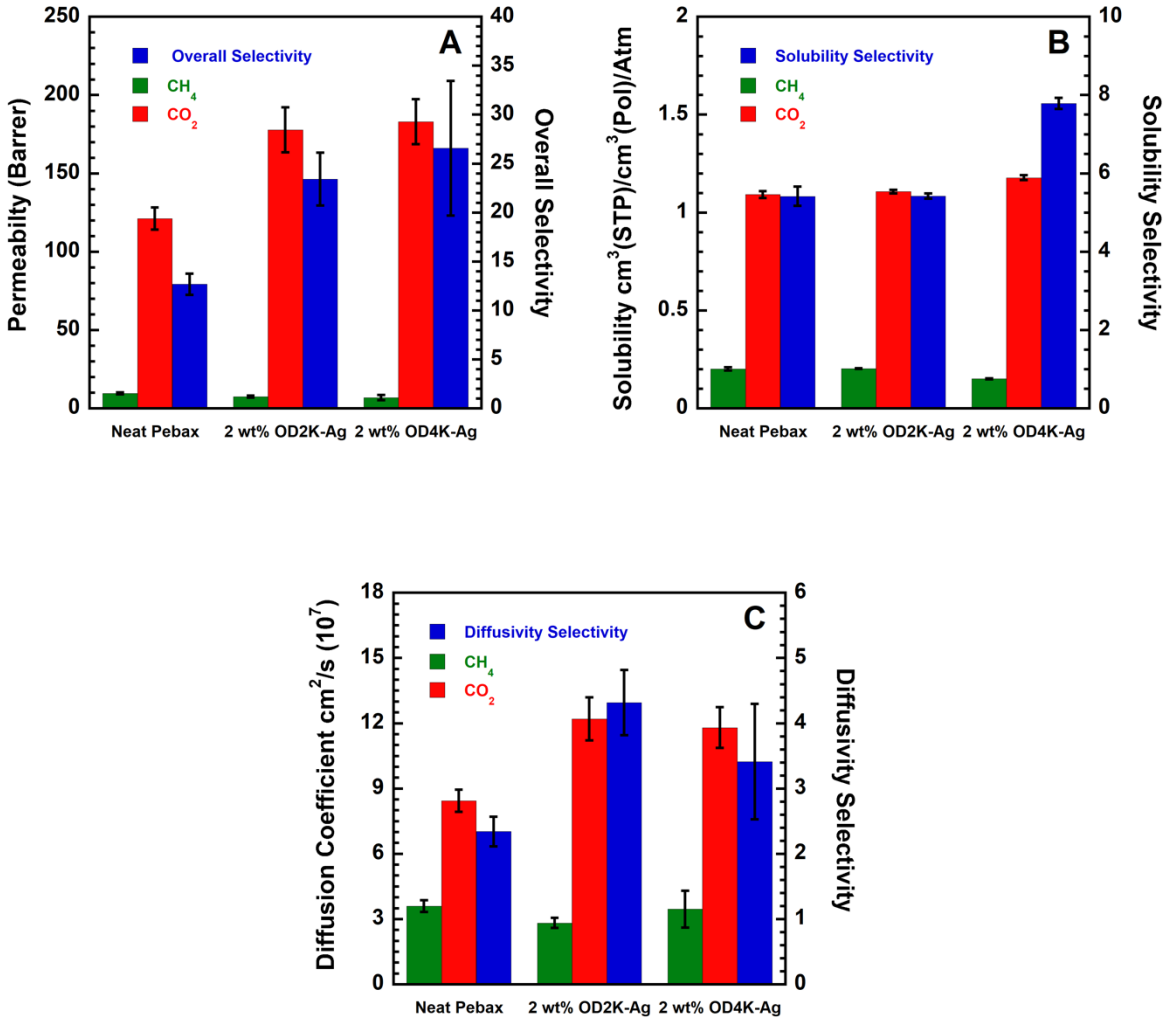

Figure 13: *A) Permeability and CO_2/CH_4 ideal selectivity, B) solubility and CO_2/CH_4 solubility-selectivity, and C) diffusivity and CO_2/CH_4 diffusivity-selectivity for Pebax 1657, Pebax +*

2OD2K-Ag, and Pebax + 2OD4K-Ag. Data are at 35°C and 1 atm. Error bars were estimated via the error propagation method.[114]

To understand the molecular origin of the resulting transport behavior, the overall permeability coefficient and selectivity were deconvoluted into their sorption and diffusion contributions. Solubility and solubility-selectivity showed no significant change in Pebax+2OD2K-Ag compared to neat Pebax 1657 (cf. Figure 13B). However, in the case of Pebax+2OD4K-Ag, CO_2 solubility increased by around 8%, whereas solubility-selectivity increased 43.8% compared to neat Pebax 1657 (cf. Figure 13B). This result suggests that the higher ether concentration in OD4K-Ag particles, about 10% above that of OD2K-Ag, could be playing a role in dictating CO_2 solubility changes. Both mixed matrix membranes experienced an impressive increase in CO_2 diffusivity (~40%) and CO_2/CH_4 diffusivity-selectivity (>50%) relative to neat Pebax 1657 (cf. Figure 9C). This physical picture is compatible with CO_2 transport being facilitated by the NPs, while the diffusion of CH_4 occurs via the standard solution-diffusion mechanism. Interestingly, the CH_4 diffusion coefficient slightly decreases upon incorporation of silver NPs with respect to neat Pebax, suggesting that the NPs might increase the tortuosity of the diffusion pathway travelled by CH_4 in the mixed matrix membrane. This effect, however, is within the experimental uncertainty. A summary of transport data at 1 atm and 35°C is shown in Table A4.

To put the performance of Pebax+2OD2K-Ag and Pebax+2OD4K-Ag in broad perspective, the ideal CO_2/CH_4 selectivity was plotted in a Robeson-type plot as a function of CO_2 permeability and compared with other materials (cf. Figure 14),[39,115–117] as well as the 2008 upper bound.[39] The simultaneous increase in CO_2 permeability and CO_2/CH_4 selectivity shifts both Pebax+2OD2K-Ag and Pebax+2OD4K-Ag closer to the upper bound, relative to the neat Pebax. For example, Pebax+2OD2K-Ag and Pebax+2OD4K-Ag possess similar pure-gas selectivity as Matrimid,

cellulose acetate and polysulfone, while pure-gas CO_2 permeability is about 35 times larger. This enhancement is quite impressive, considering that it can be achieved with a NPs loading of 2% or less.

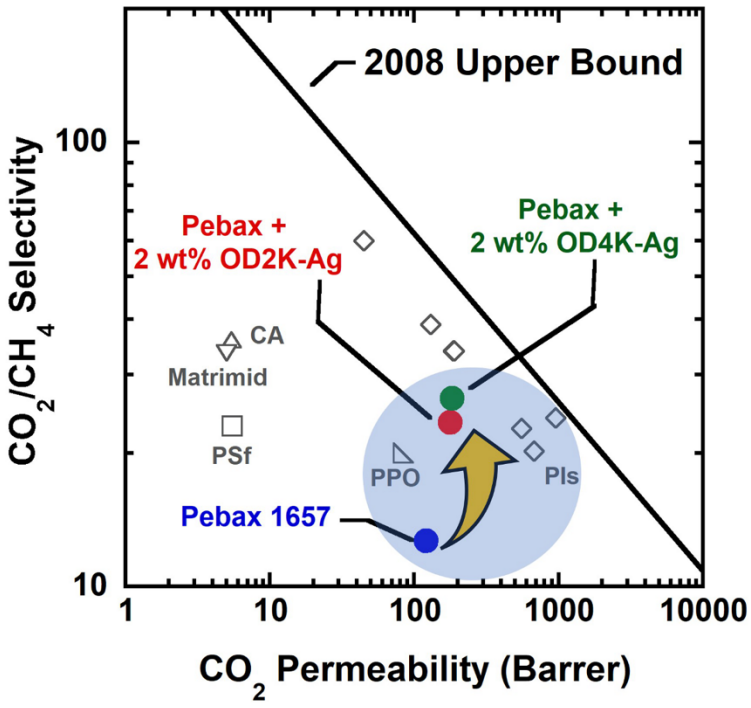

Figure 14: *Comparison among the CO_2/CH_4 separation performance of Pebax, Pebax+2OD2K-Ag, and Pebax+2OD4K-Ag with state-of-the-art materials on the 2008 upper bound.[39] Data are from pure-gas permeation measurements at 35 ºC with a feed pressure of 1-10 atm. PSf stands for polysulfone,[115] CA stand for cellulose acetate,[116] PIs stands for polyimides,[39] and PPO stands for poly(2,4-dimethly-1,4-phenylene oxide).[117]*

Obviously, an important question concerns the long-term stability of these membranes. It is well known, indeed, that silver is prone to reduction/oxidation processes in the presence of UV light and poisoning gasses, such as H_2 and H_2S, which are common contaminants in natural gas.

2.5.5. Membrane Stability.

Despite their high performance in the short time-frame, metal ion carriers usually experience photo/chemical ageing, which causes a decay of their performance within a few hours.[14,15] To

evaluate the stability of the newly synthesized materials, CO_2 and CH_4 permeability, and CO_2/CH_4 selectivity in Pebax+2OD2K-Ag and Pebax+2OD4K-Ag was measured before and after exposure to H_2 at 1 atm and 35 ºC for 24 hours (cf. Table 4).

Table 4: *CO_2 permeability and CO_2/CH_4 selectivity before and after 24-hour hydrogen exposure.*

sample	CO_2 permeability Pre-H_2 (Barrer)	CO_2/CH_4 Selectivity	CO_2 permeability Post-H_2 (Barrer)	CO_2/CH_4 Selectivity	% Change in CO_2 Permeability	% Change in CO_2/CH_4 Selectivity
Pebax+2OD2K-Ag	177.7 ± 9.0	25.8 ± 1.9	163.3 ± 8.3	24.3 ± 1.05	-8.8 %	-6.0 %
Pebax+2OD4K-Ag	187.6 ± 6.5	27.6 ± 1.8	171.9 ± 6.9	25.4 ± 2.9	-9.1 %	-8.5 %

Listed for each MMM is the CO_2 permeability (Barrer) and CO_2/CH_4 selectivity, measured at 1 atm and 35 ºC, before and after a 24-hour H_2 exposure at 1 atm and 35 ºC. The percent change in both permeability and selectivity values is included.

The CO_2 permeability in Pebax+2OD2K-Ag, both before and after H_2 treatment, are 177.7 ± 9.0 and 163.3 ± 8.3 Barrer, respectively. Upon exposure to H_2, CO_2 permeability apparently dropped by nearly 9%, with a subsequent drop in CO_2/CH_4 selectivity of 6% (cf. Table 4). However, if we consider the experimental uncertainty affecting these measurements, these drops are negligible; therefore, permeability and selectivity remained essentially unchanged, pointing out the superb stability of the mixed matrix membranes under study to H_2. Similarly, CO_2 permeability and CO_2/CH_4 selectivity in Pebax+2OD4K-Ag experienced an apparent drop of 9.1% and 8.5%, respectively. Again, if we consider the experimental uncertainty (cf. Table 4), this drop is negligible, indicating a very good stability also in the case of Pebax+2OD4K-Ag.

Remarkably, after exposure to pure H_2, the overall CO_2 permeability and CO_2/CH_4 selectivity remained 40% and 95% higher, respectively, relative to neat Pebax. For the sake of comparison, previously reported Pebax-based facilitated transport membranes containing 80 wt% $AgBF_4$ have experienced a loss in selectivity of higher than 10% after 24 hours of H_2 exposure, with a complete

loss in selectivity after 30 days,[51] indicating that our approach offers not only a simultaneous increase in permeability and selectivity, but also a decent stability enhancement. Moreover, the possibility to achieve such enhancement with a very modest NPs loading, only 2%, would benefit the economics of the process.

The analysis of the individual and synergistic effects of the NPs composition, surface grafting density, and weight loading on i) long-term (i.e., >30 days) NP photochemical stability under various conditions (i.e., H_2 and UV), ii) compatibility with the bulk membrane matrix, iii) CO_2 solubility-selectivity and iv) facilitated transport will be discussed in more detail in Chapter 3.

2.6. Conclusions

Silver NPs were rationally designed utilizing an appropriate polymeric ligand (i.e., capping agent) to be incorporated in polymers and fabricate novel facilitated transport membranes (FTMs) exhibiting enhanced CO_2 permeability, CO_2 selectivity and long-term stability. The synthesis of the capping agent, poly(amic-acid, PAAs) was performed through the polycondensation reaction of 4,4'-Oxydipthalic anhydride (ODPA) and Jeffamines exhibiting systematically varied molecular weight (i.e., ether concentration). The polymer structures were confirmed using NMR and ATR-FTIR. The degree of polymerization was similar in polymers containing each diamine, and the impact of the resulting differences in the overall molecular weight with respect to the silver NP synthesis did not change the particle size/shape morphology significantly.[111] The particles exhibited clear coordination interactions (i.e., chelation) with the PAAs carbonyl moieties, which produced individual spherical NPs. Micrographs revealed that particles with similar size/morphology were achievable despite the differences in polymer molecular weight. Though, there exist clear differences in the surface grafting density. Once incorporated into Pebax 1657, both NPs produced an impressive increase in overall CO_2 permeability (+50%) and CO_2/CH_4

selectivity (+100%), with increases, in the case of Pebax+2OD4K-Ag, in both CO_2 solubility and diffusivity. These improvements are remarkable, as they were achieved with a very low NPs loading, just 2% or less. Equally important, preliminary results indicated that our membranes exhibit high stability upon exposure to H_2, highlighting the importance of rational molecular design of the capping agent. The impact of surface grafting composition, weight loading, as well as the stability of these materials in a variety of environments will be the subject of Chapter 3.

Chapter 3. Enhancing Nanoparticle Design to Fabricate Defect-free Mixed Matrix Membranes**

3.1. Abstract

In the previous Chapter, facilitated transport membranes (FTMs) were designed by embedding poly(amic-acid) (PAA) stabilized silver nanoparticles in Pebax 1657. Although significant improvement in CO_2 permeability and CO_2/CH_4 selectivity was observed relative to neat Pebax at low filler loadings, these FTMs experience a decay in selectivity at higher filler loadings. In this study, we successfully combined experiments and theoretical modeling to *i)* discover the molecular origin of the observed behavior, and *ii)* optimize the nanoparticles design to eliminate selectivity losses at high filler loadings. We show that the length (i.e., molecular weight) of the PAA stabilizing agent directly affects the Pebax crystallinity and glass transition temperature and thus, its diffusion-selectivity. When shorter chain PAA is used, it is possible to increase the silver nanoparticles loading in Pebax without adversely affecting its structure and transport properties. Finally, the effect of the second-generation nanoparticles on the FTMs stability and mixed-gas transport behavior was investigated, and structure-property correlations were developed.

**Reproduced, with permission from Webb, et al.[118]

3.2. Introduction

Natural gas demand was projected to grow by nearly 64% between 2012 and 2040, reaching an annual demand of 180 trillion standard cubic feet.[119] However, its widespread use poses challenges due to the expensive requirement to reduce carbon dioxide levels to below 2%, which is essential to prevent pipeline corrosion.[2] Of equal importance, removing higher hydrocarbons like ethane and propane is crucial to meet the specifications for combustion and to achieve suitable heating values.[2,3] These challenges highlight the need for efficient separation technologies, not only in natural gas processing but also in related sectors, such as the separation of paraffins and olefins in petrochemical production.[6] The separation of ethane from ethylene, for example, is particularly challenging and costly due to the nearly identical condensability and sizes of these molecules.[12,120] Poly(ethylene), which represents nearly 35% of the global plastic demand with a market volume of around 100 million metric tons, requires energy-intensive processes for ethylene purification.[121] Ethylene production is the second-largest contributor to global energy consumption, using nearly 2 exaJoules per year.[10] Although facilitated transport membranes could potentially fix some shortcomings exhibited by conventional solution-diffusion membranes, such as limited selectivity,[122] they also exhibit their own limitations, such as carrier instability and sensitivity to moisture and poisoning agents.[14,51,122–125]

This study aims to build on our previous research, where silver nanoparticles (Ag NPs) were stabilized using a series of poly(amic-acid)s (PAAs) and incorporated into Pebax 1657 for facilitated CO_2 transport.[59] The resulting mixed matrix membranes (MMMs) demonstrated nearly a 100% increase in CO_2/CH_4 selectivity and a 50% increase in CO_2 permeability compared to neat Pebax at only a 2 wt% silver loading.[59] However, the effects of varying the weight loadings of Ag NPs within the polymer matrix for facilitated transport remain underexplored. This study aims to

fill this gap by exploring the motivation for using higher weight loadings of Ag NPs. Higher loadings of Ag NPs are expected to provide enhanced gas separation capabilities,[126–128] but also can present challenges related to particle dispersion and stability.[14,129,130] To broaden our range of application, key differences in CO_2/CH_4 and C_2H_4/C_2H_6 separation behaviors, particularly at higher silver weight loadings, were examined. Utilizing these differences at multiple weight loadings becomes useful in identifying potential strengths/weaknesses in the designed particles, which can then be optimized for specific separations. Both CO_2 and C_2H_4 are known to experience facilitated transport through reversible interactions with silver nanoparticles, making them ideal probes to test our newly developed facilitated transport membranes.[76,128,131–133] Capping agents, i.e., molecules or ions that bind to the particle surface, play a critical role in stabilizing silver nanoparticles and preventing their agglomeration, which is vital for maintaining their dispersion within the polymer matrix.[134–138] As shown in this study, the choice of capping agent, including its molecular weight, and chemical functionality, significantly influences the properties of Ag NPs and their interaction with both the polymer matrix and the penetrating gas species.[134,139,140] In the context of facilitated transport, it has been shown that through the use of electron acceptor groups, capping agents are essential in tuning surface polarization properties that allow for the complexation of CO_2 and olefins.[110,141,142] Previous studies have investigated the impact of surface modified Ag NPs on the gas selectivity and permeability of polymer matrices.[124,128,133,143] As shown by Chae et al., Ag NPs capped with 7,7,8,8-tetracyanoquinodimethane (TCNQ) were dispersed in polyvinylpyrroline (PVP) to form MMMs exhibiting greatly improved olefin/paraffin selectivity.[133] Thus, to optimize the performance of facilitated transport membranes, it is essential to carefully consider/modify the capping agents to balance these interactions.

We observed that increasing Ag NP loading in Pebax impacts polymer crystallinity and chain mobility, which, in turn, affects the membrane selectivity and transport properties. Through the analysis of the energetics of sorption, diffusion and permeation, we show that loss of size sieving ability occurs at higher weight loadings (i.e., $\geq$ 2.5 wt% by silver). Specifically, we demonstrate that if the particle capping agent (i.e., the PAA) has sufficient molecular weight (i.e., chain length), it can suppress the Pebax glass transition temperature (T_g) and its crystallinity, thus causing the observed loss in size sieving ability. Therefore, we hypothesized that the adverse effects on selectivity can be mitigated by reducing the molecular weight of the PAA .[70,144] This hypothesis-driven approach guided the design of a second generation of Ag NPs with shorter capping agents. We show that mixed matrix membranes (MMMs) fabricated using NPs containing shorter PAA capping agent did not show a suppressed glass transition temperature (T_g) relative to neat Pebax, even at higher nanoparticle loadings, which led to improved performance.

It is also well known that facilitated transport is susceptible to photo/chemical reduction processes.[14,51,126,145] In this study, the stability of Ag NPs exhibiting systematically different length of the capping agent upon exposure to H_2 gas for 1 week was investigated and compared to previously reported materials.

Finally, mixed gas CO_2/CH_4 and C_2H_4/C_2H_6 tests were used to gauge the effectiveness of these materials under realistic conditions, particularly to test if swelling/plasticization of highly sorbing gases, such as CO_2 and hydrocarbons, impact the observed selectivity boost from the facilitated transport mechanism.

3.3. Experimental Methods

3.3.1. Materials

For the sake of brevity, details about the chemicals used in this Chapter, and any purification routes can be found in Section B1.

3.3.2. Synthesis of Poly(amic-acid)s

Poly(amic-acids) (PAAs) were synthesized via a polycondensation reaction between 4,4'-oxydiphthalic anhydride (ODPA) and Jeffamine D-2000 (D2K), as shown in Figure 15. Details are provided in the Section B2. PAAs synthesized using a 1:1 molar ratio of D2K:ODPA are denoted as OD2K1, and PAAs synthesized using a 2:1 molar ratio are referred to as OD2K2. The rationale behind the synthesis of OD2K2 was to minimize the PAA molecular weight (i.e, chain length), to systematically analyze the effect of the PAAs molecular weight on the facilitated transport ability of the ensuing NPs. The synthesis of OD2K2 was driven by the hypothesis, which will later be demonstrated, that the effect of PAA length impacts the separation performance, particularly at high silver weight loadings, by affecting the Pebax chain mobility and crystallinity.

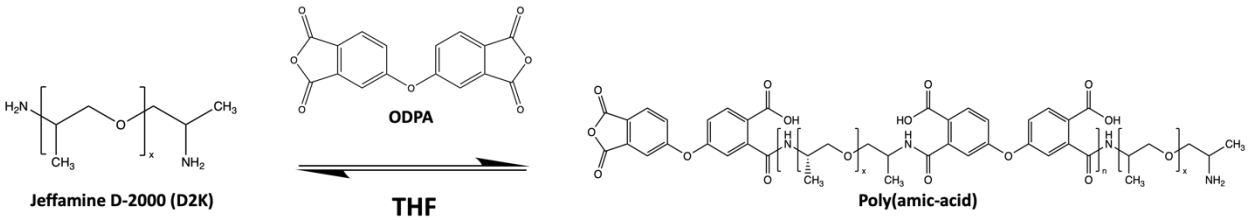

Figure 15: *Synthesis of poly(amic-acid)s (PAA)s from D2K and ODPA in tetrahydrofuran (THF). The resulting PAA structure is shown. X (~33) denotes the number of repeating segments within each D2K molecule. n denotes the number of repeating segments within the overall PAA, and is estimated to be ~9 and 2 for OD2K1 and OD2K2, respectively, based on their molecular weight (cf.* Table 5*).*

The resultant PAAs were characterized using Fourier Transform Infrared Spectroscopy (FTIR), as shown in Section C3. The molecular weight of OD2K2 was estimated using its intrinsic viscosity, based on prior gel permeation chromatography estimates for the molecular weight of OD2K1, as well as its corresponding intrinsic viscosity.[59,146,147] It is important to note that the same batch of

OD2K1 used in a previous work (formerly called OD2K) was used in the work.[59] Details of these measurements and calculations are available in Section B4.

Table 5: *D2K:ODPA molar ratio used to synthesize OD2K1 and OD2K2. The intrinsic viscosity, glass transition temperature (T_g), and estimated molecular weight (g/mol) of each polymer are also included.*

Poly(amic-acid) Type	D2K:ODPA Molar Ratio	Intrinsic Viscosity (dL/g)[a]	T_g (°C)	Molecular weight (g/mol)
OD2K1[b]	1:1	0.232 ± 0.001	-50.4	20800 ± 4310
OD2K2[c]	2:1	0.194 ± 0.001	-57.4	5310 ± 2970

[a] *Measured at 35 °C and in chloroform*
[b] *Molecular weight measured using gel permeation chromatography in chloroform*[59]
[c] *Molecular weight based on intrinsic viscosity measurements, c.f. Section B4*

3.3.3. Synthesis of Silver Nanoparticles

The protocol used to synthesize the silver nanoparticles did not change with respect to that previously reported.[59] For the sake of brevity and to avoid confusion with the use of updated nomenclature, its details are summarized in Section B5. Particles capped using OD2K1 and OD2K2 are referred to as OD2K1-Ag and OD2K2-Ag, respectively. The actual amount of PAA (i.e., either OD2K1 or OD2K2) in the resultant silver nanoparticles was determined using thermogravimetric analysis (TGA) (c.f., Sections B6 and B7). Particle morphology and size analysis was determined using transmission electron microscopy (TEM), whose details are provided in Section B7. These characterizations serve as an additional check to the consistency and reproduction of the OD2K1-Ag nanoparticles that have been reported in our previous work (previously referred to as OD2K-Ag).[59]

3.3.4. Fabrication of Mixed Matrix Membranes (MMMs)

In this study, five types of membranes were fabricated: neat Pebax 1657 (Pebax), to be used as the baseline material, mixed matrix membranes comprising Pebax and 2.5 or 4 wt%, by silver, of

OD2K1-Ag, and mixed matrix membranes comprising 2.5 or 4 wt%, by silver, of OD2K2-Ag. All membranes were fabricated via solution casting, resulting in free standing 80-100 mm thick films. Details are reported in Section B8. Membranes containing "x" wt% of silver by mass, using particles which are stabilized by PAA "y", are denoted by Pebax+xy-Ag. For example, MMMs with silver nanoparticles that were formed using OD2K1, and loaded in the membrane at 4 wt%, would be labeled as Pebax+4OD2K1-Ag. The membranes' cross-section was studied via scanning electron microscopy (SEM) (cf. Section B9).

3.3.5. Density measurements

The density of Pebax, Pebax+2.5OD2K1-Ag, and Pebax+4OD2K1-Ag was measured using an Archimedes' balance at 22 °C in heptane to investigate any trend in density between materials, as well as to correct for any changes in density that may affect sorption measurements (cf. Section B10).[114] Heptane was chosen as the buoyant liquid for the density measurements based on its negligible uptake and swelling in Pebax materials, as opposed to other solvents, such as water.[148,149]

3.3.6. Pure Gas Sorption and Permeation Measurements

Pure gas CH_4, CO_2, C_2H_6, and C_2H_4 permeation and sorption measurements in Pebax, Pebax+2.5OD2K1-Ag, and Pebax+4OD2K1-Ag were taken between 1 and 30 atm, at 15, 25, 35, and 45 °C. Pure gas sorption was measured via the pressure decay method in a constant volume apparatus.[114] Pure gas CH_4, CO_2, C_2H_6, and C_2H_4 permeation was tested on Pebax+2.5OD2K2-Ag and Pebax+4OD2K2-Ag at 1 atm and 35 °C. Details can be found in Sections B11 and B12. Gas diffusivities were then calculated using the solution diffusion model[20,34] (cf. Section B13), that is:

$$\overline{D} = \frac{P}{S} \quad \text{(Eq. 17)}$$

where P is the permeability, S is the sorption coefficient, and $\overline{D}$ is the concentration-averaged diffusion coefficient. Finally, the pure gas overall (α^P), sorption- (α^S), and diffusion- (α^D) selectivity was calculated as follows:

$$\alpha^P = \frac{P_i}{P_j} = \frac{S_i}{S_j} \times \frac{D_i}{D_j} = \alpha^D \alpha^S \quad \text{(Eq. 18)}$$

where *i* and *j* refer to the specific gases being compared. Pure gas transport properties for CH_4, CO_2, C_2H_6, and C_2H_4, at 35 °C and 1 atm, can be found in Section B14, while the dependency of transport parameters on temperature can be found in Section B15 and B16. This dependency is also discussed later in this Chapter (cf. Section 3.4.2).

3.3.7. Thermal and Structural Characterization of PAAs and MMMs

Dynamic scanning calorimetry (DSC) and wide and small angle x-ray scattering (WAXS/SAXS) characterization is discussed in Sections B17 and B18.

3.3.8. H_2 Stability test

To test the facilitated transport membranes stability, Pebax, Pebax+2.5OD2K1-Ag, and Pebax+2.5OD2K2-Ag were exposed to 1.4 atm H_2 at room temperature for 7 days. Prior to, and after the materials were treated with H_2, pure gas CO_2, CH_4, C_2H_6, and C_2H_4 permeation were measured at 35 °C and 1 atm. Changes in the overall CO_2 and C_2H_4 permeability, as well as CO_2/CH_4 and C_2H_4/C_2H_6 selectivity as a result of H_2 exposure are tabulated and compared in Section B19.

3.3.9. Mixed Gas Permeation Measurements.

Mixed gas CO_2/CH_4 and C_2H_4/C_2H_6 permeation was measured at 35°C in Pebax, Pebax+2.5OD2K-1Ag, and Pebax+2.5OD2K2-Ag using an automated constant volume, variable pressure apparatus (*Maxwell Robotics*, Austin, TX). Gas compositions for both the feed and permeate streams were analyzed using a Shimadzu GC 2030 with a Fast Fuel Analyzer setup. C_2H_4/C_2H_6 mixtures were tested using a molar feed composition of either 50/50 and 20/80%, whilst CO_2/CH_4 was tested at a molar composition of 50/50%, both targeting CO_2 and C_2H_4 partial pressures of ~1 atm, to make direct comparisons to the pure gas data. Details about these measurements are provided in Section B20.

3.4. Results and Discussion

3.4.1. Structural characterization

OD2K1-Ag and OD2K2-Ag were both incorporated into Pebax at loadings of either 2.5 or 4 wt% silver, as calculated via TGA measurements. The MMMs did not show a large change in the thermal stability relative to neat Pebax, up to 800 ºC (cf. Section B6). This result was expected, given the relatively low NP weight loadings.

SEM micrographs indicate that all MMMs are defect free up to the maximum loading of 4 wt% silver (cf. Section B9).

3.4.2. Effect of OD2K1-Ag loading on pure Gas Transport

An array of gas permeation and sorption experiments in Pebax loaded with OD2K1-Ag NPs was designed to unravel the mechanisms by which this filler affects transport properties. As discussed later in this Chapter, this information is critically important to optimize the particles design and, in turn, their gas separation performance. Upon the addition of 2.5 wt% of OD2K1-Ag into Pebax,

CO_2 permeability at 35 °C and 1 atm increased by 41% while CO_2/CH_4 ideal selectivity increased by 49% relative to neat Pebax (cf. Figure 16A). Likewise, the permeability of C_2H_4 increased by 57.4%, and the overall C_2H_4/C_2H_6 selectivity increased by 37.6% relative to neat Pebax, at 1 bar and 35 °C (cf. Figure 16B). However, upon increasing the silver weight loading of OD2K1-Ag to 4 wt% in Pebax (i.e., Pebax+4OD2K1-Ag), the overall CO_2/CH_4 and C_2H_4/C_2H_6 selectivity changed by -6.3% and +59.2%, respectively, relative to neat Pebax. It should be noted that the CO_2/CH_4 selectivity drops 37% from Pebax+2.5OD2K1-Ag to Pebax+4OD2K1-Ag. The drop in CO_2/CH_4 selectivity was accompanied by a 100% increase in CO_2 permeability from 128 ± 10 Barrer in neat Pebax to 257 ± 29 Barrer in Pebax+4OD2K1-Ag. Similarly, the C_2H_4 permeability increases to 91 Barrer (nearly 6 times that measured in neat Pebax) after adding 4 wt% of OD2K1-Ag.

To put the performance of Pebax, Pebax+2.5OD2K1-Ag, and Pebax+4OD2K1-Ag in perspective, the ideal CO_2/CH_4 and C_2H_4/C_2H_6 selectivity were plotted in a Robeson-type upper bound plot as a function of CO_2 and C_2H_4 permeability, respectively, and compared with state of the art materials (cf. Figure 16A/B).[39,85,115,116,150–153] In general, there is a simultaneous increase in permeability and selectivity in Pebax+2.5OD2K1-Ag and Pebax+4OD2K1-Ag, which shifts these materials closer to the 2008 CO_2/CH_4 and C_2H_4/C_2H_6 upper bounds, relative to neat Pebax (cf. Figure 16A/B).[39,85] Interestingly, Pebax+2.5OD2K1-Ag exhibits a maximum in the CO_2/CH_4 selectivity. Moreover, the increase in C_2H_4/C_2H_6 selectivity in the mixed matrix membrane loaded with OD2K1-Ag relative to neat Pebax becomes less prominent with increasing the filler loading, as shown by the downward concavity of the red arrow in Figure 16B.

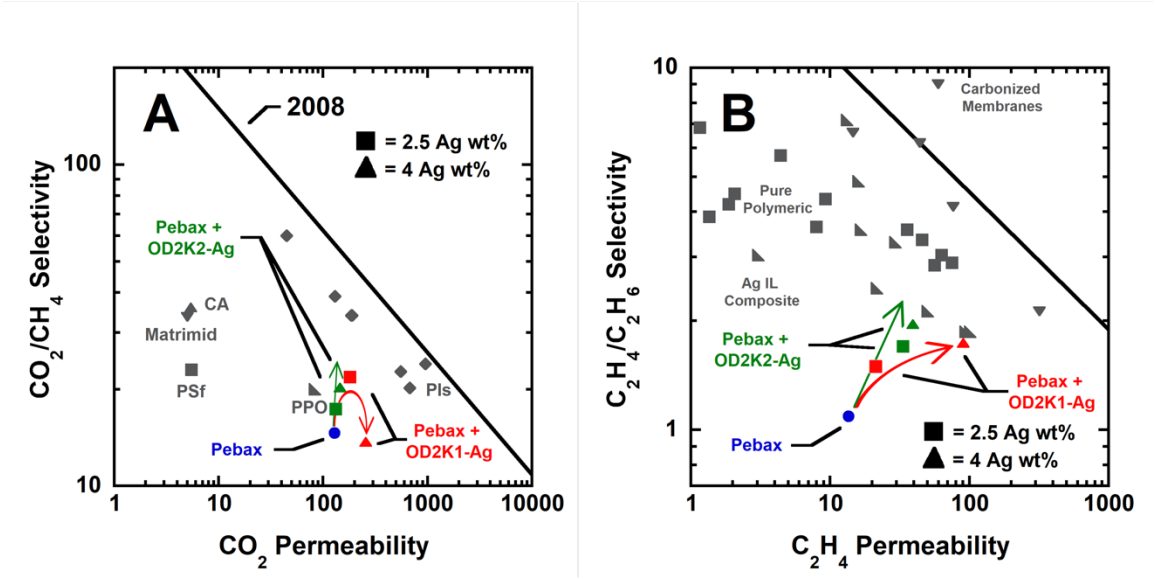

Figure 16: *Comparison among the A) CO_2/CH_4 separation performance of Pebax (blue), Pebax+2.5OD2K1-Ag (Red), Pebax+4OD2K1-Ag (Red), Pebax+2.5OD2K2-Ag (Green), and Pebax+4OD2K2-Ag (Green) with state-of-the-art materials on the 2008 Upper Bound[39]. Circles are used for neat Pebax, while squares and triangles are used to indicate a Ag weight loading of 2.5 and 4 wt%, respectively. and B) C_2H_4/C_2H_6 separation performance of Pebax (blue), Pebax+2.5OD2K1-Ag (Red), Pebax+4OD2K1-Ag (Red), Pebax+2.5OD2K2-Ag (Green), and Pebax+4.5OD2K2-Ag (Green) with state-of-the-art materials on the C_2H_4/C_2H_6 Upper Bound[85]. Circles are used for neat Pebax, while squares and triangles are used to indicate a Ag weight loading of 2.5 and 4 wt%, respectively. Arrows indicate increasing filler loading. Data are from pure-gas permeation measurements at 20-35 ℃ and with a feed pressure of 1-3 atm. PPO stands for poly(2,4-dimethly-1,4-phenylene oxide)[115], CA stand for cellulose acetate[116], PIs stands for polyimides[39], PSf stands for polysulfone[150], and Ag IL composite stands for Silver Ionic-liquid composites[152]. Additionally, various carbonized[151,153] and purely neat polymeric membranes are included in Figure 12B[85].*

To explain these trends and rationalize the effect of the silver nanoparticles on gas transport, permeability was broken into its elementary diffusion and sorption components. CO_2 sorption slightly increases with OD2K1-Ag weight loading, specifically, by 2.6 and 5.1% for the 2.5 and 4 wt% MMMs, respectively (cf. Figure 17A). This result is consistent with the idea of incorporating additional CO_2-philic sites, i.e., ether groups,[24,25,93] as well as facilitating agents,[76,154] i.e., silver nanoparticles in Pebax. Ideal (i.e., pure-gas) CO_2/CH_4 sorption selectivity in Pebax, Pebax+2.5OD2K1-Ag, and Pebax+4OD2K1-Ag are 4.85 ± 0.05, 6.02 ± 0.12, and 5.07 ± 0.12,

respectively (cf. Figure 17B). However, these values are sensitive to the high uncertainty affecting CH_4 sorption data, due to the extremely low CH_4 solubility in these materials (e.g., 0.2 cm^3(STP)/cm^3 (polymer atm). For example, CH_4 sorption was slightly suppressed upon adding 2.5 wt% OD2K1-Ag (from 0.23 to 0.19 cm^3(STP)/cm^3 (polymer atm, respectively), but it recovers a value similar to that of Pebax upon adding 4 wt% OD2K1-Ag (0.23 cm^3(STP)/cm^3 (polymer atm). It is worth noting that despite some sensitivity due to low CH_4 sorption, the CO_2/CH_4 sorption selectivity exhibited by both MMMs containing OD2K1-Ag NPs is greater than that of neat Pebax. Both Pebax+2.5OD2K1-Ag and Pebax+4OD2K1-Ag experienced an impressive increase in CO_2 diffusivity relative to neat Pebax (+37.3 and +90.5%, respectively). In contrast, CH_4 diffusion coefficient did not show significant changes among the materials, except for CH_4 diffusivity in Pebax+4OD2K1-Ag. In the case of Pebax+2.5OD2K1-Ag, CO_2/CH_4 diffusivity-selectivity increased by 20% relative to neat Pebax. The simultaneous increase in CO_2 sorption, diffusion, and overall selectivity in Pebax+2.5OD2K1-Ag provides a physical picture that is compatible with facilitated CO_2 transport, whilst CH_4 is limited to solution-diffusion transport alone. The drop in CO_2/CH_4 selectivity in Pebax+4OD2K1-Ag is rationalized by the increase in CH_4 diffusivity, in tandem with CO_2 diffusivity, where the diffusivity of CH_4 becomes almost double the values found in Pebax and Pebax+2.5OD2K1-Ag (cf. Figure 17C). Further details on the diffusion behavior in Pebax+4OD2K1-Ag are provided in Section 3.4.3, where we show that the PAA-coated NPs disrupt the local crystallinity and PEO chain mobility in Pebax, especially at higher loadings of silver. This disruption impacts diffusivity-selectivity, ultimately offsetting the beneficial effects of facilitated transport. As we will see, this issue can be effectively fixed upon utilizing these “second generation” nanoparticles, that is, OD2K2-Ag.

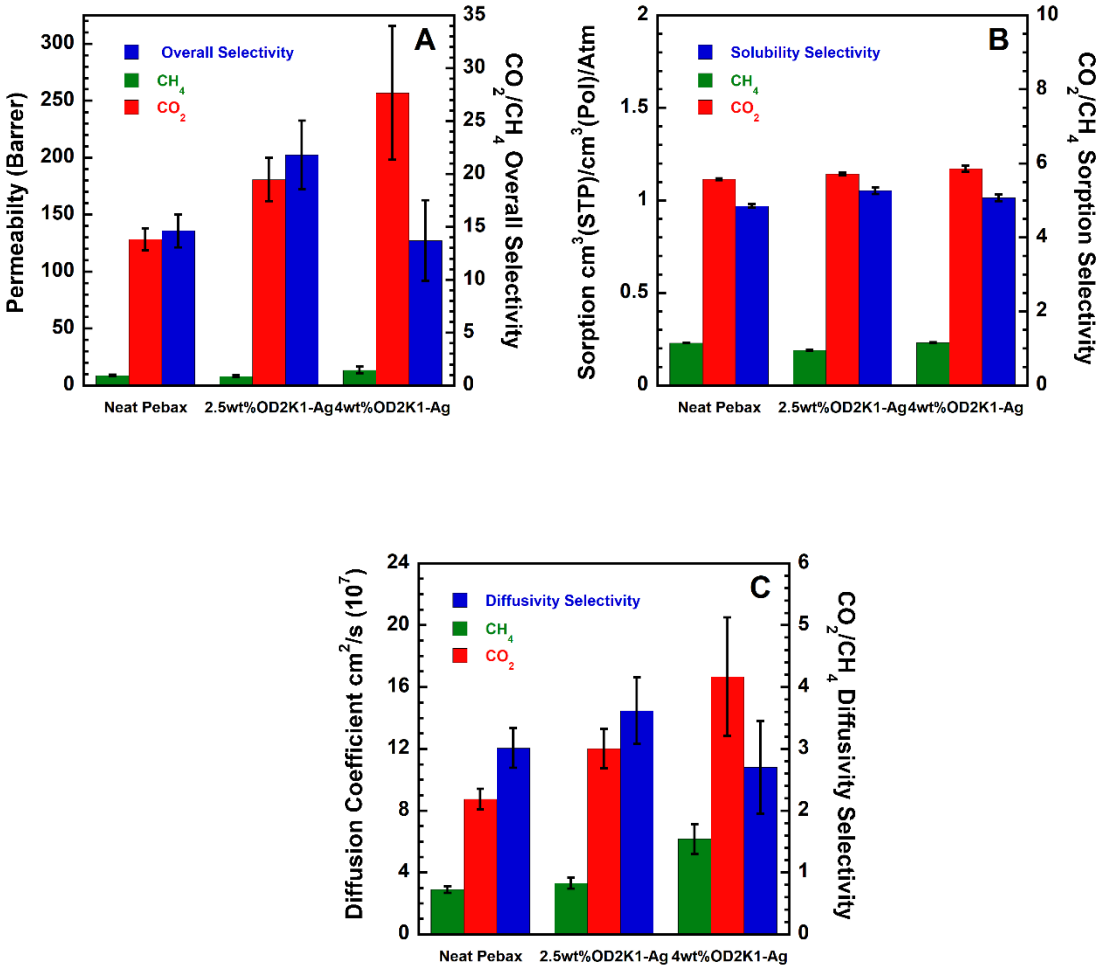

Figure 17: *Pure gas CO_2 and CH_4 A) Permeability and ideal selectivity, B) Sorption and sorption-selectivity, and C) Diffusivity and diffusivity-selectivity for Pebax, Pebax+2.5OD2K1-Ag, and Pebax+4OD2K1-Ag at 35 ℃ and 1 atm. Error bars were estimated using the linear error propagation method.*[114]

To gauge these competing effects, i.e., facilitated gas transport vs. disruption of the adjacent polymer matrix, the results for CO_2 and CH_4 are compared with C_2H_4 and C_2H_6 (cf. Figure 18A), as ethylene benefits from facilitated transport relative to ethane, exactly as CO_2 does with respect to CH_4. Moreover, it has been reported that C_2H_4 experiences much stronger binding interactions with Ag^+ with respect to CO_2,[141,155] and thus its transport is facilitated to a greater extent than CO_2. This fact is reflected by the greater increase in the overall C_2H_4 sorption and C_2H_4/C_2H_6 sorption-

selectivity as compared to the CO_2/CH_4 gas pair in MMMs containing OD2K1-Ag. For example, C_2H_4 sorption and C_2H_4/C_2H_6 sorption-selectivity increase monotonically, from 0.61 ± 0.01 cm^3(STP)/cm^3(polymer)/atm and 1.12 ± 0.01 in neat Pebax, to 0.73 ± 0.01 cm^3(STP)/cm^3(polymer)/atm and 1.23 ± 0.02 in Pebax+4OD2K1-Ag at 1 atm and 35 °C (cf. Figure 14B), which represents an overall improvement in C_2H_4 sorption by ~20%, and C_2H_4/C_2H_6 sorption-selectivity by ~9%. Unlike the case of CO_2 and CH_4, C_2H_4 diffusivity and C_2H_4/C_2H_6 diffusivity-selectivity also increased monotonically with increasing OD2K1-Ag loading in Pebax. Specifically, C_2H_4 diffusivity increased from 1.7×10^{-7} to 9.4×10^{-7} cm^2/s, and C_2H_4/C_2H_6 diffusivity-selectivity increased by +45%, from 0.98 ± 0.1 to 1.4 ± 0.1, upon adding 4 wt% OD2K1-Ag (cf. Figure 18C). Similar to CH_4, C_2H_6 sorption nor diffusivity changed significantly in the mixed matrix membranes, apart from C_2H_6 diffusivity in Pebax+4OD2K1-Ag, which increased over 3 times from neat Pebax. This result suggests that higher weight loadings could be inducing structural changes, or perhaps defects to the material, thus increasing the diffusion of each gas, and consequently, limiting the overall selectivity.

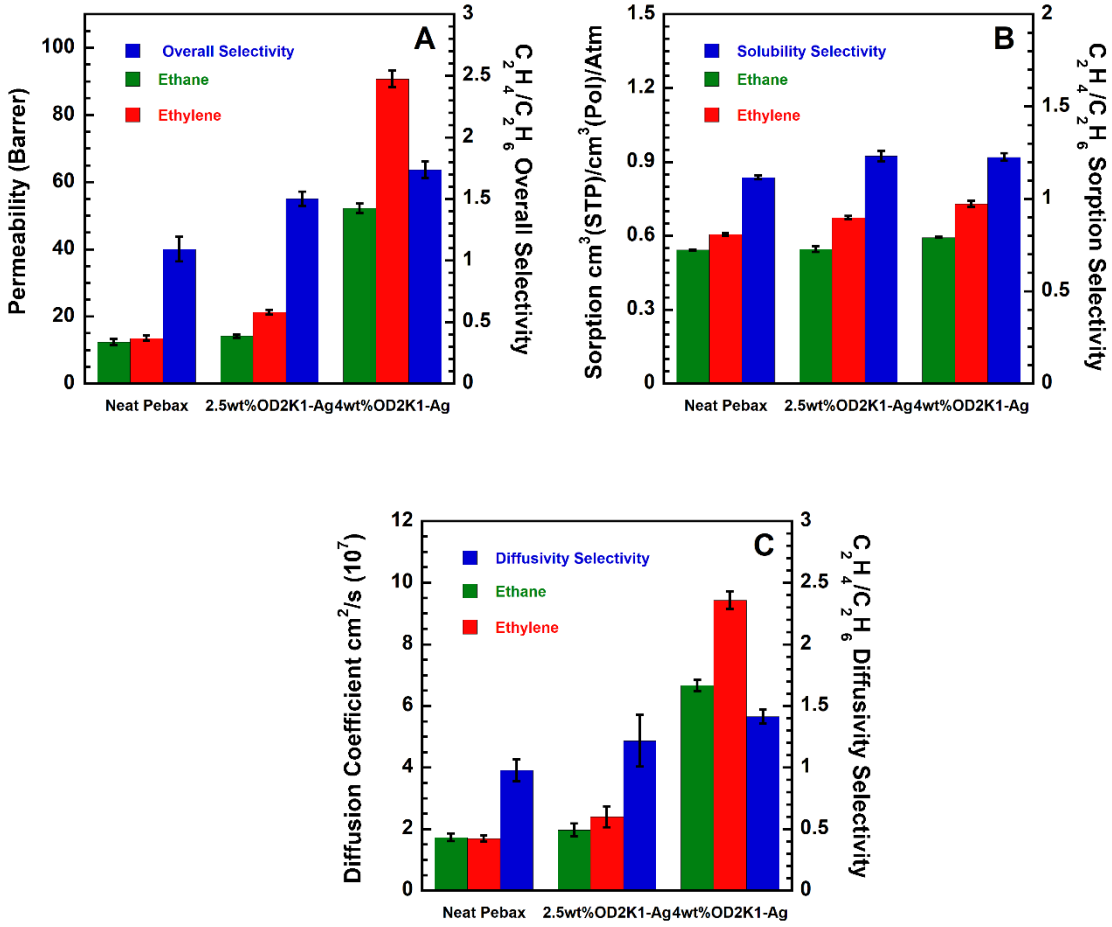

Figure 18: *Pure gas C_2H_4 and C_2H_6 A) Permeability and ideal selectivity, B) Sorption and sorption-selectivity, and C) Diffusivity and diffusivity-selectivity for Pebax, Pebax+2.5OD2K1-Ag, and Pebax+4OD2K1-Ag at 35 °C and 1 atm. Error bars were estimated using the linear error propagation method.*[114]

However, due to the similarity in kinetic diameter for C_2H_4 and C_2H_6 (0.42 nm vs. 0.44 nm, respectively), the C_2H_4/C_2H_6 diffusivity-selectivity of neat Pebax is 0.98 at 1 atm and 35 °C (cf. Figure 18C). The CO_2/CH_4 diffusivity-selectivity in the same material is 3. Consequently, matrix effects are less likely to influence the separation performance of C_2H_4/C_2H_6, i.e., the diffusivity-selectivity will mostly likely not decrease relative to neat Pebax.[156] Ultimately, this is shown through a simultaneous permeability and selectivity increase in C_2H_4/C_2H_6 up to 4 wt% of OD2K1-Ag.

A summary of transport data at 1 atm and 35°C is shown in Section B14.

3.4.3. Unveiling the effect of OD2K1-Ag on Pebax using Energetics of Transport

The analysis of the energetics of transport provides a deeper understanding of the underlying transport mechanisms and its connection to the membrane microstructure. Unlike simple permeability measurements, which offer only a snapshot of how gases move through a material, analyzing the energetics—such as activation energies of diffusion and enthalpies of sorption—allows us to discover structure-property correlations. This approach helps identify the key factors influencing the interactions between the polymer matrix and the gases, especially when incorporating nanoparticles like OD2K1-Ag. As discussed hereafter, this analysis makes it possible to explain the observed trends in gas selectivity and permeability and optimize the NPs design for enhanced gas separation performance. Pure gas CO_2, CH_4, C_2H_4, and C_2H_6, permeability (P) and sorption (S) data were collected at 15, 25, 35, and 45 °C in Pebax, Pebax+2.5OD2K1-Ag, and Pebax+4OD2K1-Ag at 1-30 bar. Permeability (P_i), sorption (S_i), and diffusivity (D_i) were fit, as a function of temperature, using the linearization of the following equations[157–159] at 1 atm, as higher pressures would disrupt the analysis due to swelling and/or potential plasticization effects:

$$P_i = P_{0,i} \exp\left(-\frac{\Delta E_{p,i}}{RT}\right) \quad \text{(Eq. 19)}$$

$$S_i = S_{0,i} \exp\left(-\frac{\Delta H_{s,i}}{RT}\right) \quad \text{(Eq. 20)}$$

$$D_i = D_{0,i} \exp\left(-\frac{\Delta E_{d,i}}{RT}\right) \quad \text{(Eq. 21)}$$

where i denotes the gas (e.g., CO_2) and $\Delta E_{p,i}, \Delta H_{s,i}, \Delta E_{d,i}$ are the activation energy of permeation, enthalpy of sorption, and activation energy of diffusion, respectively. Consequently, through the solution-diffusion model[20,34], these 3 values are related as follows:

$$\Delta E_{p,i} = \Delta H_{s,i} + \Delta E_{d,i} \quad \text{(Eq. 22)}$$

The activation energy of permeation reflects the overall energy barrier that a gas must overcome to cross the membrane, accounting for both polymer-matrix interactions (via the enthalpy of sorption) and the mobility of gas molecules within the polymer matrix (via the activation energy of diffusion).[160] The results for each gas in Pebax, Pebax+2.5OD2K1-Ag, and Pebax+4OD2K1-Ag are shown in Figure 19.

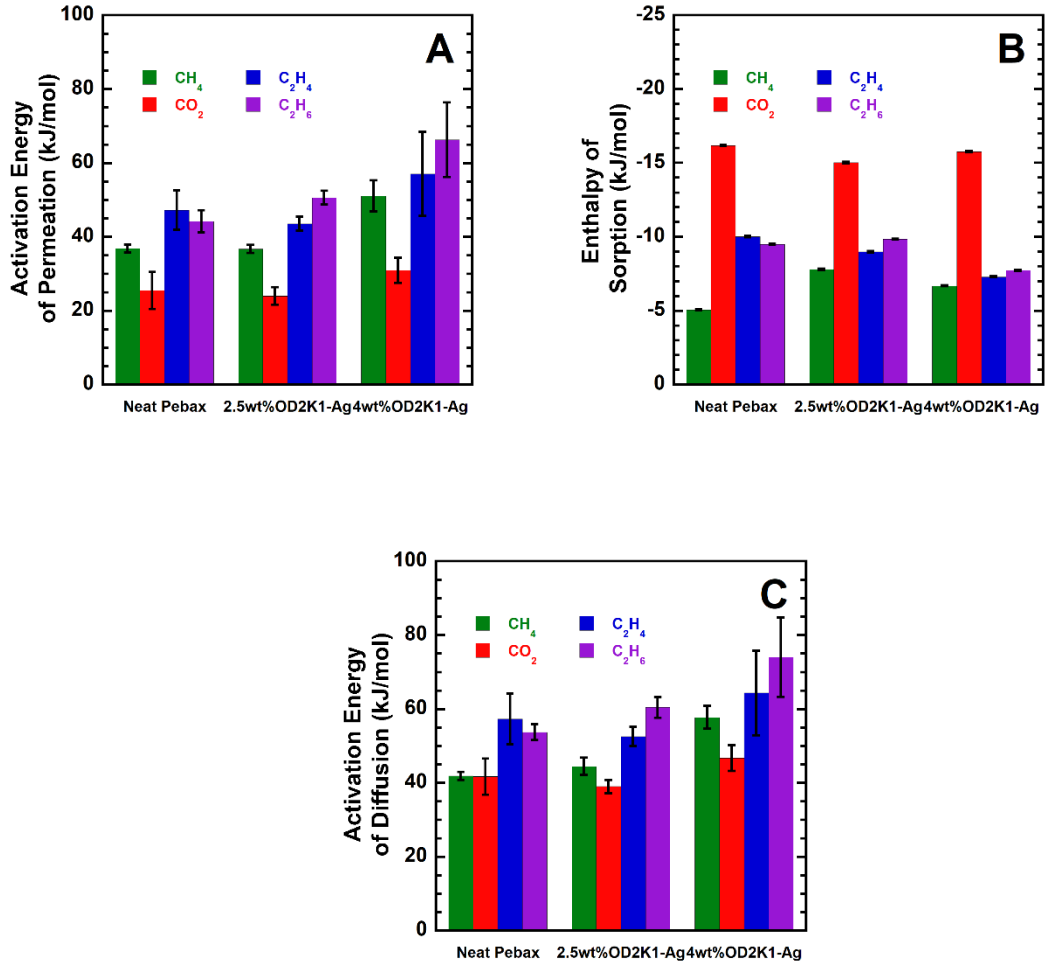

Figure 19: *Pure gas A) activation energy of Permeation, B) enthalpy of Sorption, and C) activation energy of Diffusion for CH_4, CO_2, C_2H_4, and C_2H_6 in Pebax, Pebax+2.5OD2K1-Ag, and Pebax+4OD2K1-Ag at 1 atm. These values were calculated though Eq.19-Eq.21 using*

permeation, sorption, and diffusion data for each gas, in each material, at 1 atm and 15, 25, 35, and 45 ℃. Error bars are calculated using standard error of regression.

The activation energy of permeation for neat Pebax at 1 atm for CH_4, CO_2, C_2H_4, and C_2H_6 is 36.9, 25.5, 47.3, and 44.3 kJ/mol, respectively. Noticeably, they follow the same order as the activation energy of diffusion, i.e., C_2H_4 (57.3 kJ/mol) ≥ C_2H_6 (53.8 kJ/mol) > CH_4 (41.9 kJ/mol) > CO_2 (41.7 kJ/mol), suggesting that the permeation process is controlled by diffusion.[161] As a result, both diffusion and permeation coefficients increase with temperature. Similar trends between the activation energy of permeation and activation energy of diffusion are shown for Pebax+2.5OD2K1-Ag and Pebax+4OD2K1-Ag, cf. Figure 19A-C. An overall correlation between E_p and E_D, for better visualization, can be found in Section B16. It should also be noted that the activation energy of permeation and diffusion, within experimental error, follow the order of the gas kinetic diameter, C_2H_6 (0.44 nm) > C_2H_4 (0.42 nm) > CH_4 (0.38 nm) > CO_2 (0.33 nm).[14,162] Interestingly, the activation energy of permeation and diffusion for both CO_2 and C_2H_4 decrease by 5.9 and 7.7%, respectively, upon adding 2.5 wt% of OD2K1-Ag. In contrast, $\Delta E_{p,CH_4}$ remains unaffected, and, remarkably, $\Delta E_{p,C_2H_6}$ increases by nearly 14% in Pebax+2.5OD2K1-Ag, with respect to neat Pebax. The notion of decreasing overall activation energy of permeation would be in line with the concept of facilitated diffusion which streamlines the transport of CO_2 and C_2H_4.[124] However, we must keep in mind in this interpretation that temperature will affect both the kinetics and equilibria of the π-complexation reactions, thus creating some difficulty in discerning the origin of this decrease in overall activation energy.[163] In striking contrast, the CH_4 and C_2H_6 activation energy of diffusion increases, which is likely indicative of the fact that the nanoparticles could increase the tortuosity of the diffusional pathways for the non-facilitated gases.[164] This fact remains consistent upon moving from 2.5 wt% of OD2K1-Ag to 4 wt%, whereas $\Delta E_{p,CH_4}$ and $\Delta E_{p,C_2H_6}$ both increased by 37.8 and 29.3% from neat Pebax (cf. Figure 19A/C).

The enthalpy of sorption is negative (i.e., exothermic sorption process), for all penetrants. The exothermic nature of penetrant sorption in Pebax 1657 based materials is consistent with previous reports.[165] Enthalpies of sorption generally decrease (i.e., sorption becomes more exothermic) with increasing penetrant critical temperature (T_C). One exception to this trend is CO_2, which displays a sorption enthalpy nearly 3 times more negative than that of CH_4, and 1.5 times more negative than that of both C_2H_4 and C_2H_6. This result is consistent with the highly favorable interaction between CO_2 molecules and ether groups in these materials.[24,93] Changes in the enthalpy of sorption are small relative to the changes in activation energy of diffusion when altering the NPs loading in Pebax. Specifically, the largest relative change in the enthalpy of sorption between materials is 2.7 kJ/mol, whilst the largest change for the activation energy of diffusion is 15.8 kJ/mol.

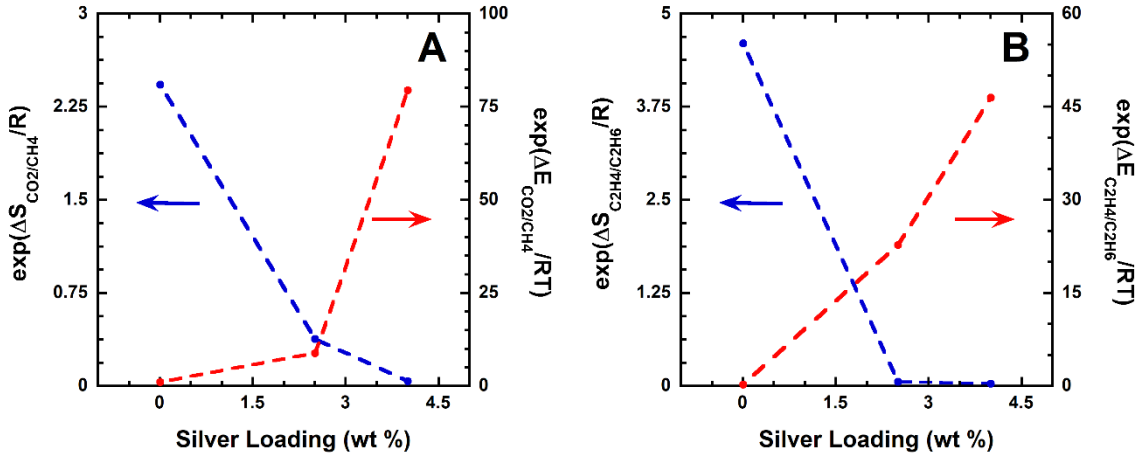

Figure 20: *A) Energetic (red) and entropic (blue) CO_2/CH_4 diffusivity selectivity in Pebax as a function of OD2K1-Ag weight loading from 0-4 wt%. A) Enthalpic (red) and entropic (blue) C_2H_4/C_2H_6 diffusivity selectivity in Pebax as a function of OD2K1-Ag weight loading from 0-4 wt%. Error bars are calculated using standard error of regression.*

Unexpectedly, increases in both the activation energy of diffusion and permeation for both CO_2 and C_2H_4 occur during the transition from Pebax+2.5OD2K1-Ag to Pebax+4OD2K1-Ag. The

overall perm-selectivity in Eq. 18 combines the effects of sorption-and diffusion selectivity. In each material and for each gas pair, diffusivity-selectivity changes more significantly than sorption-selectivity with increasing silver content, driving the overall changes in perm-selectivity. The aforementioned breakdown of the transport process shows that tuning diffusion selectivity is the key tool to improve separation performance of these materials at higher nanoparticle weight loadings. To pursue this issue further, one can probe deeper into the source of diffusional selectivity. According to the transition state theory[166]:

$$D = \frac{1}{6}\lambda^2 \frac{k_B T}{h} \exp\left(\frac{\Delta S^+}{R}\right) \exp\left(-\frac{\Delta E_D}{RT}\right) \qquad \text{(Eq. 23)}$$

where λ is the average jump length in the diffusion medium, ΔS^+ is the activation entropy of diffusion, k_B is the Boltzmann's constant, and h is Plank's constant. For the gas pairs and materials considered in this work, λ may be considered constant, and is around ~1.4 nm. This assumption is described in detail in Section B15. Comparing gas pairs, the diffusivity-selectivity can be broken down using Eq. 24, as follows.[159,160]

$$\alpha_D \equiv \frac{D_i}{D_j} = \exp\left(\frac{\Delta S_i^+ - \Delta S_j^+}{R}\right) \exp\left(-\frac{\left(\Delta E_{D,i} - \Delta E_{D,j}\right)}{RT}\right) = \exp\left(\frac{\Delta S_{i/j}}{R}\right) \exp\left(\frac{\Delta E_{i/j}}{RT}\right) \qquad \text{(Eq. 24)}$$

where *i* and *j* refer to individual components, e.g., *i* = CO_2 and *j* = CH_4. As a result, the diffusivity-selectivity of each gas pair is broken into two parts: 1) the entropic contribution $\left(\text{i.e.}, \exp\left(\frac{\Delta S_{i/j}}{R}\right)\right)$ and 2) the energetic contribution $\left(\text{i.e.}, \exp\left(\frac{\Delta E_{i/j}}{RT}\right)\right)$ to diffusivity-selectivity.[160,167] Energetic selectivity occurs due to differences in the activation energy between penetrants which is required to make diffusive jumps. Entropic selectivity refers to the effectiveness of a material to discriminate between the different sizes and shapes of penetrants. Each value was calculated for both the CO_2/CH_4 and C_2H_4/C_2H_6 gas pairs in Pebax, Pebax+2.5OD2K1-Ag, and

Pebax+4OD2K1-Ag. The entropic and energetic components are plotted as a function of silver weight loading in Figure 20.

The entropic contribution of neat Pebax for CO_2/CH_4 and C_2H_4/C_2H_6 are 2.6 and 4.6, respectively. These values are smaller than those found in rigid carbon molecular sieve membranes (up to ~15).[159,168] This result is reasonable, given that Pebax contains rubbery poly(ethylene oxide) (PEO) segments, which are not expected to provide any entropic selectivity. Upon increasing the weight loading of OD2K1-Ag in Pebax, entropic selectivity and energetic selectivity monotonically decrease and increase, respectively. One possible explanation could be an effect of the facilitated transport mechanism, which favors interactions between CO_2 and C_2H_4 and creates preferential pathways that CO_2 and C_2H_4 are more likely to follow, thus increasing energetic selectivity. On the other hand, while these gases enter temporary complexations with Ag NPs, their degree of rotational and translational freedom becomes slightly constrained, which would be consistent with the observed drop in the entropic selectivity. However, given the previously stated fact that C_2H_6 and CH_4 diffusivity increase significantly at 4 wt% loading of OD2K1-Ag, despite being non-facilitated gases, and CO_2/CH_4 overall selectivity decreases in Pebax+4OD2K1-Ag suggests otherwise. Therefore, the entropic loss in selectivity is more indicative to secondary effects, e.g., changes in the polymer matrix, occurring upon adding Ag NPs. Noticeably, these trends are more severe in the case of C_2H_4/C_2H_6, which could be due to stronger chemical interactions between silver and C_2H_4,[141,155] thus driving energetic selectivity, as well as their similarity in gas kinetic diameter (more so than CO_2/CH_4), which helps maximize entropic selectivity losses.

In summary, diffusivity, and more specifically, entropic diffusivity selectivity, plays a key role in the performance of these materials, especially at large NP weight loadings. Thus, it is hypothesized

that by also investigating potential structural evolutions in these materials, we might pinpoint the root of the problem and adjust the NP design.

3.4.4. Optimization of the NPs design: 2nd generation nanoparticles

To elucidate whether these losses in entropic selectvity were related to matrix changes, WAXS, SAXS, and DSC were used. As mentioned earlier, Pebax is a semicrystalline copolymer that contains a polyamide (PA6) and poly(ethylene oxide) (PEO) phase, with large diffraction peaks at 2θ values of 20 and 24 degrees.[169] This strong and broad peak ranging from 10° to 30° is generally considerd to be an intergration of both crystalline and amorphous phases that contain information in regards to both PA and PEO domains.[169] All other membranes fabricated in this work did not show large changes in polymer chain d-spacing, nor peak angle, from WAXS (cf. Figure 21A). However, there is a clear increase in peak intensity for MMMs with increaing weight loadings at ~33°. This result indicates the presence of the (111) face-centered cubic (FCC) facet for the silver nanoparticles.[170] WAXS data was further analyzed using peak deconvolution in an attempt to estimate the overall crystallinity (cf. Section B18). Upon adding OD2K1-Ag NPs, there is a slight drop in overall crystallinity, relative to neat Pebax, by 2-3%. However, a change in nanoscale ordered structures becomes more apparent upon adding OD2K1-Ag into Pebax, which is evident from SAXS data (cf. Figure 21B). Additionally, there is a slight increase in the interlamellar chain spacing when adding OD2K1-Ag into Pebax. Specifically, Pebax exhibits an intralamellar spacing of 101 Å, while the spacing in Pebax+2.5OD2K1-Ag and Pebax+4OD2K1-Ag are 104 Å and 106 Å, respectively (cf. Section B18). Therefore, both the increase in the SAXS d-spacing and broadening of the peak is likely related to the changes in crystalinity. This change become apparent with increasing loading of OD2K1-Ag type particles, and is consistent with the experimentally

observed increase in diffusivity and drop in CO_2/CH_4 diffusivity selectivity in Pebax+4OD2K1-Ag.[36,171]

As a second point of comparison, DSC shows a T_g for Pebax at -50 °C, which is representative of the rubbery PEO region. OD2K1, which is totally amorphous (cf. Section B18), exhibits a T_g at -54 °C. Upon adding 2.5 wt% of OD2K1-Ag into Pebax, there is little to no change in the T_g value. However, upon adding 4 wt%, the T_g experiences a drop to a temperature similar to the neat OD2K1, i.e., -54 °C. This observation suggests that at a 4 wt% loading, there is an increase in chain mobility.[172] This finding supports the picture that the nanoparticles, particularly the capping agent OD2K1, disrupt the Pebax crystallinity, leading to increased chain mobility. This result explains the observed increase in diffusivity and diffusivity-selectivity loss.[36,171,172]

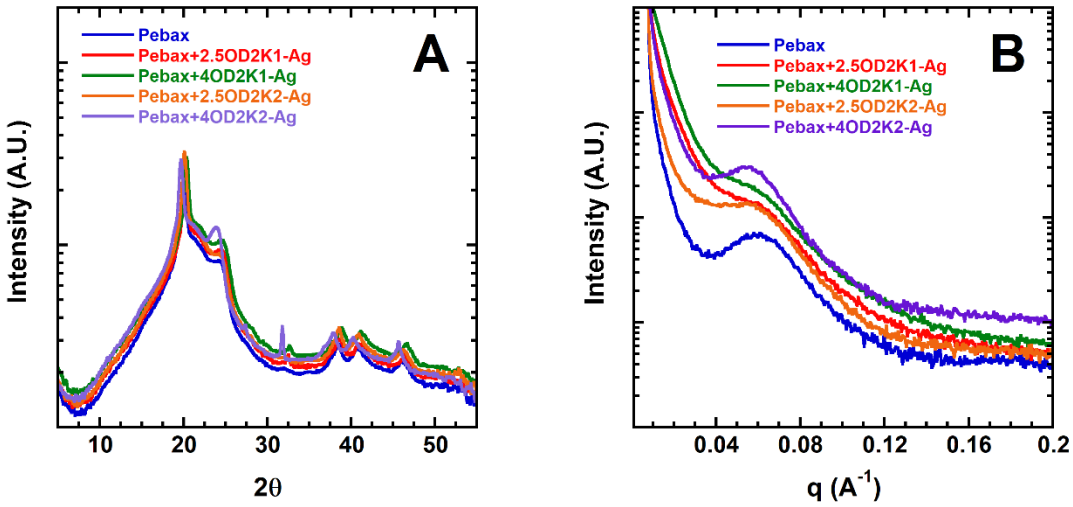

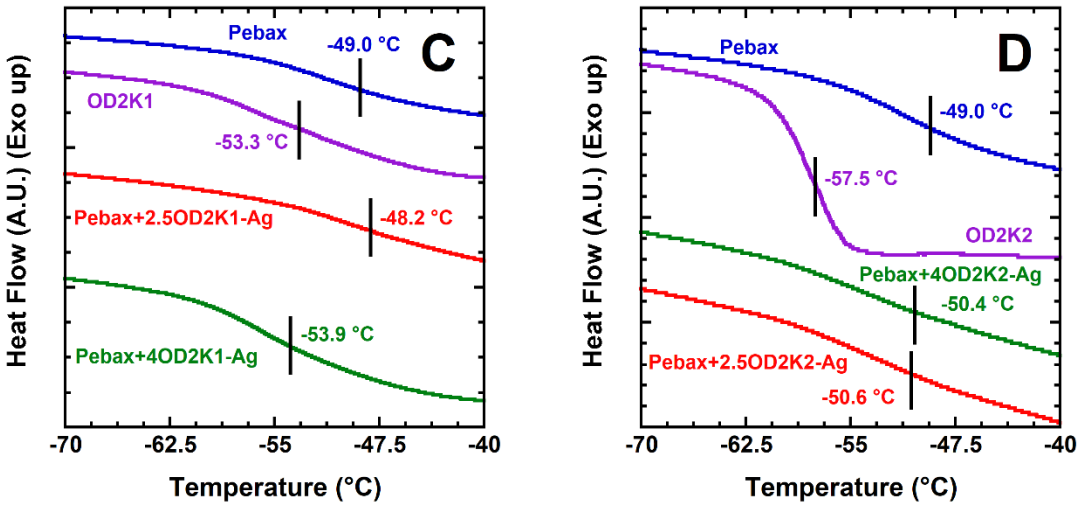

Figure 21: *A) Wide-angle x-ray scattering intensity and B) Small-angle x-ray scattering intensity for Pebax, Pebax+2.5OD2K1-Ag, Pebax+4OD2K1-Ag, and Pebax+2.5OD2K2-Ag. C) DSC thermogram for Pebax, OD2K1, Pebax+2.5OD2K1-Ag, and Pebax+4OD2K1-Ag. D) DSC thermogram for Pebax, OD2K2, Pebax+2.5OD2K2-Ag, and Pebax+4OD2K2-Ag.*

To address this issue, a new PAA batch was synthesized using a larger D2K:ODPA molar ratio, i.e., 2:1, thereby forming short-chained oligomers, OD2K2. By reducing the chain length grafted onto the surface of the silver nanoparticles, it was postulated that entaglements formed between OD2K2 and Pebax polymer chains would become limited, thus reducing the PAAs effect on crystalinity and chain mobility, especially at higher weight loadings.[70,144] As a result, OD2K2-Ag NPs are expected to maintain selectivity, even at higher silver wight loadings, as diffusive mechanisms remain limited for non-faciliated gases, i.e., CH_4 and C_2H_6. In this section, the validity of this hypothesis will be tested via pure gas transport measurements. To make comparisons with the previous materials, 2.5 and 4 wt% of OD2K2-Ag particles were added into Pebax and the overall transport of CH_4, CO_2, C_2H_4, and C_2H_6 were tested at 1 atm and 35 °C, (cf. Figure 16A/B). The CO_2 permeability does not exhibit large changes as previously seen in OD2K1-Ag containing materials. Specifically, permeability in Pebax+4OD2K2-Ag increase by ~20 Barrer relative to neat

Pebax. Gratifyingly, this time the overall CO_2/CH_4 seletivity increases monotonically in the order of neat Pebax (14.6 ± 1.6) < Pebax+2.5OD2K2-Ag (17.3 ± 1.9) < Pebax+4OD2K2-Ag (20.2 ± 2.3). Noticeably, this trend is different in that observed in OD2K1-Ag containing membranes, and is inline with the idea that shorter grafted chain can disrupt the local polymer environment to a smaller extent (cf., Figure 21C-D).

Likewise, C_2H_4 permeability increases from 14 (Pebax) to 39 (Pebax+4OD2K2-Ag) Barrer, with a corresponding increase in C_2H_4/C_2H_6 selectivity from 1.1 to 2. As shown in Figure 16B, as compared to materials containing OD2K1-Ag, selectivity also increases monotonically with OD2K2-Ag NP loading. However, the trend is quite different in terms of approaching the upper bound. For example, in both Figure 16A/B, as the amount of OD2K1-Ag NPs increase, selectivity increases initially, but it begins to drop and taper out. Remarkably, upon adding more OD2K2-Ag NPs, selectivity increases monotonically, approaching the upper bound.

As shown in Figure 21 and Section B18, the addition of 2.5 wt% OD2K2-Ag particles to Pebax appears to have a reduced effect on the change in crystallinity, relative to the change experienced in Pebax+2.5OD2K1-Ag. Additionally, no apparent change in glass transition temperature is observed between Pebax, Pebax+2.5OD2K2-Ag, and Pebax+4OD2K2-Ag (cf. Figure 21D). The changes observed in the structural analysis, upon changing particle-types, are consistent with the change in transport behavior that is observed in the upper bound figures. Thus, the mechanism underpinning the prohibition of enhancements in selectivity was outlined, and subsequently used to redesign the NP in an attempt to optimize its performance in this particular system. A schematic of the effect of the two nanoparticle series on the structure and ensuing transport properties of our facilitated transport MMMs is shown in Figure 22.

In summary, these results provide full support to our original hypothesis and confirm that using shorter capping agents avoids detrimental effects of the structure and separation performance of our MMMs. To test these materials in a more realistic scenario, we also ran mixed gas permeation tests, as detailed in Section 3.4.4.

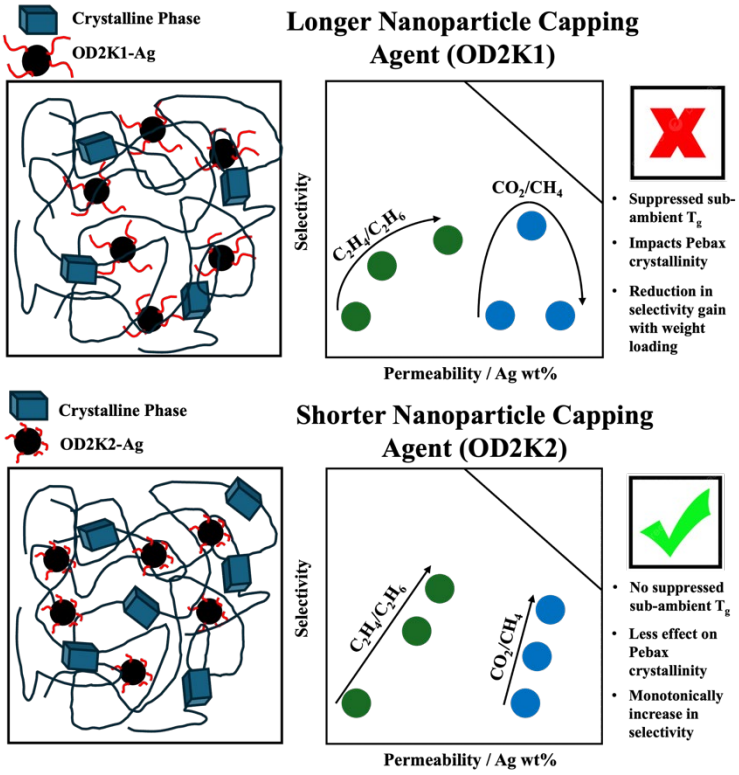

Figure 22: *Effects of OD2K1-Ag and OD2K2-Ag NPs on Pebax.*

3.4.5. Membrane Stability and Mixed Gas transport behavior

The change of the capping agent not only affects gas transport on the short time frame, but can also influence the long-term stability of particles.[134,142] Thus, the Pebax, Pebax+2.5OD2K1-Ag and Pebax+2.5OD2K2-Ag performance stability was assessed by measuring pure gas CO_2,CH_4,C_2H_4, and C_2H_6 permeability at 1 atm and 35 °C, before and after hydrogen exposure for 1 week. Pebax+2.5OD2K1-Ag and Pebax+2.5OD2K2-Ag were chosen, as their tranport properties

are somewhat comparable between both types of gas separations explored in this work, as well as limit any apparent matrix effects (e.g., a suppressed T_g relative to neat Pebax) from affecting interpretation of the stability results. A summary of CO_2 and C_2H_4 permeability in these materials after exposure to H_2, as well as relative changes in permeability and overall selectivities when compared to the fresh samples, can be found in the Section B19. Within the experimental error, Pebax showed no significant change in transport properties. Previously, a CO_2 permeability decrease by 8.8% and a CO_2/CH_4 selectivity decrease by 6% was reported for Pebax+2OD2K1-Ag, after similar exposure conditions conducted over the course of 24 hours. Extending this time frame over 7 days, CO_2/CH_4 selectivity changed by -13.4% and -9.2% in Pebax+2.5OD2K1-Ag and Pebax+2.5OD2K2-Ag, respectively. This shows, in the case of Pebax+2.5OD2K1-Ag, continuing decline in CO_2 permeability between 1 and 7 days of H_2 exposure. Moreover, C_2H_4 permeability changes by -9.3% and -27%, while C_2H_4/C_2H_6 selectivity changes by -9.5% and -29.7% for Pebax+2.5OD2K1-ag and Pebax+2.5OD2K2-Ag, respectively. Thus, although the new NPs synthesis approach enhanced the membrane transport properties, it did not substantially benefit the stability upon H_2 exposure. It should be noted, however, that membranes fabricated with OD2K2-Ag are more stable than previously reported membranes.[14,51,173] This result may be physically explained by noting that the shorter capping agent is not providing adequate protection to the silver NPs. Therefore, to further optimize the particles, the effect of the capping agents on the silver surface energy and its reactivity should be controlled more cautiously.

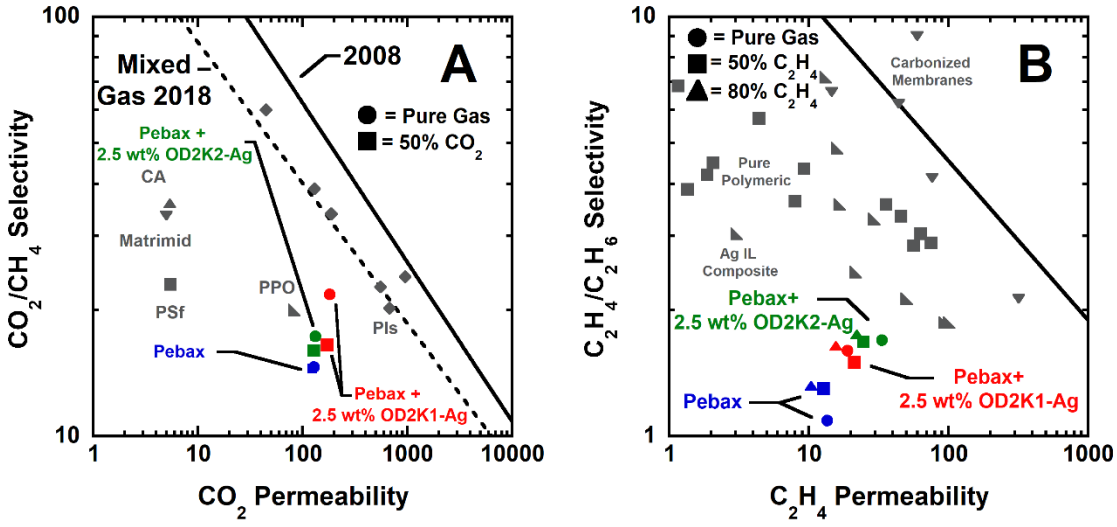

Figure 23: *A) Comparison of pure and mixed gas CO_2 permeability and CO_2/CH_4 selectivity at a CO_2 partial pressure ~ 1 atm and 35 ºC in Pebax (blue), Pebax+2.5OD2K1-Ag (red), and Pebax+2.5OD2K2-Ag (green). Circles are used for pure gas data, while squares are used for mixed gas with a feed composition of ~50 % mol CO_2 and 50 % mol CH_4. For reference, the 2008 pure gas and 2015 mixed gas CO_2/CH_4 upper bounds are included.[39,44] B) Comparison of pure and mixed gas C_2H_4 permeability and C_2H_4/C_2H_6 selectivity at a C_2H_4 partial pressures ~ 1 atm and 35 ºC in Pebax (blue), Pebax+2.5OD2K1-Ag (red), and Pebax+2.5OD2K2-Ag (green). For reference, the C_2H_4/C_2H_6 Upper bound is plotted[85]. Circles are used for pure gas data, squares are used for mixed gas with a feed composition of ~50 % mol C_2H_4 and 50 % mol C_2H_6, and triangles are used for mixed gas with a feed composition of ~20% mol C_2H_4 and 80% mol C_2H_6.*

To study the effects of different capping agents in mixed gas conditions, Pebax, Pebax+2.5OD2K1-Ag and Pebax+2.5OD2K2-Ag were tested for CO_2/CH_4 and C_2H_4/C_2H_6 mixed gas separation, at partial pressures of CO_2 and C_2H_4 around 1 atm at 35 ºC (cf. Figure 23). In the case of CO_2/CH_4, typically gas compositions of natural gas do not exceed 10 % CO_2 by molar amount, however, to test our materials under a more extreme condition, a 50% mole CO_2/ 50% mole CH_4 feed mixture was considered. In this condition, indeed, it is possible to assess the effects of CO_2 induced swelling and plasticization. In each case, minor changes in CO_2 permeability (within 6%) and noticeable decreases in CO_2/CH_4 selectivity were observed, for both Pebax+2.5OD2K1-Ag and Pebax+2.5OD2K2-Ag, relative to pure-gas conditions. For example, Pebax+2.5OD2K1-Ag

showed a mixed gas CO_2/CH_4 selectivity of 16.5, from >20 under pure gas conditions. This behavior could be ascribed to polymer swelling, which, in turn, enhances the diffusion of the largest component (i.e., CH_4) in mixed gas conditions.[36]

In contrast, in the case of C_2H_4/C_2H_6, no significant changes were observed in C_2H_4 permeability and C_2H_4/C_2H_6 selectivity among pure gas and mixed gas samples. This result is consistent with previously reported mixed gas data in neat Pebax.[174] Despite C_2H_4 and C_2H_6 being larger gas species than CO_2, they sorb to a much smaller extent in our materials relative to CO_2, which justifies the drop in CO_2/CH_4 selectivity under mixed gas conditions.[24,45] These differences in gas-polymer interactions are quantitated in Figure 15B through the enthalpy of sorption. For example, the enthalpy of sorption for CO_2 was found to be ~15 kJ/mol, while only ~10 kJ/mol for either C_2H_4 or C_2H_6. Ultimately, this leads to higher CO_2 sorption relative to either C_2H_4 or C_2H_6 in these materials. Additionally, CO_2 interactions with ether and amide groups could be interfering in hydrogen bonding between adjacent polymer chains, thus leading to the observed loss in mixed gas CO_2/CH_4 selectivity.[175,176] For both these reasons, it is not surprising that CO_2 would result in plasticization effects on selectivity more so than either C_2H_4 or C_2H_6 in these materials.

3.5. Conclusions

In this Chapter, it was demonstrated how theoretical modeling and fundamental interpretation of the experimental data can be used to optimize functional materials design. Specifically, we investigated the use of PAA stabilized Ag NPs in Pebax 1657 to enhance gas separation performance, particularly for CO_2/CH_4 and C_2H_4/C_2H_6 separations. To do so, a hypothesis-driven approach was used to optimize the nanoparticle design, focusing on analyzing the synergistic effects of both silver weight loading and PAA molecular weight.

Energetics of transport analysis, including the breakdown of the overall activation energy, as well as identification of the energetic and entropic contribution to diffusivity selectivity, was used to pinpoint the dominating factors that regulate overall selectivity. The results showed that higher loadings of the "generation 1" OD2K1-Ag particles initially improved permeability and selectivity, which are most aptly associated with facilitated transport, but eventually showed declines in the trend between selectivity and silver content. To address these limitations, a novel shorter-chain capping agent (OD2K2) was developed, which minimized matrix disruptions, allowing for enhanced or sustained selectivity at higher NP loadings.

These findings underscore the importance of hypothesis-driven NP optimization to enhance the design of MMMs and facilitated transport materials. Stability assessments under hydrogen exposure further highlighted the need for precise control over capping agent characteristics to improve resistance to chemical reduction, whilst mixed gas results showed, in most cases, little change relative to pure-gas (i.e., ideal) results. The proposed approach provides a pathway to engineering more robust and efficient membranes tailored for specific gas separation applications.

Chapter 4. Revisiting experimental techniques and theoretical models for estimating the solubility parameter of rubbery and glassy polymer membranes***

4.1. Abstract

This chapter focuses on the current estimation and correlation techniques of the Hildebrand solubility parameter (δ) of polymers and small molecules is a common practice in membrane material science and is accomplished by experimental and numerical routes. This chapter is meant to complement Chapters 2 and 3, as this information was crucial in helping design an appropriate liquid-liquid extraction protocol for the synthesized silver nanoparticles (cf. Figure 6). In this chapter, we revisit, update, and compare both routes to enhance the accuracy in the determination of δ. Best practices for the experimental determination of polymer solubility parameters are provided, and the viability of Dynamic Light Scattering (DLS) was demonstrated as an alternative to conventional time- and material-consuming techniques, such as Ubbelohde viscometry and swelling measurements. Glassy and rubbery polymers, including a microporous polymers, PIM-1, and a high fractional free volume (FFV) polymer, poly(1-trimethylsilyl-1-propyne) (PTMSP), are among the samples included in this study with great relevance to membrane science. In an attempt to enhance the accuracy of numerical estimate of polymer solubility parameters via the group contribution method, we provide updated group contribution parameters, along with their uncertainty, according to the technique recently reported by Smith et al. These updated group contribution parameters result in a mean absolute relative error of 9.0% in predicting the solubility parameter on a test set of 40 polymers, which is on par with the average 10% error reported

---

***Reproduced, with permission from Webb, et al.[107]

previously.

We also show, using machine learning techniques, that augmenting the group contribution model with extra parameters or non-linear relationships does not improve its accuracy. Results of the updated group contribution technique and dynamic light scattering measurements were compared to experimental viscometry on four test polymers, and the difference between the three techniques is compared.

4.2. Introduction

The Hildebrand solubility parameter, δ, is used to predict and correlate miscibility among substances, including low molecular weight compounds and polymers,[177–180] and is used in practical applications such as coatings,[181,182] drug delivery,[183,184] material formulation,[177] and membrane separations.[176,185–189] A general rule-of-thumb is that the solubility parameter of a good solvent should depart by no more than $\pm$ 2 $MPa^{0.5}$ from that of the polymer[190]. It is well known that the sorption of gases and liquids in polymers decreases linearly with the squared difference between the penetrant and polymer solubility parameters.[176] Due to this, liquid solvent flux through organic solvent nanofiltration (OSN) and organic solvent reverse osmosis (OSRO) membranes exhibits systematic correlations with the polymer and penetrant solubility parameters.[176,185,186,189] Burgal et al. found a strong correlation between the molecular-weight cutoff of nanofiltration membranes and the solubility parameter of solvents used in the post-fabrication treatment.[188] The solubility parameter was also used to rationalize negative retention behavior in OSN experiments.[187] These examples indicate that knowing the solubility parameters with sufficient accuracy is essential to develop structure-property correlations in membrane material science.

The solubility parameter of a pure species *i* is defined as follows:

$$\delta = \sqrt{\frac{E_{coh}}{V_m}} \quad \text{(Eq. 25)}$$

where E_{coh} and V_m are the cohesive energy and the molar volume of the pure species *i*, respectively. The δ values are normally provided at 298.15K. The solubility parameter of small molecules correlates directly with their enthalpy of vaporization and molar volume (cf. Eq. 26), both of which can be experimentally measured[191]:

$$\delta = \sqrt{\frac{\Delta H_{vap} - RT}{V_m}} \quad \text{(Eq. 26)}$$

where ΔH_{vap} is the molar enthalpy of vaporization, R is the ideal gas constant, and T is the absolute temperature at which enthalpy is measured. Polymers, however, do not have a measurable enthalpy of vaporization, so indirect methods have been developed to estimate their solubility parameter.

The two conventional experimental and modeling approaches used to estimate the solubility parameter of polymers are solvent-polymer interaction experiments (e.g., viscometry,[56] swelling measurements[192,193]) and extrapolation of small molecule data through group contribution methods,[191] respectively. Experimental methods, while providing a direct measure of the solubility parameter, can be time consuming. In contrast, theoretical techniques offer a more efficient approach for predicting solubility parameters. In recent years, machine learning (ML) techniques have been used to predict material properties, which use large datasets to accurately predict glass transition temperature (T_g), solubility parameter, and density, just to mention a few.[194]

In this study, we introduce the use of dynamic light scattering (DLS) as a new, rapid experimental route to measure the solubility parameter of polymers. Of equal importance, we updated the solubility parameter group contribution values to be consistent with recent improvements in van der Waals volume estimates[195] while providing, for the first time, the analytical error associated to each contribution. This Chapter seeks to enhance the accuracy of solubility parameter

measurements, enabling the formulation of more reliable structure-property correlations in membrane science. Thus, this paper will *i)* verify and compare experimental and theoretical approaches using both well-studied (polyvinylpyrrolidone) and newly synthesized (OD4K) polymers, and *ii)* extend the proposed approach to relevant polymers used in membrane science, including polymer of intrinsic microporosity (PIM-1) and poly(1-trimethylsilyl-1-propyne) (PTMSP).

4.3. Experimental Methods

4.3.1. Intrinsic Viscosity and Dynamic Light Scattering Measurements

Details about chemicals and polymers used in this study are provided in the Sections C1-C3. Intrinsic viscosity of four polymers, polyvinylpyrrolidone (PVP), OD4K, PTMSP, and PIM-1 (Section C3), was measured in a variety of solvents using Ubbelohde viscometers. Additionally, the hydrodynamic diameter (D_h) of PVP, OD4K, PTMSP, and PIM-1 in a variety of solvents was measured using dynamic light scattering. Both the intrinsic viscosity and hydrodynamic diameter for each polymer was plotted against the solvent solubility parameter, to elucidate any correlation. Experimental data was elaborated using the method outlined by Mangaraj[57] (cf. Sections C4 and C5), to accurately determine the solubility parameter value of each polymer. Details about intrinsic viscosity and hydrodynamic diameter measurements are provided in the Sections C6 and C7, respectively. For the sake of brevity, PTMSP data are shown in Section C8.

4.3.2. Group Contribution Method and Machine Learning

The group contribution technique defines the solubility parameter, δ, as follows:

$$\delta = \frac{\sum_{i=1}^{n} F_i}{V_W} \qquad \text{(Eq. 27)}$$

where F_i is the contribution of each functional group in the molecule to the total molar attractive force, the sum of which is normalized by the molecule's van der Waals volume (V_W). In this Chapter, V_W is calculated using contributions from each functional group ($V_{W,i}$), along with the overlap volume ($V_{overlap,j}$) between neighboring functional groups, as described by Wu et al. (cf. Eq. 28), to increase the accuracy of the volume predictions and, by extension, the group contribution values.[195]

$$V_W = \sum_{i=1}^{n} V_{W,i} - \sum_{j=1}^{m} V_{overlap,j} \quad \text{(Eq. 28)}$$

This specific method is then used to compare viscometry and DLS techniques, while simultaneously providing updated molar attractive force contribution fittings. The updated group contribution fittings can be found in Section C9, along with example calculations (cf. Section C10), as well as the optimization strategy and error estimation (cf. Section C11). Details about the machine learning model are provided in Section C12.

4.4. Results and Discussion

4.4.1. Intrinsic Viscosity and Dynamic Light Scattering Measurements

Intrinsic viscosity, as well as swelling measurements, are commonly used to study polymer interactions with solvents and determine their molecular weight.[191] The solvent in which a polymer attains the largest intrinsic viscosity normally exhibits a solubility parameter closest to that of the polymer. As the solubility parameter of the solvent deviates from that of the polymer, interactions between the polymer and solvent become unfavorable, causing polymer chains to become more coiled and compact. This well-documented technique[56,193,196] was used to estimate the solubility parameter of our baseline polymer, PVP, whose properties have been reported previously.[197] PVP exhibited the highest intrinsic viscosity (i.e., 0.433 dL/g) in acetonitrile (24.4 $MPa^{0.5}$) (cf. Figure 24A). Fitting the information from Figure 24 to Eq. C5 and constructing the corresponding

Mangaraj plot (cf. Figure 11B), results in the fitted theoretical maximum intrinsic viscosity ($\eta_{int,max}$) value of 0.435 dL/g, which provides, for PVP, a solubility parameter of 24.1 ± 0.39 $MPa^{0.5}$. Since a limited number of solvents was used for the experimental campaign, locating the position of the true maximum for the intrinsic viscosity as a function of the solvent solubility parameter may be somehow arbitrary and lead to significant errors. In contrast to just using the maximum from Figure 24A, the Mangaraj method (cf. Sections C4 and C5) can suggest polymer solubility parameters intermediate to those of the solvents used, serving as a recommended method for a reliable data elaboration.

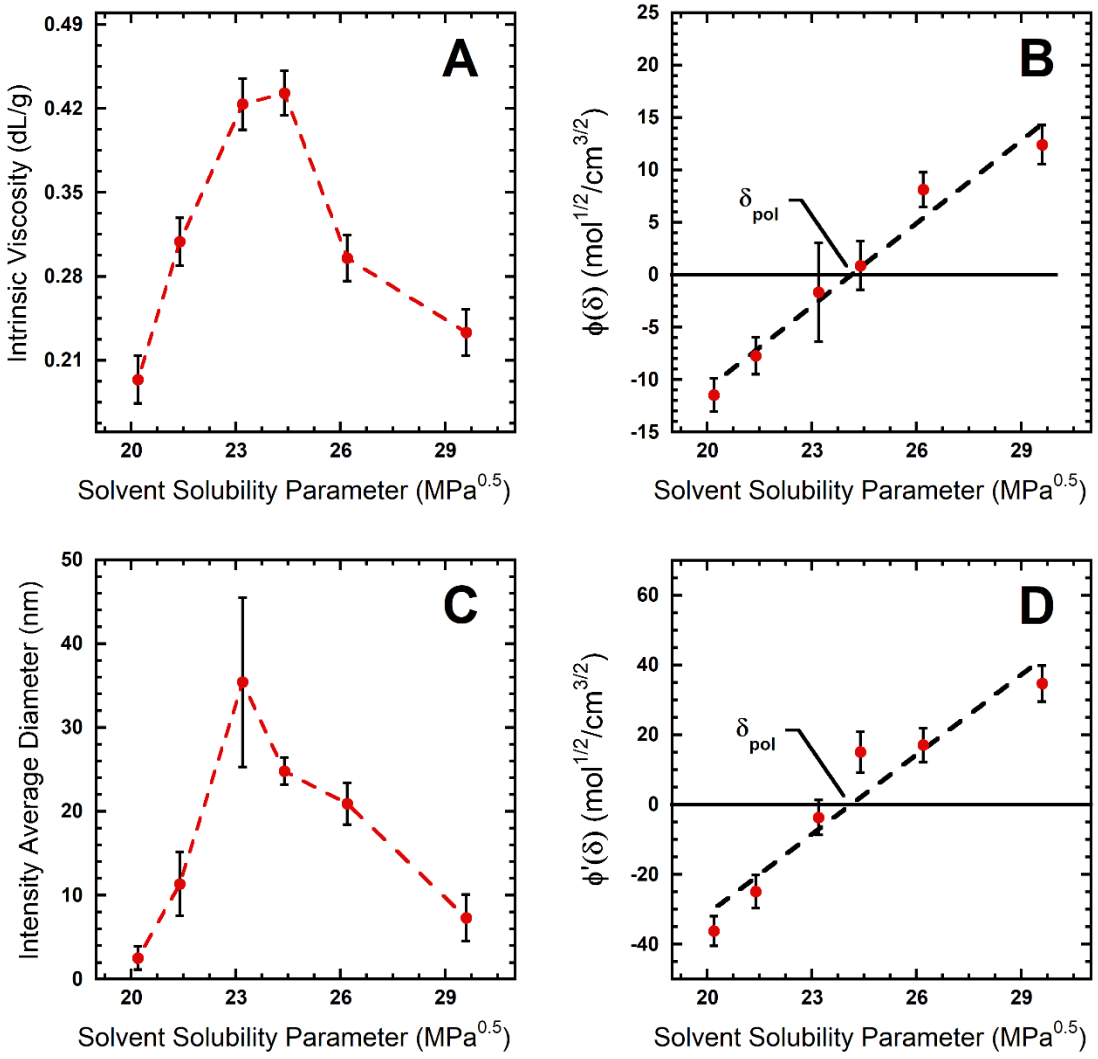

Figure 24: *A) Intrinsic viscosity of PVP as a function of the solvent solubility parameter at 25°C (lines serve to guide the eye). B) Intrinsic viscosities are used to generate the Mangaraj plot, where ϕ is plotted as a function of solvent solubility parameter for PVP. C) Intensity average diameter of PVP, obtained from DLS measurements, as a function of the solvent solubility parameter at 25 °C (lines serve to guide the eye). D) Intensity average diameters are used to generate the Mangaraj plot, where ϕ' is plotted as a function of solvent solubility parameter for PVP. The linear best fit line for both plots in B {2.6x – 63.5, R^2 = 0.97} and D {y = 7.6x – 183.9, R^2 = 0.92} are shown. Uncertainty values were calculated through repeated measurements (A and C) and linear error propagation (B and D).*

The experimental route mentioned above, however, requires viscosity data in numerous solvents at various concentrations, and therefore it is time and material consuming, which may be problematic when working with non-commercial, expensive polymers. Dynamic light scattering may offer a quicker route while consuming less material. DLS can indirectly provide information about solubility parameters by measuring the size of polymers in different solvents. Analogous to viscometry techniques, the solvent in which a polymer attains the maximum hydrodynamic diameter (i.e., maximum swelling), has a solubility parameter closest to that of the polymer. To test the applicability of DLS in this scenario, the solubility parameter of PVP, as estimated from the intrinsic viscosity (~24.1 $MPa^{0.5}$), was compared to that estimated using DLS (cf. Figure 24C). PVP experienced a maximum swelling (i.e., hydrodynamic size ~35.4 nm) in butanol (23.2 $MPa^{0.5}$), which aligns well with the values previously reported in the literature (i.e., 22.2 – 26.3 $MPa^{0.5}$)[198–200] estimated by various group contribution methods. The Mangaraj analysis (cf. Figure 24D) provides, for PVP, a solubility parameter equal to 24.1 ± 0.27 $MPa^{0.5}$ ($D_{h,\max}$ = 36.9 nm). The excellent agreement between the two approaches, depicted for the case of PVP, serves to validate the use of DLS for this purpose.

The proposed approach was then used to estimate the intrinsic viscosity and hydrodynamic diameter for OD4K, a newly synthesized poly(amic acid),[59] as a test case. According to Ubbelohde viscosity measurements, this polymer experiences the greatest intrinsic viscosity (0.268 dL/g) in

$CHCl_3$ (19 $MPa^{0.5}$) (cf. Figure 25A). The Mangaraj fitting (cf. Figure 25B) yields an $\eta_{int,max}$ value of 0.286 dL/g, with a corresponding solubility parameter of 18.6 ± 0.07 $MPa^{0.5}$. This value was then compared to the DLS approach. OD4K experienced a maximum swelling (i.e., hydrodynamic diameter ~2.5 nm) in acetone (19.9 $MPa^{0.5}$) (cf. Figure 25C). Using the Mangaraj fitting (cf. Figure 25D), $D_{h,max}$ is estimated to be 2.52 nm, with a corresponding solubility parameter of 19.9 ± 0.08 $MPa^{0.5}$. As in the case of PVP, the solubility parameter of OD4K found using DLS and viscometry are in close agreement, specifically, within 8% of one another.

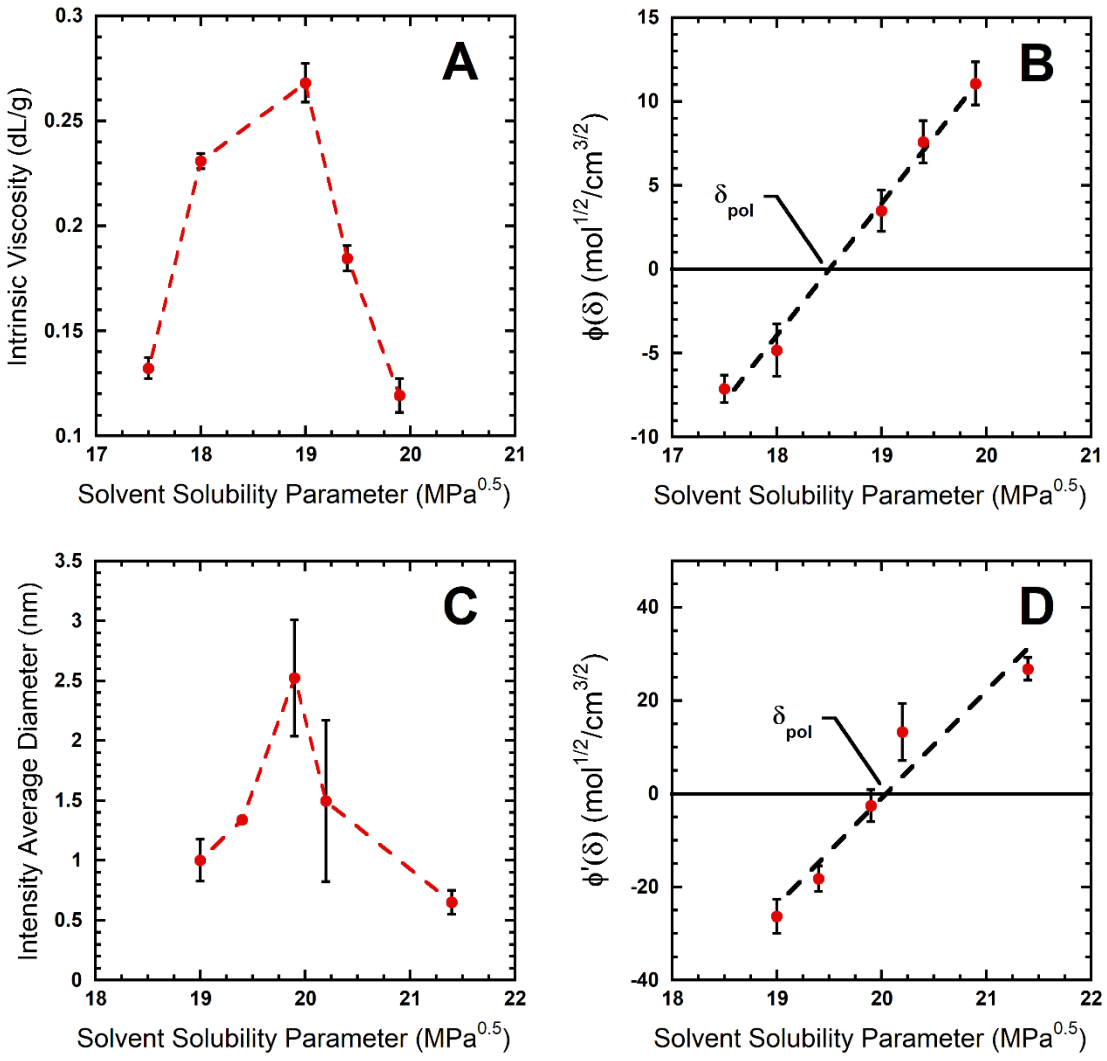

Figure 25: *A) Intrinsic viscosity of OD4K as a function of the solvent solubility parameter at 25°C (lines serve to guide the eye). B) Intrinsic viscosities are used to generate the Mangaraj plot, where ϕ is plotted as a function of solvent solubility parameter for OD4K. C) Intensity average diameter*

of OD4K, measured via DLS, as a function of the solvent solubility parameter at 25°C (lines serve to guide the eye). D) Intensity average diameters are used to generate the Mangaraj plot, where ϕ' is plotted as a function of solvent solubility parameter for OD4K. The linear best fit line for both plots B {y = 7.8x -145.2, R^2 = 0.98} and plot D {y = 20.2x – 401.7, R^2 = 0.94} are shown. Uncertainty values were calculated through repeated measurements (A and C) and linear error propagation (B and D).

PIM-1, a high T_g (> 430 °C)[201], high FFV (28.5 ± 0.5%, calculated using density)[202] microporous polymer, was included in this study (cf. Figure 26) to further assess the validity of the newly proposed methodology. Specifically, PIM-1 was selected for being a material of great interest in membrane science. PIM-1 exhibits the highest intrinsic viscosity (0.646 dL/g) in $CHCl_3$ (19.0 $MPa^{0.5}$) (cf. Figure 26A). Fitting the viscometry data to the Mangaraj plot (cf. Figure 26B) provides a solubility parameter of 19.6 ± 0.09 $MPa^{0.5}$ with a fitted maximum intrinsic viscosity of 0.772 dL/g. Likewise, the DLS data for PIM-1 (cf. Figure 26C) exhibits a trend identical to the intrinsic viscosity measurements, with the polymer attaining the largest hydrodynamic diameter (40.7 nm) in $CHCl_3$. The Mangaraj fitting on the DLS data for PIM-1 (cf. Figure 26D) yields a solubility parameter of 19.5 ± 0.19 $MPa^{0.5,}$ with a fitted maximum hydrodynamic diameter of 42.3 nm. Remarkably, also in the case of PIM-1 the agreement between viscometry and DLS data is excellent.

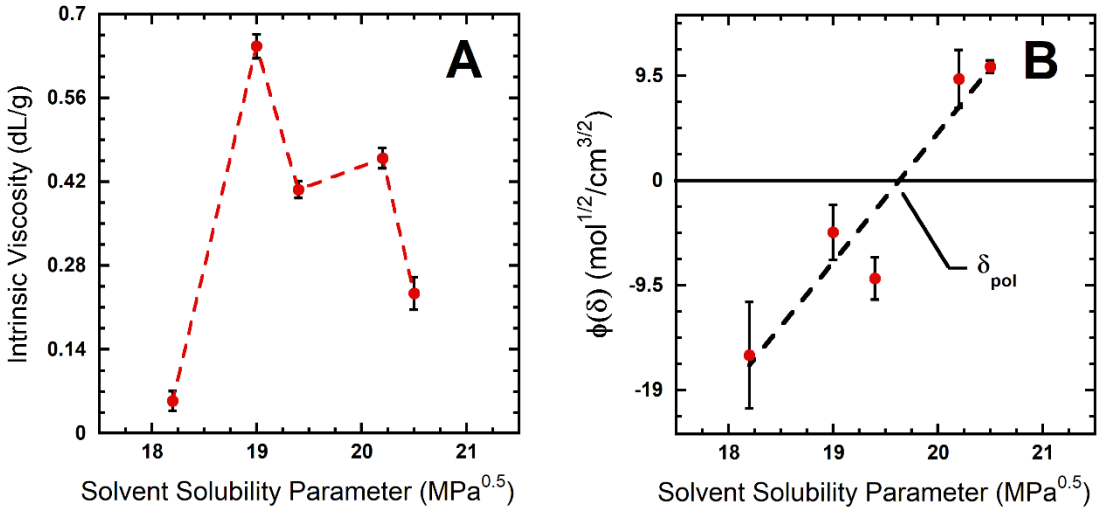

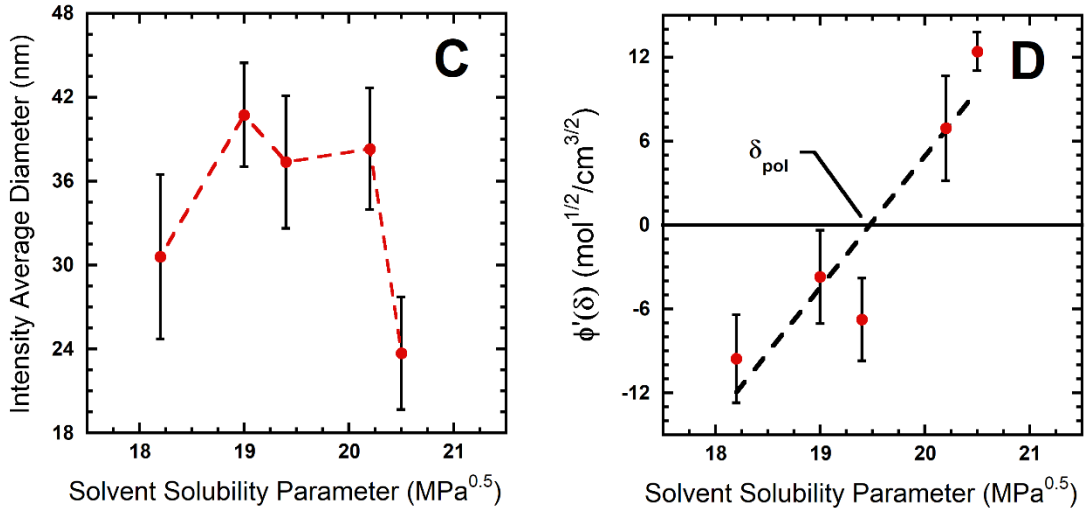

Figure 26: *A) Intrinsic viscosity of PIM-1 as a function of the solvent solubility parameter at 25°C (lines serve to guide the eye). B) Intrinsic viscosities are used to generate the Mangaraj plot, where ϕ is plotted as a function of solvent solubility parameter for PIM-1. C) Intensity average diameter of PIM-1, measured via DLS, as a function of the solvent solubility parameter at 25°C (lines serve to guide the eye). D) Intensity average diameters are used to generate the Mangaraj plot, where ϕ' is plotted as a function of solvent solubility parameter for PIM-1. The linear best fit line for both plots B {$y = 11.7x - 229.8$, $R^2 = 0.90$} and plot D {$y = 9.4x - 182.5$, $R^2 = 0.86$} are shown. Uncertainty values were calculated through repeated measurements (A and C) and linear error propagation (B and D).*

Intrinsic viscosities and hydrodynamic diameters for PIM-1 in tetrahydrofuran (THF) (19.4 MPa$^{0.5}$) tend to somehow negatively deviate from the generally observed trend (cf. Figure 26B-D). These deviations are ascribed to the presence of trace water in the solvent, as it was observed that the measured hydrodynamic diameter for PIM-1 increases in size by 25.7% when using HPLC-grade THF relative to the hydrodynamic diameter obtained when using non-HPLC grade THF. This deviation does not appear to affect the accuracy of the fitting, though. Indeed, the obtained solubility parameter value for PIM-1 (19.5 MPa$^{0.5}$) agrees with previously reported experimental values (19.0 MPa$^{0.5}$,[203] 19.5 MPa$^{0.5}$)[204]. Also in the case of PTMSP, another high T_g,[205] high FFV polymer[206] a very good agreement between viscometry and DLS data was observed. For the sake of brevity, PTMSP results are shown in the Section C8. Thus, the experimental techniques presented in this study can be successfully used to determine the solubility

parameters of modern membrane materials exhibiting rigid, bulky, and contorted monomer structures, other than rubbery polymers and low free volume glassy polymers.

4.4.2. Revisiting the Group Contribution Method

As stated earlier, the overarching goal of this study is to provide methods for fast, accurate, and reliable estimates of polymer solubility parameters. In the previous section, we proposed a new experimental method to accomplish this goal. Another important question is: *can group contribution method validate DLS measurements as a technique to estimate the solubility parameter?* In this section, we answer this question by first updating group contribution parameters and then comparing the predictions made by these new parameters to the experimental data shown in Section 4.4.1. Finally, a neural network was used to test whether improvements may be made to the prediction of solubility parameters when given the same set of data as the group contribution model. The aim of implementing the neural network herein is to use it as a tool to probe if augmentations to the group contribution techniques could be made. If there is a better way to correlate the molar volume and functional group identity than group contribution, the neural network should *per se* have a significantly lower prediction error than the group contribution technique. This is due to the neural network containing more adjustable parameters than group contribution (which uses one parameter per functional group) and having capability to approximate complex non-linear relationships.[207]

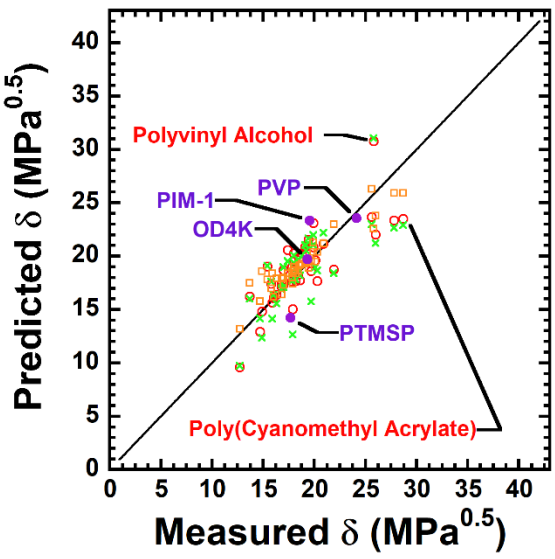

Figure 27: *Parity plot of predicted vs. measured polymer δ, in units of MPa$^{0.5}$. Red symbols are group contribution predictions, green symbols are neural network predictions, and yellow symbols are predictions from the Polymer Genome Project.[194] Polymer genome is the state-of-the-art machine learning tool, therefore it is reported separately. Purple symbols indicate group contribution predictions of PVP, OD4K, PTMSP, and PIM-1 versus the solubility parameter determined experimentally in this work.*

Experimentally determined solubility parameters of 40 polymers (cf. Section C13) were taken from a variety of literature sources and used to validate the group contribution and neural network performance.[191,208] Using the updated group contribution parameters, a mean absolute relative error (MARE) of 9.0% was achieved on the polymer dataset (cf. Figure 27 and Table C4), which is in line with the error of previous group contribution estimates.[191] Thus, using the higher accuracy molar volume predictions provided by Wu et al.[195] did not result in improved solubility parameter predictions.

Predicted and measured solubility parameter values from both group contribution and the neural network are compared in Figure 27. Both techniques gave similar predictions, and the MARE of the group contribution (9%) and neural network (10.3%) are nearly identical. Highly polar polymers, such as poly(cyanomethyl acrylate), PVA, and Nylon (6,6) tend to deviate from the parity line (16-18% error, cf. Figure 27), while predictions for nonpolar polymers, such as

poly(methyl octyl siloxane), polyisobutylene, and PDMS (1% error), tend to be more accurate. This could be interpreted as error increasing with the magnitude of the solubility parameter itself, as polar molecules tend to have larger solubility parameters than nonpolar ones. Thus, the solubility parameter of polar polymers should possibly be determined experimentally to achieve adequate accuracy, for example via viscometry or DLS measurements.

An important implication of this modeling effort is that the neural network and the group contribution solubility parameter predictions do not differ significantly (cf. Figure 27, Table C4). This finding suggests that group contribution performs optimally in the case of extrapolating a set of small molecule solubility parameters to polymers, and that augmentation to the group contribution technique (via new correlations between base functional groups) would not further improve its accuracy. Further discussion about the insights gained from the machine learning model can be found in Section C14. Also, it should be noted that machine-learning models in materials science, such as the *Polymer Genome Project*,[194] use information beyond just functional groups, such as topological polar surface area, van der Waals surface area, and other quantitative structure-property parameters. Consistently, *Polymer Genome* outperforms group contribution when making polymer solubility parameter predictions (MARE = 5.8%, cf. Figure 27 and Table C4). Therefore, if future improvements to group contribution models are to come, they will likely require additional types of information such as the ones used in *Polymer Genome.* Thus, it makes sense that the group contribution technique has not seen much improvement since its inception. Despite this shortcoming, the group contribution technique has remained a prevalent method for estimating polymer solubility parameters due to its acceptable performance and ease-of-use.

4.4.3. Comparison of Experimental and Numerical Results

Comparisons of viscometry, DLS, and group contribution in obtaining the solubility parameters of PVP, OD4K, PTMSP, and PIM-1 are shown in Table 5. For PVP, estimates from the three techniques are within error of each other. Of note, DLS and viscometry gave exactly equal values of PVP's solubility parameter. The solubility parameter of OD4K estimated from all three techniques exhibit a larger spread, with a difference among estimates close to 10%. For PIM-1 and PTMSP, numerical estimates exhibit larger deviations from the experimentally measured values, with group contribution predicting 23.36 ± 0.68 $MPa^{0.5}$ for PIM-1 (19.2% error) and 14.24 ± 0.55 $MPa^{0.5}$ for PTMSP (18.6% error). These deviations underpin the need for more experimentally determined solubility parameters of modern microporous membrane materials, such that more accurate predictive models can be constructed. A more detailed discussion regarding the origin of these deviations and the performance of the group contribution and machine learning models in predicting the solubility parameters of polyimides, another class of polymers relevant to membrane science, is provided in Section C8.

Table 6: *Summary of PVP, OD4K, PIM-1, and PTMSP solubility parameters in units of $MPa^{0.5}$. The solubility parameter for OD4K, PVP, PIM-1, and PTMSP was estimated using the Mangaraj analysis of experimental viscometry and DLS data. Solubility parameters estimated using the updated group contribution method (cf. Eq. 12) have also been included.*

polymer	viscometry method	DLS method	group contribution
PVP	24.1 ± 0.39	24.1 ± 0.27	23.6 ± 0.29
OD4K	18.6 ± 0.07	19.9 ± 0.08	19.7 ± 0.27
PIM-1	19.6 ± 0.09	19.5 ± 0.19	23.36 ± 0.68
PTMSP	17.8 ± 0.15	17.5 ± 0.14	14.24 ± 0.55

Interestingly, the maximum relative error in the solubility parameters determined using DLS and viscometry was 8.1%, which is close to the group contribution technique's MARE of 9.0%. Since the group contribution technique was trained on experimental data, it is not unreasonable to assign an expected error of approximately ± 10% for both experimental measurements and group

contribution. This magnitude of error may at first appear to disagree with the error bars listed in Table 6, which show a relative error below 2%. However, this result no longer appears contradictory when considering that the error bars from both experimental measurements and group contribution better reflect the solubility parameter's *precision* rather than its *accuracy*. That is, the error bars reflect the range of expected solubility parameters that would be estimated if viscometry or DLS experiments were to be repeated multiple times, *not* what the estimates are with respect to the true solubility parameter. These error bars do not reflect inherent errors such as instrumental bias, human error, and other systematic errors.

4.5. Conclusions

In this Chapter, dynamic light scattering, viscometry experiments, and numerical polymer solubility parameter estimation techniques were compared, discussed, and updated. First, we presented viscometry measurements to ensure reliable assessment of the polymer solubility parameter. Then, DLS was validated as an alternative experimental technique for a rapid estimation of polymer solubility parameters relative to Ubbelohde viscometry and swelling measurements, while still maintaining adequate accuracy. Also, a data elaboration procedure, based on the Mangaraj's method, was validated to achieve the best estimates from experimental measurements. For numerical estimates of the polymer solubility parameter, updated group contribution parameters featuring parameter uncertainties were provided, and group contribution was compared to machine learning techniques. Both approaches performed similarly when fit to the same data, suggesting that group contribution does not have room for augmentation unless additional molecular-level data are incorporated. DLS and the updated group contribution technique provided solubility parameter estimates of the test polymers (PVP, OD4K, PIM-1, and PTMSP) and were compared with viscometry, an established technique. Additionally, insights are provided

explaining why some classes of polymers are predicted more readily via group contribution, which resides primarily in the presence of adequate training data. From a membrane science perspective, having accurate solubility parameter estimates should, in principle, improve the self-consistency of transport and fabrication correlations both within individual studies and in meta-analyses made using large bodies of data from various researchers.

Chapter 5. Summary and Recommendations for Future Research

5.1. Summary

This dissertation provides fundamental insight into the design, fabrication, and optimization of facilitated transport films using silver nanoparticles. This project began with the rational design and characterization of novel polymer capped silver nanoparticles using a polyether based poly(amic-acid)s in an attempt to 1) stabilize the silver nanoparticles from long term aggregation and photo/chemical induced degradation, 2) tune the surface of the nanoparticle to enhance gas transport characteristics, and 3) provide a template for designing an interfacial bridge between silver and Pebax 1657.

Chapter 2 focused on the specific routes taken towards synthesizing the materials used in regard to facilitated transport. Subsequently, this Chapter provided key characterizations that highlight differences in poly(amic-acid) ether content, which may be used to rationalize the difference in performance, in terms of gas transport. It was also shown that defect-free composite materials were achieved using silver nanoparticles of around 5 nm in equivalent diameter, as chosen to boost the active silver surface area per weight loading. It was observed that using just 2 wt% of OD2K-Ag (OD2K1-Ag) increased overall CO_2/CH_4 selectivity by nearly 100%.

Chapter 3 built on Chapter 2 by exploring the possibility of utilizing higher weight loadings of silver nanoparticles for even larger enhancements in gas selectivity, and subsequently using these results to optimize the performance through tuning of the particle capping agent. In this Chapter, the individual components of sorption and diffusion were investigated, and a molecular and energetic understanding was achieved for the mechanism responsible for the permeability and selectivity. Chapter 3 worked to develop in-depth structure-property relationships connecting the origin of transport to changes in bulk properties, such as the polymer crystallinity. In turn, these

connections were used to make predictions about which particle parameter to tune for the benefit of gas selectivity, thus proving the technique and optimization pathway. Additionally, this Chapter illustrated, in the case of C_2H_4/C_2H_6, negligible changes between pure and mixed gas conditions, thus, highlighting the capability of these materials to be use in more "realistic" applications.

Chapter 4 further strengthened this work by establishing important connections to procedures identified, cultivated, and used for the purification and isolation of silver nanoparticles during the experimental synthesis and fabrication process. As justification for the liquid-liquid extraction used to obtain the final silver nanoparticles, (prior to being embedded into Pebax) the solubility parameter was estimated using group contribution, dynamic light scattering (DLS), intrinsic viscosity measurements, and machine learning. In relation to these measurements and the justification they provide, Chapter 4 explored the application of DLS as a novel route to estimate key solubility parameters pertaining to polymers, which can be useful in predicting sorption-selectivity, as well as for the modeling of specific polymer-penetrant systems using equations of state. DLS was shown to provide an alternative experimental approach to estimating the solubility parameter, which, compared to prior experimental techniques, can be less time and material intensive.

This work was supported by an NSF grant. The content of this dissertation, findings, conclusions and recommendations are those of the author(s) and do not necessarily reflect the views of the National Science Foundation.

5.2. Future Work

This research provides a certain level into the fundamental understanding of how silver nanoparticles can be apply and used in the context of facilitated transport membranes. As in any research project that embraces a general topic, there are still many routes that need to be explored and many questions to be answered.

Despite overcoming the perm-selectivity tradeoff and performing well under mixed-gas conditions, as well as successfully forming defect free materials, the silver nanoparticles exhibited loss in performance upon exposure to hydrogen gas. To fully understand the origin of this effect, there are several aspects that must be explored.

Firstly, to address the issue of chemical stability, techniques such as x-ray photoelectron spectroscopy (XPS) could be employed to study changes in the oxidation states of the silver nanoparticles as a result of the chelation process, as well as after the exposure to reducing agents, such as hydrogen. Alternatively, coupling this technique with surface modification strategies should be investigated to improve nanoparticle resilience and optimize the particle grafting agent. For example, using additional types of stabilizers such as thiols or amines, could reveal superior stability of silver nanoparticles as well as boosting overall selectivity.

Not only can we attempt to probe electronic responsibility for chemical stability, but also physical features, such as the specific facets of the silver nanoparticle which are most likely being affected, as well as the effect of the polymer grafting density on providing a physical layer of protection. To gain a deeper mechanistic understanding of the transport pathways and particle reactivity, molecular dynamics simulations should be attempted to model gas diffusion and interaction at the nanoparticle surface, to characterize the effect that the grafting density of the capping agent, as well as any adsorbed polymer chains have on the mobility and reactivity of gases at the surface.

To characterize these local transport behaviors experimentally, pulse field gradient nuclear magnetic resonance spectroscopy could be considered.

Lastly, once stability can be properly addressed, arranging these materials in industrial relevant configurations is crucial. The formation of thin film composites, whose active membrane thickness is less then 1000 nm, can exhibit differences in chemical stability as when compared to a bulk material due to a confinement of particles near the surface of the material. Additionally, gas transport properties could differ slightly due to this confinement effect as well.

Appendix A

A1. Group Contribution Method Calculation for Polymer Solubility Parameter

The poly(amic-acid) solubility parameter, δ, can be estimated using a group contribution method:

$$\delta = \frac{\sum n_i F_i}{\sum V_i} \quad \text{(Eq. A1)}$$

Where F_i is the molar attraction constant for each chemical group found in the molecule, n_i is the number of those groups, and $\sum V_i$ is total molar volume.[177] As an example, we use the repeating unit for the polymer OD2K1.

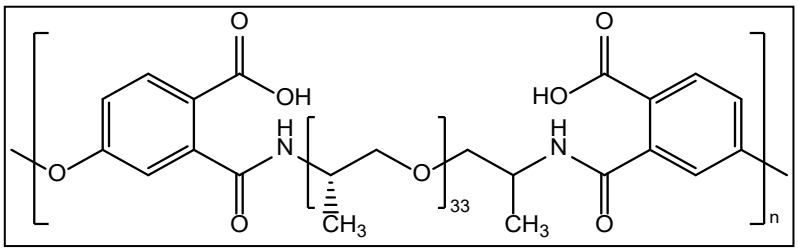

Figure A1: *Repeating chemical unit for the poly(amic-acid) OD2K, where n represents the number of repeating units within the polymer.*

The total molar volume is found by adding the Van der Waals volume contributions of individual molecule fragments, tabulated by Wu *et al*., $V_{w,i}$, while subtracting the overlapping volumes for the bonds between each fragment, $V_{overlap,j}$.[195]

$$\sum V_i = \sum n_i V_{w,i} - \sum n_j V_{overlap,j} \quad \text{(Eq. A2)}$$

Table A1: *Summary of van der Waals volume contributions.[195] Listed is each chemical structure in the polymer, their respective van der Waals Volume contribution, and the number of structures found in the repeating unit. (cf. Figure A1)*

Structure	$V_{w,i}$ (cm^3 mol^{-1})	n_i

-(COOH)	21.6	2
-(CONH)-	22.05	2
Aromatic Ring	45.48	2
-O-	8.51	34
$-CH_2-$	13.92	34
-CH-	14.63	34
CH_3-	13.15	34

$$\sum V_{w,i} = (2)\left(21.6\frac{cm^3}{mol}\right) + (2)\left(22.05\frac{cm^3}{mol}\right) + \cdots$$

$$\sum V_{w,i} = 1885.4\ \frac{cm^3}{mol}$$

Table A2: *Summary of overlapping volumes contributions.[195] Listed is each volume overlap found between chemical groups within the polymer, their respective overlapping volume contribution, and the number of each contributing structure (cf. Figure A1).*

Structure	$V_{overlap,j}$ ($cm^3\ mol^{-1}$)	n_i
Aromatic Ring-O	4.091	2
Aromatic Ring-C	4.688	4
C-C	4.614	68
C-O	3.877	66
C-N	4.018	2

$$\sum V_{overlap,j} = (2)\left(4.091\frac{cm^3}{mol}\right) + (4)\left(4.688\frac{cm^3}{mol}\right) + \cdots$$

$$\sum V_{overlap,j} = 604.6\frac{cm^3}{mol}$$

The total van der Waals volume is as follows:

$$\sum V_i = \sum n_i V_{w,i} - \sum n_j V_{overlap,j} = 1280.8\frac{cm^3}{mol}$$

The total molar attraction constant calculated was based on functional group values compatible with the molar volume method.[107]

Table A3: *Summary of molar attraction constant contributions. Listed is each chemical structure in the polymer, their respective molar attraction constant contributions, and the number of structures found in the repeating unit (cf. Figure A1).*

Structure	F_i ($MPa^{0.5}\,cm^3\,mol^{-1}$)	n_i
-(COOH)	597.1	
-(CONH)-	698.6	
Aromatic Ring	900	
-O-	148.7	
$-CH_2-$	161.9	
-CH-	156.1	
CH_3-	166	

$$\sum n_i F_i = (2)\left(597.1\frac{MPa^{0.5}\,cm^3}{mol}\right) + (2)\left(698.6\,\frac{MPa^{0.5}\,cm^3}{mol}\right) + \cdots$$

$$\sum n_i F_i = 25899.8\,\frac{MPa^{0.5}\,cm^3}{mol}$$

The solubility parameter is:

$$\delta = \left(\frac{\sum n_i F_i}{\sum V_i}\right) = \frac{\left(25899.8\,\frac{MPa^{0.5} cm^3}{mol}\right)}{\left(1280.8\,\frac{cm^3}{mol}\right)}$$

$$\delta = 20.2\ \pm 0.26\ MPa^{0.5}\ (OD2K)$$

For OD4K1, a similar calculation provides the following result:

$$\delta = 19.7\ \pm 0.27\ MPa^{0.5}\ (OD4K)$$

A2. Attenuated Total Reflectance Fourier Transform Infrared Spectroscopy (ATR-FTIR)

Results between 1500 and 1900 cm^{-1} wavenumber from ATR-FTIR, used to characterize differences between D2K, D4K, OD2K, OD4K, OD2K-Ag, and OD4K-Ag, are shown in the main manuscript (cf. Figure 3 and Figure 5). The entire recorded spectra, between 400 to 4000 cm^{-1} wavenumbers, are shown below.

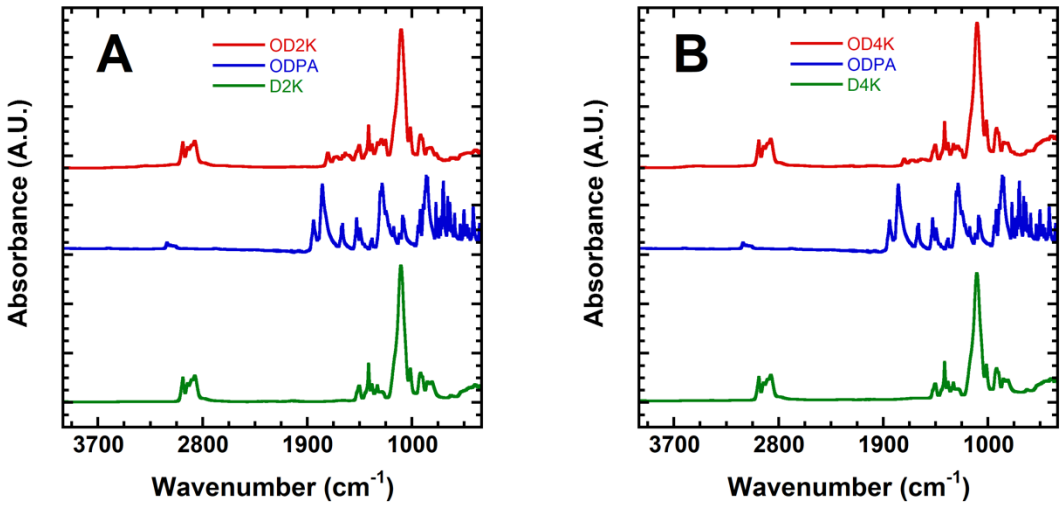

Figure A2: *A) ATR-FTIR spectra of the synthesized OD2K sample compared with the ODPA and D2K reactants, between 400 and 4000 cm^{-1} wavenumbers. B) ATR-FTIR spectra of the synthesized OD4K sample compared with the ODPA and D4K reactants, between 400 and 4000 cm^{-1} wavenumbers.*

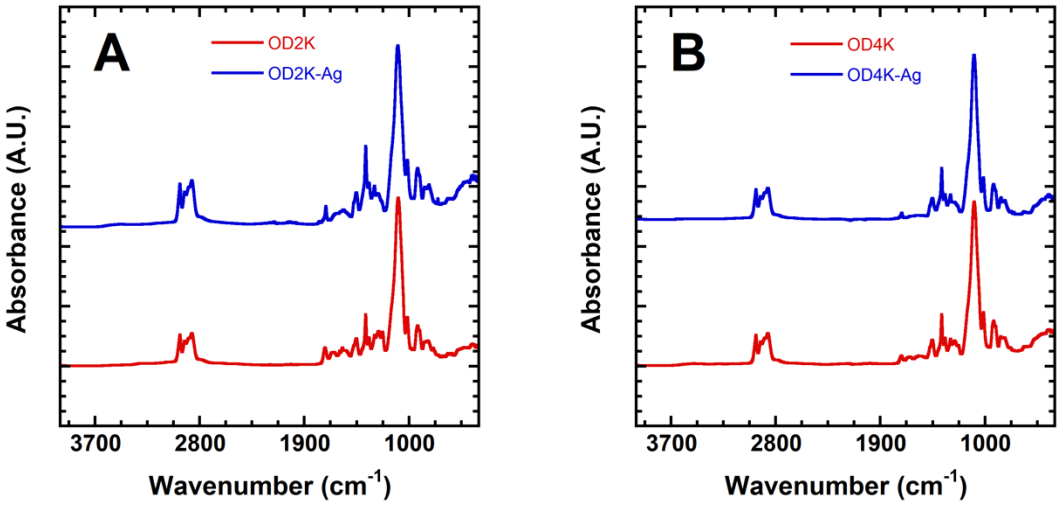

Figure A3: *A) ATR-FTIR of OD2K and the silver nanoparticles stabilized by OD2K (OD2K-Ag) between 400 and 4000 cm^{-1} wavenumbers. B) ATR-FTIR of OD4K and the silver nanoparticles stabilized by OD4K (OD4K-Ag) between 400 and 4000 cm^{-1} wavenumbers.*

A3. Inherent and Reduced Polymer Viscosity

The intrinsic viscosity (η_{int}) was calculated by the average of the following two equations[209]:

$$\eta_{int} = \lim_{c\to 0} \eta_{red} \equiv \lim_{c\to 0} \frac{t-t_0}{ct_0} \quad \text{(Eq. A3)}$$

$$\eta_{int} = \lim_{c\to 0} \eta_{inh} \equiv \lim_{c\to 0} \frac{\ln(t)-\ln(t_0)}{c} \quad \text{(Eq. A4)}$$

where t is the time the polymer solution takes to flow between the Ubbelohde viscometer ring indicators, and t_0 is the corresponding time for the neat solvent to flow between the viscometer ring indicators. The reduced viscosity (η_{red}) and inherent viscosity (η_{inh}) of OD2K and OD4K were measured at concentrations between 0.3 and 1 g dL^{-1} in $CHCl_3$ at 35 °C. Each concentration was tested five times to calculate the uncertainty. The limit for both the inherent and reduced viscosity at a concentration of 0 g dL^{-1} is defined at the intrinsic viscosity (dL g^{-1}, cf. Figure A4). The reported intrinsic viscosity was taken from the average limit of both lines, and was 0.232 ± 0.001 g dL^{-1} and 0.255 ± 0.001 g dL^{-1} for OD2K and OD4K, respectively.

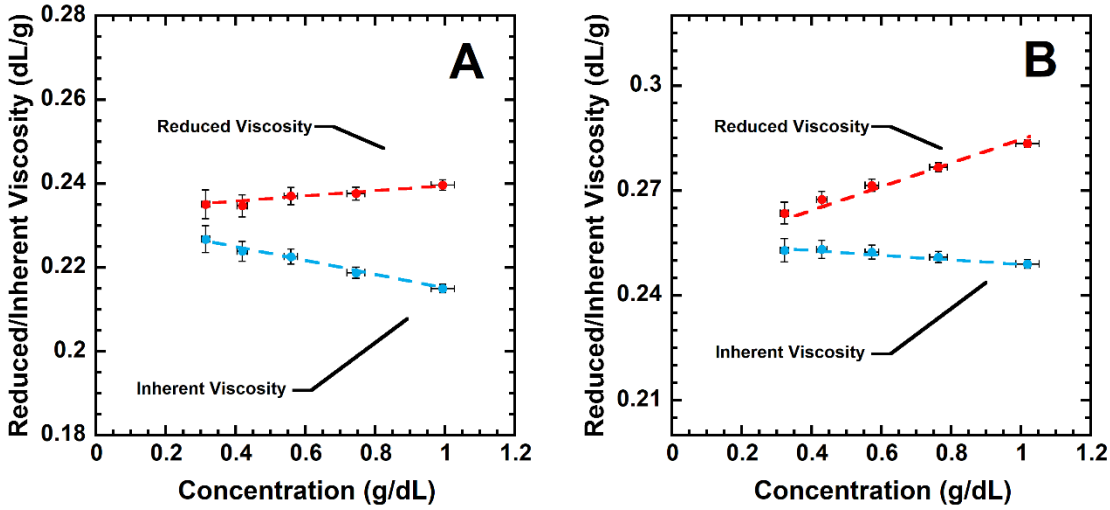

Figure A4: *Reduced (red) and inherent (blue) viscosity (dL g^{-1}) for A) OD2K and B) OD4K as a function of concentration (g dL^{-1}).*

A4. Polymer Molecular Weight Distribution

The number average molecular weight for OD2K and OD4K were found via gel permeation chromatography (GPC) and the following set of equations:

$$M_n = \frac{\sum_{t_1}^{t_2} A_i M_i}{\sum_{t_1}^{t_2} A_i} \quad \text{(Eq. A5)}$$

$$\log(M_i) = \alpha t_i + \beta \quad \text{(Eq. A6)}$$

where t_i is the time, A_i is the absorption value at t_i, M_i is the molecular weight eluted at t_i, t_1 is the onset time of elution, t_2 is the elution end time, and M_n is the number average molecular weight. α and β are constants obtained from the linear regression of $\log(M_n)$ vs. t for polystyrene standards, whose weight ranged from 1 to 500 kDa. The number average molecular weight of OD2K and OD4K are 20800 ± 4310 and 42800 ± 8890 g mol^{-1}, respectively. The overall weight distribution is shown in Figure A5.

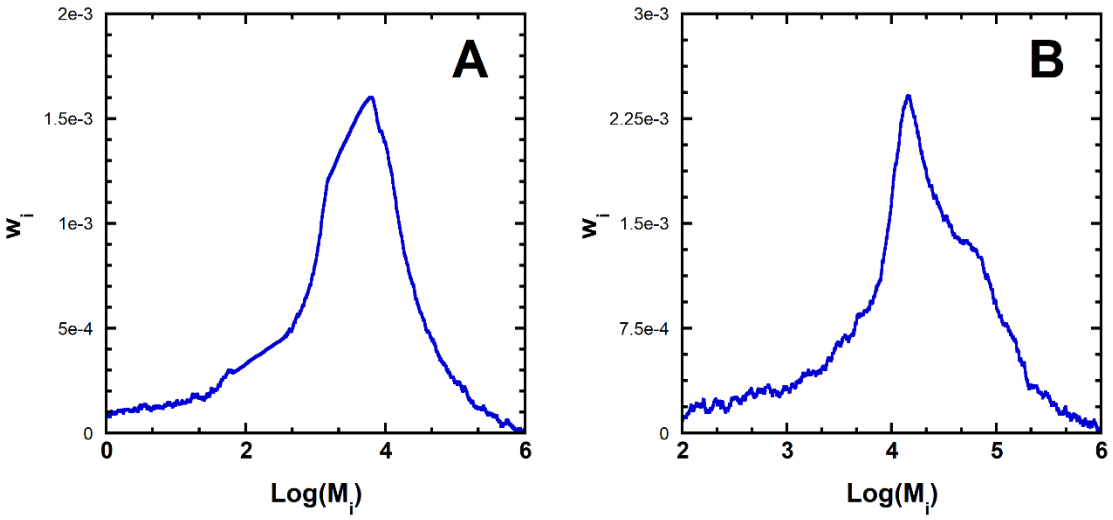

Figure A5: *The weight fraction* (w_i) *as a function of the logarithm of number average molecular weight* $\left(Log(M_i)\right)$ *for A) OD2K and B) OD4K.*

A5. Thermogravimetric Analysis (TGA)

Results of thermogravimetric analysis for OD2K-Ag and OD4K-Ag are shown in chapter 1 of this dissertation (cf. Figure 7). In Figure A6, the second derivative analysis is shown, which helps precisely determine the temperature range of individual mass loss events.

Results of TGA analysis for the neat polymers, OD2K and OD4K, are shown in Figure A7. The second derivative analysis for the neat polymers is shown in Figure A8.

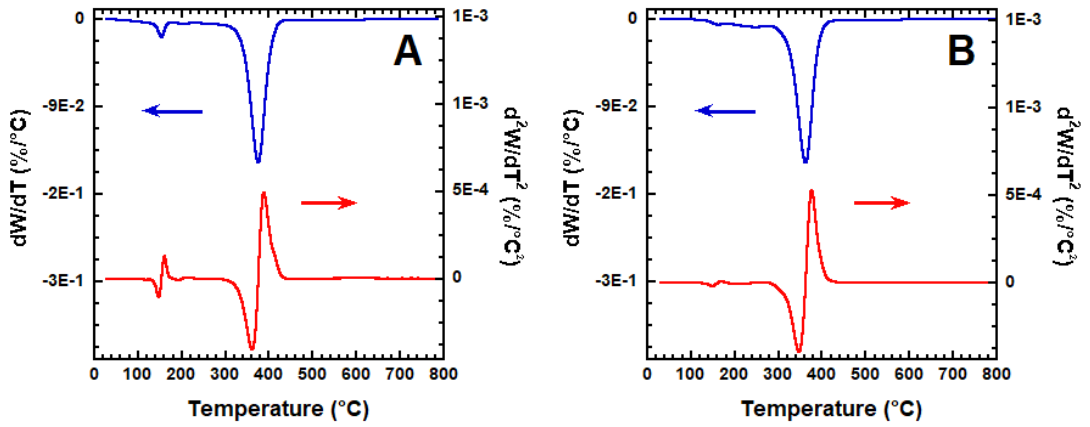

Figure A6: *TGA first (blue) and second (red) derivative analysis for weight% (W) with respect to temperature (T). These are plotted as a function of temperature for A) OD2K-Ag and B) OD4K-Ag between 28 and 800˚C. Small mass losses below 200˚C are attributed to residual solvents. Subsequent mass loss starting after 300˚C are attributed to polymer degradation. The remaining mass after 800˚C is from the silver core of the nanoparticles.*

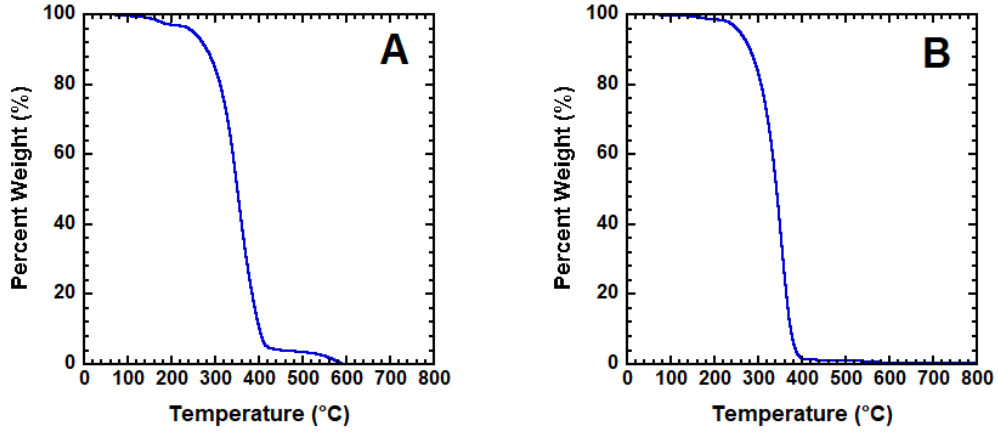

Figure A7: *TGA for the change in weight % (W) with respect to temperature (T). These are plotted as a function of temperature for A) OD2K and B) OD4K between 28 and 800˚C. Small mass losses below 200˚C are attributed to residual solvents. Subsequent mass losses after 200˚C are attributed to imidization of the amic-acid, followed by total polymer degradation.*

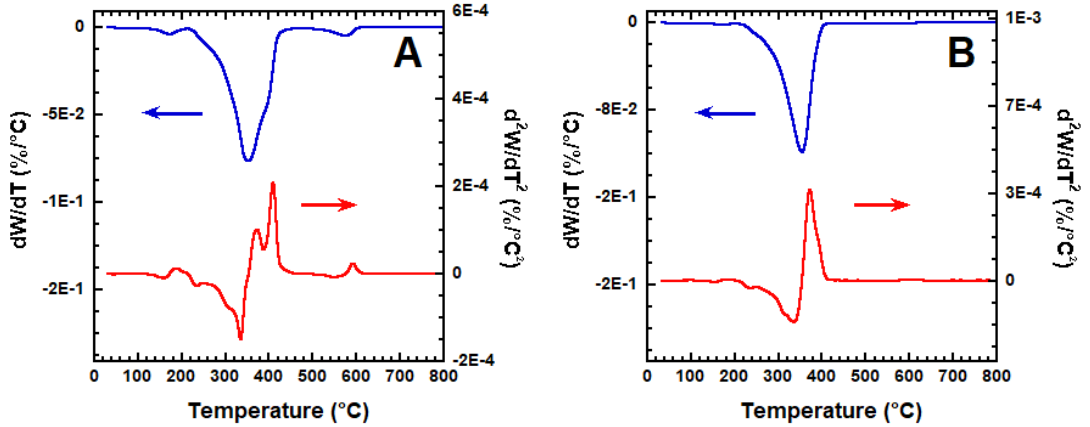

Figure A8: *TGA first (blue) and second (red) derivative analysis for the change in weight % (W) with respect to temperature (T). These are plotted as a function of temperature for A) OD2K and B) OD4K between 28 and 800˚C. Small mass losses below 200˚C are attributed to residual solvents. Subsequent mass losses after 200˚C are attributed to imidization of the amic-acid, followed by total polymer degradation.*

A6. Dynamic Light Scattering Measurements for Polymer Solubility Parameter

Dynamic light scattering (DLS) was used to measure the effective hydrodynamic diameter of OD2K and OD4K in various solvents, in attempt to corroborate the solubility parameter calculated using the group contribution method (cf. Section 1 in the Supporting Information). These measurements were performed on a NanoBrook Series Particle Analyzer using backscattered detection. Both polymers were tested 5 times at a concentration of ~0.5 mg/ml in (19 $MPa^{0.5}$) chloroform, (19.4 $MPa^{0.5}$) tetrahydrofuran, (19.9 $MPa^{0.5}$) acetone, (20.2 $MPa^{0.5}$) dichloromethane, (21.4 $MPa^{0.5}$) acetic acid, and (26.5 $MPa^{0.5}$) ethanol.[210] The effective diameter of OD2K and OD4K was plotted as a function of the solvent solubility parameter. The maximum swelling for each OD2K (1.7 nm) and OD4K (2.5 nm) was in acetone. Based on these results, the solubility parameter of each polymer most likely resides between 19.4 and 21.4 $MPa^{0.5}$.[210]

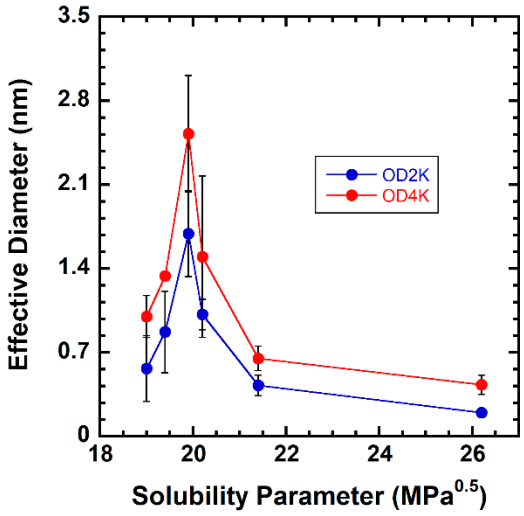

Figure A9: *Effective diameters of OD2K (red) and OD4K (blue) plotted as a function of solvent solubility parameters (lines are to guide the eyes).*

A7. Transport Measurements

A7.1. Gas Permeability

Pure gas (CH_4 and CO_2) permeability was measured at 1 bar and 35 ºC using a constant volume barometric device, wherein the membrane was situated between two large volumes, using a 47 mm HP filter holder. Prior to measurements, vacuum was pulled on the entire system for overnight to remove any humidity or other sorbed species. Pressure was charged to the upstream side of the membrane and measured using a PX-409-USHB series Omega pressure transducer (0-1000 psi). Then, gas was allowed to permeate through the membrane to the downstream volume, where the increase in pressure with time was measured using a highly sensitive PX-409-USHB series Omega pressure transducer (0-260 torr). The permeability (P, in units of Barrers) was calculated as follows:

$$P = \frac{lV_{down}}{\Delta pART}\left(\frac{dp}{dt}_{down} - \frac{dp}{dt}_{leak}\right) \quad \text{(Eq. A7)}$$

where l is the membrane thickness, A is the membrane area available to gas transport, R is the universal gas constant, T is the absolute temperature, Δp is the average transmembrane pressure, $\frac{dp}{dt}_{down}$ is the asymptotic rate of pressure increase in the downstream ballast, and $\frac{dp}{dt}_{leak}$ is the rate of pressure increase in the downstream volume whilst the charge pressure is 0. Membranes were glued with epoxy resin on a brass ring, and the passage area was accurately measured via the ImageJ software.

A7.2. Gas Solubility

Pure gas (CH_4 and CO_2) solubility was measured at 35 ºC and up to 30 bar using the pressure decay method. The system consists of two volumes connected via a valve, namely, the charge chamber

and sample chamber. Both chambers are equipped with PX-409-USHB series Omega pressure transducers (0-500 psi). The polymer sample is first added to the sampling chamber before pulling vacuum on both chambers overnight. Gas pressure is added to the charge chamber and allowed to equilibrate before quickly releasing it into the sampling chamber. The valve is then closed, thus disconnecting the chambers until each chamber equilibrates. A subsequent pressure decay in the sampling chamber is recorded, and the process is repeated in the next step without pulling vacuum. The overall sorbed gas concentration in the polymer sample is the following:

$$C_{pol,j} = \frac{\rho_{pol}}{g_{pol,dry}} \left(\sum_{i=0}^{j} \left(\frac{1}{\tilde{V}_{C0,i}} - \frac{1}{\tilde{V}_{CF,i}} \right) - \frac{V_S}{\tilde{V}_{SF,j}} \right) \quad \text{(Eq. A8)}$$

where ρ_{pol} is the polymer density, $g_{pol,dry}$ is the dry polymer mass, j is the current pressure step, V_s is the sample chamber volume, V_C is the charge chamber volume, and $\tilde{V}_{C0}$, $\tilde{V}_{CF}$, $\tilde{V}_{SF}$, are the gas molar volumes (calculated using the Peng-Robinson equation of state) for the initial charge state (prior to valve opening), final charge state, and final sample state, respectively. The solubility coefficient for each gas was determined as the slope of the linear regression of at least 4 concentration points with pressure. Pure CO_2 isotherms are shown in Figure A10, where concentration error is determined using standard linear error propagation.[114]

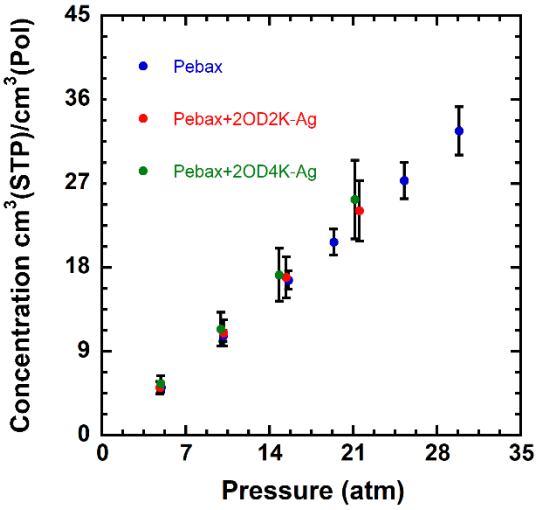

Figure A10: *CO_2 sorption isotherms at 35 ºC in Pebax, Pebax+2OD2K-Ag, and Pebax+2OD4K-Ag as a function of pressure. Error bars are calculated using standard error propagation.*[114]

A7.3. Summary of Transport Results

A summary of data shown in Figure 9 is reported in Table A1. The table includes CO_2 permeability, solubility, and diffusivity for Pebax, Pebax+2OD2K-Ag, and Pebax+2OD4K-Ag, along with selectivity data.

Table A4: *Summary of Transport Data. Listed for each membrane is the CO_2 Permeability (Barrer), solubility (cm^3(STP)/cm^3(pol)/atm), and Diffusivity ($\times 10^7$ cm^2/s), as well as the overall CO_2/CH_4 selectivity, solubility selectivity, and diffusivity selectivity at 1 atm and 35 ºC.*

Sample	CO_2 permeability (Barrer)	CO_2/CH_4 selectivity	CO_2 solubility (cm^3[STP]/cm^3[pol]/atm)	CO_2/CH_4 solubility selectivity	CO_2 diffusivity $\times 10^7$ (cm^2/s)	CO_2/CH_4 diffusivity selectivity
Neat Pebax	121.2 ± 7.0	12.7 ± 1.1	1.09 ± 0.02	5.41 ± 0.25	8.4 ± 0.3	2.3 ± 0.2
Pebax+2OD2K-Ag	177.9 ± 14.3	23.4 ± 2.7	1.11 ± 0.01	5.43 ± 0.07	12.2 ± 0.2	4.3 ± 0.5
Pebax+2OD4K-Ag	183.1 ± 14.4	26.6 ± 6.9	1.18 ± 0.01	7.79 ± 0.14	11.8 ± 0.9	3.4 ± 0.9

A8. Mixed Matrix Membrane Characterization

Thermogravimetric analysis of neat Pebax and mixed matrix membranes made from Pebax/OD2K-Ag and Pebax/OD4K-Ag, can be found in Figure A11. To precisely determine the temperature range of individual mass loss events, first and second derivative analysis was used (cf. Figure A12).

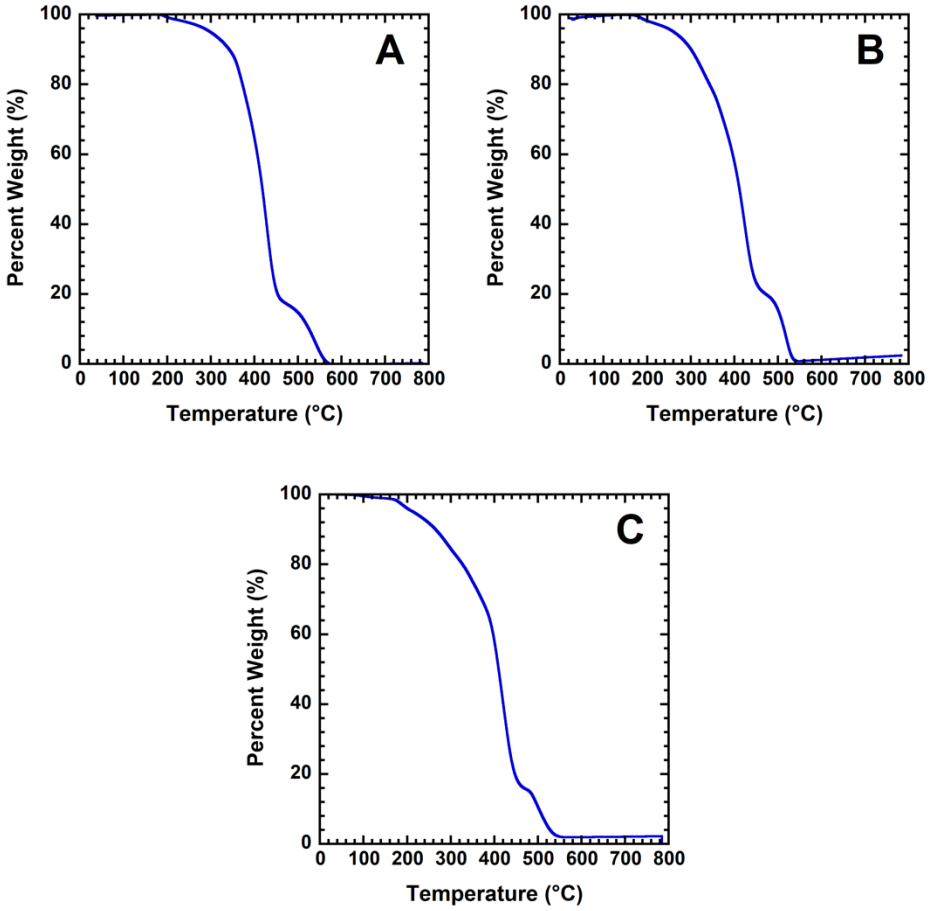

Figure A11: *TGA for the change in weight % (W) with respect to temperature (T). These are plotted as a function of temperature for A) Pebax, B) Pebax+2OD2K-Ag, and c) Pebax+2OD4K-Ag between 25 and 800˚C. Small mass losses below 200˚C are attributed to absorbed species. Subsequent mass losses after 200˚C are attributed to polymer degradation. Residual mass above 600 ˚C is attributed to silver in Pebax+2OD2K-Ag and Pebax-2OD4KAg.*

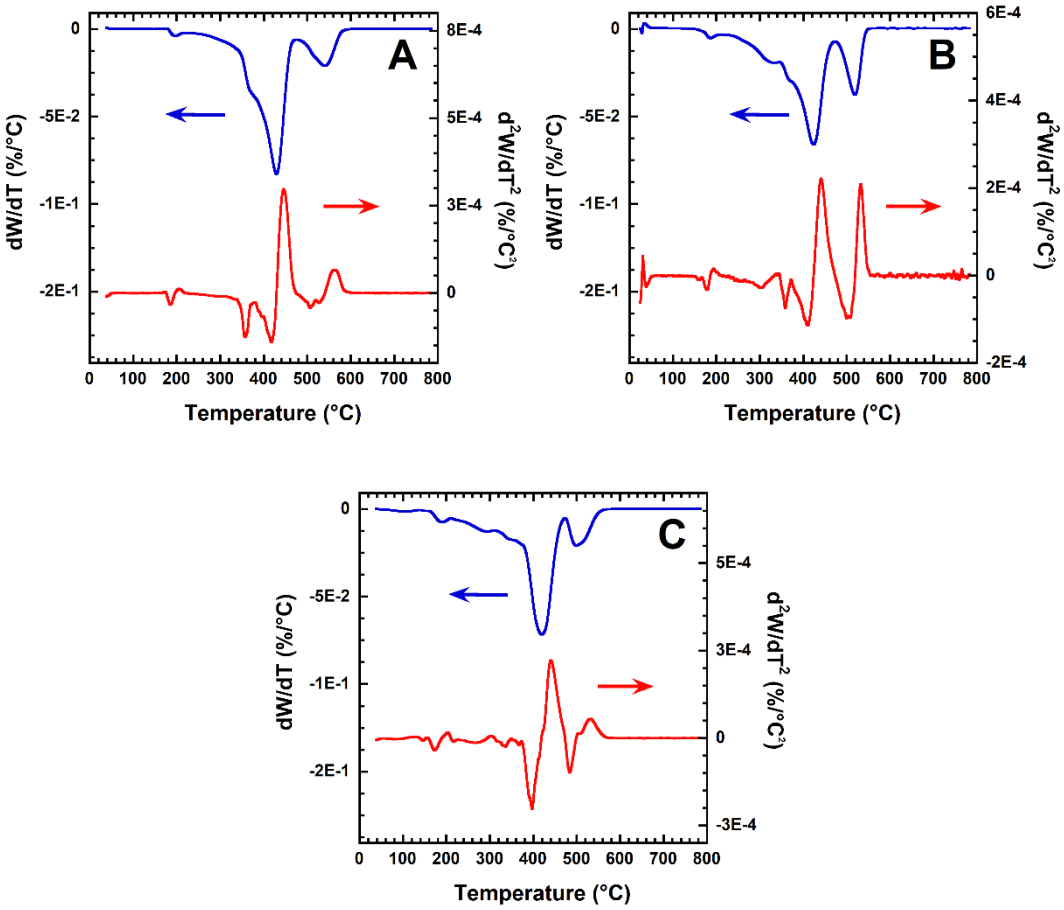

Figure A12: *TGA first (blue) and second (red) derivative analysis for the change in weight % (W) with respect to temperature (T). These are plotted as a function of temperature for A) Pebax, B) Pebax+2OD2K-Ag, and C) Pebax+2OD4K-Ag between 25 and 800˚C. Small mass losses below 200˚C are attributed to absorbed species. Subsequent mass losses after 200˚C are attributed to polymer degradation. Residual mass above 600 ˚C is attributed to silver in Pebax+2OD2K-Ag and Pebax-2OD4K-Ag.*

Appendix B

B1. Materials

4,4'-Oxydiphthalic anhydride (ODPA, 97 wt%), 3Å molecular sieves, and Chloroform ($CHCl_3$, HPLC grade) were purchased from Sigma-Aldrich. Tetrahydrofuran (THF, 99.8%), Ethylene glycol (EG, 99.5%), and 200 Proof Ethanol (EtOH, 100%) were bought from Fischer Chemical. Silver nitrate ($AgNO_3$) and Methanol (MeOH, >99%) were purchased from Acros Organics. Jeffamine D-2000 (D2K) was graciously donated by the Huntsman corporation, while Pebax 1657 was received from Arkema. The monomers used in the synthesis of the poly(amic-acid)s (PAAs), i.e., D2K and OPDA, were dried at room temperature under vacuum for at least 24 hour before use. The solvent used in the PAA synthesis, THF, was dried using 3Å molecular sieves for at least 24 hours before use. All other chemicals were used as received. Ultrapure water with an in-line resistivity of 18.2 MΩ-cm, used throughout the study, was produced via a MilliQ7000 purification system. Pure CH_4, CO_2, ethane (C_2H_6), and ethylene (C_2H_4) were obtained from AirGas with a purity higher than 99%.

B2. Synthesis of Poly(amic-acid)s

First, Jeffamine D-2000 (D2K) (30.3 ml, 15 mmol) and 30 ml of THF were mixed at room temperature in a 3-neck flask equipped with a mechanical stirrer. Following this step, the mixture was cooled to 0 ºC under a N_2 purge, and ODPA (either 4.65 g, 15 mmol or 2.33 g, 7.5 mmol) was added. Two separate PAAs were synthesized, one using a 1:1 molar ratio of D2K:ODPA (i.e., adding 4.65 g of ODPA), and other using a 2:1 molar ratio (i.e., adding 2.33 g of ODPA). PAAs synthesized using a 1:1 molar ratio of D2K:ODPA are denoted as OD2K1, whilst that synthesized using a 2:1 molar ratio are written as OD2K2.

After 10 minutes, the resulting mixture was heated up to 30 ºC under stirring for 3 hours. The product was precipitated in a water-methanol (90/10 vol%) mixture, collected, and subsequently washed using the same water-methanol mixture and filtered. The resulting PAAs (cf. Figure B1) were dried under vacuum for 24 hours at room temperature before being stored in a chemical fridge at ~ 4 ºC.

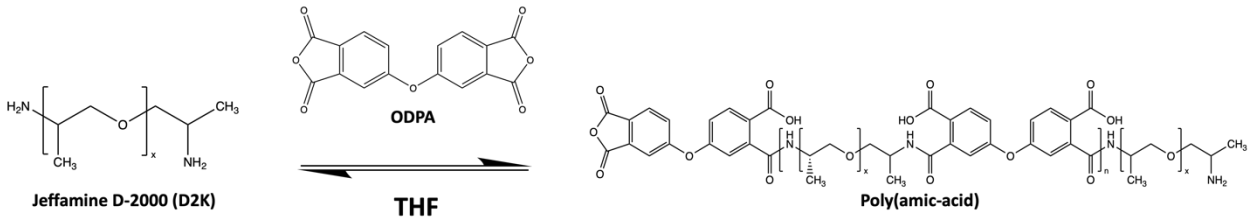

Figure B1: *Reaction between D2K and ODPA for the synthesis of Poly(amic-acid)s (PAA)s in THF. The resulting PAA structure is shown. X (which ~33) denotes the number of repeating segments within each D2K molecule. n denotes the number of repeating segments within the overall PAA, and is estimated to be ~9 and 2 for OD2K1 and OD2K2, respectively, based on their molecular weight, cf. Section B4.*

B3. Attenuated Total Reflectance Fourier Infrared Spectroscopy (ATR-FTIR)

OD2K1, OD2K2, OD2K1-Ag, OD2K2-Ag, Pebax, Pebax+2.5OD2K1-Ag, Pebax+4OD2K1-Ag, Pebax+2.5OD2K2-Ag, and Pebax+4OD2K2-Ag were analyzed using a Nicolet iS50R Fourier Transform Infrared Spectrometer (FT-IR) in the iS50 attenuated total reflectance (ATR) mode using 64 scans with a resolution of 0.4821 cm^{-1}. Results between 400 to 4000 cm^{-1} wavenumbers, are shown below.

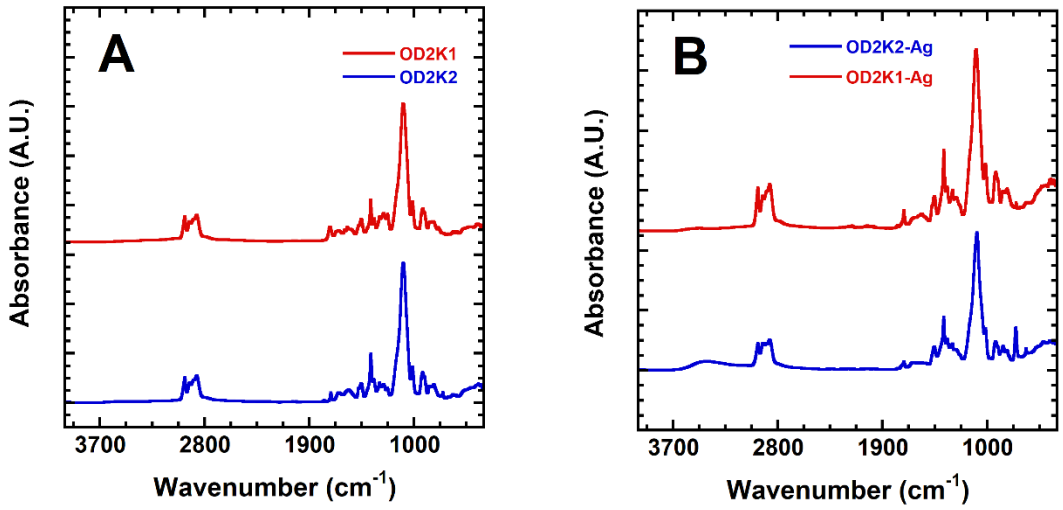

Figure B2: *A) ATR-FTIR spectra of the synthesized OD2K1 and OD2K2 samples, between 400 to 4000 cm^{-1} wavenumbers. B) ATR-FTIR spectra of the synthesized OD2K1-Ag and OD2K2-Ag silver nanoparticles stabilized by OD2K1 and OD2K2, respectively, between 400 to 4000 cm^{-1} wavenumbers.*

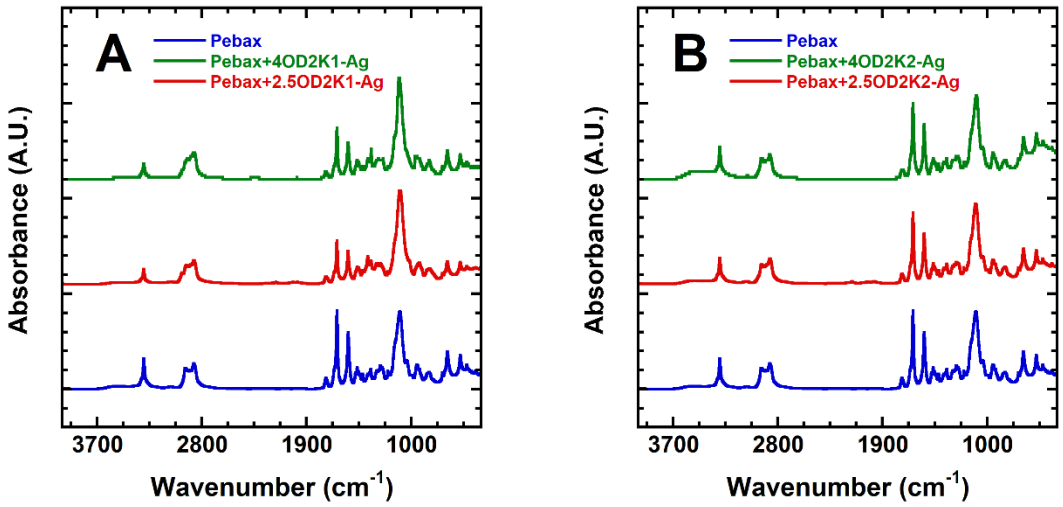

Figure B3: *A) ATR-FTIR spectra of the fabricated Pebax+2.5OD2K1-Ag and Pebax+4OD2K1-Ag membranes, compared to neat Pebax, between 400 to 4000 cm^{-1} wavenumbers. B) ATR-FTIR spectra of the fabricated Pebax+2.5OD2K2-Ag and Pebax+4OD2K2-Ag membranes, compared to neat Pebax, between 400 to 4000 cm^{-1} wavenumbers.*

B4. Intrinsic Viscosity Measurements

The intrinsic viscosity (η_{int}) of the same batch of OD2K1 (previously called OD2K) used in this study, with a molecular weight of 20,800 g/mol in $CHCl_3$ at 35 °C has been previously reported.[59] Following the same technique, the intrinsic viscosity of OD2K2 was measured using a size 0C Ubbelohde viscometer purchased from Cannon Instruments, calibrated with a viscometer constant of 0.003309 cSt/s^2. Solutions of OD2K2 in $CHCl_3$ were prepared at concentrations that range from 0.4 – 1 g/dL and tested at 35 °C. The inherent (η_{inh}) and reduced (η_{red}) viscosity were measured at least 5 times at 4 different concentrations, and were calculated using the following equations:

$$\eta_{red} = \frac{t - t_0}{c t_0} \quad \text{(Eq. B1)}$$

$$\eta_{inh} = \frac{\ln(t) - \ln(t_0)}{c} \quad \text{(Eq. B2)}$$

Where t is the time the polymer solution takes to flow between the viscometer ring indicators, t_0 is the corresponding time for the neat solvent to flow between the viscometer ring indicators, and c is the polymer concentration in g/dL.

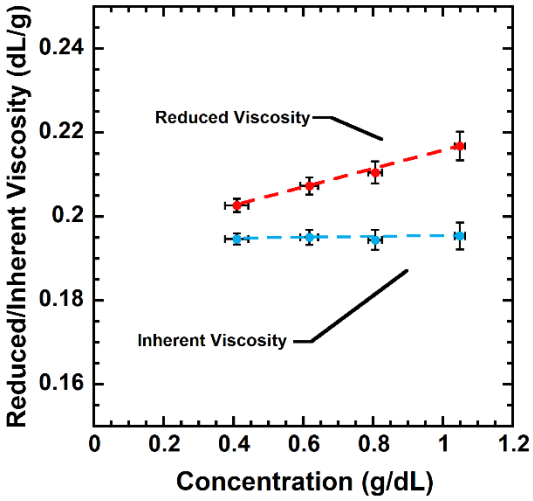

Figure B4: *Reduced (red) and inherent (blue) viscosity (dL/g) for OD2K2 as a function of concentration (g/dL). The linear best fit line for both inherent viscosity {y = 0.0008x + 0.1943}*

and reduced viscosity {y = 0.0218x + 0.1936}. Error bars are calculated using linear error propagation.

The intrinsic viscosity was determined to be the average value of both η_{inh} and η_{red}, extrapolated at a concentration of 0 g/dL, i.e., the y-intercept value. The intrinsic viscosity was used to compared relative molecular sizes of OD2K1 and OD2K2. The reported intrinsic viscosity was 0.232 ± 0.001 dL/g and 0.194 ± 0.001 dL/g for OD2K1 and OD2K2, respectively. Using the number average molecular weight and intrinsic viscosity of OD2K1 (20800 g/mol, 0.232 dL/g), as well as a similarly structured poly(amic-acid), OD4K (42800 g/mol, 0.255 dL/g)[59], the molecular weight of OD2K2 was estimated using the following relationship.[146]

$$\eta_{int} = KM^{a} \qquad \text{(Eq. B3)}$$

Where M is the polymer molecular weight in g/mol, and K and a are constants, which depend on the particular polymer-solvent system. In the case of this two-point system, the values of K and a are 0.131 (dL mol^{a} /g$^{(1+a)}$) and 0.063, respectively. The estimated molecular weight of OD2K2 is 5310 ± 2970 g/mol.

B5. Synthesis of Silver Nanoparticles

The synthesis procedure for the silver nanoparticles, whose details have been previously reported,[59] is briefly summarized: First, either 200 mg of OD2K1 or OD2K2 was added to a three-neck flask equipped with a magnetic stirrer, water jacketed reflux column, and a nitrogen blanketed atmosphere. 40 ml of EG was added to the flask and the mixture was heated to 100 ºC using a hotplate. Aqueous $AgNO_3$ (40 wt%) was prepared by dissolving $AgNO_3$ in ultrapure water. 2 ml of this solution was rapidly injected into the reaction flask using a syringe. The reaction was maintained for 30 minutes before removing the flask from heat, and immersing it in a 20 ºC bath to quench the reaction. To denote the particle type, Ag is added to the end of the PAA used in the synthesis (e.g., OD2K2-Ag are silver NPs created using OD2K2).

The particles, which are still in EG, were transferred into a separatory funnel and mixed with $CHCl_3$ at a 40/60 (EG/$CHCl_3$) vol% ratio. Ultrapure water was added, creating a EG/$CHCl_3$/H_2O (~25/35/40) vol% mixture. The $CHCl_3$ layer (now containing the Ag particles) was removed and the funnel cleaned before adding this $CHCl_3$ extract back into the funnel. The particles were rinsed 3 additional times in the separatory funnel using water, at a 30/70 ($CHCl_3$/H_2O) vol% ratio. Between each wash, the $CHCl_3$ layer is extracted and used for subsequent washes. The final particle suspension was stored in a chemical fridge (~ 4 ºC) using PTFE lined amber vials.

B6. Thermogravimetric Analysis (TGA)

TGA was used to determine the nominal silver weight loading in each MMM fabricated in this work. Additionally, each particle type, OD2K1-Ag and OD2K2-Ag, were tested to determine the final PAA:Ag ratio to ensure consistency between batches (cf. Figure B5). About 5-10 mg of dry particle mass was loaded into a TA Instruments TGA 500 under nitrogen gas, flowing at 10 ml/min. Since the particles are suspended in chloroform, the TGA pan was filled dropwise with the particle solution using a 100 µL Eppendorf pipette. The chloroform was allowed to evaporate from the pan before adding another 100 µL of particle solution. This process was repeated until sufficient dry mass was reached. The samples were first heated from room temperature to 40 °C and held isothermally for 5 hours to remove any residual solvent or moisture. The samples were then heated from 50 °C to 800 °C at a rate of 10 °C/min. First and second derivative analysis was used to determine the temperature ranges of individual mass losses.

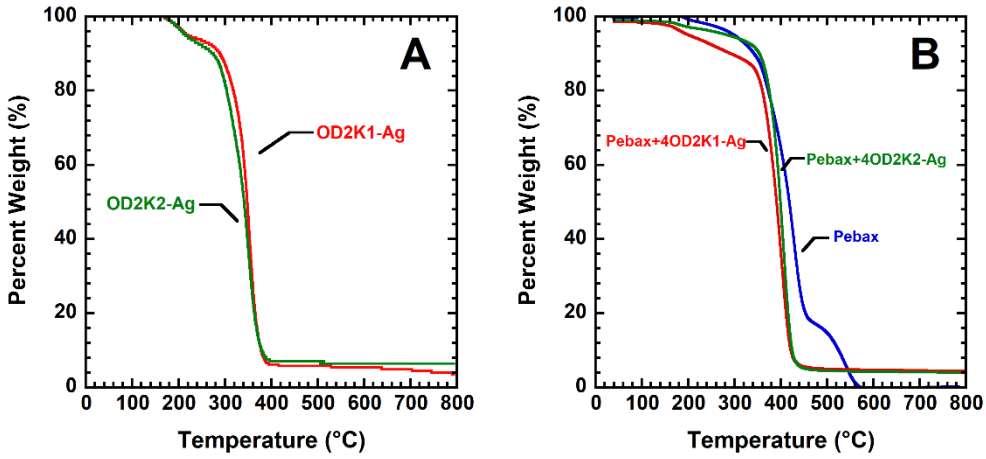

Figure B5: *TGA for the A) change in weight % (W) as a function of temperature for OD2K1-Ag (Red) and OD2K2-Ag (Green), B) TGA for change in weight % (W) as a function of temperature for Pebax (Blue), Pebax+4OD2K1-Ag (Red), and Pebax+4OD2K2-Ag (Green). Each Figure spans the experimental temperature ramp range between 40 and 800˚C. Small mass losses below 200˚C are attributed to residual solvents. Subsequent mass loss starting after 300˚C are attributed to polymer degradation. The remaining mass after 800˚C is from the silver core of the nanoparticles.*

B7. Transmission Electron Microscopy (TEM)

Electron micrographs of the OD2K1-Ag and OD2K2-Ag were imaged using a JEOL 2000FX transmission electron microscope (TEM) at 200kV with a LaB_6 electron source. 20-40 μL of a silver NP suspension (in $CHCl_3$) was dropped onto a 3 mm copper TEM grid with carbon support. The particle shape, and size distribution was determined based on at least 200 NPs, using the Fiji image analysis.[100]

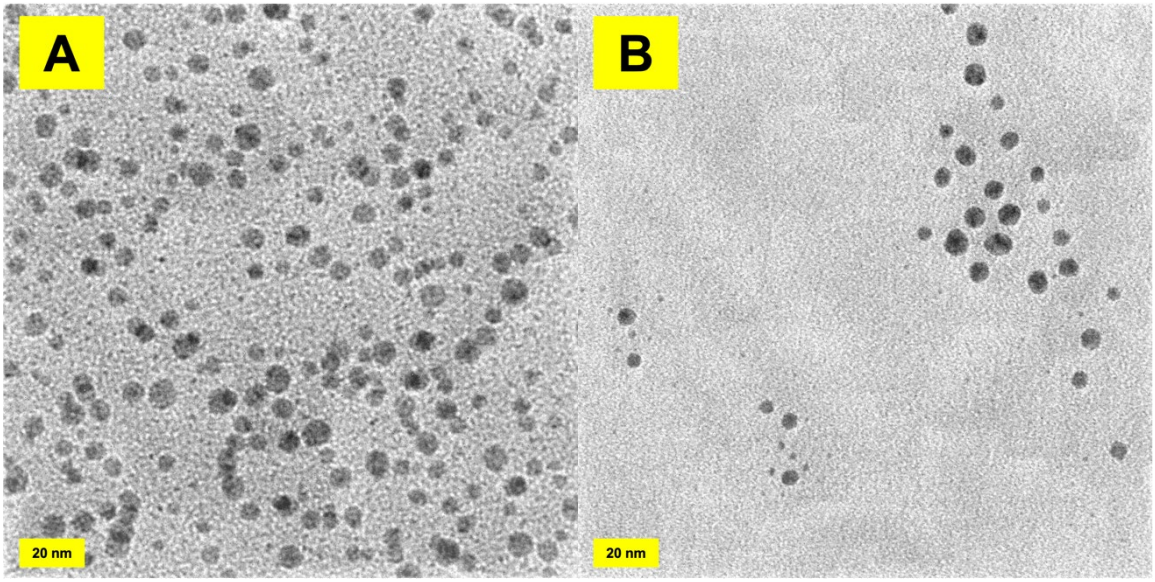

Figure B6: *TEM micrographs of A) OD2K1-Ag and B) OD2K2-Ag, imaged at 100kX magnification.*

Table B1: *Summary of Silver Nanoparticle Size, Composition, and Surface Grafting Density*

Name	Equivalent Diameter (nm)[a]	Ag/Polymer Mass Ratio (%)[b]	Grafting Density (Chains nm^{-2})[c]
OD2K1-Ag[d]	6.5 ± 1.6	4.79 ± 0.2	6.9 ± 1.7
OD2K2-Ag[e]	6.9 ± 3.2	8.46 ± 0.2	16.2 ± 4.0

[a] *Equivalent diameter based on the TEM size measurement of at least 200 individual particles.*
[b] *OD2K1-Ag and OD2K2-Ag silver to polymer mass ratio (Ag/polymer mass ratio) determined using TGA*
[c] *OD2K1-Ag and OD2K2-Ag silver grafting density calculated using the particle equivalent diameter, Ag/Polymer mass ratio, and polymer molecular weight values.*
[d] *The polymer molecular weight of OD2K1 was previously obtained using gel permeation chromatography.*[59]
[e] *The polymer molecular weight of OD2K2 was estimated using intrinsic viscosity, c.f. Section B4.*[59,146]

B8. Fabrication of Mixed Matrix Membranes (MMMs)

Neat Pebax 1657 (Pebax) membranes were produced via the solution-casting method using a 2.5 wt% Pebax solution in a blend of EtOH and $CHCl_3$ (50/50 vol%) dissolved at 50-55 °C. Mixed matrix membranes were fabricated by incorporating either OD2K1-Ag or OD2K2-Ag particles, which have been suspended in $CHCl_3$, into the polymer solution. The target silver concentration in these membranes varied between 0-4 wt%. Adjustments were made to the final solvent composition to maintain a consistent mixture of Pebax and particles at a 50/50 vol% ratio of EtOH and $CHCl_3$, considering the particles' suspension in $CHCl_3$.

Each mixture underwent 5 minutes of sonication before being poured onto a leveled glass dish at room temperature within a nitrogen-filled glove bag. In the case of the MMMs, each casting plate was also covered in aluminum foil, to prevent any photo-induced degradation of the silver NPs. Following a 3-day drying period, the membrane thickness was measured using a Mitutoyo micrometer ten times, yielding measurements between 80-100 μm. Membranes containing x% of silver by mass, using particles which are stabilized by polymer y, are denoted by Pebax+xy-Ag. For example, particles that were formed using OD2K2, which were subsequently used to fabricate membranes with a silver loading of 4 wt% would be Pebax+4OD2K2-Ag.

B9. Scanning Electron Microscopy (SEM)

The cross-section of Pebax, Pebax+2.5OD2K1Ag, Pebax+4OD2K1Ag, Pebax+2.5OD2K2-Ag, and Pebax+4OD2K2-Ag were imaged using scanning electron microscopy to characterize the structure morphology. Cross-sections were prepared by first immersing the samples into liquid nitrogen and fracturing them. As a consequence, a few cracks were formed from this process and remain as small artifacts in Figure B7. Before imaging, each sample was coated with a thin layer (a few nanometers) of iridium, using a sputter coater. The images were taken at 10Kx using an accelerating voltage of 10 KeV on a ThermoFischer Quattro device.

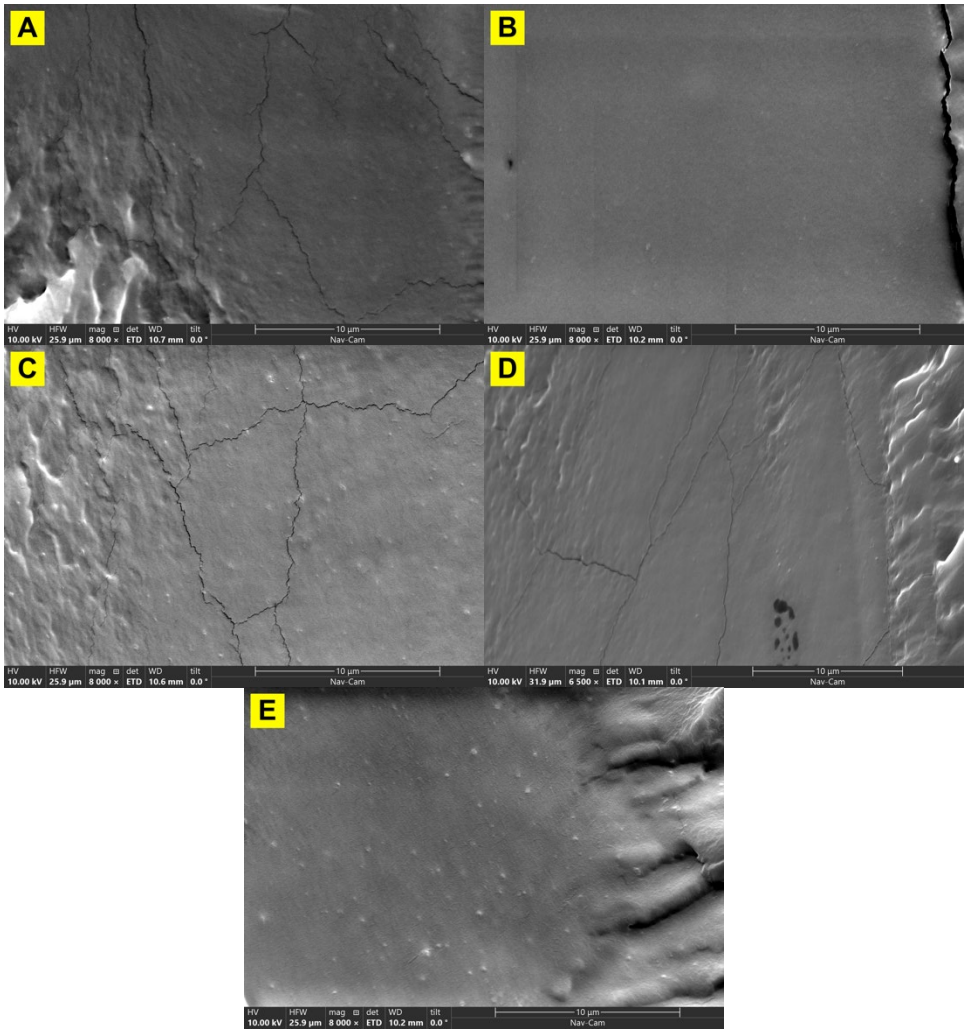

Figure B7: *SEM micrographs of the cross-sections of A) Pebax, B) Pebax+2.5OD2K1-Ag, C) Pebax+4OD2K1-Ag, D) Pebax+2.5OD2K2-Ag, and E) Pebax+4OD2K2-Ag. Imaged at 10kX magnification with and with an accelerating voltage of 10 KeV.*

B10. Density Measurements

The membrane density (ρ) of films fabricated in this work were measured using a Mettler Toldeo balance equipped with a density kit. The density was calculated after weighing the samples in air (m_{air}) and in heptane (m_{C7}) at 22 ºC:

$$\rho = \frac{m_{air}}{m_{air} - m_{C7}}(\rho_{C7} - \rho_{air}) + \rho_{air} \qquad \text{(Eq. B4)}$$

Where ρ_{air} is the density of air (0.00119 g/ml) and ρ_{C7} is the density of heptane (0.684 g/ml).

Table B2: *Experimental densities of neat Pebax, Pebax+2.5OD2K1-Ag, and Pebax+4OD2K1-Ag.*

Name	Density (g/ml)[a]
Pebax	1.14 ± 0.03
Pebax+2.5OD2K1-Ag	1.10 ± 0.02
Pebax+4OD2K1-Ag	1.18 ± 0.03

[a] *Pebax, Pebax+2.5DO2K1-Ag, and Pebax+4OD2K1-Ag values were determined using buoyancy measurements in n-heptane at 22 ℃.*

The density of neat Pebax, Pebax+2.5OD2K1-Ag, and Pebax+4OD2K1-Ag were used in gas sorption measurements, cf. Section B12.

B11. Pure Gas Permeation Measurements

Pure gas (CH_4, CO_2, C_2H_4, and C_2H_6) permeability was measured between 1-30 atm at 15, 25, 35, and 45 ºC using a constant volume barometric device, wherein the membrane was situated between two large volumes, using a 47 mm HP filter holder. Prior to measurements, vacuum was pulled on the entire system overnight to remove any humidity or other sorbed species. Pressure was charged to the upstream side of the membrane and measured using a PX-409-USHB series Omega pressure transducer (0-1000 psi). Then, gas was allowed to permeate through the membrane to the downstream volume, where the increase in pressure with time was measured using a highly sensitive PX-409-USHB series Omega pressure transducer (0-260 torr). The permeability (P, in units of Barrers) was calculated as follows:

$$P = \frac{lV_{down}}{\Delta pART}\left(\frac{dp}{dt}_{down} - \frac{dp}{dt}_{leak}\right) \quad \text{(Eq. B5)}$$

where l is the membrane thickness, A is the membrane area available to gas transport, R is the universal gas constant, T is the absolute temperature, Δp is the average transmembrane pressure, $\frac{dp}{dt}_{down}$ is the asymptotic rate of pressure increase in the downstream ballast, and $\frac{dp}{dt}_{leak}$ is the rate of pressure increase in the downstream volume whilst the charge pressure is 0. Membranes were glued with epoxy resin on a brass ring, and the passage area was accurately measured via the ImageJ software.[100] Filter paper was used as a backing to reduce the risk of sample breakage.

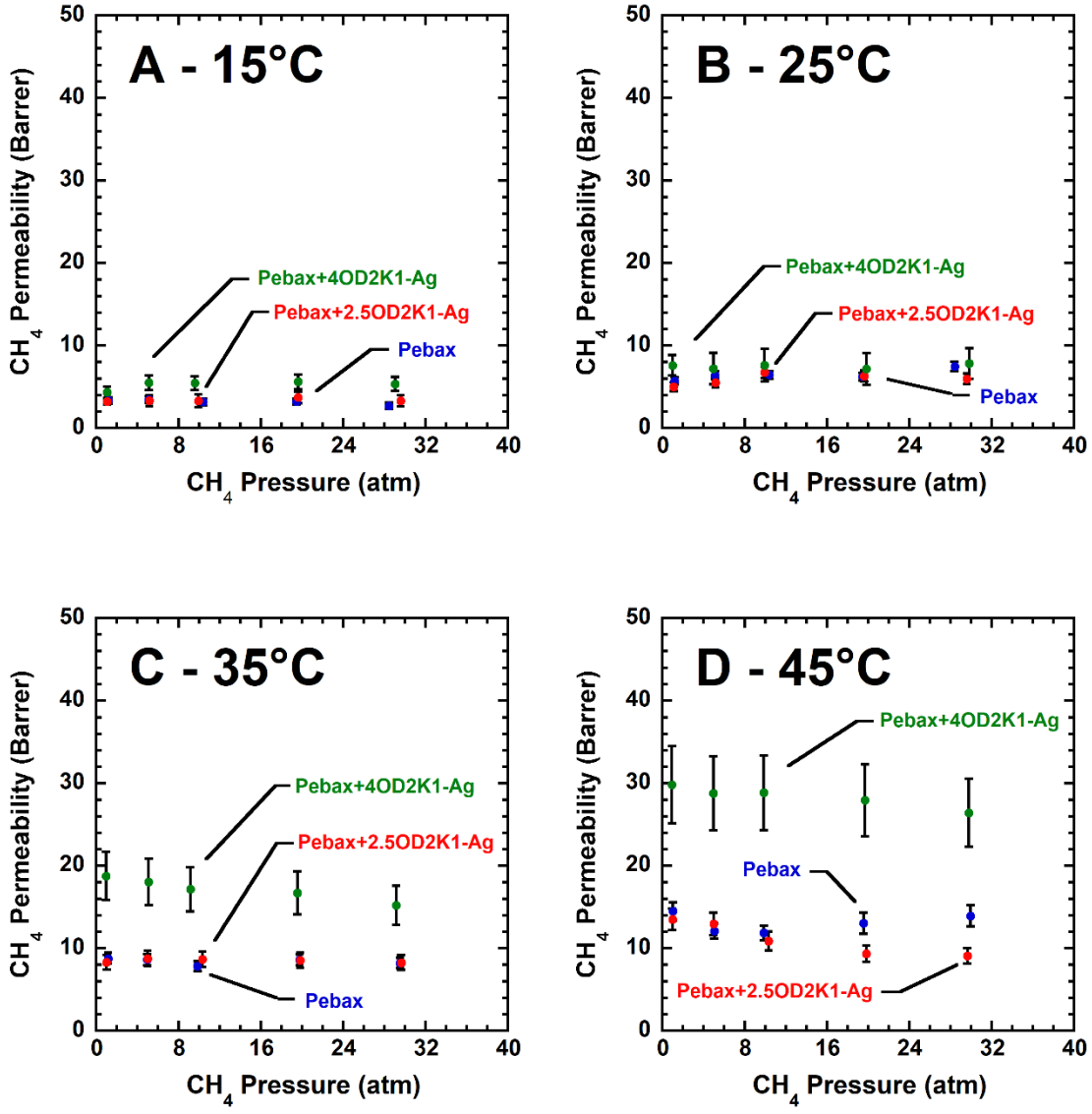

Figure B8: *Permeability isotherms of CH_4 at A), 15 ℃ B) 25 ℃, C) 35 ℃, and D) 45 ℃ in Pebax (blue), Pebax+2.5OD2K1-Ag (red), and Pebax+4OD2K1-Ag (green) in Barrer as a function of pure gas pressure, ranging up to 30 atm. Error bars were calculated via linear error propagation.*

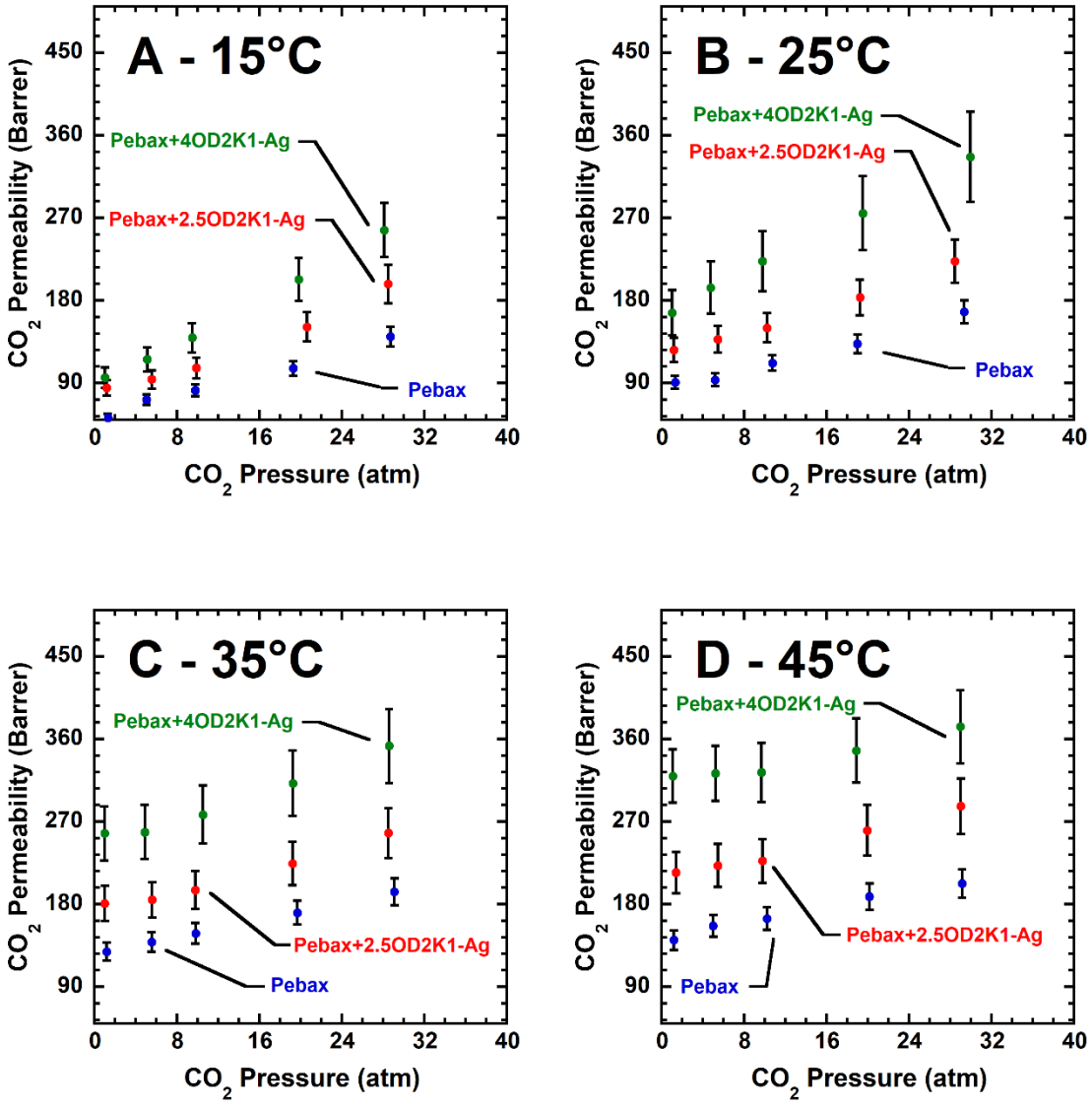

Figure B9: *Permeability isotherms of CO_2 at A), 15 ℃ B) 25 ℃, C) 35 ℃, and D) 45 ℃ in Pebax (blue), Pebax+2.5OD2K1-Ag (red), and Pebax+4OD2K1-Ag (green) in Barrer as a*

function of pure gas pressure, ranging up to 30 atm. Error bars were calculated via linear error propagation.

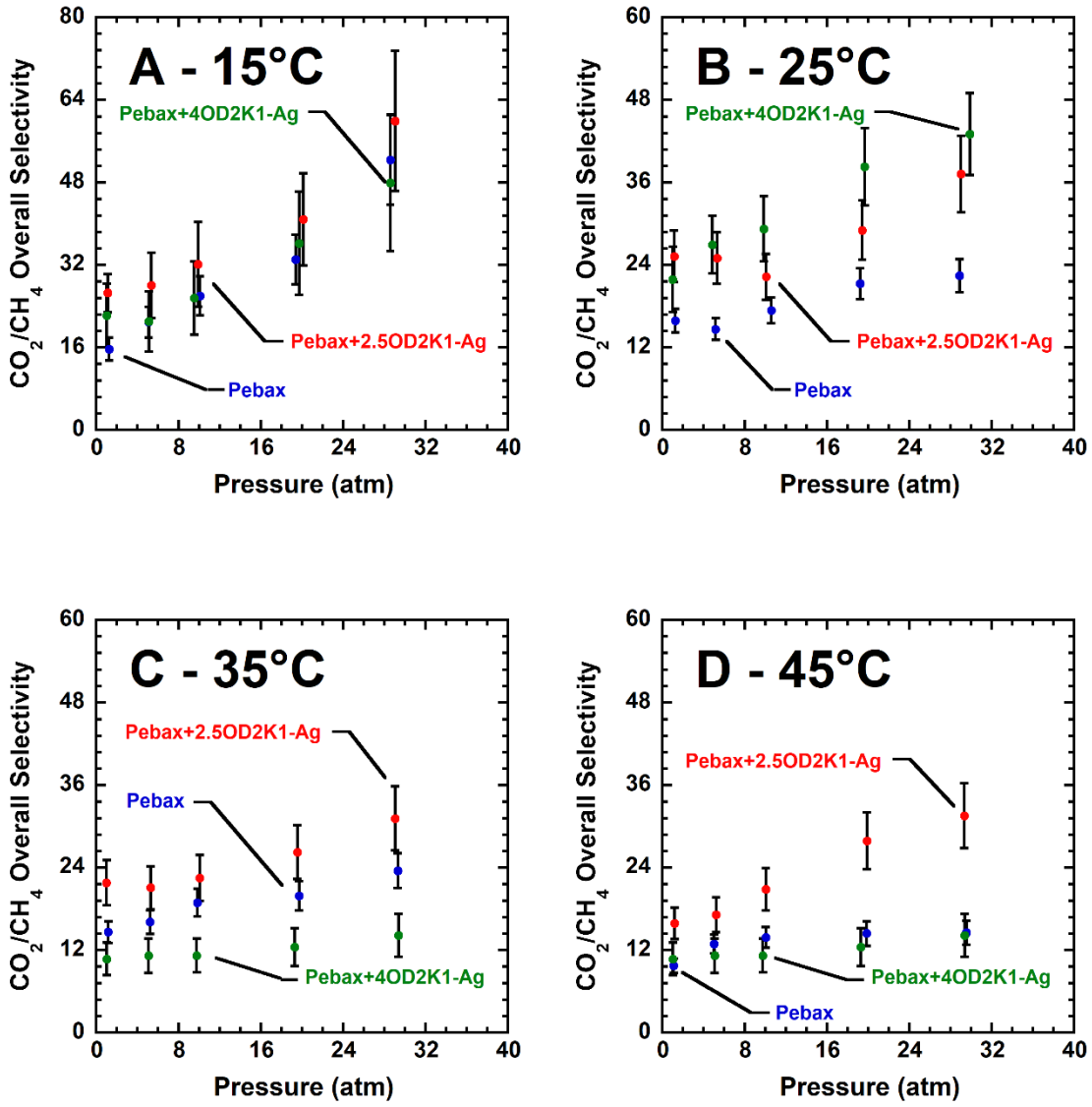

Figure B10: Ideal *CO_2/CH_4 overall selectivity at A), 15 ℃ B) 25 ℃, C) 35 ℃, and D) 45 ℃ in Pebax (blue), Pebax+2.5OD2K1-Ag (red), and Pebax+4OD2K1-Ag (green) as a function of pure gas pressure, ranging up to 30 atm. Error bars were calculated via linear error propagation.*

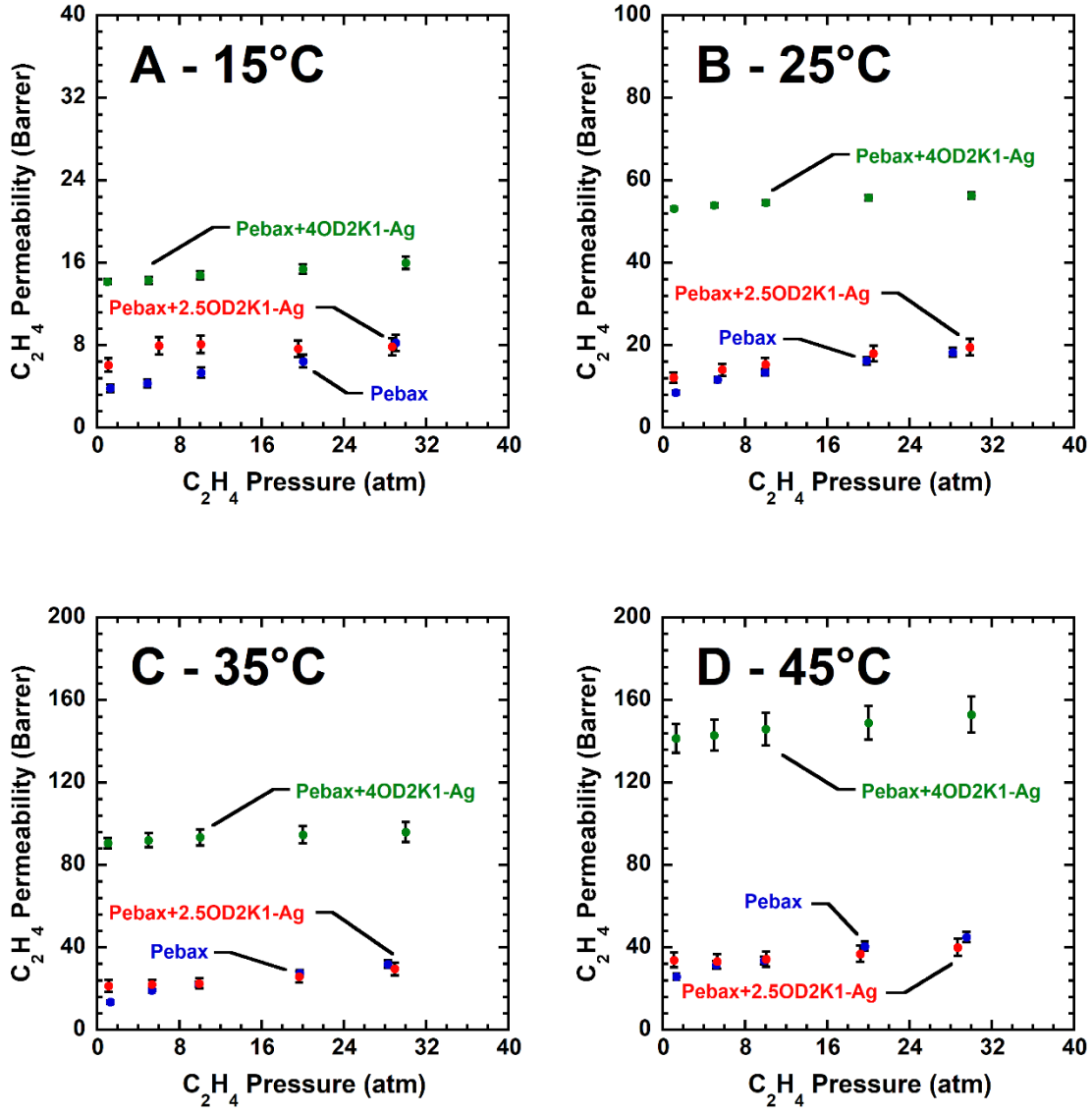

Figure B11: *Permeability isotherms of C_2H_4 at A), 15 ℃ B) 25 ℃, C) 35 ℃, and D) 45 ℃ in Pebax (blue), Pebax+2.5OD2K1-Ag (red), and Pebax+4OD2K1-Ag (green) in Barrer as a function of pure gas pressure, ranging up to 30 atm. Error bars were calculated via linear error propagation.*

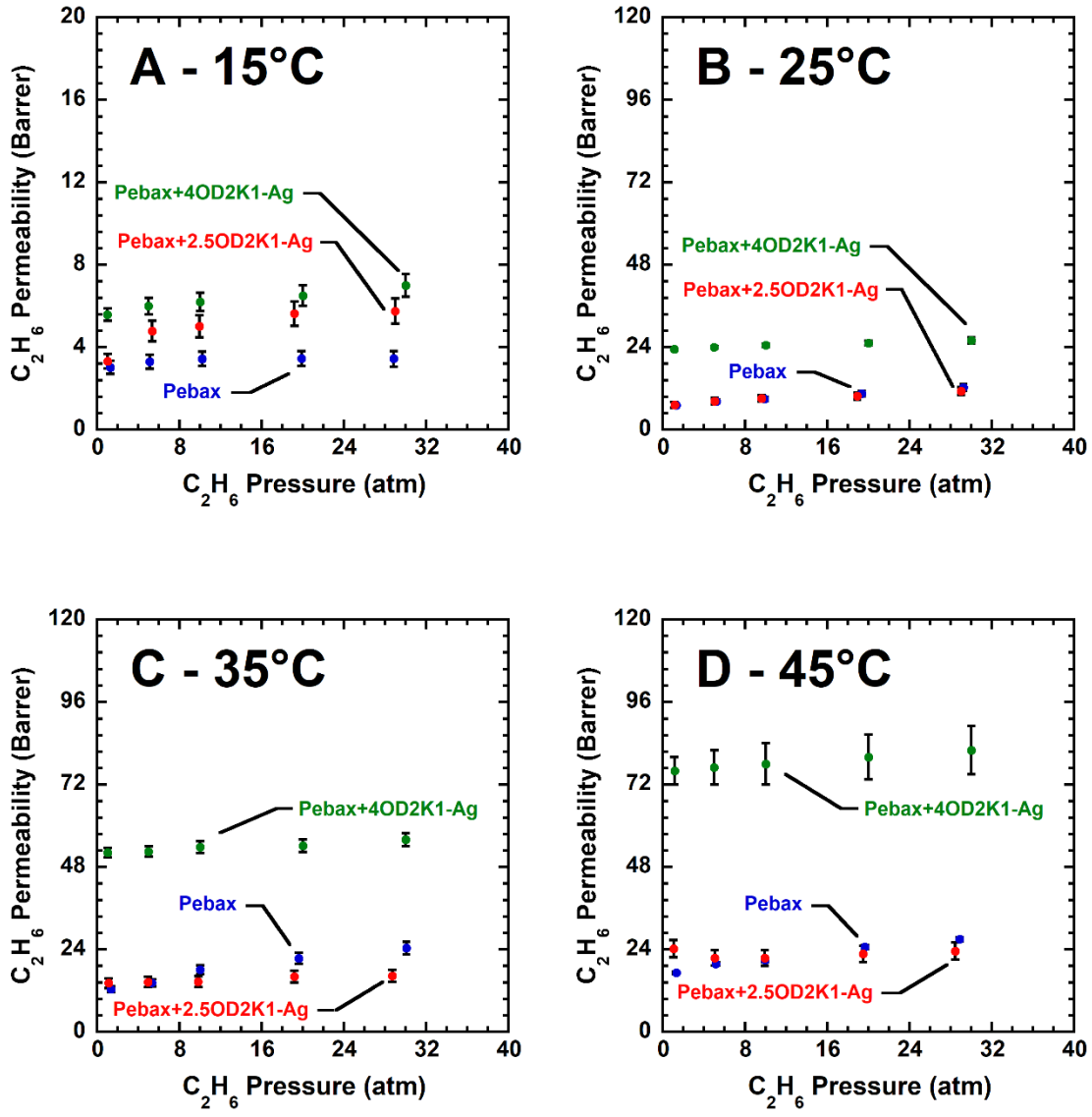

Figure B12: *Permeability isotherms of C_2H_6 at A), 15 ℃ B) 25 ℃, C) 35 ℃, and D) 45 ℃ in Pebax (blue), Pebax+2.5OD2K1-Ag (red), and Pebax+4OD2K1-Ag (green) in Barrer as a function of pure gas pressure, ranging up to 30 atm. Error bars were calculated via linear error propagation.*

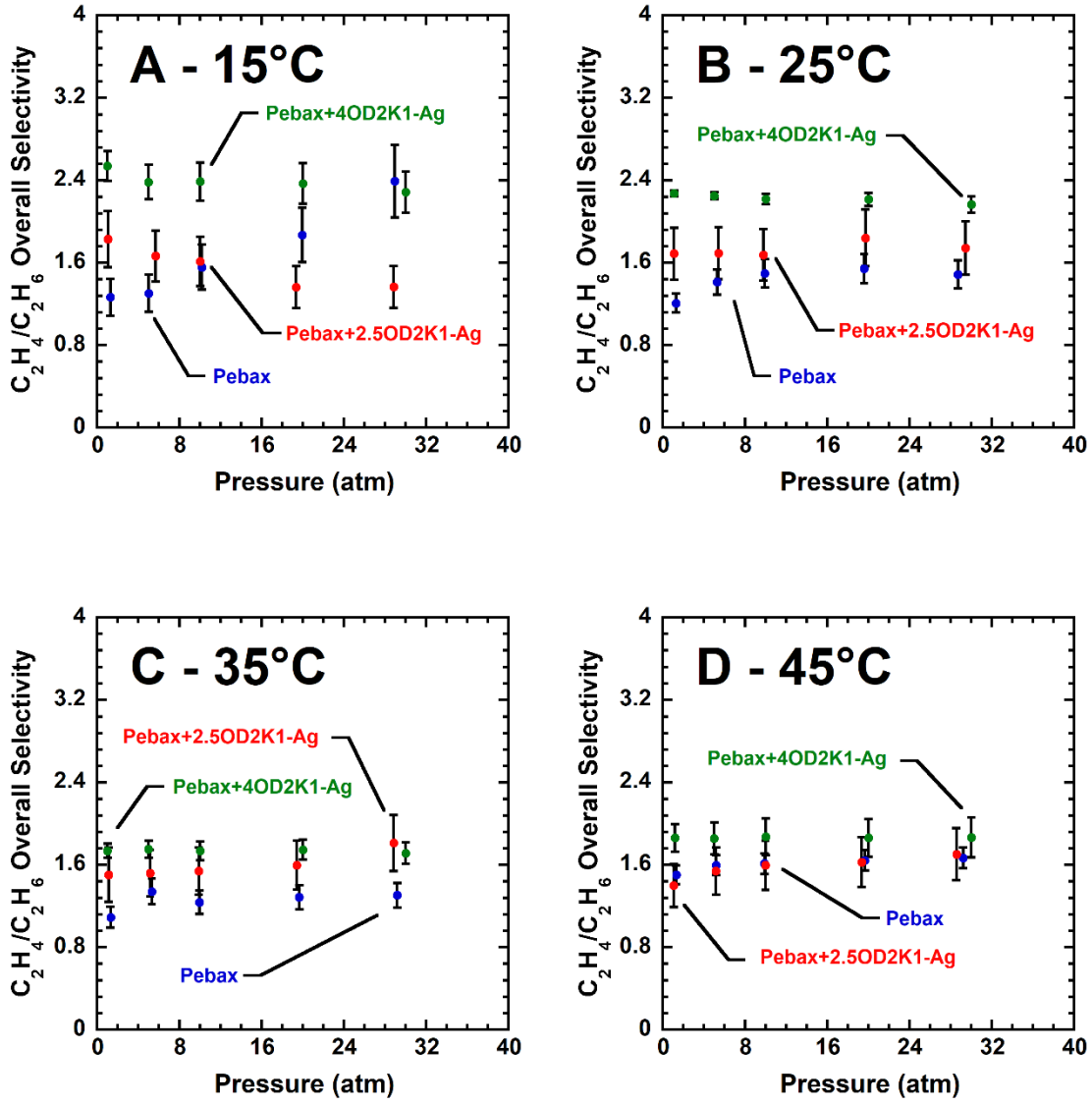

Figure B13: Ideal *C_2H_4/C_2H_6 overall selectivity at A), 15 ℃ B) 25 ℃, C) 35 ℃, and D) 45 ℃ in Pebax (blue), Pebax+2.5OD2K1-Ag (red), and Pebax+4OD2K1-Ag (green) as a function of pure gas pressure, ranging up to 30 atm. Error bars were calculated via linear error propagation.*

B12. Pure Gas Sorption Measurements

Pure gas (CH_4, CO_2, C_2H_4, and C_2H_6) sorption was measured at 15, 25, 35, and 45 ºC and up to 30 atm using the pressure decay method. The system consists of two volumes connected via a valve, namely, the charge chamber and sample chamber. Both chambers are equipped with PX-409-USHB series Omega pressure transducers (0-500 psi). The polymer sample is first added to the sampling chamber before pulling vacuum on both chambers overnight. Gas pressure is added to the charge chamber and allowed to equilibrate before quickly releasing it into the sampling chamber. The valve is then closed, thus disconnecting the chambers until each chamber equilibrates. A subsequent pressure decay in the sampling chamber is recorded, and the process is repeated in the next step without pulling vacuum. The overall sorbed gas concentration in the polymer sample is the following[114]:

$$C_{pol,j} = \frac{\rho_{pol}}{g_{pol,dry}}\left(V_c \sum_{i=0}^{j}\left(\frac{1}{\tilde{V}_{C0,i}} - \frac{1}{\tilde{V}_{CF,i}}\right) - \frac{V_S}{\tilde{V}_{SF,j}}\right) \qquad \text{(Eq. B6)}$$

where ρ_{pol} is the polymer density, $g_{pol,dry}$ is the dry polymer mass, j is the current pressure step, i is the previous pressure step, V_s is the sample chamber volume, V_C is the charge chamber volume, and $\tilde{V}_{C0}$, $\tilde{V}_{CF}$, $\tilde{V}_{SF}$, are the gas molar volumes (calculated using the Peng-Robinson equation of state) for the initial charge state (prior to valve opening), final charge state, and final sample state, respectively. The sorption coefficient for each gas was determined as the slope of the linear regression of at least 4 concentration points with pressure. Pure gas isotherms are shown in Figure B14-Figure B17, where concentration error is determined using standard linear error propagation and the uncertainty of the sorption coefficient is determined from the standard error of regression.

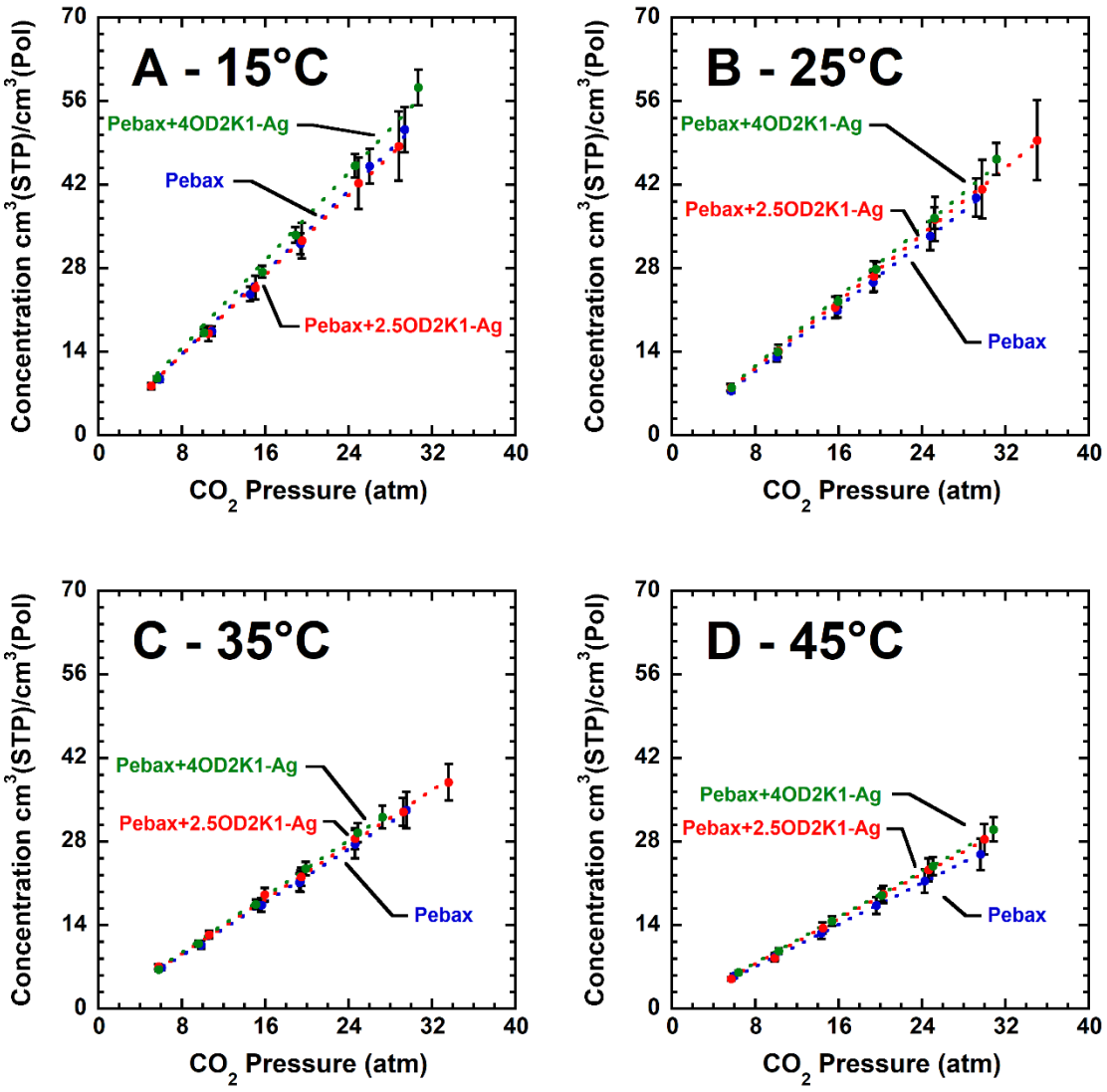

Figure B14: *Concentration isotherms of CO_2 at A), 15 ℃ B) 25 ℃, C) 35 ℃, and D) 45 ℃ in Pebax (blue), Pebax+2.5OD2K1-Ag (red), and Pebax+4OD2K1-Ag (green) in* $\frac{cm^3(STP)}{cm^3(Pol)}$ *as a function of pure gas pressure in atm. Error bars were found via linear error propagation.*

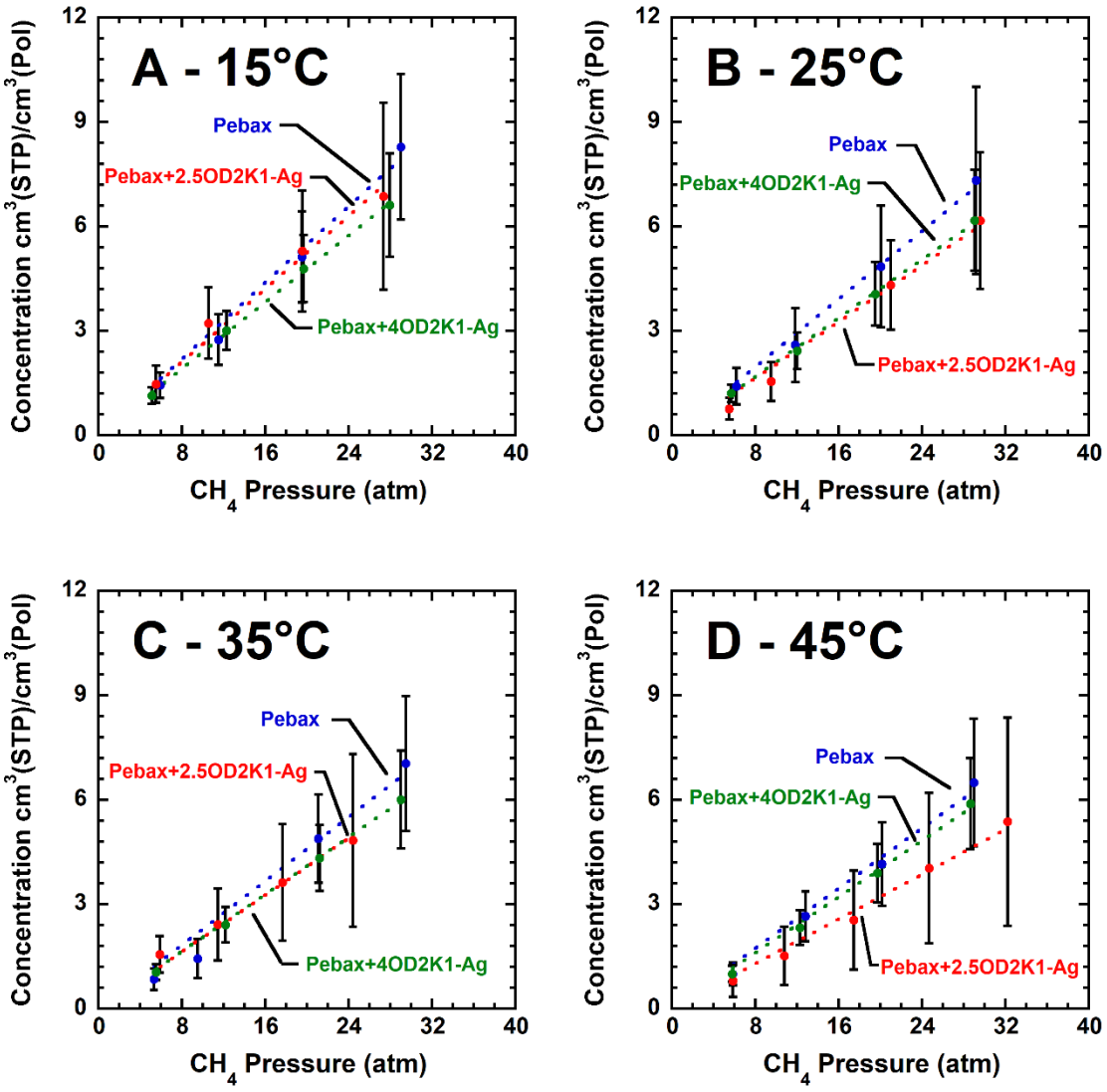

Figure B15: *Concentration isotherms of CH_4 at A), 15 ℃ B) 25 ℃, C) 35 ℃, and D) 45 ℃ in Pebax (blue), Pebax+2.5OD2K1-Ag (red), and Pebax+4OD2K1-Ag (green) in* $\frac{cm^3(STP)}{cm^3(Pol)}$ *as a function of pure gas pressure in atm. Error bars were found via linear error propagation.*

Table B3: *CO_2/CH_4 sorption selectivity at 15, 25, 35 and 45 ℃ in Pebax, Pebax+2.5OD2K1-Ag, and Pebax+4OD2K1-Ag. Uncertainty is found using the standard error of regression.*

Material	15C	25C	35C	45C
Pebax	6.46 ± 0.25	5.50 ± 0.13	4.85 ± 0.05	4.14 ± 0.12
Pebax+2.5OD2K1-Ag	7.56 ± 0.55	6.90 ± 0.52	6.03 ± 0.11	5.77 ± 0.33
Pebax+4OD2K1-Ag	6.74 ± 0.12	6.04 ± 0.49	5.07 ± 0.08	4.81 ± 0.10

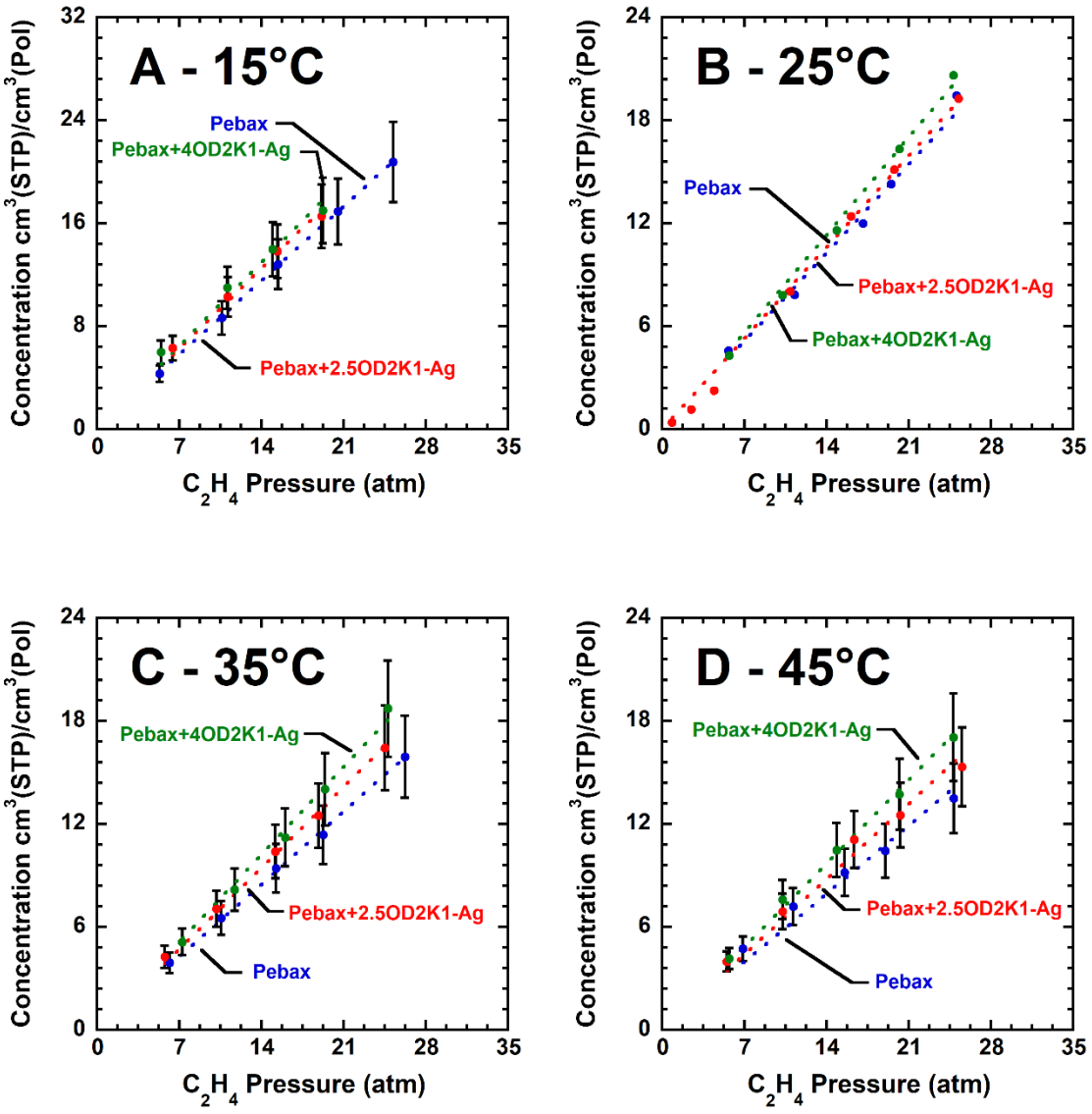

Figure B16: *Concentration isotherms of C_2H_4 at A), 15 ℃ B) 25 ℃, C) 35 ℃, and D) 45 ℃ in Pebax (blue), Pebax+2.5OD2K1-Ag (red), and Pebax+4OD2K1-Ag (green) in* $\frac{cm^3(STP)}{cm^3(Pol)}$ *as a function of pure gas pressure in atm. Error bars were found via linear error propagation.*

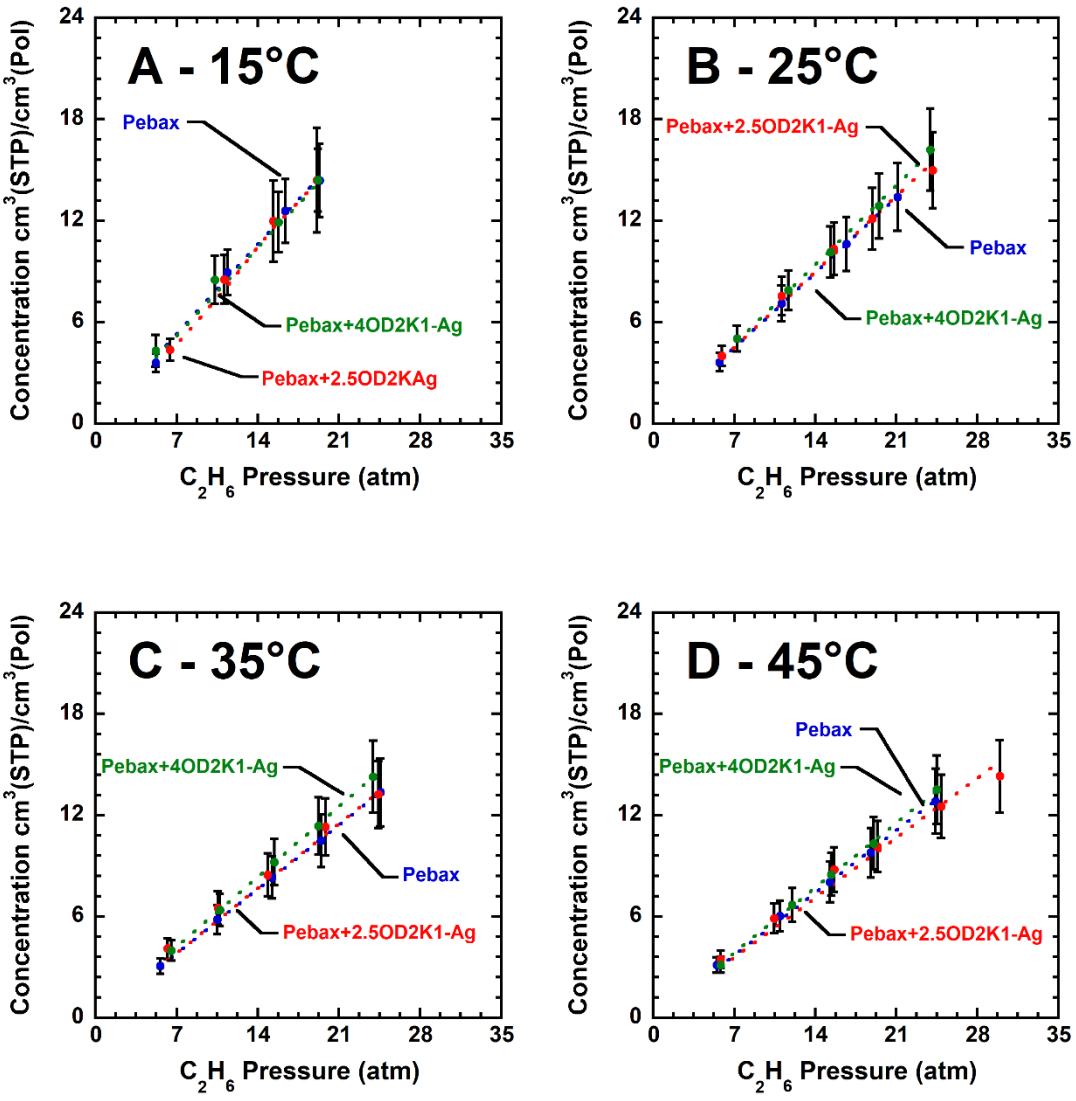

Figure B17: *Concentration isotherms of C_2H_4 at A), 15 ℃ B) 25 ℃, C) 35 ℃, and D) 45 ℃ in Pebax (blue), Pebax+2.5OD2K1-Ag (red), and Pebax+4OD2K1-Ag (green) in* $\frac{cm^3(STP)}{cm^3(Pol)}$ *as a function of pure gas pressure in atm. Error bars were found via linear error propagation.*

Table B4: *C_2H_4/C_2H_6 sorption selectivity at 15, 25, 35 and 45 ℃ in Pebax, Pebax+2.5OD2K1-Ag, and Pebax+4OD2K1-Ag. Uncertainty is found using the standard error of regression.*

Material	15C	25C	35C	45C
Pebax	1.09 ± 0.02	1.16 ± 0.06	1.12 ± 0.01	1.08 ± 0.04
Pebax+2.5OD2K1-Ag	1.21 ± 0.10	1.19 ± 0.03	1.23 ± 0.03	1.24 ± 0.05
Pebax+4OD2K1-Ag	1.24 ± 0.08	1.21 ± 0.02	1.23 ± 0.02	1.26 ± 0.02

B13. Pure Gas Diffusivity Coefficients

Pure gas diffusivity isotherms for CH_4, CO_2, C_2H_4, and C_2H_6, at 15, 25, 35, and 45 °C, up to 30 atm, are shown in Figure B18-Figure B23. Diffusivity coefficients were calculated using the Solution-Diffusion Model.[20] Error bars are determined using standard linear error propagation.

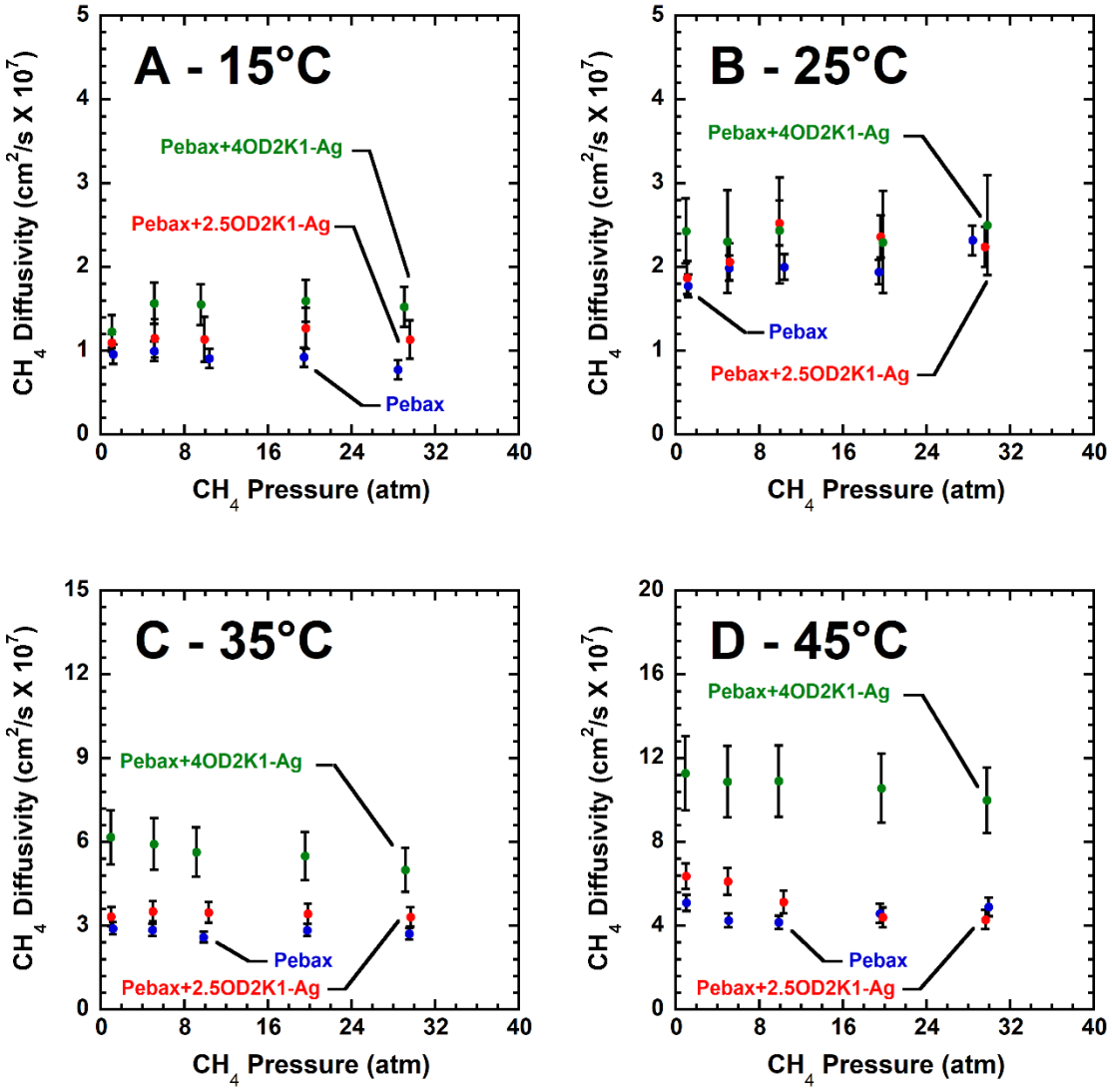

Figure B18: *Concentration averaged diffusivity coefficients of CH_4 at A), 15 ℃ B) 25 ℃, C) 35 ℃, and D) 45 ℃ in Pebax (blue), Pebax+2.5OD2K1-Ag (red), and Pebax+4OD2K1-Ag (green) in* $\frac{cm^2}{s}(10^7)$ *as a function of pure gas pressure in atm. Error bars were found via linear error propagation and values were calculated assuming solution diffusion from permeability and solubility data.*

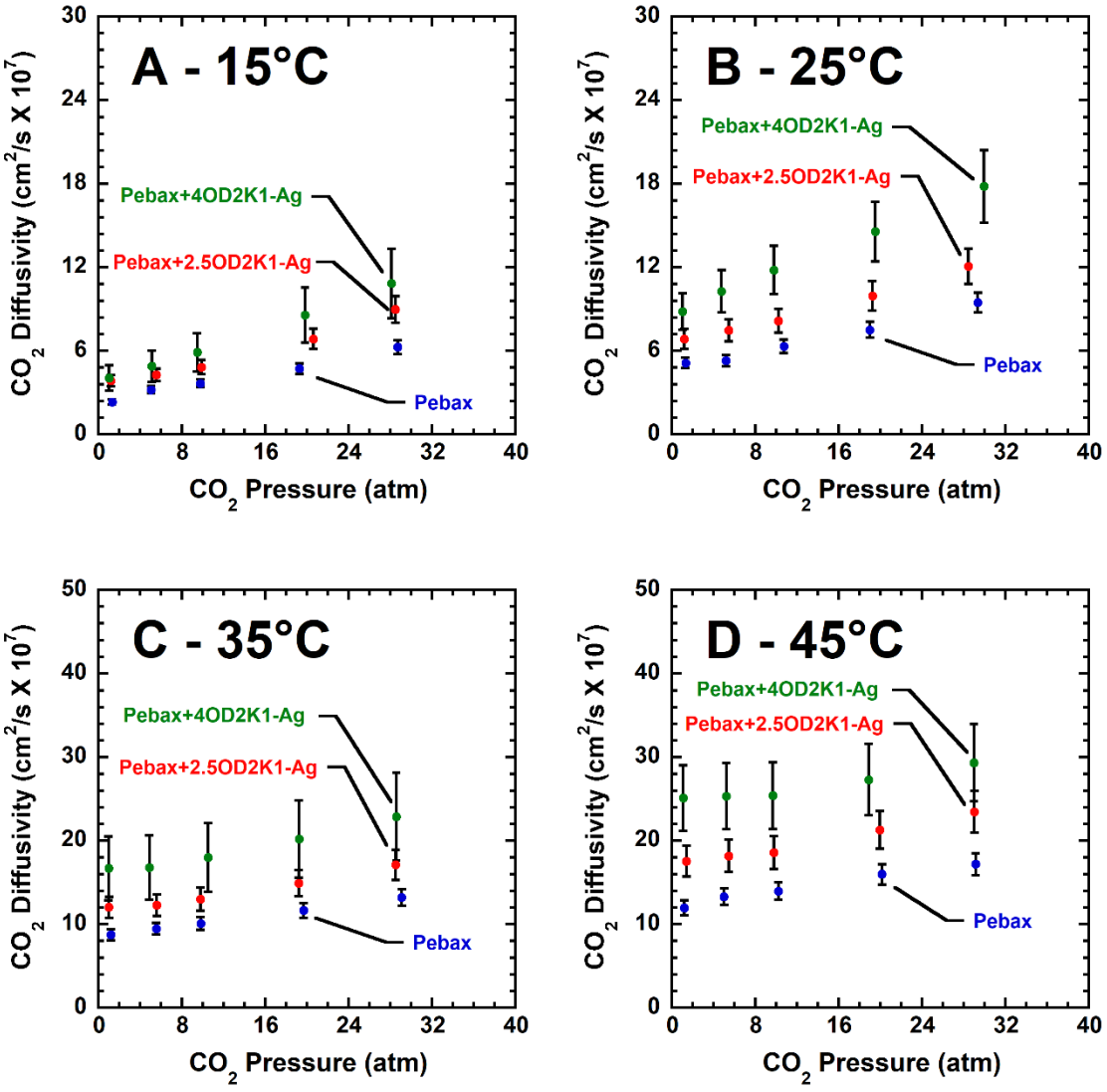

Figure B19: *Concentration averaged diffusivity coefficients of CO_2 at A), 15 ℃ B) 25 ℃, C) 35 ℃, and D) 45 ℃ in Pebax (blue), Pebax+2.5OD2K1-Ag (red), and Pebax+4OD2K1-Ag (green) in* $\frac{cm^2}{s}(10^7)$ *as a function of pure gas pressure in atm. Error bars were found via linear error propagation and values were calculated assuming solution diffusion from permeability and solubility data.*

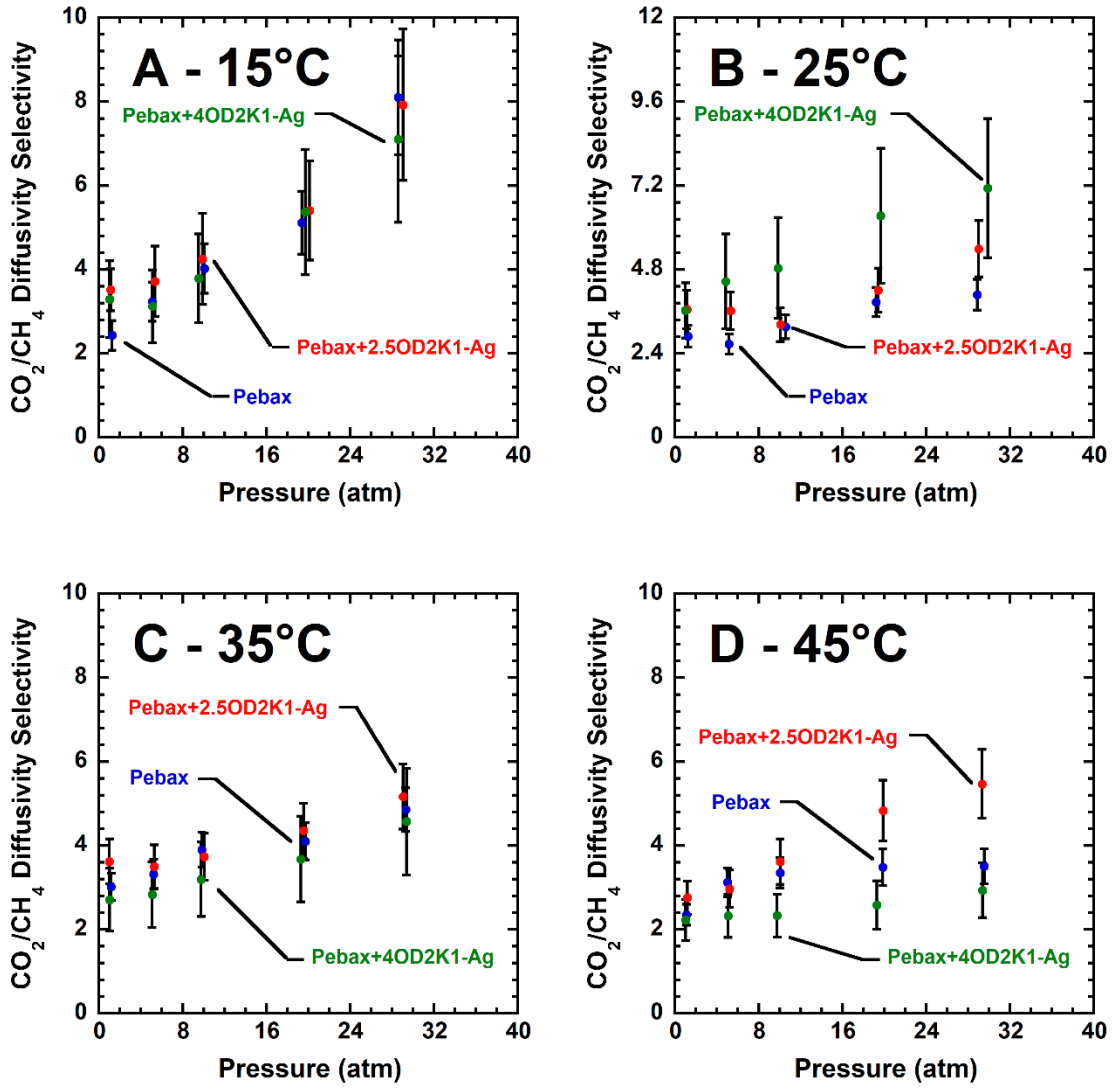

Figure B20: *Pure gas CO_2/CH_4 diffusivity selectivity at A), 15 ℃ B) 25 ℃, C) 35 ℃, and D) 45 ℃ in Pebax (blue), Pebax+2.5OD2K1-Ag (red), and Pebax+4OD2K1-Ag (green) as a function of pure gas pressure, ranging up to 30 atm. Error bars were calculated via linear error propagation.*

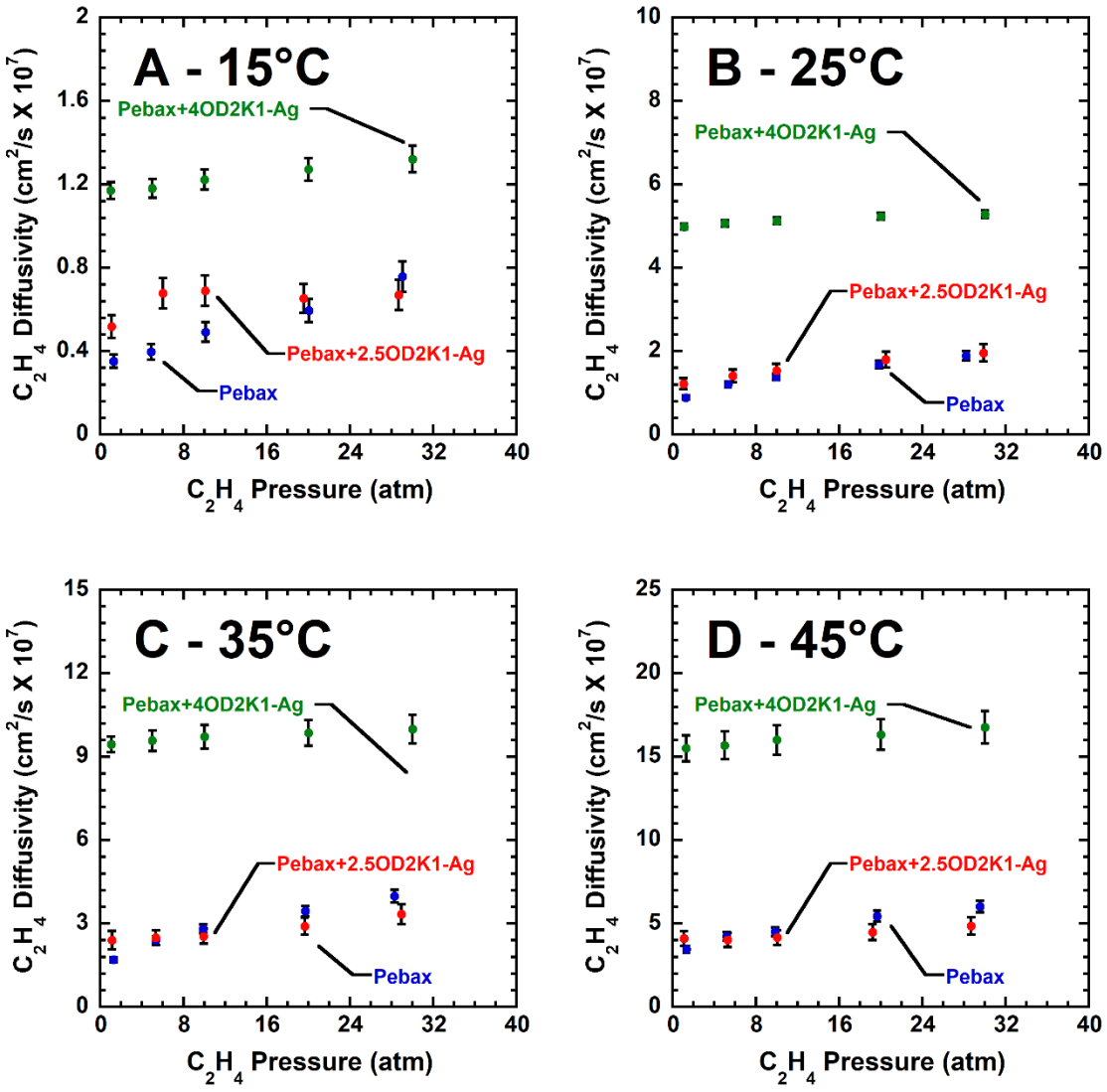

Figure B21: *Concentration averaged diffusivity coefficients of C_2H_4 at A), 15 ℃ B) 25 ℃, C) 35 ℃, and D) 45 ℃ in Pebax (blue), Pebax+2.5OD2K1-Ag (red), and Pebax+4OD2K1-Ag (green) in* $\frac{cm^2}{s}(10^7)$ *as a function of pure gas pressure in atm. Error bars were found via linear error propagation and values were calculated assuming solution diffusion from permeability and solubility data.*

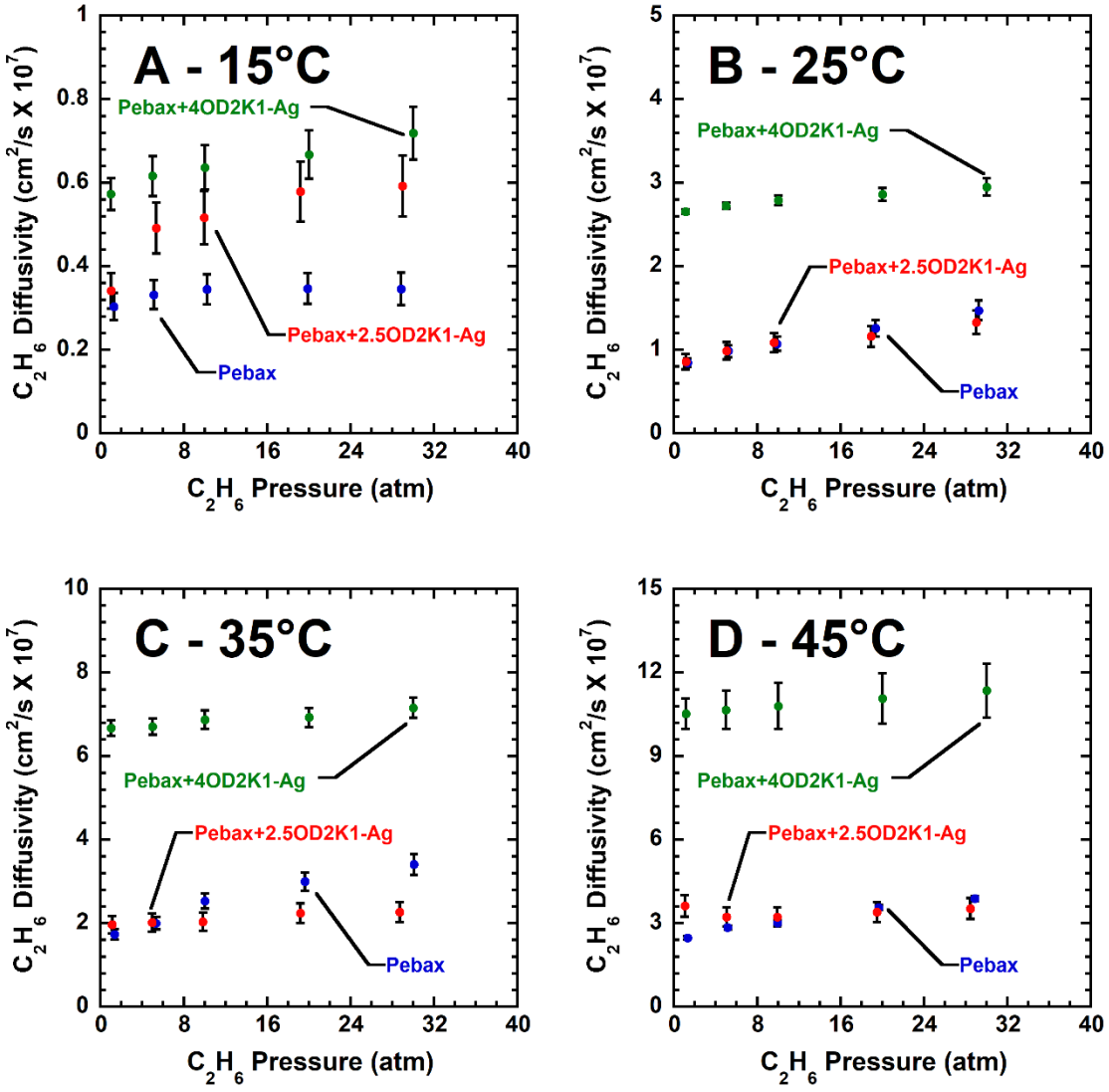

Figure B22: *Concentration averaged diffusivity coefficients of C_2H_6 at A), 15 ℃ B) 25 ℃, C) 35 ℃, and D) 45 ℃ in Pebax (blue), Pebax+2.5OD2K1-Ag (red), and Pebax+4OD2K1-Ag (green) in* $\frac{cm^2}{s}(10^7)$ *as a function of pure gas pressure in atm. Error bars were found via linear error propagation and values were calculated assuming solution diffusion from permeability and solubility data.*

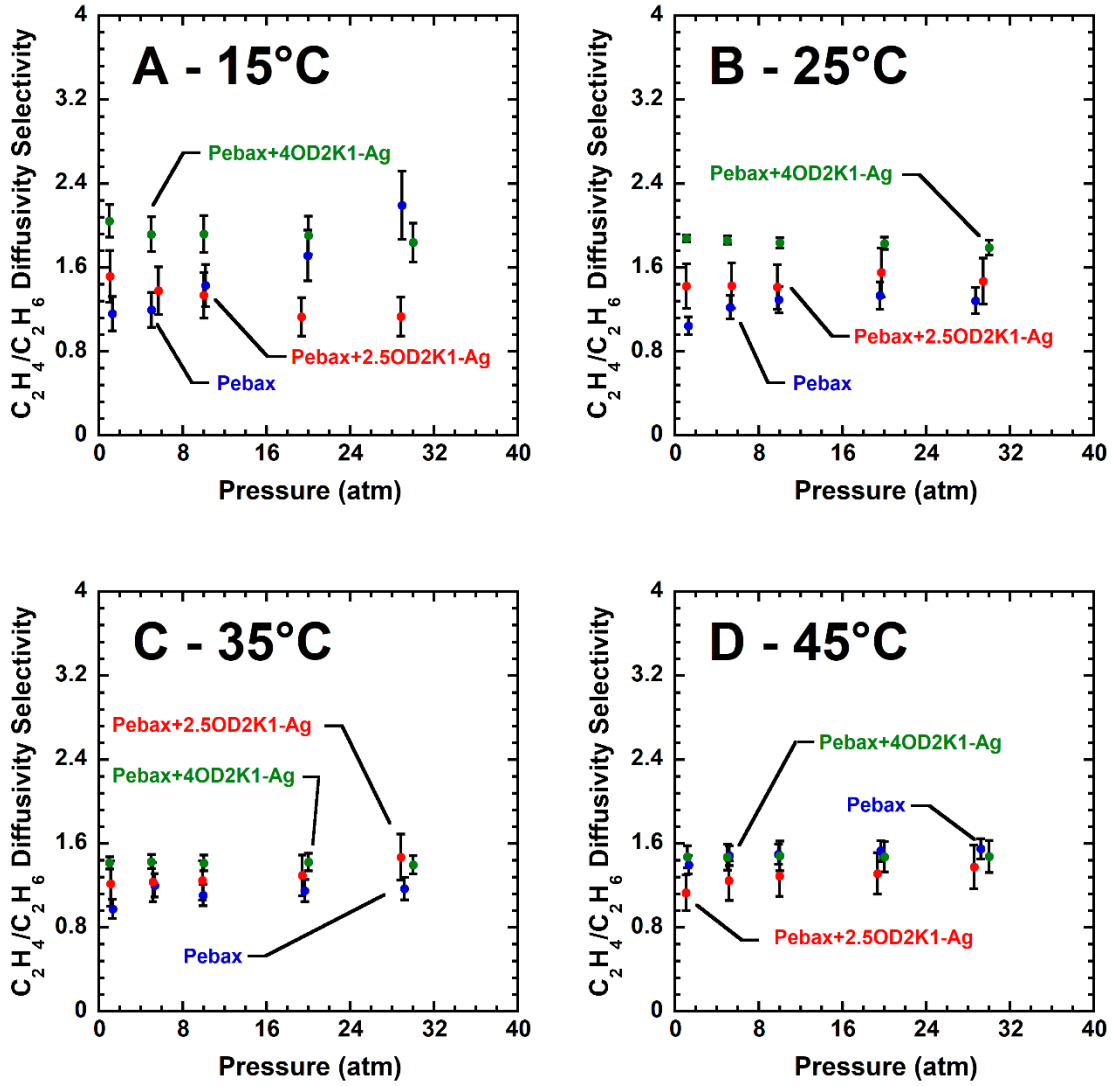

Figure B23: *Pure gas C_2H_4/C_2H_6 diffusivity selectivity at A), 15 ℃ B) 25 ℃, C) 35 ℃, and D) 45 ℃ in Pebax (blue), Pebax+2.5OD2K1-Ag (red), and Pebax+4OD2K1-Ag (green) as a function of pure gas pressure, ranging up to 30 atm. Error bars were calculated via linear error propagation.*

B14. Summary of Transport Results at 35 °C and 1 atm

A summary of data shown in Figure B8-Figure B23 is reported in Table B5 and Table B6 for data collected at 35 ºC and 1 atm. Table B5 includes the CO_2 permeation, sorption, and diffusion coefficients for Pebax, Pebax+2.5OD2K1-Ag, and Pebax+4OD2K1-Ag, along with selectivity data. CO_2 permeability and CO_2/CH_4 overall selectivity are also reported in this table for Pebax+2.5OD2K2-Ag and Pebax+4OD2K2-Ag.

Table B5: *Summary of Transport Data. Listed in different materials is the CO_2 permeability (Barrer), sorption (cm^3(STP)/cm^3(pol)/atm), and diffusivity ($\times 10^7$ cm^2/s), as well as the overall CO_2/CH_4 selectivity, sorption selectivity, and diffusivity selectivity at 1 atm and 35 ºC.*

Sample	CO_2 permeability (Barrer)	CO_2/CH_4 selectivity	CO_2 solubility (cm^3[STP]/cm^3[pol]/atm)	CO_2/CH_4 solubility selectivity	CO_2 diffusivity $\times 10^7$ (cm^2/s)	CO_2/CH_4 diffusivity selectivity
Neat Pebax	128.4 ± 9.7	14.6 ± 1.6	1.11 ± 0.01	4.85 ± 0.05	8.7 ± 0.7	3.0 ± 0.3
Pebax+2.5OD2K1-Ag	180.9 ± 19.0	21.8 ± 3.3	1.14 ± 0.01	6.02 ± 0.12	12.0 ± 1.3	3.6 ± 0.5
Pebax+4OD2K1-Ag	257.1 ± 29.4	13.7 ± 3.8	1.17 ± 0.02	5.07 ± 0.08	16.7 ± 3.8	2.7 ± 0.8
Pebax+2.5OD2K2-Ag	133.0 ± 7.2	17.3 ± 1.9	---	---	---	---
Pebax+4OD2K2-Ag	145.0 ± 8.2	20.2 ± 2.3	---	---	---	---

Table B6 includes the C_2H_4 permeation, sorption, and diffusion coefficients for Pebax, Pebax+2.5OD2K1-Ag, and Pebax+4OD2K1-Ag, along with selectivity data. C_2H_4 permeability and C_2H_4/C_2H_6 overall selectivity are also reported in this table for Pebax+2.5OD2K2-Ag and Pebax+4OD2K2-Ag.

Table B6: *Summary of Transport Data. Listed in different materials is the C_2H_4 permeability (Barrer), sorption (cm^3(STP)/cm^3(pol)/atm), and diffusivity ($\times 10^7$ cm^2/s), as well as the overall C_2H_4/C_2H_6 selectivity, sorption selectivity, and diffusivity selectivity at 1 atm and 35 ºC.*

Sample	C_2H_4 permeability (Barrer)	C_2H_4/C_2H_6 selectivity	C_2H_4 solubility (cm^3[STP]/cm^3[pol]/atm)	C_2H_4/C_2H_6 solubility selectivity	C_2H_4 diffusivity $\times 10^7$ (cm^2/s)	C_2H_4/C_2H_6 diffusivity selectivity

Neat Pebax	13.5 ± 0.75	1.09 ± 0.1	0.61 ± 0.01	1.12 ± 0.01	1.7 ± 0.1	1.0 ± 0.1
Pebax+2.5OD2K1-Ag	21.3 ± 2.98	1.50 ± 0.3	0.67 ± 0.01	1.23 ± 0.03	2.4 ± 0.3	1.2 ± 0.2
Pebax+4OD2K1-Ag	90.7 ± 2.5	1.73 ± 0.1	0.73 ± 0.01	1.23 ± 0.02	9.4 ± 0.3	1.4 ± 0.1
Pebax+2.5OD2K2-Ag	33.5 ± 1.0	1.70 ± 0.1	---	---	---	---
Pebax+4OD2K2-Ag	39.4 ± 1.1	1.96 ± 0.1	---	---	---	---

B15. Transport Dependence on Temperature

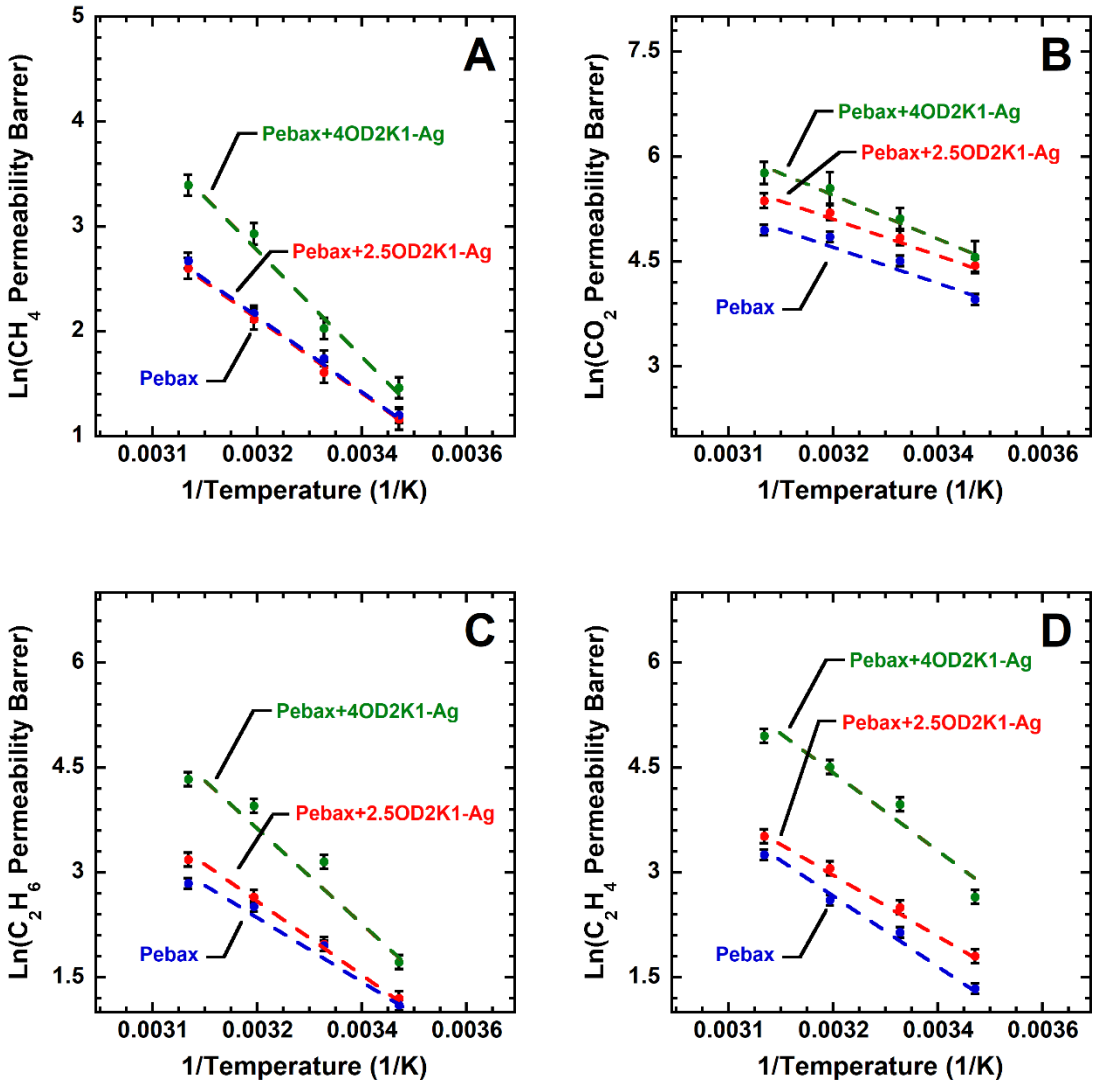

Figure B24: *Natural logarithm of permeability at 1 atm of A) CH_4, B) CO_2, C) C_2H_6, and D) C_2H_4 in Pebax (blue), Pebax+2.5OD2K1-Ag (red), and Pebax+4OD2K1-Ag (green) as a function of reciprocal temperature (1/K). The linear best fit lines for each sample in plots A-D are shown. The slope is proportional to the activation energy of permeation. Uncertainty values were calculated through linear error propagation.*

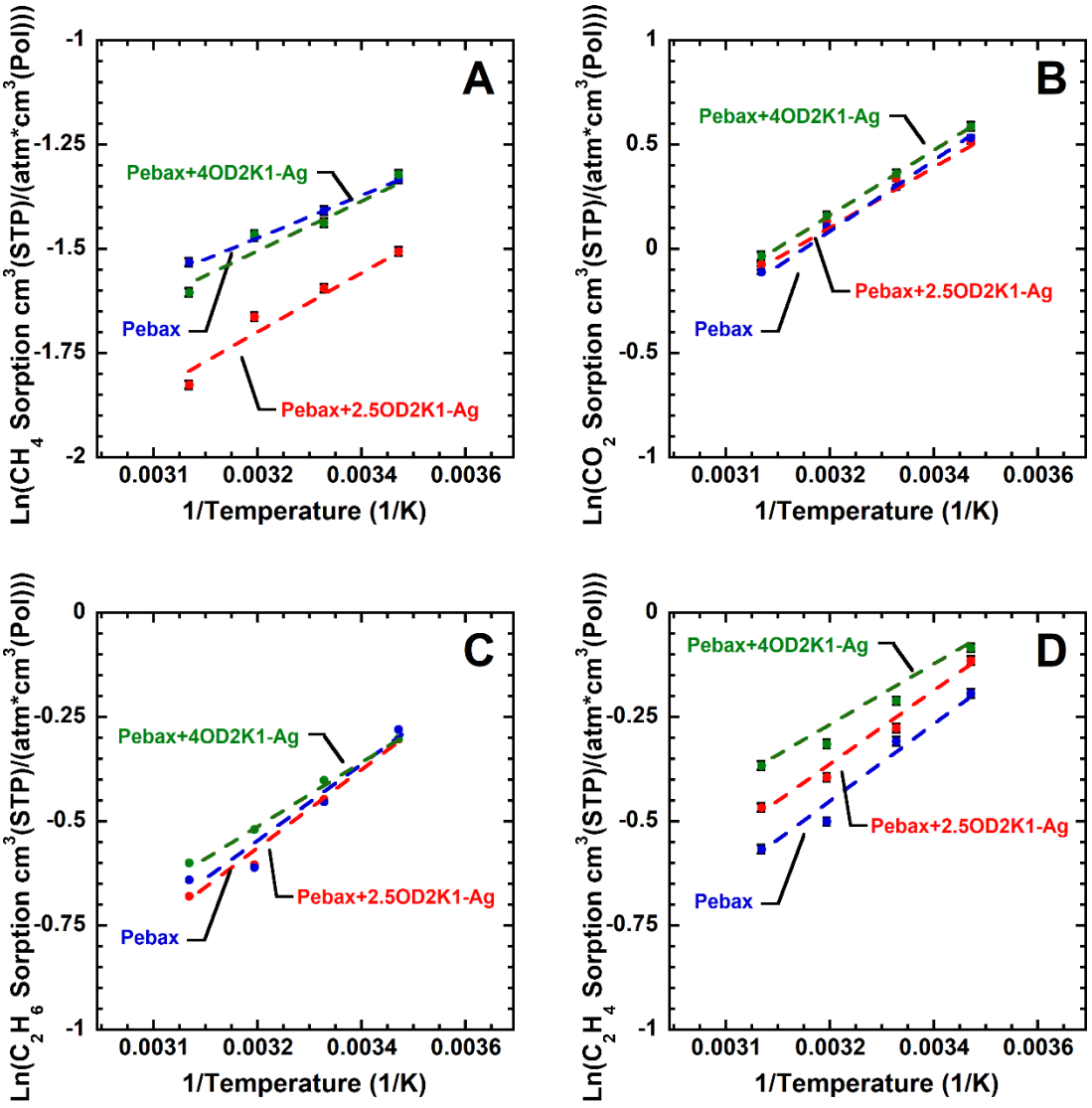

Figure B25: *Natural logarithm of Sorption at 1 atm of A) CH_4, B) CO_2, C) C_2H_6, and D) C_2H_4 in Pebax (blue), Pebax+2.5OD2K1-Ag (red), and Pebax+4OD2K1-Ag (green) as a function of reciprocal temperature (1/K). The linear best fit lines for each sample in plots A-D are shown. The slope is proportional to the enthalpy of sorption. Uncertainty values were calculated through linear error propagation.*

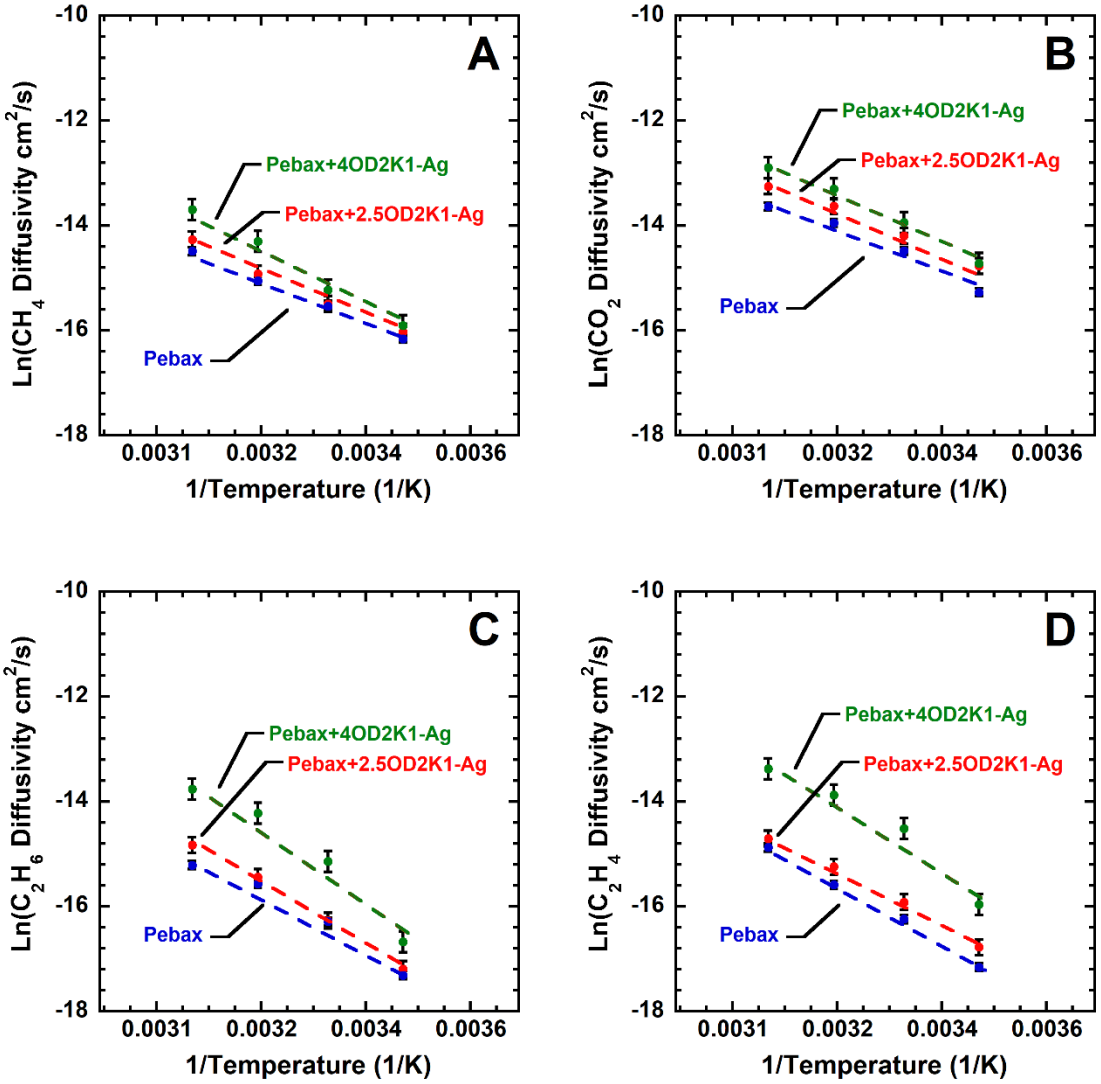

Figure B26: *Natural logarithm of diffusivity at 1 atm of A) CH_4, B) CO_2, C) C_2H_6, and D) C_2H_4 in Pebax (blue), Pebax+2.5OD2K1-Ag (red), and Pebax+4OD2K1-Ag (green) as a function of reciprocal temperature (1/K). The linear best fit lines for each sample in plots A-D are shown. The slope is proportional to the enthalpy of sorption. Uncertainty values were calculated through linear error propagation.*

B16. Energetics of Transport: Correlations and Assumptions

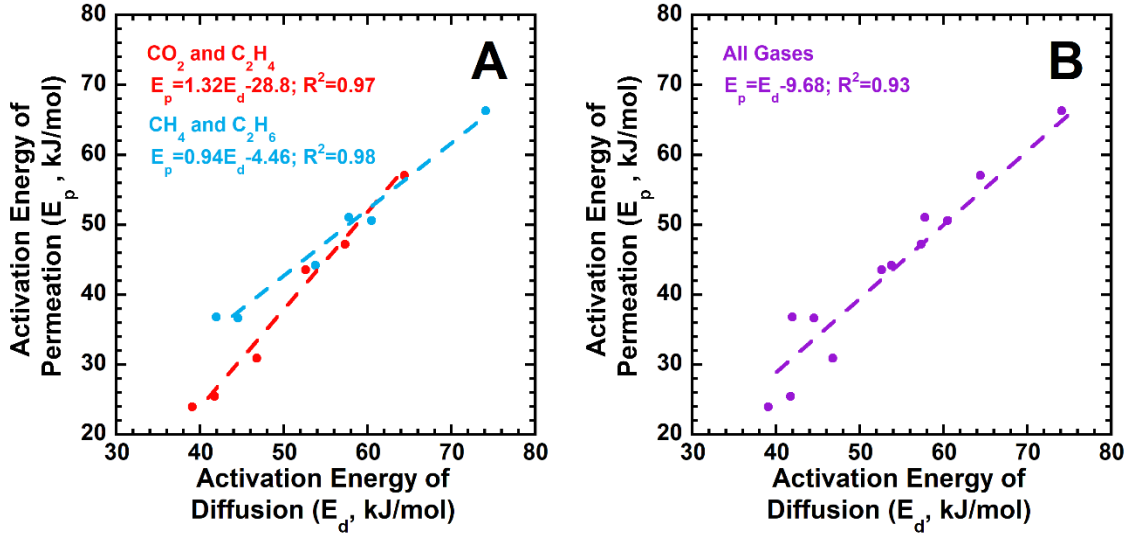

Figure B27: *A) Activation energy of permeation for facilitated gases, i.e., CO_2 and C_2H_4 (red), and non-facilitated gases, i.e., CH_4 and C_2H_6 (blue) in Pebax, Pebax+2.5OD2K1-Ag, and Pebax+4OD2K1-Ag. These activation energies of permeation are plotted as a function of the corresponding activation energies of diffusion. B) Activation energy of permeation for all gases (CO_2, CH_4, C_2H_4, and C_2H_6) as a function of the activation energy of diffusion.*

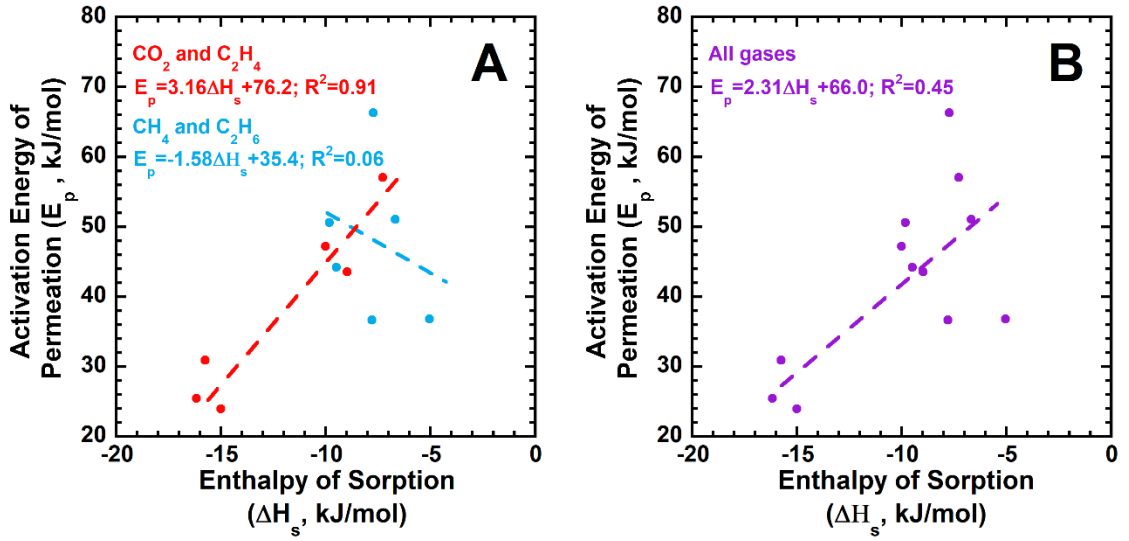

Figure B28: *A) Activation energy of permeation for facilitated gases, i.e., CO_2 and C_2H_4 (red), and non-facilitated gases, i.e., CH_4 and C_2H_6 (blue) in Pebax, Pebax+2.5OD2K1-Ag, and Pebax+4OD2K1-Ag. These activation energies of permeation are plotted as a function of the corresponding enthalpy of sorption. B) Activation energy of permeation for all gases (CO_2, CH_4, C_2H_4, and C_2H_6) as a function of the enthalpy of sorption.*

In order to separate the diffusivity selectivity into its entropic and energetic components, the average jump length in the diffusion medium, i.e., λ, was assumed to be the same for each gas used in this study (CO_2, CH_4, C_2H_4, and C_2H_6). Using the activation energy of diffusion (E_d), λ can be approximated using the Meares' model[55]:

$$E_d = \frac{\pi}{4}\lambda N_A \delta^2 d^2 \qquad \text{(Eq. B7)}$$

Wherein, δ is the solubility parameter, d is the gas diameter, and N_A is Avogadro's number. Because the solubility parameter for each membrane in this work was not determined, the solubility parameter of neat Pebax (22 $MPa^{0.5}$) was used from literature for each sample. The results can be found in Table B7.

Table B7: *Average jump length of CH_4, CO_2, C_2H_4, and C_2H_6 in Pebax, Pebax+2.5OD2K1-Ag, and Pebax+4OD2K1-Ag. Error bars were calculated using standard error of regression and linear error propagation.*

sample	CH_4 Jump Length (nm)	CO_2 Jump Length (nm)	C_2H_4 Jump Length (nm)	C_2H_6 Jump Length (nm)
Pebax	1.27 ± 0.03	1.67 ± 0.20	1.45 ± 0.05	1.19 ± 0.15
Pebax+2.5OD2K1-Ag	1.35 ± 0.07	1.57 ± 0.07	1.33 ± 0.07	1.34 ± 0.07
Pebax+4OD2K1-Ag	1.75 ± 0.10	1.87 ± 0.14	1.63 ± 0.27	1.64 ± 0.25

From Table B7, λ ranges from 1.27 to 1.87 nm between every gas species in Pebax, Pebax+2.5OD2K1-Ag, and Pebax+4OD2K1-Ag. Recall that E_d is based on the slope of the linear regression of the natural logarithm of the gas diffusion coefficient, as a function of reciprocal temperature. Based on this fact, coupled from Eq. B7 and Eq. 23 from Chapter 3, the assumption that λ is intendent of gas type for these materials, will only affect the entropic contribution to diffusivity selectivity. That is, the diffusivity selectivity entropic component will change for the CO_2/CH_4 and C_2H_4/C_2H_6 gas pairs by a factor of $\left(\frac{\lambda_{CO_2}}{\lambda_{CH_4}}\right)^2$ and $\left(\frac{\lambda_{C_2H_4}}{\lambda_{C_2H_6}}\right)^2$, respectively. However,

given the additional assumptions that go into calculating λ , as well as the small range in which they seem to vary, λ can be considered as a constant.

B17. Differential Scanning Calorimetry (DSC)

DSC was used to evaluate the sub-ambient glass transition temperature of OD2K1, OD2K2, Pebax, Pebax+2.5OD2K1-Ag, Pebax+4OD2K1-Ag, Pebax+2.5OD2K2-Ag, and Pebax+4OD2K2-Ag using a TA Instruments DSC 2500. 5-10 mg of sample were heated in hermetically sealed aluminum pan. To allow for sorbed gases and moisture to escape, the pan was pierced on its lid using a tac. Each sample was heated at a rate of 10 °C/min until 40 °C and held for 5 minutes to held evolved any sorbed species. Then, the samples were cooled from 40 °C until -80 °C at 10 °C/min, before being reheated to 40 °C at 10 °C/min. This cycle was repeated twice under a nitrogen gas flow.

B18. Wide and small angle X-ray spectroscopy (WAXS/SAXS)

Wide-angle X-ray scattering (WAXS) and small-angle X-ray scattering (SAXS) transmission measurements were performed on Pebax, Pebax+2.5OD2K1-Ag, Pebax+4OD2K1-Ag, Pebax+2.5OD2K2-Ag, and Pebax+4OD2K2-Ag using a Xenocs XEUSS 3.0 with Cu-K-alpha (1.54 Å). The apparatus was operated at 50 kV and 0.6 mA with a q-range of 0.0036 to 3 $Å^{-1}$ and 0.00028 to 0.5 $Å^{-1}$ with an exposure time of 60 and 120 mins for WAXS and SAXS respectively. To calculate the fractional crystallinity, a program was used to fit a baseline followed by a Gaussian curve to each peak and the amorphous halo. To avoid overfitting of the data, the WAXS peak between 2θ = 5 to 2θ = 35 was deconvoluted into an amorphous curve, and 3 additional, more crystalline, peaks. That is the total peak intensity ($I_{total}(q)$) is broken up as follows,

$$I_{total}(q) = I_{amorphous}(q) + I_1(q) + I_2(q) + I_3(q) \qquad \text{(Eq. B8)}$$

Where each of the curves on the right hand-hand side of equation S7 are represented through Gaussian curves, i.e.,

$$I_x(q) = a_x * \exp\left(-\left(\frac{1}{2} * \frac{(q-b_x)}{c_x}\right)^2\right) \qquad \text{(Eq. B9)}$$

Where x represents either the amorphous, 1, 2, or 3, peak fitting. These curves are summed to create the total peak, $I_{total}(q)$, which is fit against the experimental WAXS data. As an example of this fitting, the WAXS data of Pebax is shown below in Figure B29A. Crystallinity is then calculated as follows:

$$\%\, Crystallinty = 100 * \left(1 - \frac{A_{amorphous}}{A_{amorphous}+A_1+A_2+A_3}\right) \qquad \text{(Eq. B10)}$$

Where $A_{amorphous}, A_1, A_2, and\ A_3$ refer to the area under the curves for the amorphous peak, peak 1, peak 2, and peak 3, respectively.

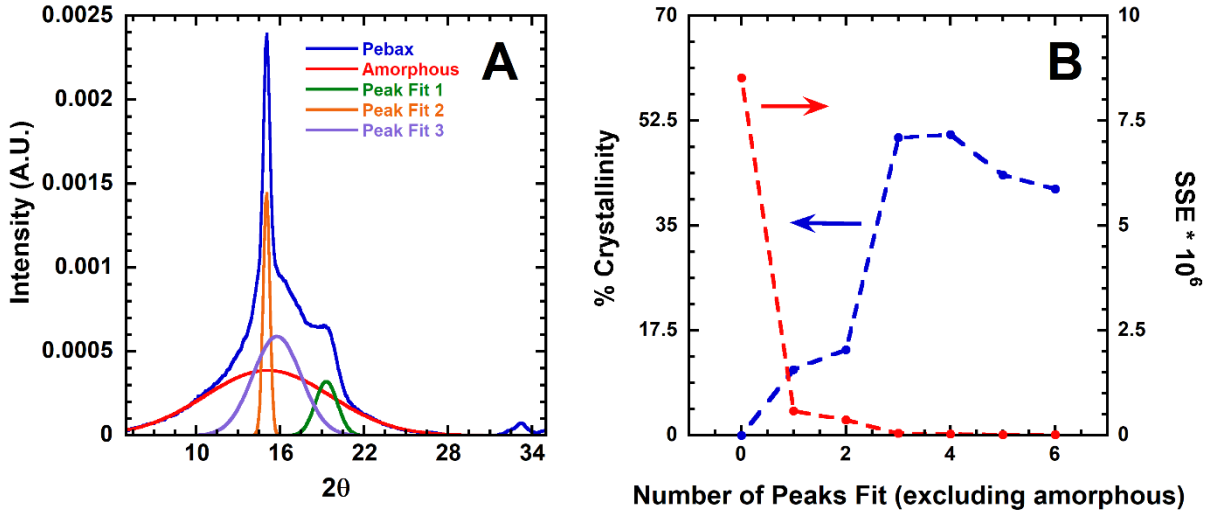

Figure B29: *A) Fitting of the amorphous peak and 3 peak deconvolution of wide-angle x-ray scattering intensity (WAXS) for Pebax and B) The calculated crystallinity (blue) in Pebax as a function of the number of peaks used to deconvolute the WAXS data, as well as the standard sum error of the fitting as a function of number of peaks used. The number of peaks exclude the amorphous peak being fit, i.e., 0 peaks would mean that only an amorphous halo was fit.*

Additionally, it should be discussed that the number of peaks being used in the WAXS fitting can alter the crystallinity values that are calculated. Thus, to enhance the accuracy of this discussion, the % Crystallinity in Pebax as a function of the number of peaks being used in the fitting it shown in Figure B29B. The sum of square error (SSE) between the model $\left(I(q_{total})\right)$ and the experimental intensity data is also shown in this figure. The number of peaks chosen was 3. After 3 peaks are used in the case of these materials, there are diminished returned in the fitting, as evident by the SSE. Thus, at small numbers of peaks, the model does not accurately fit the experimental data, and at high number of peaks, issues in the number of fitted parameters and diminished returns can lead to overfitting of the data. The results of the polymer crystallinity for each sample are shown in Table B8.

Table B8: *Summary of the amorphous and crystalline fraction in each material, as well as q value (q_{max}) and d-spacing corresponding to the peak maximum in SAXS.*

Sample	Amorphous (%)	Crystallinity (%)	q_{max} (Å^{-1})	d-spacing (Å)
Neat Pebax	50.31	49.69	0.0620	101.4
Pebax+2.5OD2K1-Ag	53.51	46.49	0.0603	104.2
Pebax+4OD2K1-Ag	52.99	47.01	0.0592	106.2
Pebax+2.5OD2K2-Ag	50.56	49.44	0.0558	112.5
Pebax+4OD2K2-Ag	48.52	51.48	0.0570	110.3

The d-spacing (d) was calculated using the SAXS information, from using the q value that corresponds to the peak maximum in SAXS (q_{max}) (cf. Table B8).

$$d = \frac{2\pi}{q_{max}} \qquad \text{(Eq. B11)}$$

Grazed incident wide-angle scattering (GIWAXS) and small-angle x-ray scattering (GISAXS) were performed on OD2K1 and OD2K2 using a Xenocs XEUSS 3.0 with Cu-K-alpha (1.54 Å). The apparatus was operated at 50 kV and 0.6 mA with a q-range of 0.002 to 3.15 Å^{-1} and 0.00025 to 0.55 Å^{-1} with an exposure time of 90 minutes for WAXS and SAXS respectively. The incident angle was set to 18°.

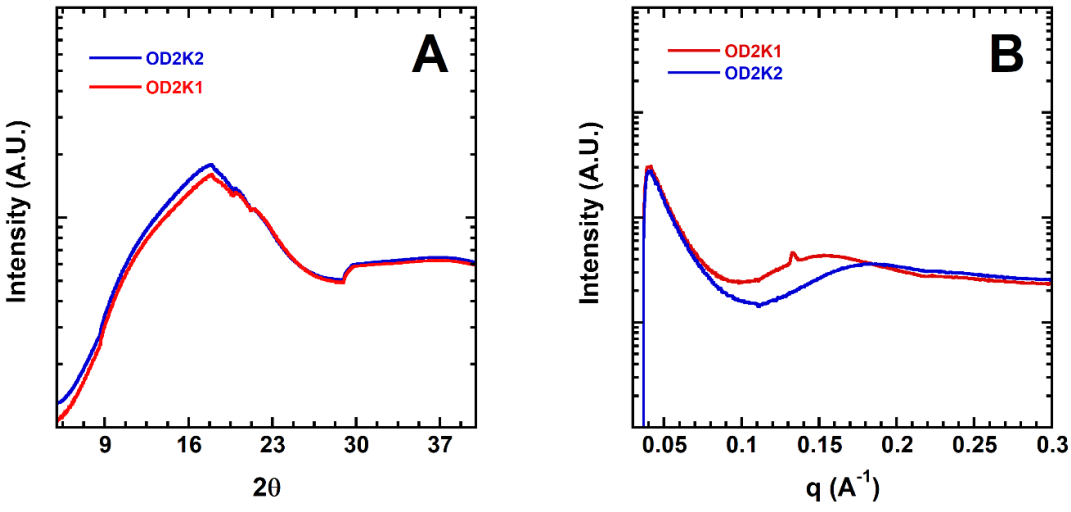

Figure B30: *A) Grazed incident wide-angle x-ray scattering intensity and B) Grazed incident small-angle x-ray scattering intensity for OD2K1 (red) and OD2K2 (blue).*

B19. Hydrogen Stability Test

A summary of data for CO_2/CH_4 and C_2H_4/C_2H_6 separations in Pebax, Pebax+2.5OD2K1-Ag, and Pebax+2.5OD2K2-Ag after 1 week being exposed of H_2 gas at 1.4 atm, as well as relative changes in gas permeability/selectivity is reported in Table B9 and Table B10.

Table B9: *Summary of Transport Data at 1 atm and 35 ºC after exposure to 1.4 atm H_2 gas for 7 days. Listed in different materials is the CO_2 permeability (Barrer) and overall CO_2/CH_4, as well as the % change in both these parameters, relative to the untreated samples.*

sample	CO_2 permeability Post-H_2 (Barrer)	CO_2/CH_4 Selectivity	% Change in CO_2 Permeability	% Change in CO_2/CH_4 Selectivity
Pebax	112.4 ± 2.8	15.2 ± 0.5	-7.8 ± 7.3	4.1 ± 11.9
Pebax+2.5OD2K1-Ag	157.0 ± 2.0	19.2 ± 0.2	-13.2 ± 9.2	-13.4 ± 13.4
Pebax+2.5OD2K2-Ag	128.3 ± 4.3	15.9 ± 0.8	-8.1 ± 5.9	-9.2 ± 6.7

Table B10: *Summary of Transport Data at 1 atm and 35 ºC after exposure to 1.4 atm H_2 gas for 7 days. Listed in different materials is the C_2H_4 permeability (Barrer) and overall C_2H_4/C_2H_6, as well as the % change in both these parameters, relative to the untreated samples.*

sample	C_2H_4 permeability Post-H_2 (Barrer)	C_2H_4/C_2H_6 Selectivity	% Change in C_2H_4 Permeability	% Change in C_2H_4/C_2H_6 Selectivity
Pebax	13.9 ± 0.4	1.16 ± 0.04	2.0 ± 6.2	6.3 ± 8.7
Pebax+2.5OD2K1-Ag	19.3 ± 0.3	1.41 ± 0.02	-9.3 ± 9.6	-9.5 ± 12.7
Pebax+2.5OD2K2-Ag	24.4 ± 0.8	1.31 ± 0.06	-27.2 ± 3.3	-29.7 ± 4.9

B20. Mixed Gas Permeation Measurements

Mixed gas CO_2/CH_4 and C_2H_4/C_2H_6 permeation was tested in Pebax, Pebax+2.5OD2K-1Ag, and Pebax+2.5OD2K2-Ag using a constant volume, variable pressure apparatus that is automated using a control system purchased from Maxwell Robotics. Gas compositions for both the feed and permeate streams were analyzed using a Shimzadzu GC 2030 with a Fast Fuel Analyzer setup. C_2H_4/C_2H_6 mixtures were tested using a molar feed composition of either 50/50 and 20/80%, whilst CO_2/CH_4 was tested at a molar composition of 50/50%, both targeting CO_2 and C_2H_4 partial pressures ~1 atm to make direct comparisons to the pure gas data. Temperature for each experiment was maintained at 35 °C. Similar to pure gas measurements, the membrane was situated between two volumes, using a 47 mm HP filter holder. Feed mixtures were generated at a desired composition using a Bronkhorst mass flow controller set between 100 – 400 SCCM, which swept across the upstream side of the membrane to limit the stage cut below 1%, reducing effects of concentration polarization. Prior to measurements, vacuum was pulled on the entire system overnight to remove any humidity or other sorbed species. Pressure was charged to the upstream side of the membrane and measured using a PX-409-USHB series Omega pressure transducer (0-1000 psi). Then, gas was allowed to permeate through the membrane to the downstream volume, where the increase in pressure with time was measured using a highly sensitive MKS Baratron pressure transducer (0-10 torr). The permeability of each gas within the mixture (P_i, in units of Barrers, where i refers to the gas component) was calculated as follows:

$$P_i = \frac{lV_{down}y_{i,down}}{ART(y_{i,up}P_{up} - y_{i,down}P_{down})}\left(\frac{dp}{dt}_{down} - \frac{dp}{dt}_{leak}\right) \quad \text{(Eq. B12)}$$

where l is the membrane thickness, A is the membrane area available to gas transport, R is the universal gas constant, T is the absolute temperature, P_{up} is the average upstream pressure, P_{down} is the average downstream pressure, $\frac{dp}{dt}_{down}$ is the asymptotic rate of pressure increase in the downstream ballast, and $\frac{dp}{dt}_{leak}$ is the rate of pressure increase in the downstream volume whilst the charge pressure is 0. The concentration of species i was determined from the average of two separate GC injections. The relative peak areas of each component are then converted into molar fractions using calibration curves, where $y_{i,down}$ and $y_{i,up}$ are the molar fraction of species i on the upstream and downstream side of the membrane, respectively. Membranes were glued with epoxy resin on a brass ring, and the passage area was accurately measured via the ImageJ software. Filter paper was used as a backing to reduce the risk of sample breakage. A summary of the data for each sample can be found in Table B11-Table B13.

Table B11: *Summary of transport in mixed gas conditions, i.e., ~50% mol CH_4 and 50% mol CO_2, at ~2.2 atm and 35 ºC. Listed in different materials is the CO_2 partial pressure, CO_2 molar fraction, CO_2 permeability (Barrer), and the overall CO_2/CH_4 selectivity.*

Sample	CO_2 Partial Pressure (atm)	CO_2 Molar Fraction	CO_2 permeability (Barrer)	CO_2/CH_4 selectivity
Neat Pebax	1.21	0.56	124.0 ± 3.5	14.5 ± 0.98
Pebax+2.5OD2K1-Ag	1.22	0.55	172.0 ± 6.4	16.5 ± 0.69
Pebax+2.5OD2K2-Ag	1.14	0.56	129.1 ± 3.8	16.0 ± 1.3

Table B12: *Summary of transport in mixed gas conditions, i.e., ~50% mol C_2H_4 and 50% mol C2H6, at ~2.2 atm and 35 ºC. Listed in different materials is the C_2H_4 partial pressure, C_2H_4 molar fraction, C_2H_4 permeability (Barrer), and the overall C_2H_4/C_2H_6 selectivity.*

Sample	C_2H_4 Partial Pressure (atm)	C_2H_4 Molar Fraction	C_2H_4 permeability (Barrer)	C_2H_4/C_2H_6 selectivity
Neat Pebax	1.08	0.49	13.0 ± 0.3	1.3 ± 0.1
Pebax+2.5OD2K1-Ag	1.07	0.51	18.9 ± 0.4	1.60 ± 0.1

Pebax+2.5OD2K2-Ag	1.10	0.52	24.7 ± 0.6	1.68 ± 0.1

Table B13: *Summary of transport in mixed gas conditions, i.e., ~20% mol C_2H_4 and 80% mol C2H6, at ~5.7 atm and 35 ºC. Listed in different materials is the C_2H_4 partial pressure, C_2H_4 molar fraction, C_2H_4 permeability (Barrer), and the overall C_2H_4/C_2H_6 selectivity.*

Sample	C_2H_4 Partial Pressure (atm)	C_2H_4 Molar Fraction	C_2H_4 permeability (Barrer)	C_2H_4/C_2H_6 selectivity
Neat Pebax	1.18	0.20	10.6 ± 0.2	1.3 ± 0.1
Pebax+2.5OD2K1-Ag	1.10	0.20	15.7 ± 0.3	1.64 ± 0.1
Pebax+2.5OD2K2-Ag	1.12	0.21	22.1 ± 0.5	1.75 ± 0.1

Appendix C

C1. Materials

Polyvinylpyrrolidone (PVP, ThermoFisher Scientific) was used as baseline material. 4,4-Oxydiphthalic anhydride (97 wt%, Sigma-Aldrich) and a D-series Jeffamine (Mw = 4000 g/mol, Fisher Scientific) were used to synthesize, via the polycondensation reaction, a poly(amic-acid) polymer denoted as OD4K (cf. Section C2),[59] which served as test material to validate the experimental and theoretical methodologies proposed in this study. PTMSP was purchased from Gelest Inc. (Morrisville, USA)

For the synthesis of PIM-1, tetrafluoroterephthalonitrile (TFTPN, 98%) was purchased from TCI Chemicals, 5,5',6,6'-Tetrahydroxy-3,3,3',3'-tetramethyl-1,1'-spirobisindane (TTSBI, 97%) was purchased from Alfa Aesar, potassium carbonate (K_2CO_3) was purchased from Sigma Aldrich, and N,N-dimethylformamide (DMF, anhydrous) was purchased from Supelco. TFTPN and TTSBI were dried at 30 °C and 110 °C, respectively, in a vacuum oven overnight before use without any further purification. The amounts of TFTPN and TTSBI used in the synthesis of PIM-1 were adjusted for the listed purity. Potassium carbonate was ground in a mortar and pestle, sieved through a 220 mesh (0.065 mm) Titan brand stainless steel sieve, and dried at 110 °C in a vacuum oven overnight before use. For the final precipitation bath, acetone (99.5%) purchased from Fisher Chemical, and tetrahydrofuran (THF, HPLC, inhibitor free) purchased from Macron Fine Chemicals were used.

The following solvents were used throughout this study to experimentally determine the solubility parameter of PVP, OD4K, PTMSP, and PIM-1: chloroform ($CHCl_3$, 99.8%), dichloromethane (DCM , ≥99.8%), and cyclohexane (99.5%) were purchased from Sigma-Aldrich; octanoic acid (99%), butanol (99%), and 1,2-dichlorobenzene (>99%) were purchased from ThermoFisher

Scientific; acetic acid (99.85%), was purchased from Research Products International; toluene (HPLC, 99.8%) was purchased from Fisher Chemical; n-hexane (>95%) was purchased from Alfa Aesar; and the previously mentioned THF.

C2. Polymer Synthesis

OD4K, a polyamic acid, was synthesized through a nucleophilic substitution reaction between an amine group, located on a polyetheramine named Jeffamine, and an anhydride carbonyl carbon on 4,4-oxydiphthalic anhydride (ODPA) (cf. Figure C1). The reaction was performed under an inert nitrogen atmosphere using a 100 ml three-necked flask equipped with a mechanical stirrer. The flask was first charged with 30 ml of tetrahydrofuran (THF) and 15 mmol of Jeffamine and mixed until homogenous. Next, the solution was cooled to 0 ℃, using an ice bath, and 15 mmol of ODPA was added. After 10 minutes, the reaction flask was heated to 35 ℃ using a bath of white mineral oil and allowed to react for 30 minutes. Once complete, the newly formed OD4K polymer was precipitated in a methanol/water (10/90 vol%) mixture and subsequently washed using this mixture with a vacuum filtration flask. Finally, the washed OD4K was dried using a vacuum oven at room temperature for 24 hours before being stored in a chemical refrigerator at 4 ℃.

OD4K was selected as a test polymer as our Research Group is using it within a separate project, of which this short communication is part.

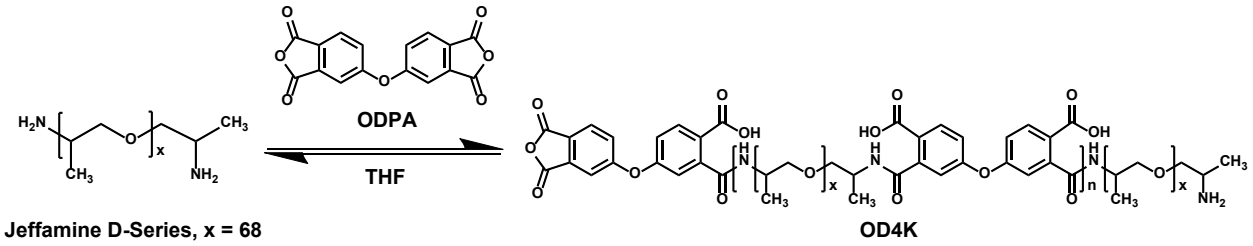

Figure C1: *Reaction between Jeffamine and ODPA for the synthesis of OD4K in THF. The resulting structure is shown, where x (= 68) denotes the number of repeating segments within each Jeffamine molecule and n denotes the number of repeating segments within the overall polymer (n ~ 9.93; M_n = 42,800 g/mol).*

PIM-1 was synthesized in house using a high-temperature polycondensation technique (cf. Figure C2). All glassware was dried at 130 °C in an oven overnight before use. A 250 ml 3-neck round bottom flask was equipped with a mechanical stirrer, reflux, addition funnel, and purge gas

inlets/outlets. 13.44 mmol of TFTPN, 13.43 mmol of TTSBI, and 27 ml of DMF were added under a 5 ml/second dry nitrogen purge. The monomers were gently stirred until they fully dissolved to form an orange-brown solution. The stir rate was then set to 200 rpm, and 40.52 mmol of K_2CO_3 was added using a powder funnel. Following this step, 14 ml of toluene was immediately added using an addition funnel and the flask was submerged in a pre-heated oil bath at 160 °C. A bright yellow solution formed, and after 5 minutes, the viscosity increased. A further 9 ml of toluene was then added to dilute the solution and reduce the viscosity. After 30 minutes of stirring, another 18 ml of toluene was added, and the flask removed from the oil bath. The reaction mixture was precipitated into 500 ml of methanol to yield bright yellow fibers. The fibers were solvent exchanged with water to remove residual salts from the reaction. Specifically, the fibers were soaked in hot water (95°C) for 1 hour. The water in this bath was decanted off and changed, repeating the exchange process 3 times. The fibers were dried at 130 °C in a vacuum oven overnight. The resulting PIM-1 was then dissolved in 250 ml of chloroform and precipitated into a 1:1 (v:v) solution of acetone:THF to extract low-molecular weight residues. The solvents were decanted, and the resulting fibers were then soaked in a water bath at 95 °C, and the exchange process was repeated three additional times to further remove any residual salts. The fibers were then dried at 130 °C in a vacuum oven overnight to yield the finished product (86.4% yield).

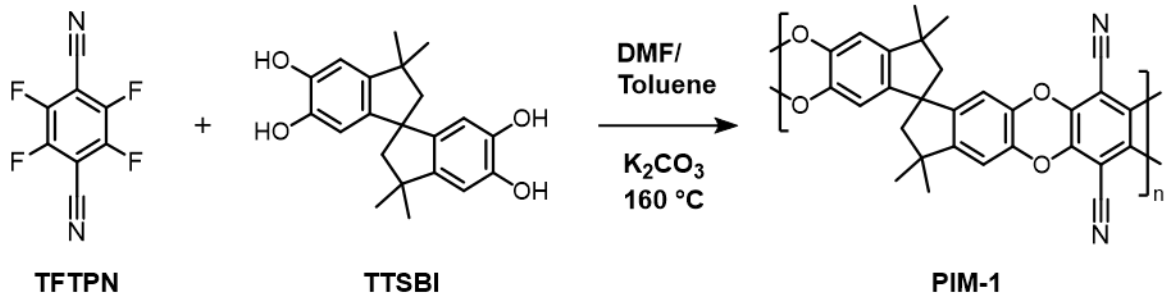

Figure C2: *Synthesis scheme for PIM-1.*

C3. Polymer Characterization

The physical properties of the polymers utilized in the experimental portion of this study are summarized in Table C1. A broad range of molecular weights, glass transition temperatures, and dispersities were observed across the polymers studied. The variability in these properties did not appear to affect the accuracy or applicability of the experimental techniques demonstrated in this work.

Table C1: *Physical properties of the polymers used in this study.*

Polymer	***Molecular Weight (kDa)***	***Dispersity, Đ***	***Glass Transition Temperature, T_g (°C)***
OD4K	*42.8*[a]	*5.56*	*-63*[b]
PVP	*53.2*[a]	*1.93*	*176*[b]
PTMSP	*56.4*[a]	*2.02*	*>250*[205]
PIM-1	*96.5*[a]	*1.59*	*>430*[211]

[a]*Number averaged molecular weight, as measured using gel permeation chromatography (GPC) in chloroform against polystyrene standards.*
[b]*Measured using dynamic scanning calorimetry with a scan rate of 10 K/min.*

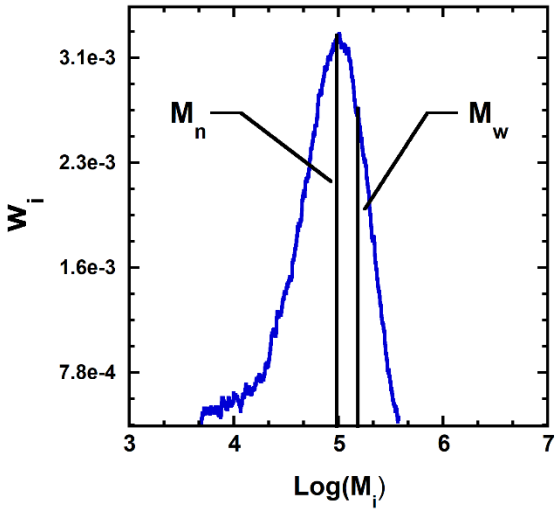

Figure C3: *Molecular weight distribution of the synthesized PIM-1 measured from GPC using polystyrene standards.*

Molecular weights of OD4K and PIM-1 were analyzed using a Waters™ 717 plus auto sampler with a 7.5 x 250 mm Agilent polypore column at a flowrate of 1 ml/min and at 40 ºC. The eluent

was detected using a Waters™ 490E UV-VIS multi-wavelength detector set to 298 nm. The weight-average molecular weight was found using equation:

$$M_n = \frac{\sum_{t_1}^{t_2} A_i M_i}{\sum_{t_1}^{t_2} A_i} \quad \text{(Eq.C1)}$$

$$\log(M_i) = \alpha t_i + \beta \quad \text{(Eq. C2)}$$

where t_i is the time, A_i is the absorption value at t_i, M_i is the molecular weight eluted at t_i, t_1 is the onset time of elution, t_2 is the elution end time, and M_n is the number average molecular weight. α/β are constants obtained from the linear regression of $\log(M_n)$ vs. t for polystyrene standards, whose weight ranged from 1 to 500 kDa. As an example, the molecular weight distribution for PIM-1 is shown in Figure S3.

As the solubility behavior of polymers may be influenced by their molecular weight/molecular weight distribution and the varying functionality of polymer chain ends, having an adequately high molecular weight with a relatively narrow molecular weight distribution may be an important factor in determining a representative solubility parameter. As can be seen in Figure S3, the molecular weight distribution of PIM-1 is fairly uniform and has comparable molecular weights (M_n = 96.5 kDa) and dispersity (Đ = 1.59) to those used in membrane literature.[212–214]

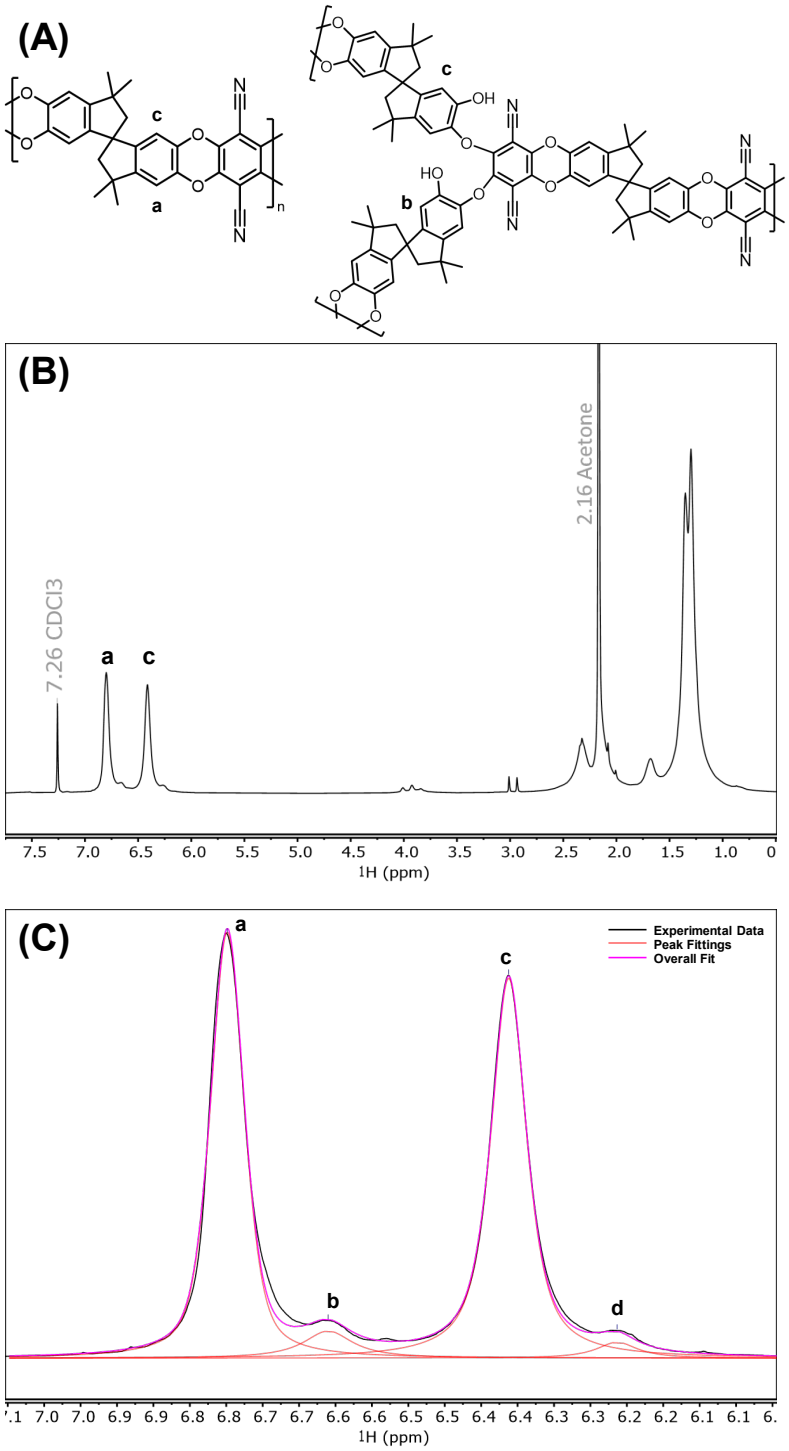

Figure C4: *(A) Linear and branched structures of PIM-1 with labels **a**, **b**, **c**, **d** corresponding to aromatic protons used in the branching analysis.[212] (B) NMR spectrum of the synthesized PIM-1, labeled with peak labels **a** and **c** corresponding to the aromatic protons in the linear subunit of PIM-1. (C) Closeup of the Lorentzian peak fitting used to analyze the degree of branching in PIM-1, where the shoulders **b** and **d** correspond to the protons in the branched subunit of PIM-1.*

^{1}H NMR of PIM-1 was performed on a Varian VNMRS 400 MHz NMR in deuterated chloroform (99.8%, Cambridge Isotope Laboratories) to confirm the successful synthesis and branching content of PIM-1. PIM-1 can incorporate branching due to substitution of two TTSBI monomers at one of the TFTPN monomers during polymerization. Figure C4A visualizes the linear and branched subunits present in PIM-1. The presence of this branching can lead to the formation of cross-linked networks. The branched subunits incorporate extra hydroxyl groups compared to the linear subunit, which can potentially affect the experimentally measured solubility parameter.[212] Figure C4B shows the ^{1}H NMR of the synthesized PIM-1, which exhibited the conventional peaks associated with PIM-1.[212,215] Figure C4C portrays the peak fittings used to deconvolute the branched residues, and the degree of branching was calculated according to the method reported by Yu et al.[212] The degree of branching, defined as the total percentage of subunits that exhibit branching, was calculated to be 15.4%. This degree of branching did not seem to affect the solubility in common solvents for PIM-1, such as chloroform or THF, and solutions of PIM-1 in chloroform could easily be filtered through 0.45 μm syringe filters for GPC analysis with no issue.

C4. Mangaraj Fitting Theory

Since a limited number of solvents was used for the experimental campaign, locating the position of the true maximum for the polymer hydrodynamic diameter as a function of the solvent solubility parameter may be challenging and lead to significant errors. The same issue arises when trying to locate the maximum intrinsic viscosity measured for each polymer. This one true maximum must be found since it corresponds most closely to the solubility parameter of the polymer. Therefore, the data obtained from both DLS and viscometry was linearized and shown in the form of a Mangaraj plot.[57,215] To do so, the following parameters, ϕ and ϕ', were calculated:

$$\phi(\delta) = \left(\frac{1}{V_{m,s}} \ln\left(\frac{\eta_{int,max}}{\eta_{int}}\right)\right)^{\frac{1}{2}} \quad \text{(Eq. C3)}$$

$$\phi'(\delta) = \left(\frac{1}{V_{m,s}} \ln\left(\frac{D_{h,max}^3}{D_h^3}\right)\right)^{\frac{1}{2}} \quad \text{(Eq. C4)}$$

where $V_{m,s}$ is the molar volume of the solvent being used, η_{int} is the polymer intrinsic viscosity, D_h is the polymer effective hydrodynamic diameter, $\eta_{int,max}$ is the fitted maximum intrinsic viscosity, and $D_{h,max}$ is the fitted maximum polymer effective hydrodynamic diameter. By plotting ϕ and ϕ' against δ, the solubility parameter of the polymer, δ_{pol}, is found from the x-intercept, based on a linear regression of these plots. $\eta_{int,max}$ and $D_{h,max}$ were varied to minimize the error between the fit and experimental data (cf. Section C5).

C5. Mangaraj Fitting Example

Using the data obtained from viscometry measurements of OD4K, as well as information regarding the solvent molar volume and solubility parameter (cf. Table C2), the Mangaraj plot can be created.

Table C2: *Solvents used in the intrinsic viscosity measurements of OD4K, and their molar volume, solubility parameter, and resulting OD4K intrinsic viscosity.*

Solvent Name	***Molar Volume (g/ml)***	***Solubility Parameter ($MPa^{0.5}$)***	***Intrinsic Viscosity (dL/g)***
Octanoic Acid	*158.6*	*17.5*	*0.132*
Toluene	*106.3*	*18*	*0.231*
Chloroform	*80.2*	*19*	*0.268*
Tetrahydrofuran	*81.3*	*19.4*	*0.185*
Acetone	*74.0*	*19.9*	*0.119*

ϕ, as shown from Eq. S3, is calculated as follows[57]:

$$\phi = \left(\frac{1}{V_m}\ln\left(\frac{\eta_{int,max}}{\eta_{int}}\right)\right)^{\frac{1}{2}} = K^{\frac{1}{2}}\delta_{pol} - K^{\frac{1}{2}}\delta \qquad \text{(Eq. C5)}$$

When plotting ϕ vs. δ, we can see that the above equation is linear, where $K^{0.5}$ is the slope. Thus, we can minimize the error in the linear regression of this curve by changing $\eta_{int,max}$. However, using this equation to linearize the data does not directly result in a straight line. Instead, a point of symmetry causes two linear regions that mirror each other, above and below the solubility parameter that corresponds to the $\eta_{int,max}$ (or $D_{h,max}$) (cf. Figure C5A).

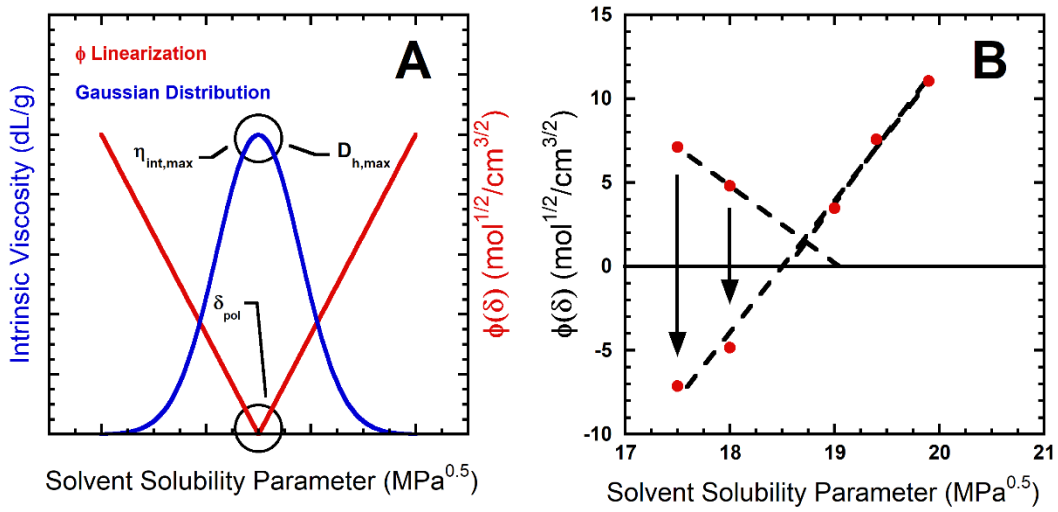

Figure C5: *A) Linearization of a Gaussian distribution that is a function of the solubility parameter. B) Point shifting to create a single linearization of the model (i.e., Mangaraj plot).*

To create the Mangaraj plot, a single linear regression is used, instead of the average of two individual regressions, to maximize the number of points in the fitting. To accomplish this, each ϕ value located at a solubility parameter lower than that of the polymer solubility parameter are given a front factor of -1 (cf. Figure C5B). δ_{pol} becomes the ratio between the negative of the intercept to the slope, from the overall linear regression. In the case of this example, $\delta_{pol} = 18.6 \pm 0.07$ MPa$^{0.5}$.

C6. Intrinsic Viscosity Measurements

The reduced viscosity (η_{red}) of PVP, OD4K, PTMSP, and PIM-1 were measured at concentrations between 0.3 and 1 g/dL in various solvents such as hexane (δ = 14.9 $MPa^{0.5}$), cyclohexane (δ = 16.8 $MPa^{0.5}$), toluene (δ = 18 $MPa^{0.5}$), $CHCl_3$ (δ = 19 $MPa^{0.5}$), THF (δ = 19.4 $MPa^{0.5}$), acetone (δ = 19.9 $MPa^{0.5}$), DCM (δ = 20.2 $MPa^{0.5}$), 1,2-dichlorobenzene (δ = 20.5 $MPa^{0.5}$), acetic acid (δ = 21.4 $MPa^{0.5}$), butanol (δ = 23.2 $MPa^{0.5}$), acetonitrile (δ = 24.4 $MPa^{0.5}$), ethanol (δ = 26.2 $MPa^{0.5}$) and methanol (δ = 29.6 $MPa^{0.5}$) using a 0C Ubbelohde viscometer purchased from Cannon Instruments, calibrated with a viscometer constant of 0.003309 cSt/s. Although toluene and hexane are not true solvents for PIM-1 and PTMSP, respectively, each polymer formed cloudy solutions capable of being measured by both viscometry and DLS. The reduced viscosity of OD4K in octanoic acid (δ = 17.5 $MPa^{0.5}$) was also measured using a 1C Ubbelohde viscometer from Cannon Instruments, calibrated with a viscometer constant of 0.03041 cSt/s. The reason for the specific use of the 1C size relates to octanoic acid's kinematic viscosity (5.2 mm^2/s), which was outside the calibrated range of the 0C device. Each concentration was tested five times at 25 °C to calculate the experimental uncertainty. The limit for the reduced viscosity at a concentration of 0 g/dL is defined as the intrinsic viscosity (η_{int})(cf. Eq. C6).

$$\eta_{int} = \lim_{c \to 0} \eta_{red} \equiv \lim_{c \to 0} \frac{(t - t_0)}{tc} \qquad \text{(Eq. C6)}$$

where c is the polymer concentration in g/dL, t_0 is the time that the pure solvent takes to flow between the viscometer ring indicators, and t is the time taken by each polymer solution to flow. The intrinsic viscosity of PVP, OD4K, PTMSP, and PIM-1 in each solvent was then plotted against the respective solvent's overall solubility parameter to elucidate any correlation.

C7. Dynamic Light Scattering Measurements (DLS)

DLS was used to measure the hydrodynamic diameter of PVP, OD4K, PTMSP, and PIM-1 in a variety of solvents at 25 °C, in an effort to find a relationship between the polymer size, while in solution, and the respective solvent's solubility parameter. Measurements were taken using a NanoBrook Series Particle Analyzer using backscattered detection. Each polymer was tested at least five times in various solvents such as hexane, cyclohexane, toluene, $CHCl_3$, THF, acetone, DCM, 1,2-dichlorbenzene, acetic acid, butanol, acetonitrile, ethanol, and methanol. The intensity averaged hydrodynamic diameter of PVP, OD4K, PTMSP, and PIM-1 was then plotted against each respective solvent's overall solubility parameter.

To ensure that single peaks were identifiable, and that the polymer was in a minimal unaggregated state, each sample was diluted and re-tested until unimodal distributions of light scattering data were obtainable. In most samples, the final concentration tested was between 0.2-0.5 mg/mL, with a corresponding count rate of ~100 kcps. Prior to testing, each sample was sonicated for 10 minutes and ran through a Whatman™ 0.45 μm PTFE syringe filter.

C8. Experimental and Computational Estimates of δ for PTMSP and polyimides

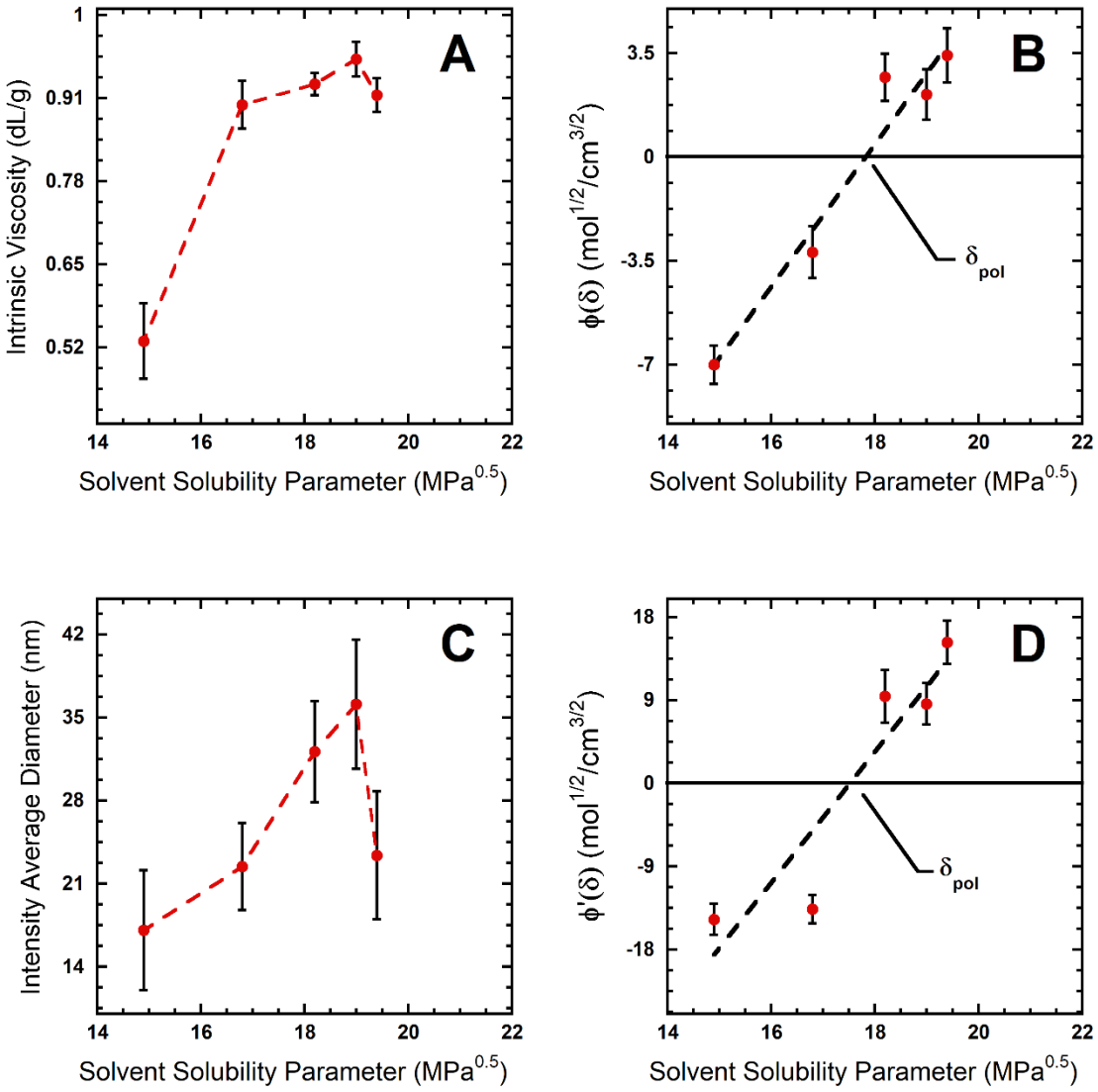

Figure C6: *A) Intrinsic viscosity of PTMSP as a function of the solvent solubility parameter at 25 °C (lines are drawn to guide the eye). B) Intrinsic viscosities are used to generate the Mangaraj plot, where ϕ is displayed as a function of the solvent solubility parameter for PTMSP. C) Intensity average diameter of PTMSP, obtained from DLS measurements, as a function of the solvent solubility parameter at 25 °C (lines are drawn to guide the eye). D) Intensity average diameters are used to generate the Mangaraj plot, where ϕ' is plotted as a function of solvent solubility parameter for PTMSP. The linear best fit line for both plots in B {2.4x – 42.8, R^2 = 0.95} and D {y = 7.1x – 124.3, R^2 = 0.85} are shown. Uncertainty values were calculated through repeated measurements (A and C) and linear error propagation (B and D).*

The solubility parameter of PTMSP was estimated and compared using both experimental (DLS and viscometry) and computational (group contribution and a neural network) methods. PTMSP exhibited the highest intrinsic viscosity (i.e., 0.97 dL/g) in $CHCl_3$ (19 $MPa^{0.5}$) (cf. Figure C6A). Upon fitting the data to Eq. S3 and plotting the Mangaraj plot (cf. Figure C6B), the resulting fitted maximum intrinsic viscosity ($\eta_{int,max}$) is 1 dL/g, whereas the solubility parameter of PTMSP is 17.8 ± 0.15 $MPa^{0.5}$. This value was then compared to the results obtained through DLS measurements. PTMSP experienced a maximum hydrodynamic diameter (i.e., 36.1 nm) in $CHCl_3$ (19 $Mpa^{0.5}$) (cf. Figure C6C). Using the Mangaraj fitting (cf. Figure C6D), the fitted maximum hydrodynamic diameter was 44.0 nm, with a corresponding solubility parameter of 17.5 ± 0.14 $MPa^{0.5}$. These results are in excellent agreement with each other and the experimental study by Ilyin et al., which reports for PTMSP a solubility parameter of 16.8 $MPa^{0.5}$.[216] Previous reports[217,218] of PTMSP's solubility parameter found using group contribution methods[106] range from 14.5-15.8 $MPa^{0.5}$, which, in light of the experimental results, appear to be slight underestimates. The excellent agreement of the experimental results on PTMSP suggest that the experimental methodology utilized herein may be readily extended to high FFV, high T_g materials (PTMSP: FFV = 38%, T_g > 250 °C)[205] without further modification.

Theoretical predictions of PTMSP's solubility parameter, using group contribution (14.24 ± 0.55 $MPa^{0.5}$) and the neural network (12.2 $MPa^{0.5}$), exhibit a negative deviation from experimental values. The primary reason for this, with respect to both the neural network and group contribution methods, was the lack of sufficient data to fit. Within the entire solubility parameter dataset available, the presence of silicon atoms occurred 20 times in total. Other functional groups, such as methylene (1767 occurrences) and chlorine (305 occurrences), are more prevalent in the data set used for fitting. Being present in a more diverse set of chemicals allows the theoretical methods

used to better distinguish the contribution of each particular group to the overall solubility parameter. This principle justifies the predictions of PIM-1, which align closer to experimental techniques than PTMSP, as PIM-1 can be segmented into functional groups that are more common (e.g., ethers, methyl groups, and aromatic rings) and appear frequently in the data set used for fitting. An extended library of experimental solubility parameter data on high T_g, high FFV polymers would certainly improve predictions of modern membrane materials, but at the time of writing this paper this body of data is not available.

A final comparison worth considering due to its relevance in membrane science is the prediction of polyimide solubility parameters. Polyimides whose solubility parameters is available in the literature, such as 6FDA-TFDB, Matrimid, and 6FDA-TMPD, were selected and compared with both our group contribution and machine learning model predictions. 6FDA-TFDB was predicted by the group contribution and machine learning methods to have a solubility parameter of 23.7 ± 0.4 $MPa^{0.5}$ and 20.27 $MPa^{0.5}$ respectively, which compared favorably to its experimental value of 23.8 ± 0.1 $MPa^{0.5}$.[219,220] Matrimid, estimated to have a solubility parameter of 22 $MPa^{0.5}$, was estimated by our methods to be 24.14 ± 0.25 $MPa^{0.5}$ and 23.27 $MPa^{0.5}$ for the group contribution and machine learning, respectively. Finally, 6FDA-TMPD was estimated to be 25.74 ± 0.31 $MPa^{0.5}$ and 25.1 $MPa^{0.5}$ for group contribution and machine learning, respectively, compared to its estimated literature value of 26.5 $MPa^{0.5}$.[106] These predictions all reside within the 10% average error (consistent with previous comparisons in this work) for both methods and demonstrate a general agreement with literature values and the solubility behavior of polyimides.

C9. Updated Molar Attraction Force Group Contribution Values

Table C3: *Reference IDs, structures, molar attraction contributions (F), and their errors (σ_F). F is the contribution of each functional group to the cohesive energy of the molecule in which it resides, as it appears in* Eq. C7*, and σ_F is the uncertainty of this contribution, which may be used in combination with linear error propagation to get the overall error of the solubility parameter derived from the group contribution method. Substructures colored in black are the structure of interest, while the red bonds indicate the connections to other unspecified atoms in the overall molecule.*

Reference ID	Structure	$F\ (MPa^{0.5}\ cm^3\ mol^{-1})$	$\sigma_F\ (MPa^{0.5}\ cm^3\ mol^{-1})$
G1	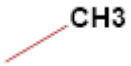	166.0	3.17
G2	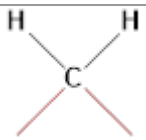	161.9	1.50
G3	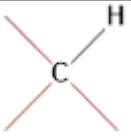	156.1	6.80
G4	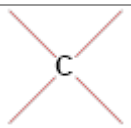	15.85	17.4
G5	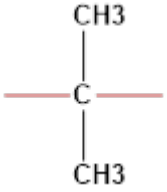	437.9	10.4
G6		947.8	16.1

G7	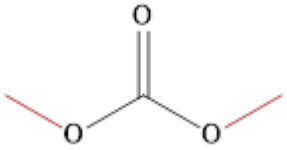	760.0	27.5
G8	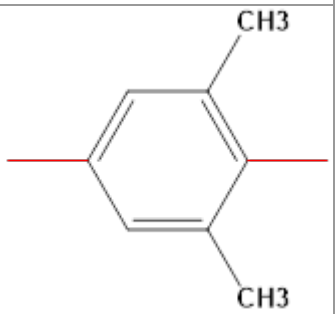	1238.6	111
G9	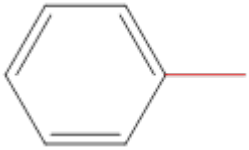	921.9	11.4
G10	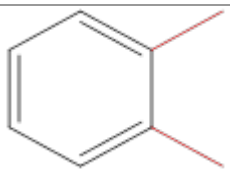	905.8	14.3
G11	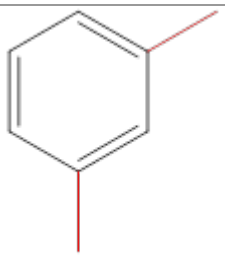	890.5	34.4
G12	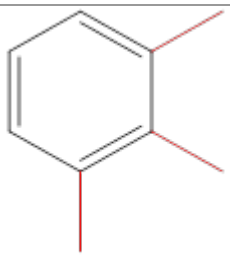	897.4	32.8
G13	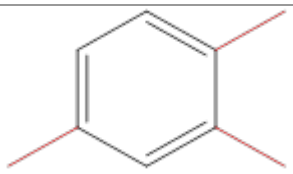	900.0	20.5

G14	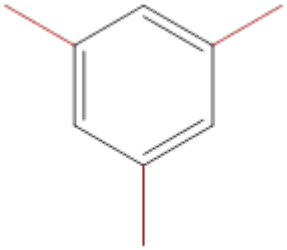	903.4	58.1
G15	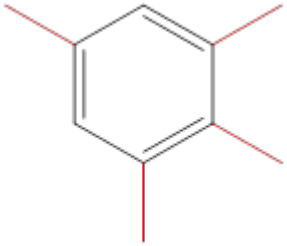	782.4	49.6
G16	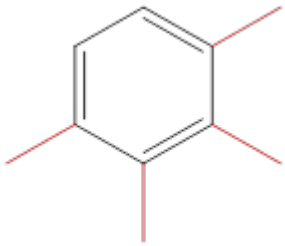	839.3	68.5
G17	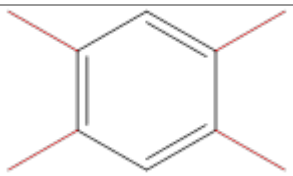	962.5	68.7
G18	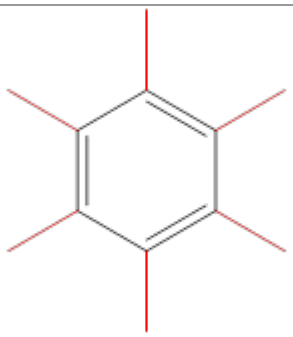	760.8	54.9
G19	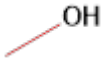	401.6	5.6
G20	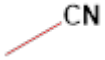	387.8	7.4

G21	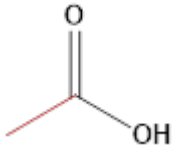	597.1	12.3
G22	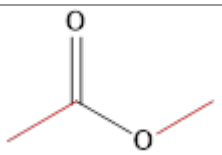	445.0	9.5
G23	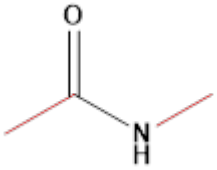	698.6	29.4
G24	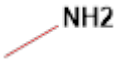	297.3	6.5
G25	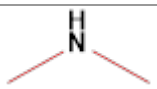	245.3	12.7
G26	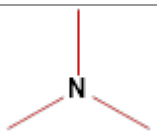	228.2	13.6
G27	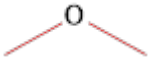	148.7	5.4
G28	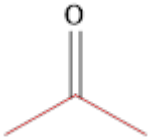	366.1	5.4
G29	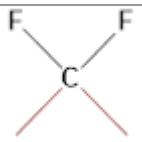	153.5	13.0
G30		322.0	15.3
G31		83.6	5.9

G32		234.2	4.0
G33		331.5	8.4
G34		626.6	28.3
G35	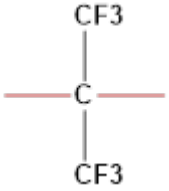	916.6	75.1
G36	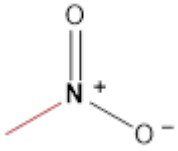	603.7	12.6
G37	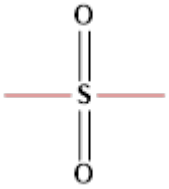	943.3	35.8
G38	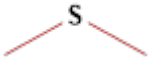	317.0	9.2
G39	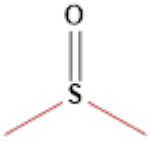	707.7	35.3
G40	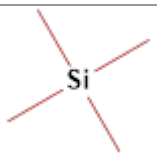	119.4	22.9
G41	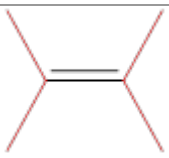	223.3	28.2

G42	$\mathbf{S_{Ar}}^{a}$	298.0	37.6
G43	$\mathbf{N_{Ar}}^{a}$	215.35	15.8
G44	$\mathbf{C_{Ar}}^{a}$	147.1	5.5

[a] The 'Ar' subscript refers to an atom participating in an aromatic ring, rather than implying a lone "aromatic atom". The purpose of this is to respect the altered properties of aromatic systems (e.g., shorter bond lengths) while allowing users to construct arbitrary aromatic systems, such as heterocycles or nitrogen/sulfur containing compounds.

C10. Example Calculation using the Updated Group Contribution Technique

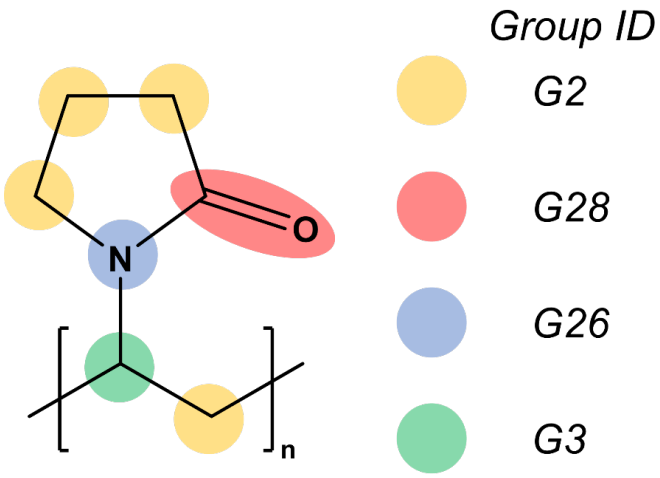

Figure C7: *Group fragmentation of polyvinylpyrrolidone. As with most group contribution techniques, using the largest available fragments will tend to give the best numerical results. Here, carbonyl and tertiary amine groups are used rather than a tertiary amide. This was because of the insufficient occurrences of tertiary amides in the training data set to accurately determine its molar attractive constant.*

The solubility parameter can be calculated using the data in this paper paired with the van der Waals group contribution approach from Wu et al.[195] This calculation can be quite sensitive to the VdW volume used. Since group contributions in this paper were fitted using volumes calculated exclusively by the method reported by Wu et al., using their technique will give the best results. According to Eq. C7, the molar attraction constant of each of the groups in Figure C7 is multiplied by its number of occurrences added up, and the resulting total attraction energy is divided by the molar volume.

$$\delta = \frac{\sum_{i=1}^{n} F_i}{V_W} \qquad \text{(Eq. C7)}$$

The van der Waals volume was calculated to be 59.34 cm^3 mol^{-1}. Then, the molar attraction term is calculated as follows:

$$\sum_{i=1}^{n} F_i = [4 \times 161.9 + 156.1 + 366.1 + 228.2] = 1398 \ (MPa^{0.5}\ cm^3\ mol^{-1})$$

Which then gives us:

$$\delta = \frac{\sum_{i=1}^{n} F_i}{V_W} = \frac{1398\ \mathrm{MPa^{0.5}\ cm^3\ mol^{-1}}}{59.34\ \mathrm{cm^3\ mol^{-1}}} = 23.6\ \pm\ 0.29\ \mathrm{MPa^{0.5}}$$

The uncertainty was estimated using linear error propagation.[221]

C11. Model Optimization and Uncertainty

Both group contribution and the machine learning model are optimized using mean squared error (L2 loss) target functions. Group contribution is then optimized via the L-BFGS algorithm, and the neural network is trained via the ADAM optimizer. It is possible to quantify uncertainty on the minimizer values,[222] that is, the error of the fit contributions of each functional group. Specifically, the covariance matrix (Σ) (of which the diagonal values are the variance of each group's contribution) is found by evaluating the inverse scaled hessian matrix (H^{-1}) of the objective function with respect to the minimizer values. More formally:

$$\Sigma = \frac{\sum_{i=0}^{n_{meas}}\left[\left(\delta_{pred}-\delta_{meas}\right)^2\right]}{n_{meas}-n_{groups}} H^{-1} \qquad \text{(Eq. C8)}$$

The scaling factor corrects bias in the resulting covariance and can be otherwise phrased as the total sum of errors at the found local minimum normalized by the degrees of freedom in the model, which is $n_{meas} - n_{groups}$ as each functional group adds one fitted parameter to the model.

To train both the group contribution and neural network, small molecule solubility parameter data was first collected from Hansen's solubility parameter handbook[177] and pruned to 783 small molecules containing functional groups of interest, that is, molecules containing functional groups that may be used to construct a wide variety of polymers exhibiting various chemistries (e.g. hydrocarbon-based polymers, fluoropolymers, and silicon-based polymers). Of this data, 80% (i.e., 626 molecules) were used to independently train the group contribution and neural network, while the remaining 20% (i.e., 157 molecules) were set aside to test how well both models made solubility parameter predictions on small molecules alone.

Once trained with the 626 randomly selected molecules, both the group contribution and neural network adequately predicted the solubility parameter of the 157 test molecules. The predicted solubility parameters from group contribution and neural network versus the measured (literature)

value for the training and testing small molecule datasets are shown in Figure C8A/B, respectively. The error in these predictions is quantified and shown in Table C4, where the mean absolute relative error (MARE) of the group contribution model is 5.7% in the small molecule training dataset and 6.1% in the testing dataset (the 157 molecules not trained on). In comparison, the neural network exhibited similar results, where the MARE of the small molecule training and testing set is 6.1% and 6.3%, respectively.

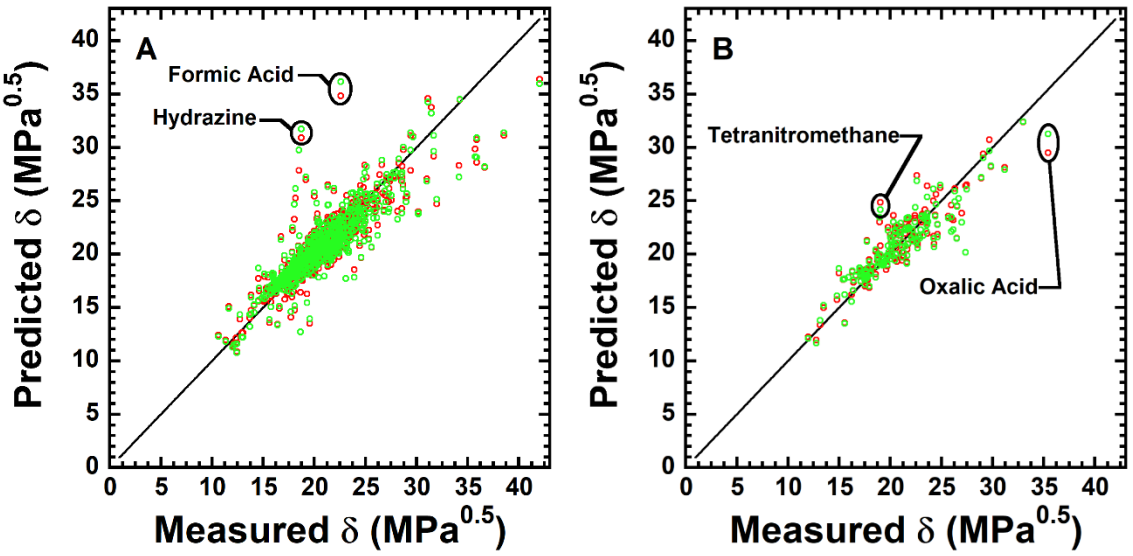

Figure C8: *Parity plots of the group contribution (red circles) and neural network (green circles) predictions of the solubility parameter in units of $MPa^{0.5}$. Data used to train the models are shown in A, data reserved for making predictions of molecules the models had not previously seen are shown in B.*

Table C4: *Mean Absolute Relative Error (MARE) of small molecule training and testing solubility parameter data and polymer solubility parameter data (predictions only). Polymer Genome predictions[194] are provided as a reference to the state of the art.*

Technique	***Small Molecule Training MARE[a]***	***Small Molecule Testing MARE[a]***	***Polymer Prediction MARE[a]***
Group Contribution	*5.7%*	*6.1%*	*9.0%*
Neural Network	*6.1%*	*6.3%*	*10.3%*

Polymer Genome Project[b]	---	---	*5.8%*

[a]MARE = $\frac{100}{N}\sum_{i=1}^{N}\left|\frac{\delta_{i,Predicted}-\delta_{i,Measured}}{\delta_{i,Measured}}\right|$

[b]Data from the online database *Polymer Genome*[194]

C12. Machine Learning Model

Modern techniques, such as machine learning, have the capability to outperform group contribution, but generally do so when provided with more fitted parameters and types of information. A machine learning model was implemented to both assess the performance of the group contribution method and to see if machine learning results align better with experimental measurements (i.e., viscometry and DLS) than that of group contribution, which would suggest group contribution could be improved without including more information. We used a graph convolutional neural network, a type of machine learning model well suited to predict chemical properties such as the solubility parameter, to fit the same solubility parameter data as the group contribution model. This is done by comparing the predictive ability of the machine learning model and the group contribution technique.

The neural network structure was chosen to utilize the same information as group contribution while minimizing the risk of overfitting (cf., Figure C9). Overfitting, also referred to as memorization, occurs when the model learns to predict only the data set it was exposed to, without being able to generalize its predictions to previously unseen molecules. Although this may occur in both group contribution models and machine learning models, it is more likely to occur when more parameters are included in the model, and thus neural networks are particularly prone to memorization.

In this network, the chemical's functional groups are first fed to an embedding layer, which translates each functional group into a vector (i.e., a series of values), mirroring a more general case of group contribution's single value input. The resulting matrix (referred to as the feature matrix of the functional group graph) is then sent to a graph convolution layer, which operates on

both the values of a group as well as its connections. This allows groups to interact with each other, mirroring a general case of binary and tertiary interactions.

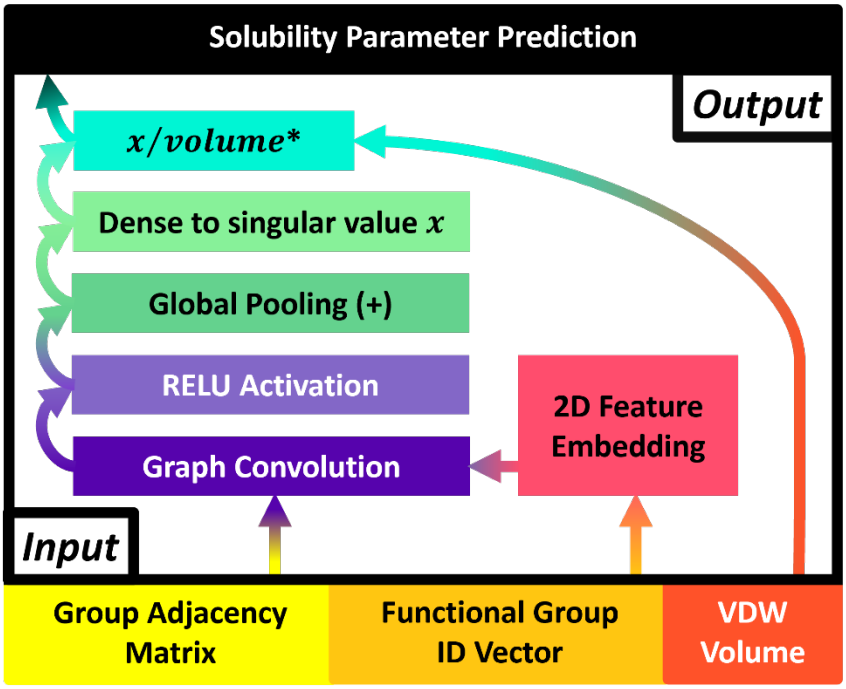

Figure C9: *Schematic of the graph neural network structure. The bottom row denotes input values, arrows denote the flow of information, and the top row denotes the output prediction. The asterisk by volume indicates that it is an optional operation, needed only for parameters that must be normalized, such as the solubility parameter.*

If this black box model can significantly outperform group contribution, then the information present within the functional groups and their connectivity likely is not being fully utilized by the current group contribution model, and modifications to group contribution (e.g., extra parameters, or a non-linear correlation) may be necessary to further improve prediction accuracy. Otherwise, should both methods perform similarly, improvements upon fundamental group contribution models may instead require additional types of information to be incorporated into the model, such as polar surface area, van der Waals surface area, bond properties such as rotatability and bond length, and other structure-property descriptors.

C13. Polymer Data Curated for Predictions of Solubility Parameters

Table C5: *Polymer solubility parameters as found in literature.*

polymer	$\delta_{measured}\ (MPa^{0.5})$
Polyethylene	15.8
Polypropylene	16.8
Polyisobutylene	16.0
Polystyrene	17.4
Poly(vinyl chloride)	19.2
Poly(vinyl bromide)	19.4
Poly(vinylidene chloride)	20.3
Poly(tetrafluoroethylene)	12.7
Poly(chlorotrifluoroethylene)	14.7
Poly(vinyl alcohol)	25.8
Poly(vinyl acetate)	19.1
Poly(vinyl propionate)	18.0
Poly(methyl acrylate)	19.9
Poly(ethyl acrylate)	18.8
Poly(propyl acrylate)	18.5
Poly(butyl acrylate)	18.0
Poly(isobutyl acrylate)	17.8
Poly(2,2,3,3,4,4,4-heptafluorobutyl acrylate)	13.7
Poly(methyl methacrylate)	18.6
Poly(ethyl methacrylate)	18.2
Poly(butyl methacrylate)	17.8
Poly(isobutyl methacrylate)	16.8
Poly(tert.-butyl methacrylate)	17.0
Poly(benzyl methacrylate)	20.1
Poly(ethoxyethyl methacrylate)	18.4
Polyacrylonitrile	25.6
Polymethacrylonitrile	21.9
Poly(a-cyanomethyl acrylate)	28.7
Polyformaldehyde	20.9
Poly(tetramethylene oxide)	17.0
Poly(propylene oxide)	15.4
Poly(epichlorohydrin)	19.2
Poly(ethylene terephthalate)	19.9
Poly(8-aminocaprylic acid)	26.0
Nylon 6,6	27.8
Poly(dimethyl siloxane)	14.9
Poly(methyl propyl siloxane)	15.9

Poly(methyl octyl siloxane)	16.3
Poly(phenyl methyl siloxane)	19.7
Poly(trifluoropropyl methyl siloxane)	17.9

C14. Machine Learning Outcome and Analysis

As discussed in Chapter 4, predictions from the neural network and group contribution model exhibit similar performance. A post-training analysis revealed that the embedding layer (i.e., the layer of the neural network that assigns values to functional groups) of the neural network very closely resembles the corresponding fit values in group contribution. That is, when comparing the neural network's representation of a functional group with that same functional group's molar attraction constant value in the updated group contribution technique, both the neural network and the group contribution technique tend to represent the same information (cf., Figure C10). This suggests that the neural network is not discovering an improved process to predict solubility parameters compared to that of the group contribution model, and is instead "re-discovering" group contribution, despite being composed of much more flexible and generalized versions of the tools available within the group contribution model, such as non-linear relationships and the connectivity between functional groups.

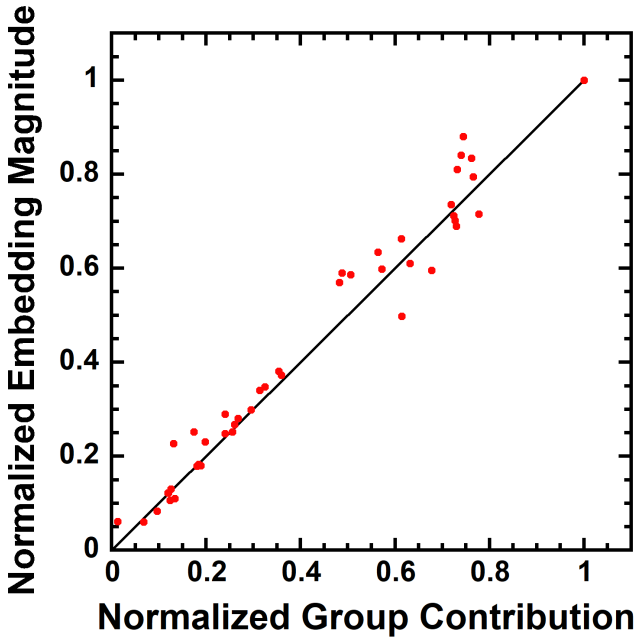

Figure C10: *Parity plot between the neural networks embedding layer values and the traditional group contribution's fitted values, group contribution is normalized by the highest functional*

group's molar attractive force constant (F), the embedding magnitudes are normalized by the highest value in the layer.

References

(1) Energy Agency, I. *World Energy Outlook 2016*; 2040.
(2) Hoek, E.; Tarabara, V. V.; Lin, H.; Loyd, S.; Lokhandwala, K.; Baker, R. W. Natural Gas Purification. *Encyclopedia of Membrane Science and Technology* **2013**, 1–25.
(3) Yoro, K. O.; Daramola, M. O. CO2 Emission Sources, Greenhouse Gases, and the Global Warming Effect. In *Advances in Carbon Capture: Methods, Technologies and Applications*; Elsevier, 2020; pp 3–28. https://doi.org/10.1016/B978-0-12-819657-1.00001-3.
(4) Baker, R. W.; Low, B. T. Gas Separation Membrane Materials: A Perspective. *Macromolecules* **2014**, *47* (20), 6999–7013. https://doi.org/10.1021/ma501488s.
(5) Environmental Protection Agency. *Global Greenhouse Gas Emissions Data*.
(6) D.S. Sholl, R. P. L. Seven Chemical Separations to Change the World. *Nature* **2016**, *532*, 435–437.
(7) Sholl-2016-Seven-Chemical-Separations-to-Chang.
(8) Baker, R. W.; Lokhandwala, K. Natural Gas Processing with Membranes: An Overview. *Industrial and Engineering Chemistry Research*. April 2, 2008, pp 2109–2121. https://doi.org/10.1021/ie071083w.
(9) Global-Polyethylene-Market-Analysis-by-Demand-By.
(10) Yao, Y.; Graziano, D. J.; Riddle, M.; Cresko, J.; Masanet, E. Prospective Energy Analysis of Emerging Technology Options for the United States Ethylene Industry. *Ind Eng Chem Res* **2016**, *55* (12), 3493–3505. https://doi.org/10.1021/acs.iecr.5b03413.
(11) Eldridge, R. B. *Olefin/Paraffin Separation Technology: A Review*; 1993; Vol. 32. https://pubs.acs.org/sharingguidelines.
(12) Spallina, V.; Velarde, I. C.; Jimenez, J. A. M.; Godini, H. R.; Gallucci, F.; Van Sint Annaland, M. Techno-Economic Assessment of Different Routes for Olefins Production through the Oxidative Coupling of Methane (OCM): Advances in Benchmark Technologies. *Energy Convers Manag* **2017**, *154*, 244–261. https://doi.org/10.1016/j.enconman.2017.10.061.
(13) Comesaña-Gándara, B.; Chen, J.; Bezzu, C. G.; Carta, M.; Rose, I.; Ferrari, M. C.; Esposito, E.; Fuoco, A.; Jansen, J. C.; McKeown, N. B. Redefining the Robeson Upper Bounds for CO2/CH4 and CO2/N2 Separations Using a Series of Ultrapermeable Benzotriptycene-Based Polymers of Intrinsic Microporosity. *Energy Environ Sci* **2019**, *12* (9), 2733–2740. https://doi.org/10.1039/c9ee01384a.
(14) Yampolskii, Y.; Freeman, B. *Membrane Gas Separation*; John Wiley and Sons, 2010. https://doi.org/10.1002/9780470665626.
(15) Cheng, L.; Liu, G.; Jin, W. Recent Advances in Facilitated Transport Membranes for Olefin/Paraffin Separation. *Discover Chemical Engineering* **2021**, *1* (1). https://doi.org/10.1007/s43938-020-00001-4.
(16) Robeson, L. M. *Correlation of Separation Factor versus Permeability for Polymeric Membranes*.
(17) Rezakazemi, M.; Amooghin, A. E.; Montazer-Rahmati, M. M.; Ismail, A. F.; Matsuura, T. State-of-the-Art Membrane Based CO2 Separation Using Mixed Matrix Membranes (MMMs): An Overview on Current Status and Future Directions. *ProgressInPolymerScience* **2014**, *39* (5), 817–861.

(18) Kang, Y. S.; Kang, S. W.; Kim, H.; Kim, J. H.; Won, J.; Kim, C. K.; Char, K. Interaction with Olefins of the Partially Polarized Surface of Silver Nanoparticles Activated by P-Benzoquinone and Its Implications for Facilitated Olefin Transport. *Advanced Materials* **2007**, *19* (3), 475–479. https://doi.org/10.1002/adma.200601009.
(19) Quaroni, L.; Chumanov, G. Preparation of Polymer-Coated Functionalized Silver Nanoparticles [9]. *Journal of the American Chemical Society*. November 17, 1999, pp 10642–10643. https://doi.org/10.1021/ja992088q.
(20) Wijmans, J. G.; Baker, R. W. *The Solution-Diffusion Model: A Review*; 1995; Vol. 107.
(21) Crank, J. *The Mathematics of Diffusion*.
(22) Robesont, L. M.; Burgoyne, W. F.; Langsam, M.; Savoca, A. C.; Tien, C. F. *High Performance Polymers for Membrane Separation**.
(23) Gleason, K. L.; Smith, Z. P.; Liu, Q.; Paul, D. R.; Freeman, B. D. Pure- and Mixed-Gas Permeation of CO2 and CH4 in Thermally Rearranged Polymers Based on 3,3'-Dihydroxy-4,4'-Diamino-Biphenyl (HAB) and 2,2'-Bis-(3,4-Dicarboxyphenyl) Hexafluoropropane Dianhydride (6FDA). *J Memb Sci* **2015**, *475*, 204–214. https://doi.org/10.1016/j.memsci.2014.10.014.
(24) Huang, L.; Liu, J.; Lin, H. Thermally Stable, Homogeneous Blends of Cross-Linked Poly(Ethylene Oxide) and Crown Ethers with Enhanced CO2 Permeability. *J Memb Sci* **2020**, *610*. https://doi.org/10.1016/j.memsci.2020.118253.
(25) Lin, H.; Freeman, B. D. Gas Solubility, Diffusivity and Permeability in Poly(Ethylene Oxide). *J Memb Sci* **2004**, *239* (1), 105–117. https://doi.org/10.1016/j.memsci.2003.08.031.
(26) Mahajan, R.; Koros, W. J. Factors Controlling Successful Formation of Mixed-Matrix Gas Separation Materials. *Ind Eng Chem Res* **2000**, *39* (8), 2692–2696. https://doi.org/10.1021/ie990799r.
(27) Roy, A.; Venna, S. R.; Rogers, G.; Tang, L.; Fitzgibbons, T. C.; Liu, J.; Mccurry, H.; Vickery, D. J.; Flick, D.; Fish, B. Membranes for Olefin-Paraffin Separation: An Industrial Perspective. **2021**, *118*. https://doi.org/10.1073/pnas.2022194118/-/DCSupplemental.
(28) M.B. Hägg; R. Quinn. *Polymeric Facilitated Transport Membranes for Hydrogen Purification Survey of Polymeric FT Membranes*; 2006. https://doi.org/https://doi.org/10.1557/mrs2006.188.
(29) Deng, L.; Kim, T. J.; Hägg, M. B. Facilitated Transport of CO2 in Novel PVAm/PVA Blend Membrane. *J Memb Sci* **2009**, *340* (1–2), 154–163. https://doi.org/10.1016/j.memsci.2009.05.019.
(30) Gordon, C. P.; Andersen, R. A.; Copéret, C. Metal Olefin Complexes: Revisiting the Dewar−Chatt−Duncanson Model and Deriving Reactivity Patterns from Carbon-13 NMR Chemical Shift. *Helv Chim Acta* **2019**, *102* (9). https://doi.org/10.1002/hlca.201900151.
(31) Arous, O.; Kerdjoudj, H.; Seta, P. Comparison of Carrier-Facilitated Silver (i) and Copper (Ii) Ions Transport Mechanisms in a Supported Liquid Membrane and in a Plasticized Cellulose Triacetate Membrane. *J Memb Sci* **2004**, *241* (2), 177–185. https://doi.org/10.1016/j.memsci.2004.04.024.
(32) Bryan, P. F. Removal of Propylene from Fuel-Grade Propane. *Separation and Purification Reviews*. 2004, pp 157–182. https://doi.org/10.1081/SPM-200042095.
(33) Campos, A. C. C.; Dos Reis, R. A.; Ortiz, A.; Gorri, D.; Ortiz, I. A Perspective of Solutions for Membrane Instabilities in Olefin/Paraffin Separations: A Review. *Ind Eng Chem Res* **2018**, *57* (31), 10071–10085. https://doi.org/10.1021/acs.iecr.8b02013.

(34) Galizia, M.; Chi, W. S.; Smith, Z. P.; Merkel, T. C.; Baker, R. W.; Freeman, B. D. 50th Anniversary Perspective: Polymers and Mixed Matrix Membranes for Gas and Vapor Separation: A Review and Prospective Opportunities. *Macromolecules* **2017**, *50* (20), 7809–7843. https://doi.org/10.1021/acs.macromol.7b01718.
(35) Bondar, V. I.; Freeman, B. D.; Pinnau, I. *Gas Sorption and Characterization of Poly(Ether-b-Amide) Segmented Block Copolymers*; 1999; Vol. 37.
(36) Bondar, V. I.; Freeman, B. D.; Pinnau, I. *Gas Transport Properties of Poly(Ether-b-Amide) Segmented Block Copolymers*; 2000; Vol. 38.
(37) Robeson, L. M.; Smith, Z. P.; Freeman, B. D.; Paul, D. R. Contributions of Diffusion and Solubility Selectivity to the Upper Bound Analysis for Glassy Gas Separation Membranes. *J Memb Sci* **2014**, *453*, 71–83. https://doi.org/10.1016/j.memsci.2013.10.066.
(38) Deng, J.; Huang, Z.; Sundell, B. J.; Harrigan, D. J.; Sharber, S. A.; Zhang, K.; Guo, R.; Galizia, M. State of the Art and Prospects of Chemically and Thermally Aggressive Membrane Gas Separations: Insights from Polymer Science. *Polymer*. Elsevier Ltd August 16, 2021. https://doi.org/10.1016/j.polymer.2021.123988.
(39) Robeson, L. M. The Upper Bound Revisited. *J Memb Sci* **2008**, *320* (1–2), 390–400. https://doi.org/10.1016/j.memsci.2008.04.030.
(40) Koros, W. J. MODEL FOR SORPTION OF MIXED GASES IN GLASSY POLYMERS. *Journal of polymer science. Part A-2, Polymer physics* **1980**, *18* (5), 981–992. https://doi.org/10.1002/pol.1980.180180506.
(41) Rezakazemi, M.; Sadrzadeh, M.; Matsuura, T. Thermally Stable Polymers for Advanced High-Performance Gas Separation Membranes. *Progress in Energy and Combustion Science*. Elsevier Ltd May 1, 2018, pp 1–41. https://doi.org/10.1016/j.pecs.2017.11.002.
(42) Mashhadikhan, S.; Ahmadi, R.; Ebadi Amooghin, A.; Sanaeepur, H.; Aminabhavi, T. M.; Rezakazemi, M. Breaking Temperature Barrier: Highly Thermally Heat Resistant Polymeric Membranes for Sustainable Water and Wastewater Treatment. *Renewable and Sustainable Energy Reviews*. Elsevier Ltd January 1, 2024. https://doi.org/10.1016/j.rser.2023.113902.
(43) Bos, A.; Ènt, I. G. M. P.; Wessling, M.; Strathmann, H. *CO 2-Induced Plasticization Phenomena in Glassy Polymers*.
(44) Mizrahi Rodriguez, K.; Lin, S.; Wu, A. X.; Storme, K. R.; Joo, T.; Grosz, A. F.; Roy, N.; Syar, D.; Benedetti, F. M.; Smith, Z. P. Penetrant-Induced Plasticization in Microporous Polymer Membranes. *Chemical Society Reviews*. Royal Society of Chemistry January 31, 2024, pp 2435–2529. https://doi.org/10.1039/d3cs00235g.
(45) Matesanz-Niño, L.; Webb, M. T.; González-Ortega, A.; Palacio, L.; Álvarez, C.; Lozano, Á. E.; Galizia, M. Plasticization Resistant Gas Separation Membranes Derived from Polyimides Exhibiting Polyethylene-Oxide Moieties. *Polymer (Guildf)* **2024**, *290*, 126535.
(46) Condes, L. C.; Landry, A. E.; Webb, M. T.; Box, W. J.; Gali, A.; Galizia, M. Inter-Crosslinked Spirocyclic Mixed Matrix Membranes Exhibiting Enhanced Gas Permeability, Selectivity, and Plasticization Resistance. *J Memb Sci* **2024**, *709*. https://doi.org/10.1016/j.memsci.2024.123081.
(47) Zimmerman, C. M.; Singh, A.; Koros, W. J. *Tailoring Mixed Matrix Composite Membranes for Gas Separations*; 1997; Vol. 137.
(48) Hussain, M.; König, A. Mixed-Matrix Membrane for Gas Separation: Polydimethylsiloxane Filled with Zeolite. *Chem Eng Technol* **2012**, *35* (3), 561–569. https://doi.org/10.1002/ceat.201100419.

(49) Lin, R.; Ge, L.; Hou, L.; Strounina, E.; Rudolph, V.; Zhu, Z. Mixed Matrix Membranes with Strengthened MOFs/Polymer Interfacial Interaction and Improved Membrane Performance. *ACS Appl Mater Interfaces* **2014**, *6* (8), 5609–5618. https://doi.org/10.1021/am500081e.

(50) Kurimura, Y.; Ohta, F.; Gohda, J.; Nishide, H.; Tsuchida, E. Polymer-supported Dinitrogen Complexes of Manganese. Coordination of Molecular Nitrogen in Solid-gas Phase Reaction under Mild Conditions. *Die Makromolekulare Chemie* **1982**, *183* (12), 2889–2900. https://doi.org/10.1002/macp.1982.021831202.

(51) Merkel, T. C.; Blanc, R.; Ciobanu, I.; Firat, B.; Suwarlim, A.; Zeid, J. Silver Salt Facilitated Transport Membranes for Olefin/Paraffin Separations: Carrier Instability and a Novel Regeneration Method. *J Memb Sci* **2013**, *447*, 177–189. https://doi.org/10.1016/j.memsci.2013.07.010.

(52) Hun Park, H.; Won, J.; Oh, S. G.; Kang, Y. S. Effect of Nonionic N-Octyl β-D-Glucopyranoside Surfactant on the Stability Improvement of Silver Polymer Electrolyte Membranes for Olefin/Paraffin Separation. *J Memb Sci* **2003**, *217* (1–2), 285–293. https://doi.org/10.1016/S0376-7388(03)00146-7.

(53) Fallanza, M.; Ortiz, A.; Gorri, D.; Ortiz, I. Polymer-Ionic Liquid Composite Membranes for Propane/Propylene Separation by Facilitated Transport. *J Memb Sci* **2013**, *444*, 164–172. https://doi.org/10.1016/j.memsci.2013.05.015.

(54) Nahar, M.; Gallardo, I. F.; Gleason, K. L.; Becker, M. F.; Keto, J. W.; Kovar, D. Metal-on-Oxide Nanoparticles Produced Using Laser Ablation of Microparticle Aerosols. *Journal of Nanoparticle Research* **2011**, *13* (8), 3455–3464. https://doi.org/10.1007/s11051-011-0267-5.

(55) Alentiev, A. Y.; Yampolskii, Y. P. *Meares Equation and the Role of Cohesion Energy Density in Diffusion in Polymers*; 2002; Vol. 206.

(56) Huglin, M. B.; Pass, D. J. Cohesive Energy Density of Polytetrahydrofuran. *J Appl Polym Sci* **1968**, *12* (3), 473–485. https://doi.org/10.1002/app.1968.070120308.

(57) Mangaraj, D. Cohesive Energy Densities of High Polymers. Part I. Determination of Cohesive Energy Density from Swelling Measurements. *Die Makromolekulare Chemie* **1963**, *65* (1), 29–38. https://doi.org/10.1002/macp.1963.020650104.

(58) Kubica, P.; Wolinska-Grabczyk, A. Correlation between Cohesive Energy Density, Fractional Free Volume, and Gas Transport Properties of Poly(Ethylene-Co-Vinyl Acetate) Materials. *Int J Polym Sci* **2015**, *2015*. https://doi.org/10.1155/2015/861979.

(59) Webb, M. T.; Condes, L. C.; Ly, H. G.; Galizia, M.; Razavi, S. Rational Design, Synthesis, and Characterization of Facilitated Transport Membranes Exhibiting Enhanced Permeability, Selectivity and Stability. *J Memb Sci* **2023**, *685*. https://doi.org/10.1016/j.memsci.2023.121910.

(60) Wang, L.; Hasanzadeh Kafshgari, M.; Meunier, M. Optical Properties and Applications of Plasmonic-Metal Nanoparticles. *Advanced Functional Materials*. Wiley-VCH Verlag December 1, 2020. https://doi.org/10.1002/adfm.202005400.

(61) Zhang, Y. X.; Wang, Y. H. Nonlinear Optical Properties of Metal Nanoparticles: A Review. *RSC Advances*. Royal Society of Chemistry 2017, pp 45129–45144. https://doi.org/10.1039/c7ra07551k.

(62) Shipway, A. N.; Katz, E.; Willner, I. Nanoparticle Arrays on Surfaces for Electronic, Optical, and Sensor Applications. *ChemPhysChem*. Wiley-VCH Verlag August 4, 2000, pp 18–52. https://doi.org/10.1002/1439-7641(20000804)1:1<18::AID-CPHC18>3.0.CO;2-L.

(63) Li, Y.; Wu, Y.; Ong, B. S. Facile Synthesis of Silver Nanoparticles Useful for Fabrication of High-Conductivity Elements for Printed Electronics. *J Am Chem Soc* **2005**, *127* (10), 3266–3267. https://doi.org/10.1021/ja043425k.
(64) Nayak, L.; Mohanty, S.; Nayak, S. K.; Ramadoss, A. A Review on Inkjet Printing of Nanoparticle Inks for Flexible Electronics. *J Mater Chem C Mater* **2019**, *7* (29), 8771–8795. https://doi.org/10.1039/c9tc01630a.
(65) Kamyshny, A.; Magdassi, S. Conductive Nanomaterials for Printed Electronics. *Small*. Wiley-VCH Verlag September 10, 2014, pp 3515–3535. https://doi.org/10.1002/smll.201303000.
(66) Murphy, M.; Ting, K.; Zhang, X.; Soo, C.; Zheng, Z. Current Development of Silver Nanoparticle Preparation, Investigation, and Application in the Field of Medicine. *Journal of Nanomaterials*. Hindawi Limited 2015. https://doi.org/10.1155/2015/696918.
(67) Zhang, L.; Gu, F. X.; Chan, J. M.; Wang, A. Z.; Langer, R. S.; Farokhzad, O. C. Nanoparticles in Medicine: Therapeutic Applications and Developments. https://doi.org/10.1038/sj.clp.
(68) Hoftmann-Amtenbrink, M.; Grainger, D. W.; Hofmann, H. Nanoparticles in Medicine: Current Challenges Facing Inorganic Nanoparticle Toxicity Assessments and Standardizations. *Nanomedicine:Nanotechnology,BiologyandMedicine* **2015**, *11* (7), 1689–1694.
(69) De Jong, W. H.; Borm, P. J. *Drug Delivery and Nanoparticles: Applications and Hazards*; 2008; Vol. 3.
(70) Corbierre, M. K.; Cameron, N. S.; Sutton, M.; Laaziri, K.; Lennox, R. B. Gold Nanoparticle/Polymer Nanocomposites: Dispersion of Nanoparticles as a Function of Capping Agent Molecular Weight and Grafting Density. *Langmuir* **2005**, *21* (13), 6063–6072. https://doi.org/10.1021/la047193e.
(71) Liu, Y.; Zhang, J.; Tan, X. High Performance of PIM-1/ZIF-8 Composite Membranes for O2/N2 Separation. *ACS Omega* **2019**, *4* (15), 16572–16577. https://doi.org/10.1021/acsomega.9b02363.
(72) Moaddeb, M.; Koros, W. J. *Gas Transport Properties of Thin Polymeric Membranes in the Presence of Silicon Dioxide Particles*; 1997; Vol. 125.
(73) Thompson, J. A.; Chapman, K. W.; Koros, W. J.; Jones, C. W.; Nair, S. Sonication-Induced Ostwald Ripening of ZIF-8 Nanoparticles and Formation of ZIF-8/Polymer Composite Membranes. *Microporous and Mesoporous Materials* **2012**, *158*, 292–299. https://doi.org/10.1016/j.micromeso.2012.03.052.
(74) Merkel, T. C.; He, Z.; Pinnau, I.; Freeman, B. D.; Meakin, P.; Hill, A. J. Effect of Nanoparticles on Gas Sorption and Transport in Poly(1-Trimethylsilyl-1-Propyne). *Macromolecules* **2003**, *36* (18), 6844–6855. https://doi.org/10.1021/ma0341566.
(75) Matteucci, S.; Kusuma, V. A.; Sanders, D.; Swinnea, S.; Freeman, B. D. Gas Transport in TiO2 Nanoparticle-Filled Poly(1-Trimethylsilyl-1-Propyne). *J Memb Sci* **2008**, *307* (2), 196–217. https://doi.org/10.1016/j.memsci.2007.09.035.
(76) Davenport, M. N.; Bentley, C. L.; Brennecke, J. F.; Freeman, B. D. Ethylene and Ethane Transport Properties of Hydrogen-Stable Ag+-Based Facilitated Transport Membranes. *J Memb Sci* **2022**, *647*. https://doi.org/10.1016/j.memsci.2022.120300.
(77) Ho, W. S.; Dalrymple, D. C. *Facilitated Transport of Olefins in Ag+-Containing Polymer Membranes*; 1994; Vol. 91.

(78) National Academies Press. National Academics of Science, Engineering, and Medicine, Division on Earth and Life Sciences, Board on Chemical Sciences and Technology, Committee on a Research Agenda for a New Era in Separation Science. *A Research Agenda for Transforming Separation Science* **2019**.
(79) Luo, S.; Zhang, Q.; Zhu, L.; Lin, H.; Kazanowska, B. A.; Doherty, C. M.; Hill, A. J.; Gao, P.; Guo, R. Highly Selective and Permeable Microporous Polymer Membranes for Hydrogen Purification and CO2 Removal from Natural Gas. *Chemistry of Materials* **2018**, *30* (15), 5322–5332. https://doi.org/10.1021/acs.chemmater.8b02102.
(80) Omidvar, M.; Stafford, C. M.; Lin, H. Thermally Stable Cross-Linked P84 with Superior Membrane H2/CO2 Separation Properties at 100 °C. *J Memb Sci* **2019**, *575*, 118–125. https://doi.org/10.1016/j.memsci.2019.01.003.
(81) Jang, E. S.; Kamcev, J.; Kobayashi, K.; Yan, N.; Sujanani, R.; Talley, S. J.; Moore, R. B.; Paul, D. R.; Freeman, B. D. Effect of Water Content on Sodium Chloride Sorption in Cross-Linked Cation Exchange Membranes. *Macromolecules* **2019**, *52* (6), 2569–2579. https://doi.org/10.1021/acs.macromol.8b02550.
(82) Box, W. J.; Huang, Z.; Guo, R.; Galizia, M. The Mechanism of Light Gas Transport through Configurational Free Volume in Glassy Polymers. *J Memb Sci* **2022**, *656*. https://doi.org/10.1016/j.memsci.2022.120608.
(83) Han, Y.; Ho, W. S. W. Facilitated Transport Membranes for H2 Purification from Coal-Derived Syngas: A Techno-Economic Analysis. *J Memb Sci* **2021**, *636*. https://doi.org/10.1016/j.memsci.2021.119549.
(84) Eriksen, O. I.; Aksnes, E.; Dahl, I. M. *Facilitated Transport of Ethene through Nafion Membranes. Part I. Water Swollen Membranes*; 1993; Vol. 85.
(85) Rungta, M.; Zhang, C.; Koros, W. J.; Xu, L. Membrane-Based Ethylene/Ethane Separation: The Upper Bound and Beyond. *AIChE Journal* **2013**, *59* (9), 3475–3489. https://doi.org/10.1002/aic.14105.
(86) Kim, J. H.; Min, R.; Kim, H. S.; Won, J.; Kang, Y. S. *Facilitated Transport of Ethylene across Polymer Membranes Containing Silver Salt: Effect of HBF 4 on the Photoreduction of Silver Ions*; 2003; Vol. 212.
(87) Jung, J. P.; Park, C. H.; Lee, J. H.; Park, J. T.; Kim, J. H.; Kim, J. H. Facilitated Olefin Transport through Membranes Consisting of Partially Polarized Silver Nanoparticles and PEMA-g-PPG Graft Copolymer. *J Memb Sci* **2018**, *548*, 149–156. https://doi.org/10.1016/j.memsci.2017.11.020.
(88) Zhao, Y.; Winston Ho, W. S. Steric Hindrance Effect on Amine Demonstrated in Solid Polymer Membranes for CO 2 Transport. *J Memb Sci* **2012**, *415–416*, 132–138. https://doi.org/10.1016/j.memsci.2012.04.044.
(89) Kim, Y. R.; Lee, J. H.; Choi, H.; Cho, W.; Kang, Y. S. Chemical Stability of Olefin Carrier Based on Silver Cations and Metallic Silver Nanoparticles against the Formation of Silver Acetylide for Facilitated Transport Membranes. *J Memb Sci* **2014**, *463*, 11–16. https://doi.org/10.1016/j.memsci.2014.03.057.
(90) Liu, Y.; Li, X.; Qin, Y.; Guo, R.; Zhang, J. Pebax–Polydopamine Microsphere Mixed-Matrix Membranes for Efficient CO2 Separation. *J Appl Polym Sci* **2017**, *134* (10). https://doi.org/10.1002/app.44564.
(91) Kariuki, V. M.; Yazgan, I.; Akgul, A.; Kowal, A.; Parlinska, M.; Sadik, O. A. Synthesis and Catalytic, Antimicrobial and Cytotoxicity Evaluation of Gold and Silver

Nanoparticles Using Biodegradable, Π-Conjugated Polyamic Acid. *Environ Sci Nano* **2015**, *2* (5), 518–527. https://doi.org/10.1039/c5en00053j.
(92) Guo, W.; Tran, T. N.; Mondal, H.; Schaefer, S.; Huang, L.; Lin, H. Superior CO2/N2 Separation Performance of Highly Branched Poly(1,3 Dioxolane) Plasticized by Polyethylene Glycol. *J Memb Sci* **2022**, *648*. https://doi.org/10.1016/j.memsci.2022.120352.
(93) Liu, J.; Zhang, G.; Clark, K.; Lin, H. Maximizing Ether Oxygen Content in Polymers for Membrane CO 2 Removal from Natural Gas. *ACS Appl Mater Interfaces* **2019**, *11* (11), 10933–10940. https://doi.org/10.1021/acsami.9b01079.
(94) Li, Y.; Yavari, M.; Baldanza, A.; Di Maio, E.; Okamoto, Y.; Lin, H.; Galizia, M. Volumetric Properties and Sorption Behavior of Perfluoropolymers with Dioxolane Pendant Rings. *Ind Eng Chem Res* **2020**, *59* (12), 5276–5286. https://doi.org/10.1021/acs.iecr.9b03411.
(95) van Essen, M.; Thür, R.; Houben, M.; Vankelecom, I. F. J.; Borneman, Z.; Nijmeijer, K. Tortuous Mixed Matrix Membranes: A Subtle Balance between Microporosity and Compatibility. *J Memb Sci* **2021**, *635*. https://doi.org/10.1016/j.memsci.2021.119517.
(96) Shahid, S.; Nijmeijer, K.; Nehache, S.; Vankelecom, I.; Deratani, A.; Quemener, D. MOF-Mixed Matrix Membranes: Precise Dispersion of MOF Particles with Better Compatibility via a Particle Fusion Approach for Enhanced Gas Separation Properties. *J Memb Sci* **2015**, *492*, 21–31. https://doi.org/10.1016/j.memsci.2015.05.015.
(97) Lin, J.-J.; Tsai, W.-C.; Hsu, yen-C.; Chang, W.-H. Polymeric Polyamines and Method for Stabilizing Silver Nanoparticle by Employing the Same. 8013048B2.
(98) Muñoz, D. M.; De La Campa, J. G.; De Abajo, J.; Lozano, A. E. Experimental and Theoretical Study of an Improved Activated Polycondensation Method for Aromatic Polyimides. *Macromolecules* **2007**, *40* (23), 8225–8232. https://doi.org/10.1021/ma070842j.
(99) Kim, J.-S. *Reduction of Silver Nitrate in Ethanol by Poly(N-Vinylpyrrolidone)*; 2007; Vol. 13.
(100) Schindelin, J.; Arganda-Carreras, I.; Frise, E.; Kaynig, V.; Longair, M.; Pietzsch, T.; Preibisch, S.; Rueden, C.; Saalfeld, S.; Schmid, B.; Tinevez, J. Y.; White, D. J.; Hartenstein, V.; Eliceiri, K.; Tomancak, P.; Cardona, A. Fiji: An Open-Source Platform for Biological-Image Analysis. *Nature Methods*. July 2012, pp 676–682. https://doi.org/10.1038/nmeth.2019.
(101) Benoit, D. N.; Zhu, H.; Lilierose, M. H.; Verm, R. A.; Ali, N.; Morrison, A. N.; Fortner, J. D.; Avendano, C.; Colvin, V. L. Measuring the Grafting Density of Nanoparticles in Solution by Analytical Ultracentrifugation and Total Organic Carbon Analysis. *Anal Chem* **2012**, *84* (21), 9238–9245. https://doi.org/10.1021/ac301980a.
(102) Larkin, P. *Infrared and Raman Spectroscopy: Principles and Spectral Interpretation*; Elsevier, 2017.
(103) Silverstein, R. M.; Webster, F. X.; Kiemle, D. J. *Spectrometric Identification of Organic Compounds*, 7th Edition.; 2005.
(104) Günther, H. *NMR Spectroscopy:Basic Principles, Concepts, and Applications in Chemistry, 3rd Edition*, 3rd Edition.; Wiley, 2013.
(105) Miller-Chou, B. A.; Koenig, J. L. A Review of Polymer Dissolution. *Progress in Polymer Science (Oxford)*. August 2003, pp 1223–1270. https://doi.org/10.1016/S0079-6700(03)00045-5.

(106) Fedors, R. F. A Method for Estimating Both the Solubility Parameters and Molar Volumes of Liquids. *Polym Eng Sci* **1974**, *14* (2), 147–154. https://doi.org/10.1002/pen.760140211.
(107) Webb, M. T.; Condes, L. C.; Box, W. J.; Ly, H. G.; Razavi, S.; Galizia, M. Revisiting Experimental Techniques and Theoretical Models for Estimating the Solubility Parameter of Rubbery and Glassy Polymer Membranes. *Journal of Membrane Science Letters* **2023**, *3* (2). https://doi.org/10.1016/j.memlet.2023.100060.
(108) Buszewski, B.; Rafińska, K.; Pomastowski, P.; Walczak, J.; Rogowska, A. Novel Aspects of Silver Nanoparticles Functionalization. *Colloids Surf A Physicochem Eng Asp* **2016**, *506*, 170–178. https://doi.org/10.1016/j.colsurfa.2016.05.058.
(109) Sigel, H.; Martin, B. *Coordinating Properties of the Amide Bond. Stability and Structure of Metal Ion Complexes of Peptides and Related Ligands*. https://pubs.acs.org/sharingguidelines.
(110) Lee, J. H.; Kang, S. W.; Yeom, M. S.; Kim, Y. R.; Choi, H.; Song, D.; Won, J.; Kang, Y. S. A Strong Linear Correlation between the Surface Charge Density on Ag Nanoparticles and the Amount of Propylene Adsorbed. *J Mater Chem A Mater* **2014**, *2* (19), 6987–6993. https://doi.org/10.1039/c4ta00026a.
(111) Shimmin, R. G.; Schoch, A. B.; Braun, P. V. Polymer Size and Concentration Effects on the Size of Gold Nanoparticles Capped by Polymeric Thiols. *Langmuir* **2004**, *20* (13), 5613–5620. https://doi.org/10.1021/la036365p.
(112) Isanejad, M.; Azizi, N.; Mohammadi, T. Pebax Membrane for CO2/CH4 Separation: Effects of Various Solvents on Morphology and Performance. *J Appl Polym Sci* **2017**, *134* (9). https://doi.org/10.1002/app.44531.
(113) Farashi, Z.; Azizi, S.; Rezaei-Dasht Arzhandi, M.; Noroozi, Z.; Azizi, N. Improving CO2/CH4 Separation Efficiency of Pebax-1657 Membrane by Adding Al2O3 Nanoparticles in Its Matrix. *J Nat Gas Sci Eng* **2019**, *72*. https://doi.org/10.1016/j.jngse.2019.103019.
(114) Box, W. J.; Webb, M. T.; Galizia, M. Evaluating the Experimental Uncertainty in Gas and Vapor Sorption/Adsorption Measurements: Fundamental Considerations and Experimental Design Implications. *Ind Eng Chem Res* **2022**, *61* (27), 9856–9868. https://doi.org/10.1021/acs.iecr.2c01414.
(115) Ghosal, K.; Chern, R. T.; Freeman, B. D.; Daly, W. H.; Negulescu, I. I. *Effect of Basic Substituents on Gas Sorption and Permeation in Polysulfone*.
(116) Achoundong, C. S. K.; Bhuwania, N.; Burgess, S. K.; Karvan, O.; Johnson, J. R.; Koros, W. J. Silane Modification of Cellulose Acetate Dense Films as Materials for Acid Gas Removal. *Macromolecules* **2013**, *46* (14), 5584–5594. https://doi.org/10.1021/ma4010583.
(117) Wright, C. T.; Paul, D. R. *Gas Sorption and Transport in UV-Irradiated Poly(2,6-Dimethyl-1,4-Phenylene Oxide) Films*; 1998; Vol. 67.
(118) Webb, M.; Condes, L.; Ly, H.; Box, W.; Razavi, S.; Galizia, M. Mixed Matrix Membranes Containing Silver Nanoparticles: Effect of the Capping Agent Length on the Gas Separation Performance
(119) Energy Agency, I. *World Energy Outlook 2016*; 2040.
(120) Eldridge, R. B. *Olefin/Paraffin Separation Technology: A Review*; 1993; Vol. 32. https://pubs.acs.org/sharingguidelines.
(121) Baker, I. Polyethylene. In *Fifty Materials That Make the World*; Springer International Publishing: Cham, 2018; pp 163–168. https://doi.org/10.1007/978-3-319-78766-4_31.

(122) Han, Y.; Winston Ho, W. S. Recent Advances in Polymeric Facilitated Transport Membranes for Carbon Dioxide Separation and Hydrogen Purification. *Journal of Polymer Science*. John Wiley and Sons Inc 2020, pp 2435–2449. https://doi.org/10.1002/pol.20200187.
(123) Cheng, L.; Liu, G.; Jin, W. Recent Advances in Facilitated Transport Membranes for Olefin/Paraffin Separation. *Discover Chemical Engineering* **2021**, *1* (1). https://doi.org/10.1007/s43938-020-00001-4.
(124) Zhou, T.; Luo, L.; Hu, S.; Wang, S.; Zhang, R.; Wu, H.; Jiang, Z.; Wang, B.; Yang, J. Janus Composite Nanoparticle-Incorporated Mixed Matrix Membranes for CO2 Separation. *J Memb Sci* **2015**, *489*, 1–10. https://doi.org/10.1016/j.memsci.2015.03.070.
(125) Noble, R. D. *ANALYSIS OF FACILITATED TRANSPORT WITH FIXED SITE CARRIER MEMBRANES*; 1990; Vol. 50.
(126) Campos, A. C. C.; Dos Reis, R. A.; Ortiz, A.; Gorri, D.; Ortiz, I. A Perspective of Solutions for Membrane Instabilities in Olefin/Paraffin Separations: A Review. *Ind Eng Chem Res* **2018**, *57* (31), 10071–10085. https://doi.org/10.1021/acs.iecr.8b02013.
(127) Zarca, R.; Ortiz, A.; Gorri, D.; Ortiz, I. Generalized Predictive Modeling for Facilitated Transport Membranes Accounting for Fixed and Mobile Carriers. *J Memb Sci* **2017**, *542*, 168–176. https://doi.org/10.1016/j.memsci.2017.08.010.
(128) Kang, S. W.; Char, K.; Kang, Y. S. Novel Application of Partially Positively Charged Silver Nanoparticles for Facilitated Transport in Olefin/Paraffin Separation Membranes. *Chemistry of Materials* **2008**, *20* (4), 1308–1311. https://doi.org/10.1021/cm071516l.
(129) Šupová, M.; Martynková, G. S.; Barabaszová, K. Effect of Nanofillers Dispersion in Polymer Matrices: A Review. *Sci Adv Mater* **2011**, *3* (1), 1–25. https://doi.org/10.1166/sam.2011.1136.
(130) Adams, R.; Johnson, J. R.; Zhang, C.; Lively, R.; Dai, Y.; Esekhile, O.; Liu, J.; Koros, W. J. *MIXED-MATRIX MEMBRANES*; 2013.
(131) Murshid, N.; Kitaev, V. Role of Poly(Vinylpyrrolidone) (PVP) and Other Sterically Protecting Polymers in Selective Stabilization of (111) and (100) Facets in Pentagonally Twinned Silver Nanoparticles. *Chemical Communications* **2014**, *50* (10), 1247–1249. https://doi.org/10.1039/c3cc48003h.
(132) Peng, D.; Liu, Y.; Wang, S.; Tian, Z.; Xin, Q.; Wu, H.; Chen, J.; Jiang, Z. Facilitated Transport Membranes by Incorporating Different Divalent Metal Ions as CO2 Carriers. *RSC Adv* **2016**, *6* (69), 65282–65290. https://doi.org/10.1039/c6ra09782k.
(133) Chae, I. S.; Kang, S. W.; Park, J. Y.; Lee, Y. G.; Lee, J. H.; Won, J.; Kang, Y. S. Surface Energy-Level Tuning of Silver Nanoparticles for Facilitated Olefin Transport. *Angewandte Chemie - International Edition* **2011**, *50* (13), 2982–2985. https://doi.org/10.1002/anie.201007557.
(134) Restrepo, C. V.; Villa, C. C. Synthesis of Silver Nanoparticles, Influence of Capping Agents, and Dependence on Size and Shape: A Review. *Environ Nanotechnol Monit Manag* **2021**, *15*. https://doi.org/10.1016/j.enmm.2021.100428.
(135) Thanh, N. T. K.; Maclean, N.; Mahiddine, S. Mechanisms of Nucleation and Growth of Nanoparticles in Solution. *Chemical Reviews*. American Chemical Society August 13, 2014, pp 7610–7630. https://doi.org/10.1021/cr400544s.
(136) Kim, D.; Jeong, S.; Moon, J. Synthesis of Silver Nanoparticles Using the Polyol Process and the Influence of Precursor Injection. *Nanotechnology* **2006**, *17* (16), 4019–4024. https://doi.org/10.1088/0957-4484/17/16/004.

(137) Murshid, N.; Kitaev, V. Role of Poly(Vinylpyrrolidone) (PVP) and Other Sterically Protecting Polymers in Selective Stabilization of (111) and (100) Facets in Pentagonally Twinned Silver Nanoparticles. *Chemical Communications* **2014**, *50* (10), 1247–1249. https://doi.org/10.1039/c3cc48003h.
(138) Naik, A. N.; Patra, S.; Sen, D.; Goswami, A. Evaluating the Mechanism of Nucleation and Growth of Silver Nanoparticles in a Polymer Membrane under Continuous Precursor Supply: Tuning of Multiple to Single Nucleation Pathway. *Physical Chemistry Chemical Physics* **2019**, *21* (8), 4193–4199. https://doi.org/10.1039/c8cp06202a.
(139) Li, C. C.; Chang, S. J.; Su, F. J.; Lin, S. W.; Chou, Y. C. Effects of Capping Agents on the Dispersion of Silver Nanoparticles. *Colloids Surf A Physicochem Eng Asp* **2013**, *419*, 209–215. https://doi.org/10.1016/j.colsurfa.2012.11.077.
(140) Shahid, S.; Nijmeijer, K.; Nehache, S.; Vankelecom, I.; Deratani, A.; Quemener, D. MOF-Mixed Matrix Membranes: Precise Dispersion of MOF Particles with Better Compatibility via a Particle Fusion Approach for Enhanced Gas Separation Properties. *J Memb Sci* **2015**, *492*, 21–31. https://doi.org/10.1016/j.memsci.2015.05.015.
(141) Feng, S.; Du, X.; Luo, J.; Zhuang, Y.; Wang, J.; Wan, Y. A Review on Facilitated Transport Membranes Based on π-Complexation for Carbon Dioxide Separation. *Sep Purif Technol* **2023**, *309*. https://doi.org/10.1016/j.seppur.2022.122972.
(142) Savchenko, P.; Zelikovich, D.; Elgavi Sinai, H.; Baer, R.; Mandler, D. The Effect of the Capping Agents of Nanoparticles on Their Redox Potential. *J Am Chem Soc* **2024**. https://doi.org/10.1021/jacs.4c02524.
(143) Chae, I. S.; Kang, S. W.; Park, J. Y.; Lee, Y.; Lee, J. H.; Won, J.; Kang, Y. S. Surface Energy-Level Tuning of Silver Nanoparticles for Facilitated Olefin Transport. *Angewandte Chemie* **2011**, *123* (13), 3038–3041. https://doi.org/10.1002/ange.201007557.
(144) Chandran, S.; Begam, N.; Padmanabhan, V.; Basu, J. K. Confinement Enhances Dispersion in Nanoparticle-Polymer Blend Films. *Nat Commun* **2014**, *5*. https://doi.org/10.1038/ncomms4697.
(145) Sanchez, C. M.; Song, T.; Brennecke, J. F.; Freeman, B. D. Hydrogen Stable Supported Ionic Liquid Membranes with Silver Carriers: Propylene and Propane Permeability and Solubility. *Ind Eng Chem Res* **2020**, *59* (12), 5362–5370. https://doi.org/10.1021/acs.iecr.9b04886.
(146) Quackenbos, H. M. Relation between Intrinsic Viscosity and Molecular Weight. *J Appl Polym Sci* **1980**, *25* (7), 1435–1442. https://doi.org/10.1002/app.1980.070250717.
(147) A. Masuelli, M. Intrinsic Viscosity Determination of High Molecular Weight Biopolymers by Different Plot Methods. Chia Gum Case. *Journal of Polymer and Biopolymer Physics Chemistry* **2018**, *6* (1), 13–25. https://doi.org/10.12691/jpbpc-6-1-2.
(148) Scholes, C. A.; Chen, G. Q.; Lu, H. T.; Kentish, S. E. Crosslinked PEG and PEBAX Membranes for Concurrent Permeation Ofwater and Carbon Dioxide. *Membranes (Basel)* **2015**, *6* (1). https://doi.org/10.3390/membranes6010001.
(149) Yuan, H.; Liu, X.; Zhang, S.; Lu, J. Pervaporative Desulfurization of N-Heptane/Thiophene Model Gasoline for Modified Polyether-Block-Amide (Pebax) Membrane. *Chemical Engineering and Processing - Process Intensification* **2019**, *144*. https://doi.org/10.1016/j.cep.2019.107632.
(150) Wright, C. T.; Paul, D. R. *Gas Sorption and Transport in UV-Irradiated Poly(2,6-Dimethyl-1,4-Phenylene Oxide) Films*; 1998; Vol. 67.

(151) Salinas, O.; Ma, X.; Wang, Y.; Han, Y.; Pinnau, I. Carbon Molecular Sieve Membrane from a Microporous Spirobisindane-Based Polyimide Precursor with Enhanced Ethylene/Ethane Mixed-Gas Selectivity. *RSC Adv* **2017**, *7* (6), 3265–3272. https://doi.org/10.1039/c6ra24699k.
(152) Tomé, L. C.; Mecerreyes, D.; Freire, C. S. R.; Rebelo, L. P. N.; Marrucho, I. M. Polymeric Ionic Liquid Membranes Containing IL-Ag+ for Ethylene/Ethane Separation via Olefin-Facilitated Transport. *J Mater Chem A Mater* **2014**, *2* (16), 5631–5639. https://doi.org/10.1039/c4ta00178h.
(153) Rungta, M.; Xu, L.; Koros, W. J. Carbon Molecular Sieve Dense Film Membranes Derived from Matrimid® for Ethylene/Ethane Separation. *Carbon N Y* **2012**, *50* (4), 1488–1502. https://doi.org/10.1016/j.carbon.2011.11.019.
(154) Alebrahim, T.; Esmaeili, N.; Zhang, G.; Lin, H. Retarded O2 Transport in Co2+-Coordinated Supramolecular Polymer Networks for Membrane CO2/O2 Separations. *J Mater Chem A Mater* **2024**, *12* (27), 16921–16927. https://doi.org/10.1039/d4ta02376e.
(155) Pozun, Z. D.; Tran, K.; Shi, A.; Smith, R. H.; Henkelman, G. Why Silver Nanoparticles Are Effective for Olefin/Paraffin Separations. *Journal of Physical Chemistry C* **2011**, *115* (5), 1811–1818. https://doi.org/10.1021/jp110579s.
(156) Alentiev, A.; Yampolskii, Y. Correlation of Gas Permeability and Diffusivity with Selectivity: Orientations of the Clouds of the Data Points and the Effects of Temperature. *Ind Eng Chem Res* **2013**, *52* (26), 8864–8874. https://doi.org/10.1021/ie302680r.
(157) Costello, L. M.; Koros, W. J. *Temperature Dependence of Gas Sorption and Transport Properties in Polymers: Measurement and Applications Background and Theory*; 1992; Vol. 31. https://pubs.acs.org/sharingguidelines.
(158) Lasseuguette, E.; Malpass-Evans, R.; Carta, M.; McKeown, N. B.; Ferrari, M. C. Temperature and Pressure Dependence of Gas Permeation in a Microporous Tröger's Base Polymer. *Membranes (Basel)* **2018**, *8* (4). https://doi.org/10.3390/membranes8040132.
(159) Fu, S.; Sanders, E. S.; Kulkarni, S. S.; Wenz, G. B.; Koros, W. J. Temperature Dependence of Gas Transport and Sorption in Carbon Molecular Sieve Membranes Derived from Four 6FDA Based Polyimides: Entropic Selectivity Evaluation. *Carbon N Y* **2015**, *95*, 995–1006. https://doi.org/10.1016/j.carbon.2015.09.005.
(160) Singh, A.; Koros, W. J. *Significance of Entropic Selectivity for Advanced Gas Separation Membranes*; 1996. https://pubs.acs.org/sharingguidelines.
(161) Costello, L. M.; Koros, W. J. *Temperature Dependence of Gas Sorption and Transport Properties in Polymers: Measurement and Applications Background and Theory*; 1992; Vol. 31. https://pubs.acs.org/sharingguidelines.
(162) Merkel, T. C.; Bondar, V.; Nagai, K.; Freeman, B. D.; Yampolskii, P. Y. Gas Sorption, Diffusion, and Permeation in Poly(2,2-Bis(Trifluoromethyl)-4,5-Difluoro-l,3-Dioxole-Co-Tetrafluoroethylene). *Macromolecules* **1999**, *32* (25), 8427–8440. https://doi.org/10.1021/ma990685r.
(163) Liu, L.; Feng, X.; Chakma, A. Unusual Behavior of Poly(Ethylene Oxide)/AgBF4 Polymer Electrolyte Membranes for Olefin-Paraffin Separation. *Sep Purif Technol* **2004**, *38* (3), 255–263. https://doi.org/10.1016/j.seppur.2003.11.013.
(164) Shelekhin, A. B.; Dixon, A. G.; Ma, Y. H. *Theory of Gas Diffusion and Permeation in Inorganic Molecular-Sieve Membranes*.
(165) Rahman, M. M.; Shishatskiy, S.; Abetz, C.; Georgopanos, P.; Neumann, S.; Khan, M. M.; Filiz, V.; Abetz, V. Influence of Temperature upon Properties of Tailor-Made PEBAX®

MH 1657 Nanocomposite Membranes for Post-Combustion CO2 Capture. *J Memb Sci* **2014**, *469*, 344–354. https://doi.org/10.1016/j.memsci.2014.06.048.
(166) Glasstone, S. ; L. K. J. ; E. H. *The Theory of Rate Processes*; McGraw-Hill: New York, 1941.
(167) Fu, S.; Sanders, E. S.; Kulkarni, S. S.; Wenz, G. B.; Koros, W. J. Temperature Dependence of Gas Transport and Sorption in Carbon Molecular Sieve Membranes Derived from Four 6FDA Based Polyimides: Entropic Selectivity Evaluation. *Carbon N Y* **2015**, *95*, 995–1006. https://doi.org/10.1016/j.carbon.2015.09.005.
(168) Rungta, M.; Xu, L.; Koros, W. J. Carbon Molecular Sieve Dense Film Membranes Derived from Matrimid® for Ethylene/Ethane Separation. *Carbon N Y* **2012**, *50* (4), 1488–1502. https://doi.org/10.1016/j.carbon.2011.11.019.
(169) Wang, S.; Liu, Y.; Huang, S.; Wu, H.; Li, Y.; Tian, Z.; Jiang, Z. Pebax-PEG-MWCNT Hybrid Membranes with Enhanced CO2 Capture Properties. *J Memb Sci* **2014**, *460*, 62–70. https://doi.org/10.1016/j.memsci.2014.02.036.
(170) Asad, S.; Anwar, N.; Shah, M.; Anwar, Z.; Arif, M.; Rauf, M.; Ali, K.; Shah, M.; Murad, W.; Albadrani, G. M.; Altyar, A. E.; Abdel-Daim, M. M. Biological Synthesis of Silver Nanoparticles by Amaryllis Vittata (L.) Herit: From Antimicrobial to Biomedical Applications. *Materials* **2022**, *15* (16). https://doi.org/10.3390/ma15165478.
(171) Lau, C. H.; Li, P.; Li, F.; Chung, T. S.; Paul, D. R. Reverse-Selective Polymeric Membranes for Gas Separations. *Progress in Polymer Science*. May 2013, pp 740–766. https://doi.org/10.1016/j.progpolymsci.2012.09.006.
(172) Van Krevelen, D. W. *Properties of Polymers: Their Correlation with Chem Structure: Their Numerical Estimation and Prediction from Additive Group Contributions*; Elsevier: Amsterdam, The Netherlands, 1990.
(173) Kim, J. H.; Min, R.; Kim, H. S.; Won, J.; Kang, Y. S. *Facilitated Transport of Ethylene across Polymer Membranes Containing Silver Salt: Effect of HBF 4 on the Photoreduction of Silver Ions*; 2003; Vol. 212.
(174) Martínez-Izquierdo, L.; Perea-Cachero, A.; Malankowska, M.; Téllez, C.; Coronas, J. A Comparative Study between Single Gas and Mixed Gas Permeation of Polyether-Block-Amide Type Copolymer Membranes. *J Environ Chem Eng* **2022**, *10* (5). https://doi.org/10.1016/j.jece.2022.108324.
(175) Wu, S.; Liang, J.; Shi, Y.; Huang, M.; Bi, X.; Wang, Z.; Jin, J. Design of Interchain Hydrogen Bond in Polyimide Membrane for Improved Gas Selectivity and Membrane Stability. *J Memb Sci* **2021**, *618*. https://doi.org/10.1016/j.memsci.2020.118659.
(176) Bye, K. P.; Loianno, V.; Pham, T. N.; Liu, R.; Riffle, J. S.; Galizia, M. Pure and Mixed Fluid Sorption and Transport in Celazole® Polybenzimidazole: Effect of Plasticization. *J Memb Sci* **2019**, *580*, 235–247. https://doi.org/10.1016/j.memsci.2019.03.031.
(177) Hansen; Charles M. *HANSEN SOLUBILITY PARAMETERS A User's Handbook Second Edition*; 2007.
(178) Larocca, N. M.; Pessan, L. A. Effect of Antiplasticisation on the Volumetric, Gas Sorption and Transport Properties of Polyetherimide. *J Memb Sci* **2003**, *218* (1–2), 69–92. https://doi.org/10.1016/S0376-7388(03)00139-X.
(179) Lee, J. S.; Leisen, J.; Choudhury, R. P.; Kriegel, R. M.; Beckham, H. W.; Koros, W. J. Antiplasticization-Based Enhancement of Poly(Ethylene Terephthalate) Barrier Properties. *Polymer (Guildf)* **2012**, *53* (1), 213–222. https://doi.org/10.1016/j.polymer.2011.11.006.

(180) Zekriardehani, S.; Joshi, A. S.; Jabarin, S. A.; Gidley, D. W.; Coleman, M. R. Effect of Dimethyl Terephthalate and Dimethyl Isophthalate on the Free Volume and Barrier Properties of Poly(Ethylene Terephthalate) (PET): Amorphous PET. *Macromolecules* **2018**, *51* (2), 456–467. https://doi.org/10.1021/acs.macromol.7b02230.
(181) Hoy, K. L. *Solubility Parameter as a Design Parameter for Water Borne Polymers and Coatings*.
(182) Hansen, C. M. 50 Years with Solubility Parameters - Past and Future. *Prog Org Coat* **2004**, *51* (1), 77–84. https://doi.org/10.1016/j.porgcoat.2004.05.004.
(183) Ghebremeskel, A. N.; Vemavarapu, C.; Lodaya, M. Use of Surfactants as Plasticizers in Preparing Solid Dispersions of Poorly Soluble API: Selection of Polymer-Surfactant Combinations Using Solubility Parameters and Testing the Processability. *Int J Pharm* **2007**, *328* (2), 119–129. https://doi.org/10.1016/j.ijpharm.2006.08.010.
(184) Hancock " ', B. C.; York, P.; Rowe, R. C. *Intemational Journal of Pharmaceutics The Use of Solubility Parameters in Pharmaceutical Dosage Form Design*; 1997; Vol. 148.
(185) Karan, S.; Jiang, Z.; Livingston, A. G. Sub–10 Nm Polyamide Nanofilms with Ultrafast Solvent Transport for Molecular Separation. *Science (1979)* **2015**, *348*, 1347–1351.
(186) Kushida, W.; Gonzales, R. R.; Shintani, T.; Matsuoka, A.; Nakagawa, K.; Yoshioka, T.; Matsuyama, H. Organic Solvent Mixture Separation Using Fluorine-Incorporated Thin Film Composite Reverse Osmosis Membrane. *J Mater Chem A Mater* **2022**, *10* (8), 4146–4156. https://doi.org/10.1039/d1ta09192a.
(187) Postel, S.; Spalding, G.; Chirnside, M.; Wessling, M. On Negative Retentions in Organic Solvent Nanofiltration. *J Memb Sci* **2013**, *447*, 57–65. https://doi.org/10.1016/j.memsci.2013.06.009.
(188) da Silva Burgal, J.; Peeva, L.; Marchetti, P.; Livingston, A. Controlling Molecular Weight Cut-off of PEEK Nanofiltration Membranes Using a Drying Method. *J Memb Sci* **2015**, *493*, 524–538. https://doi.org/10.1016/j.memsci.2015.07.012.
(189) Andecochea Saiz, C.; Darvishmanesh, S.; Buekenhoudt, A.; Van der Bruggen, B. Shortcut Applications of the Hansen Solubility Parameter for Organic Solvent Nanofiltration. *J Memb Sci* **2018**, *546*, 120–127. https://doi.org/10.1016/j.memsci.2017.10.016.
(190) Venkatram, S.; Kim, C.; Chandrasekaran, A.; Ramprasad, R. Critical Assessment of the Hildebrand and Hansen Solubility Parameters for Polymers. *J Chem Inf Model* **2019**. https://doi.org/10.1021/acs.jcim.9b00656.
(191) van Krevelen, D. W. *Properties of Polymers: Their Correlation with Chemical Structure, Their Numerical Estimation and Prediction from Additive Group Contributions*, 3rd ed.; Elsevier: Amsterdam, 1990.
(192) Gee, B. G. *282. Gee, Ibid., 276 ; Cf. Also Flory*; Gee and Treloar, 1942; Vol. 10.
(193) Mah, C. H.; Wu, Q. Y.; Deen, G. R. Effect of Nature of Chemical Crosslinker on Swelling and Solubility Parameter of a New Stimuli-Responsive Cationic Poly(N-Acryloyl-N′-Propyl Piperazine) Hydrogel. *Polymer Bulletin* **2018**, *75* (1), 221–238. https://doi.org/10.1007/s00289-017-2029-8.
(194) Kim, C.; Chandrasekaran, A.; Huan, T. D.; Das, D.; Ramprasad, R. Polymer Genome: A Data-Powered Polymer Informatics Platform for Property Predictions. *Journal of Physical Chemistry C*. American Chemical Society August 9, 2018, pp 17575–17585. https://doi.org/10.1021/acs.jpcc.8b02913.
(195) Wu, A. X.; Lin, S.; Mizrahi Rodriguez, K.; Benedetti, F. M.; Joo, T.; Grosz, A. F.; Storme, K. R.; Roy, N.; Syar, D.; Smith, Z. P. Revisiting Group Contribution Theory for

Estimating Fractional Free Volume of Microporous Polymer Membranes. *J Memb Sci* **2021**, *636*. https://doi.org/10.1016/j.memsci.2021.119526.
(196) Kent, D. J.; Rowe, R. C. Solubility Studies on Ethyl Cellulose Used in Film Coating. *Journal of Pharmacy and Pharmacology* **1978**, *30* (1), 808–810. https://doi.org/10.1111/j.2042-7158.1978.tb13403.x.
(197) Franco, P.; De Marco, I. The Use of Poly(N-Vinyl Pyrrolidone) in the Delivery of Drugs: A Review. *Polymers*. MDPI AG May 1, 2020. https://doi.org/10.3390/POLYM12051114.
(198) Li, L.; Jiang, Z.; Xu, J.; Fang, T. Predicting Poly(Vinyl Pyrrolidone)'s Solubility Parameter and Systematic Investigation of the Parameters of Electrospinning with Response Surface Methodology. *J Appl Polym Sci* **2014**, *131* (11). https://doi.org/10.1002/app.40304.
(199) Nasouri, K.; Shoushtari, A. M.; Mojtahedi, M. R. M. Thermodynamic Studies on Polyvinylpyrrolidone Solution Systems Used for Fabrication of Electrospun Nanostructures: Effects of the Solvent. *Advances in Polymer Technology* **2015**, *34* (3). https://doi.org/10.1002/adv.21495.
(200) Pina, M. F.; Zhao, M.; Pinto, J. F.; Sousa, J. J.; Craig, D. Q. M. The Influence of Drug Physical State on the Dissolution Enhancement of Solid Dispersions Prepared via Hot-Melt Extrusion: A Case Study Using Olanzapine. *J Pharm Sci* **2014**, *103* (4), 1214–1223. https://doi.org/10.1002/jps.23894.
(201) Yin, H.; Chua, Y. Z.; Yang, B.; Schick, C.; Harrison, W. J.; Budd, P. M.; Böhning, M.; Schönhals, A. First Clear-Cut Experimental Evidence of a Glass Transition in a Polymer with Intrinsic Microporosity: PIM-1. *Journal of Physical Chemistry Letters* **2018**, *9* (8), 2003–2008. https://doi.org/10.1021/acs.jpclett.8b00422.
(202) Minelli, M.; Friess, K.; Vopička, O.; De Angelis, M. G. Modeling Gas and Vapor Sorption in a Polymer of Intrinsic Microporosity (PIM-1). *Fluid Phase Equilib* **2013**, *347*, 35–44. https://doi.org/10.1016/j.fluid.2013.03.003.
(203) Yushkin, A. A.; Anokhina, T. S.; Bazhenov, S. D.; Borisov, I. L.; Budd, P. M.; Volkov, A. V. Sorption and Nanofiltration Characteristics of PIM-1 Material in Polar and Non-Polar Solvents. *Petroleum Chemistry* **2018**, *58* (13), 1154–1158. https://doi.org/10.1134/S096544411813011X.
(204) Thomas, S.; Pinnau, I.; Du, N.; Guiver, M. D. Pure- and Mixed-Gas Permeation Properties of a Microporous Spirobisindane-Based Ladder Polymer (PIM-1). *J Memb Sci* **2009**, *333* (1–2), 125–131. https://doi.org/10.1016/j.memsci.2009.02.003.
(205) Nagai, K.; Masuda, T.; Nakagawa, T.; Freeman, B. D.; Pinnau, I. *Poly[1-(Trimethylsilyl)-1-Propyne] and Related Polymers: Synthesis, Properties and Functions*. www.elsevier.com/locate/ppolysci.
(206) Morisato, A.; Freeman, B. D.; Pinnau, I.; Casillas, C. G. Pure Hydrocarbon Sorption Properties of Poly(1-Trimethylsilyl-1-Propyne) (PTMSP), Poly(1-Phenyl-1-Propyne) (PPP), and PTMSP/PPP Blends. *J Polym Sci B Polym Phys* **1996**, *34* (11), 1925–1934. https://doi.org/10.1002/(SICI)1099-0488(199608)34:11<1925::AID-POLB10>3.0.CO;2-B.
(207) Hornik, K.; Stinchcombe, M.; White, H. Multilayer Feedforward Networks Are Universal Approximators, Neural Networks. *Neural Networks* **1989**, *2*, 359–366.
(208) Barton, A. F. M. *CRC Handbook of Polymer-Liquid Interaction Parameters and Solubility Parameters*; CRC Press: Boca Raton, 1990.

(209) Covitch, M. J.; Trickett, K. J. How Polymers Behave as Viscosity Index Improvers in Lubricating Oils. *Advances in Chemical Engineering and Science* **2015**, *05* (02), 134–151. https://doi.org/10.4236/aces.2015.52015.
(210) ACCU DYNE TEST. Surface Tension, Hansen Solubility Parameters, Molar Volume, Enthalpy of Evaporation, and Molecular Weight of Selected Liquids. *https://www.accudynetest.com/solubility_table.html* **2024**.
(211) Yin, H.; Chua, Y. Z.; Yang, B.; Schick, C.; Harrison, W. J.; Budd, P. M.; Böhning, M.; Schönhals, A. First Clear-Cut Experimental Evidence of a Glass Transition in a Polymer with Intrinsic Microporosity: PIM-1. *Journal of Physical Chemistry Letters* **2018**, *9* (8), 2003–2008. https://doi.org/10.1021/acs.jpclett.8b00422.
(212) Yu, M.; Foster, A. B.; Alshurafa, M.; Luque-Alled, J. M.; Gorgojo, P.; Kentish, S. E.; Scholes, C. A.; Budd, P. M. CO2 Separation Using Thin Film Composite Membranes of Acid-Hydrolyzed PIM-1. *J Memb Sci* **2023**, *679*. https://doi.org/10.1016/j.memsci.2023.121697.
(213) Li, F. Y.; Xiao, Y.; Chung, T. S.; Kawi, S. High-Performance Thermally Self-Cross-Linked Polymer of Intrinsic Microporosity (PIM-1) Membranes for Energy Development. *Macromolecules* **2012**, *45* (3), 1427–1437. https://doi.org/10.1021/ma202667y.
(214) Jue, M. L.; McKay, C. S.; McCool, B. A.; Finn, M. G.; Lively, R. P. Effect of Nonsolvent Treatments on the Microstructure of PIM-1. *Macromolecules* **2015**, *48* (16), 5780–5790. https://doi.org/10.1021/acs.macromol.5b01507.
(215) Mah, C. H.; Wu, Q. Y.; Deen, G. R. Effect of Nature of Chemical Crosslinker on Swelling and Solubility Parameter of a New Stimuli-Responsive Cationic Poly(N-Acryloyl-N′-Propyl Piperazine) Hydrogel. *Polymer Bulletin* **2018**, *75* (1), 221–238. https://doi.org/10.1007/s00289-017-2029-8.
(216) Ilyin, S. O.; Makarova, V. V.; Arinina, M. P.; Litvinova, E. G.; Khotimskii, V. S.; Kulichikhin, V. G. Phase Equilibrium and Rheology of Poly(1-Trimethylsilyl-1-Propyne) Solutions. *Polymer Science - Series A* **2017**, *59* (1), 1–11. https://doi.org/10.1134/S0965545X17010059.
(217) Malakhov, A. O.; Dibrov, G. A.; Litvinova, E. G.; Novitsky, E. G. Gas Permeability of Homogeneous and Composite Membranes Based on Poly(Trimethylsilylpropyne)/Poly(Vinyltrimethylsilane) Blends. *Petroleum Chemistry* **2015**, *55* (10), 803–809. https://doi.org/10.1134/S096554411510014X.
(218) Nagai, K.; Higuchi, A.; Nakagawa, T. Gas Permeability and Stability of Poly(1-trimethylsilyl-1-propyne-co-1-phenyl-1-propyne) Membranes. *J Polym Sci B Polym Phys* **1995**, *33* (2), 289–298. https://doi.org/10.1002/polb.1995.090330214.
(219) Chen, H.; Zhang, E.; Dai, X.; Yang, W.; Liu, X.; Qiu, X.; Liu, W.; Ji, X. Influence of Solvent Solubility Parameter on the Power Law Exponents and Critical Concentrations of One Soluble Polyimide in Solution. *Journal of Polymer Research* **2019**, *26* (2). https://doi.org/10.1007/s10965-018-1694-0.
(220) Dong, G.; Li, H.; Chen, V. Factors Affect Defect-Free Matrimid® Hollow Fiber Gas Separation Performance in Natural Gas Purification. *J Memb Sci* **2010**, *353* (1–2), 17–27. https://doi.org/10.1016/j.memsci.2010.02.012.
(221) Bevington, P. R.; Robinson, D. K. *Data Reduction and Error Analysis for the Physical Sciences*, 3rd ed.; McGraw-Hill: Boston, 2003.
(222) Tellinghuisen, J. Statistical Error Propagation. *Journal of Physical Chemistry A* **2001**, *105* (15), 3917–3921. https://doi.org/10.1021/jp003484u.